Title
Synthesis and Ligand-Enabled Reactivity of Transition Metal Complexes Bearing a Redox-Active Bis(phenoxy)amide Ligand

Author
Hollas, Aaron M.

Publication Date
2016

UNIVERSITY OF CALIFORNIA,
IRVINE

Synthesis and Ligand-Enabled Reactivity of Transition Metal Complexes Bearing a Redox-Active Bis(phenoxy)amide Ligand

DISSERTATION

submitted in partial satisfaction of the requirements
for the degree of

DOCTOR OF PHILOSOPHY

in Chemistry

by

Aaron M. Hollas

Dissertation Committee:
Professor Alan F. Heyduk, Chair
Professor Andrew S. Borovik
Professor William J. Evans

2016

DEDICATION

To

My family and friends

TABLE OF CONTENTS

LIST OF FIGURES

LIST OF TABLES

LIST OF SCHEMES

LIST OF CHARTS

ACKNOWLEDGMENTS

I would like to thank my family, whose support and encouragement throughout every stage of my life have gotten me this far. I would also like to thank my friends; words can’t express how important your support and friendship have been throughout grad school.

Professor Alan Heyduk, thank you for your mentorship and guidance for the past five years. I’d also like to thank Professor Andy Borovik and Professor Bill Evans for serving on all my committees throughout grad school.

I’m grateful for the excellent facilities available at UCI and the people who maintain and run them. Thank you Dr. Joe Ziller, Dr. Phil Dennison, Dr. John Greaves, Dr. Dmitry Fishman, Dr. Beniam Berhane, and Dr. Nathan Crawford for all you do to ensure the availability of the tools needed for research to progress here at UCI. I’d also like to thank the Borovik group for allowing use of their EPR spectrometer and the Evans group for allowing use of their elemental analysis instrument.

Thank you to Dr. Jordan Corbey and Jason Jones for the work you’ve done for me in the X-ray facility.

Thank you to past Heyduk group members who helped train me when I first joined the group; Dr. Rui Munha, Dr. Geza Szigethy, Dr. Dave Shaffer, Dr. Wes Kramer, and Dr. Janice Wong. Thank you to the current group members who make every day in lab a joy and also helped with dissertation edits; Elaine Seraya, Kyle Rosenkoetter, Lindsay Cameron, Mikey Wojnar, and Wing-Sy Derioux. I would also like to thank Dr. Ryan Zarkesh, whose previous work in the group laid the foundation for Chapters 2 & 3.

The work described was supported by grants from the National Science Foundation.

CURRICULUM VITAE

Aaron M. Hollas

Education

University of California, Irvine, CA *2011-2016*
Ph.D., Chemistry
Research Advisor: Professor Alan F. Heyduk
Dissertation: Synthesis and Ligand-Enabled Reactivity of Transition Metal Complexes Bearing a Redox-Active Bis(phenoxy)amide Ligand

Texas A&M University, College Station, TX *2006-2010*
B.S., *magna cum laude*, Chemistry
Research Advisor: Professor Oleg V. Ozerov

Research Experience

University of California, Irvine, Department of Chemistry *2011-2016*
Graduate Research Advisor, Professor Alan F. Heyduk

- Examined the Synthesis and Reactivity of Redox-Active Ligand-Supported Transition Metal Complexes

Synthesis and reactivity studies of tantalum-oxo complexes

- Prepared tantalum-oxo complexes supported by a redox-active ligand and investigated their C–H bond activation and oxygen-atom transfer reactivity. Characterized complexes by multinuclear NMR and electronic absorption spectroscopy along with X-ray diffraction analysis and cyclic voltammetry.

Synthesis and characterization of chromium complexes of a redox-active ligand

- Established synthetic methods to prepare chromium complexes of a redox-active ligand in a range of ligand oxidation states. Established metal and ligand oxidation states utilizing electronic absorption spectroscopy, Evans method analysis, and X-ray diffraction analysis. Provided further insight into electronic structure and solution behavior with cyclic voltammetry.

Modulation of electrochemical properties of a redox-active ligand

- Recognized the tunability of ligand-based redox events over one volt through variation of ancillary ligand donor strength in $(ONO^{sq})TaX_3$ complexes. Established the electronic influence of the ancillary ligands through cyclic voltammetry and electron paramagnetic resonance spectroscopy.

ExxonMobil Chemical, Baytown, TX *2010-2011*
Laboratory Technician

- Synthesized group 4 transition metal complexes
  - Developed synthetic methods for ligand frameworks and metallation strategies to generate new metallocene-based olefin polymerization catalysts of the group 4 transition metals, resulting in patentable technology.

Texas A&M University, College Station, TX *2009-2010*
Undergraduate Research Advisor, Professor Oleg V. Ozerov

- Synthesized and characterized palladium complexes
  - Executed new synthetic routes for carbazole-based pincer complexes of palladium, gaining introductory knowledge into ligand design principles and synthetic inorganic techniques.

Publications, Presentations, and Patents

- **Hollas, A.M**.; Ziller, J.W.; Heyduk, A.F. "O_2 Activation and Substrate Oxidations using a Redox-Active [ONO] Ligand Complex of Tantalum(V)", *Manuscript in Preparation*
- **Hollas, A.M.**, Heyduk, A.F. Chromium complexes of the redox-active [ONO] ligand and oxygen-atom transfer reactivity, 251st ACS National Meeting, March 2016, San Diego, CA (*Oral Presentation*)
- **Hollas, A.M.**, Heyduk, A.F. Chromium complexes of the redox-active ONO ligand, 248th ACS National Meeting, August 2014, San Francisco, CA (*Oral Presentation*)
- Stewart, I.C.; Brown, S.D.; Atienza, C.C.H.; Harris, D.T.; **Hollas, A.M.** (ExxonMobil Chemical) "Process of Producing Polyolefins Using Metallocene Polymerization Catalysts and Copolymers Therefrom", WO 2014169017 A1, October 16, 2014.
- **Hollas, A.M.**; Gu, W.; Bhuvanesh, N.; Ozerov, O.V. "Synthesis and Characterization of Pd Complexes of a Carbazolyl/Bis(Imine) NNN Pincer Ligand", *Inorg. Chem.* **2011**, *50*, 3673-3679.
- **Hollas, A.M.**, Ozerov, O.V. Novel Synthesis of Carbazole-Based NNN Pincer Ligands: Group 10 Metal Complexes, 239th ACS National Meeting, March 2010, San Francisco, CA (*Poster Presentation*)
- **Hollas, A.M.**, Ozerov, O.V. Synthesis of (NNN)Pd-X Complexes and Their Potential Application to Water Oxidation, CCI Solar Annual Meeting, February 2010, Huntington Beach, CA (*Poster Presentation*)

Teaching Experience

University of California, Irvine, Department of Chemistry

- Inorganic Chemistry Lab – Head TA *Winter 2015 & 2016, Spring 2015*
  - Organized and directed weekly TA meetings, coordinated and performed laboratory maintenance and weekly reagent/equipment availability with stockroom manager. Directed experiment troubleshooting and resulting laboratory manual updates and corrections.
- Organic Synthesis Lab *Fall 2014 & 2015*
  - Taught advanced organic techniques (safe use of pyrophorics, synthesis of chiral products, etc.) to senior level students.
- Inorganic Chemistry Lab *Spring 2012 & 2013,Winter 2014*
  - Trained senior level students in synthetic inorganic chemistry, including schlenk line and glove box use of air-sensitive chemicals.
- Organic Chemistry Lab *Fall 2011, Winter 2012*
  - Provided instruction of introductory level organic laboratory techniques to sophomore level students.
- Inorganic Chemistry Lecture *Fall 2012*
  - Conducted bi-weekly discussion sections and demonstrated problem-solving approaches with prepared problem sets.

ABSTRACT OF THE DISSERTATION

Synthesis and Ligand-Enabled Reactivity of Transition Metal
Complexes Bearing a Redox-Active Bis(phenoxy)amide Ligand

By

Aaron M. Hollas

Doctor of Philosophy in Chemistry

University of California, Irvine, 2016

Professor Alan F. Heyduk, Chair

The work described herein focuses on the ability of redox-active ligands to enable multi-electron reactivity at transition metal centers. A parallel theme is the effect of ancillary ligands on controlling and modulating the electronic structure of the redox-active ligand and metal center in addition to ancillary ligand effects as they relate to controlling the primary coordination sphere of the metal.

Chapter 1 provides a basic introduction to the field of redox-active ligands, describing general features of this ligand class and providing a sample of specific case-studies which detail how redox-active ligands have been utilized in enabling redox-reactions at a transition metal center.

Chapter 2 describes the effects of ancillary ligands on a redox-active ligand containing complex of the general formula $(ONO^{sq})TaX_3$ (where $(ONO^{cat})H_3$ = bis(3,5-di-tert-butyl- 2-phenol)amine). The effect of the ancillary ligand X on the electronic structure of the $(ONO^{sq})^{2-}$ ligand is probed by cyclic voltammetry and electron paramagnetic resonance spectroscopy, both of which indicate a strong correlation between the $(ONO^{sq})^{2-}$ electronic structure and the donor strength of ligand X.

Chapter 3 details the synthesis and characterization of tantalum-oxo complexes of the ONO ligand platform. Oxo complexes of the formula $[(ONO^{q})Ta(OR)_2(\mu\text{–}O)]_2$ were prepared with two alkoxide –R groups, *tert*-butoxide and trifluoroethoxide, which were also compared in Chapter 2. Both complexes were found to affect C–H activation of 9,10-dihydroanthracene and also oxygen-atom transfer to trimethylphosphine, redox processes enabled at a d^0 metal center by the redox-active ligand. A kinetic comparison between the two complexes is also presented.

Chapter 4 presents the synthesis and characterization of chromium complexes of the ONO ligand. Complexes bearing the three stable redox forms of the ONO ligand have been prepared, with the chromium center showing a strong proclivity for the Cr(III) oxidation state. Dimeric ONO complexes of chromium are also described and the affects of neutral ancillary ligands on structural morphology are presented.

Chapter 5 reports the synthesis of ONO and DOPO (where DOPO = 2,4,6,8-tetra-*tert*-butyl-1,9-dioxophenoxazinate) complexes of chromium which bear weakly coordinating trifluoromethanesulfonate (triflate) groups. The complexes are used to pursue chromium-oxo complexes by deprotonation of coordinated water in an attempt to achieve sulfide oxidation. Evidence for water coordination and deprotonation via electronic absorption spectroscopy is presented.

Chapter 6 describes the synthesis of heteroleptic ONO complexes of titanium, vanadium, manganese, and nickel. The titanium, manganese, and nickel complexes represent the final members of the first-row transition metal series of heteroleptic ONO complexes. Fundamental studies establishing the metal oxidation state and ONO ligand form are achieved by electronic absorption spectroscopy, X-ray diffraction analysis, and EPR spectroscopy.

Chapter 1
Introduction

Background of Redox-Active Ligands

Classical coordination chemistry describes ligands as X-type donors, such as halides, alkoxides, and amides, and L-type donors, such as amines, phosphines, and ethers.[1] This descriptive system for innocent ligands allows a straightforward assignment of the metal oxidation state and *d*-electron count as a function of the type and number of donor groups.[1,2] The simplicity of this approach breaks down upon incorporation of redox non-innocent ligands into the coordination sphere of a transition metal. The redox non-innocent class of ligands are not well-described by the X-type and L-type formalisms, displaying significant orbital mixing from energetically similar metal and ligand orbitals and introducing ambiguity as to the charge assignment on the ligand and the oxidation state of the metal.[2–5] Though often used interchangeably, the term redox-active refers to ligands which can access multiple redox forms when coordinated to a metal center. While some ligands can be described by either term in different instances, the interchangeable use of these terms is often a contentious subject. One might argue that when experiment and theory allow for an assignment of the charge on a potentially non-innocent ligand (which can also access multiple redox forms), and therefore also assign the corresponding metal oxidation state, the ligand is best-described as being redox-active.[6] An early example of ligand non-innocence was recognized in dithiolene complexes of nickel, wherein nickel complexes were coordinated to two dithiolene ligands in a square planar geometry.[7–9] Electronic structure assignments were proposed for these complexes (Scheme 1.1) which placed the metal center in the Ni(II) or Ni(IV) oxidation state.[7,10,11] In-depth experimental and theoretical analysis of these complexes determined the best description as a Ni(II) center coordinated by two dithiolate radical anions, with significant covalency in the between the metal and ligand frontier molecular orbitals.[9] The redox-active nature of dithiolene ligands was demonstrated electrochemically and synthetically, wherein the neutral, anionic, and dianionic members of the electron transfer series were reported as stable species (Scheme 1.1).[10,12,13] In all cases, ligand-centered reduction and conservation of the Ni(II) oxidation state occurred.

Scheme 1.1. **Top**. Previously proposed electronic structures of neutral nickel-dithiolene complexes. **Bottom**. Electron transfer series of nickel-dithiolene complexes.

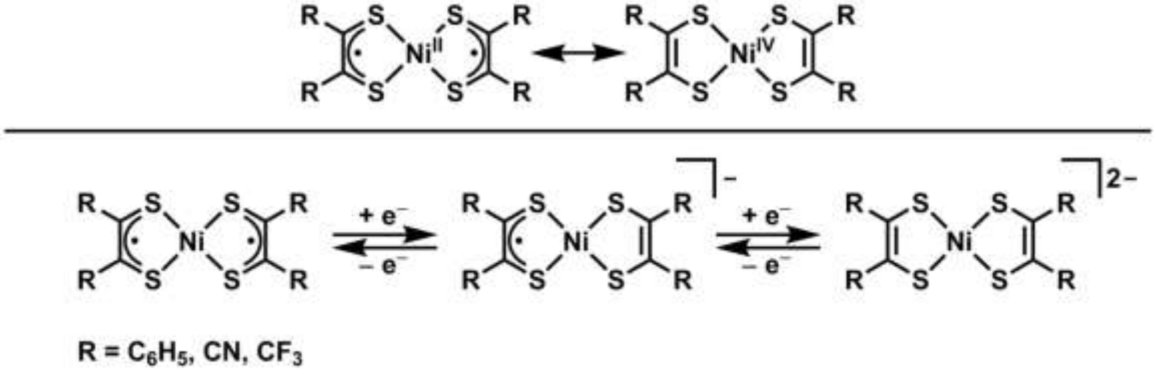

Fundamental Aspects of Redox-Active Ligands

Following the seminal work on dithiolenes as redox-active ligands, the redox-active ligand class experienced a broad expansion. These ligands are typified by conjugated π-systems featuring oxygen, nitrogen, and sulfur-based donor groups, with some of the more common motifs depicted in Chart 1.1 as their oxidized forms.[9,14–17] The presence of conjugated π-systems within redox-active ligands serves to provide the requisite low lying π^* orbitals (or, if in the fully reduced form, high lying π orbital) for ligand-based redox events to occur. This conjugation also serves to stabilize ligand-based radicals through delocalization[18], though in sulfur-based ligands there is significant sulfur character in the ligand-based SOMO.[19,20]

Chart 1.1. Common structural motifs of redox-active ligands.

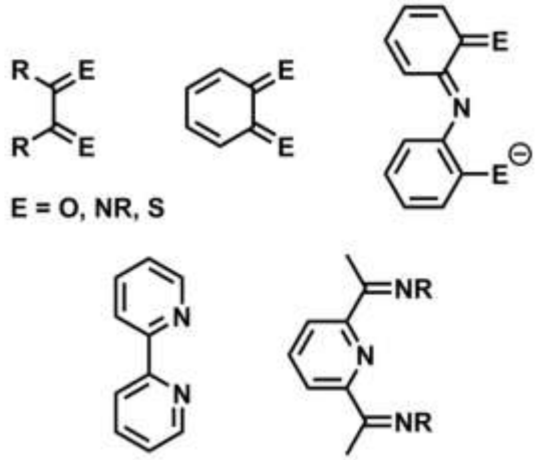

The redox-behavior of the oxygen and nitrogen containing ligands is exemplified in Chart 1.2 by the redox-active catecholate ligand, which can undergo two successive redox events to yield the dianionic catecholate, monoanionic semiquinonate, and neutral quinone forms of the ligand. The ability of redox-active ligands to undergo oxidation and reduction events has led to their use in enabling redox-reactivity at transition metal centers by mediating electron transfer events (a topic described more extensively herein). More fundamentally than their use in enabling reactivity, the accessibility of these ligand forms can result in initial ambiguity of the metal oxidation state, represented by the three resonance structures in Chart 1.2. For a transition metal complex bearing a single catechol ligand, three possible assignments of the ligand charge and metal oxidation state exist. Represented on the far left, a fully-reduced catecholate ligand would result in an assignment of the metal center as M(n+II) (with n dependant on the nature of the other ligands). Alternatively, the catecholate ligand may adopt the monoanionic semiquinonate form, yielding a M(n+I) center, or the neutral quinone form, yielding a M(n) center.

Chart 1.2. Redox activity of catecholate and potential electronic assignments of catecholate-metal complexes.

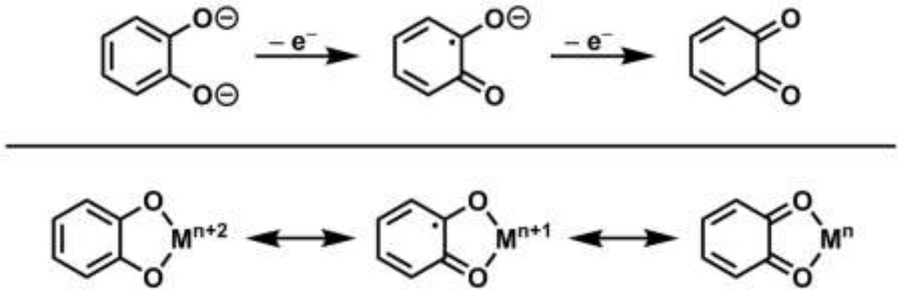

The potential assignment of multiple combinations of metal oxidation state and ligand charge has led researchers to develop a battery of techniques for use in the assignment of redox-active ligand forms. The most predominant method utilized in assigning the redox form of redox-active ligands is X-ray diffraction analysis. Bond length contractions upon oxidation of the catechol ligand in Chart 1.2 are indeed observed experimentally, and in-depth analysis of intraligand bond lengths have resulted in quantifiable calculations of the ligand charge for catechol, amidophenol, and ONO (where $(ONO^{cat})H_3$ = bis(3,5-di-tert-butyl- 2-phenol)amine) ligands utilizing solid state bond metrics.[21,22] The π-systems of redox-active ligands also result in informative electronic absorption[19,23–25] and infrared[26] spectra for a number of ligand redox forms, providing another experimental method for determining the charge on the ligand. The presence of diagnostic near-infrared (near-IR) features in the electronic absorption spectra of redox-active ligands is especially notable for the ONO ligand platform, a feature that will be utilized extensively within the proceeding chapters.[27–32] Furthermore, electron paramagnetic resonance (EPR) spectroscopy can be a powerful tool in identifying the presence of organic ligand-based radicals.[19,25,31–33]

Donor Group Effects on Redox-Potential

The extensive family of redox-active ligands allows for significant tunability of the steric environment around the metal, the denticity of the ligand, and most notably, the electrochemical redox potential of the ligand. As shown in Chart 1.1, isostructural families of redox-active ligands where only the identity of the heteroatom donor differs have been described. Wieghardt et al. have reported homoleptic chromium complexes of catecholate and amidophenolate ligands and their electrochemical properties (Chart 1.3, Table 1.1).[20,34] Each of the complexes was characterized as containing a Cr(III) metal center and three radical anion ligands, ie. $(L^{sq})_3Cr$. The anodic shift in the $[Cr]^{0/-}$ and $[Cr]^{0/+}$ redox events upon replacing the nitrogen donors with oxygen is consistent with the decreased electronegativity of nitrogen relative to oxygen and provides a means for altering the electrochemical properties of redox-active ligands by substitution of the donor group.

Chart 1.3. Catecholate and amidophenolate ligands investigated by Wieghardt et al. Ligands represented in fully reduced forms.

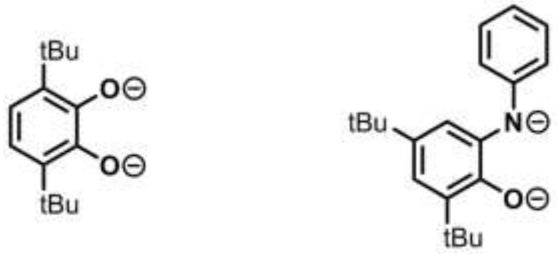

$L_{O,O}$ $L_{N,O}$

Table 1.1.Redox potentials for the first oxidation and first reduction events for homoleptic complexes reported by Wieghardt et al.

	E°' (V vs $Cp_2Fe^{0/+}$)	
	$[Cr]^{0/-}$	$[Cr]^{0/+}$
$(L^{sq}_{O,O})_3Cr$	−0.63	0.58
$(L^{sq}_{N,O})_3Cr$	−1.26	−0.10

In a related study, Lever et al. directly probed the redox-mediating effect of stepwise heteroatom substitution in catecholate-type ligands.[35,36] In a series of ruthenium complexes of the formula $LRu(bipy)_2$ (where L = redox-active ligand), methodical substitution of oxygen donors for nitrogen donors revealed a similar outcome to the studies of Wieghardt et al. with homoleptic chromium complexes. As demonstrated in Table 1.2,, installing nitrogen donors in place of oxygen results in a cathodic shift in the ligand-centered redox couples, with shifts of 400-570 mV per substitution. These results demonstrate that a powerful redox-mediating effect can occur even in complexes bearing a single redox-active ligand.

Scheme 1.2. Electrochemical behavior of $LRu(bipy)_2$ complexes reported by Lever et al.

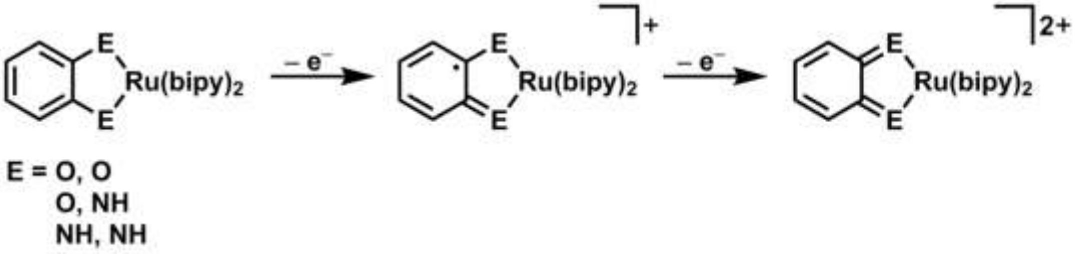

Table 1.2. Redox potentials for the $[Ru]^{0/+}$ and $[Ru]^{+/2+}$ redox events for $LRu(bipy)_2$ complexes reported by Lever et al.

	E°' (V vs SCE)	
$(L_{E,E})Ru(bipy)_2$	$[Ru]^{0/+}$	$[Ru]^{+/2+}$
$(L^{cat}_{O,O})Ru(bipy)_2$	−0.33	0.56
$(L^{cat}_{O,NH})Ru(bipy)_2$	−0.75	0.10
$(L^{cat}_{NH,NH})Ru(bipy)_2$	−1.15	−0.47

Ligand-Enabled Reactivity

Classical complexes of d^0 early-transition-metals are typically limited to redox-neutral reaction pathways owing to the difficulty associated with accessing low-valent states of these metals. The incorporation of redox-active ligands into the coordination sphere of d^0 transition metals has appeared as a viable approach towards enabling reactivity which necessitates redox changes.[37] This reactivity has been demonstrated for oxidative addition at a zirconium(4+) metal center coordinated to two fully reduced amidophenolate ligands (Scheme 1.3).[25,38] Addition of either Cl_2 or Br_2 to a cold solution of $Zr(ap)_2(THF)_2$ (where $(ap)^{2-}$ = 4,6-di-*tert*-butyl-2-*tert*-butylamidophenolate) results in ligand-mediated oxidative addition to the metal center, yielding the complex $ZrX_2(isq)_2$ (where X = Br or Cl and $(isq)^-$ = 4,6-di-*tert*-butyl-2-*tert*-butyliminosemiquinonate) which has undergone a one-electron oxidation of each ligand, yielding a two-electron redox reaction at a redox-inert metal center.

Scheme 1.3. Oxidative addition of halogens to $Zr(ap)_2(THF)_2$.

The complimentary reaction to oxidative addition, reductive elimination, has also been demonstrated with the $Zr(ap)_2$ manifold.[39] The dianionic complex $[ZrPh_2(ap)_2]^{2-}$ forms the putative complex $ZrPh_2(isq)_2$ upon oxidation with $[Cp_2Fe]^+ PF_6^-$ at cold temperature. At ambient temperature this complex undergoes reductive elimination of the phenyl moieties to yield biphenyl and $Zr(ap)_2(THF)_2$. Concerted reductive elimination, instead of radical expulsion, was supported by crossover experiments wherein mixtures of $[ZrPh_2(ap)_2]^{2-}$ and $[Zr^{Me}Ph_2(ap)_2]^{2-}$ were treated with $[Cp_2Fe]^+ PF_6^-$ and yielded only trace amounts of mixed biphenyl products.

Scheme 1.4. Reductive elimination of biphenyl from $ZrPh_2(isq)_2$.

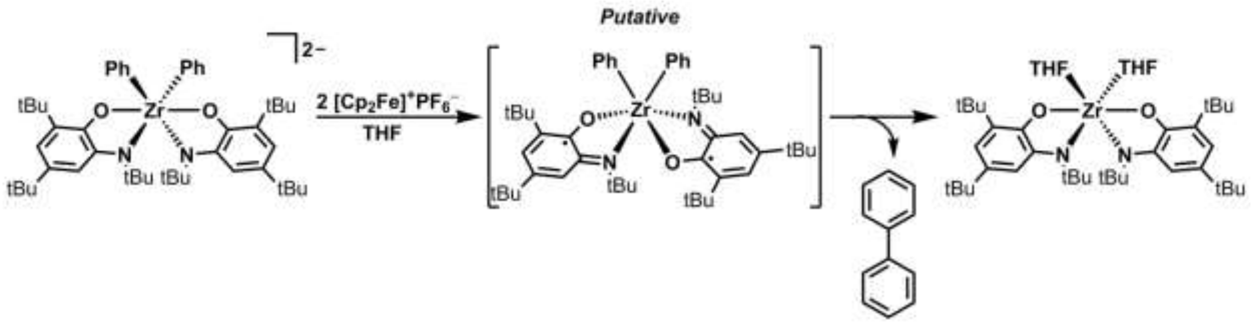

Reactivity studies examining bidentate amidophenolate and catecholate supported complexes revealed that oxidation to the neutral iminoquinone or quinone forms, respectively, typically results in decoordination and formation of free ligand.[25,40,41] For instance, the use of two equivalents of Br_2 in the reaction depicted in Scheme 1.3 results in the formation of $ZrBr_4$ and two equivalents of free iminoquinone.[25] The low binding affinity of the neutral forms relative to the monoanionic and dianionic forms has led to an increased investigation of tridentate, pincer-type redox-active ligands to maintain coordination upon two electron oxidation of the ligand.[42] Depicted in Chart 1.4, a trianionic pincer manifold is capable of undergoing two oxidation events but, unlike its bidentate analogues, maintains an anionic charge that preserves metal binding in this oxidized form.

Chart 1.4. Redox behavior of trianionic, pincer-type redox-active ligands.

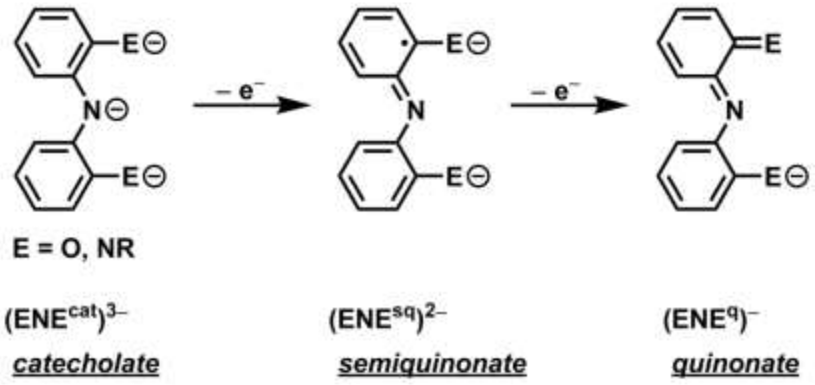

The utility of tridentate redox-active ligands in enabling redox-dependant reactions at d^0 transition metals is exemplified in group transfer reactivity of the zirconium complex $(NNN^{cat})ZrCl(CN^tBu)_2$ (where $(NNN^{cat})^{3-}$ = bis(2-isopropylamido-4-methoxyphenyl)amide).[43] Treating $(NNN^{cat})ZrCl(CN^tBu)_2$ with an organoazide results in a two electron oxidation of the ligand to yield a zirconium-imido moiety supported by a monoanionic ligand, $(NNN^q)ZrCl(=NR)(CN^tBu)$ (Scheme 1.5). Migratory insertion of the imido group into an isocyanide ligand yields a new bond and an intermediate η^2-carbodiimide. Ligand-enabled reductive elimination of the carbodiimide regenerates the fully reduced ligand in $(NNN^{cat})ZrCl(CN^tBu)$ and allows for catalytic formation of carbodiimide.[44]

Scheme 1.5. Catalytic nitrene transfer reactivity of $(NNN^{cat})ZrCl(CN^tBu)_2$.

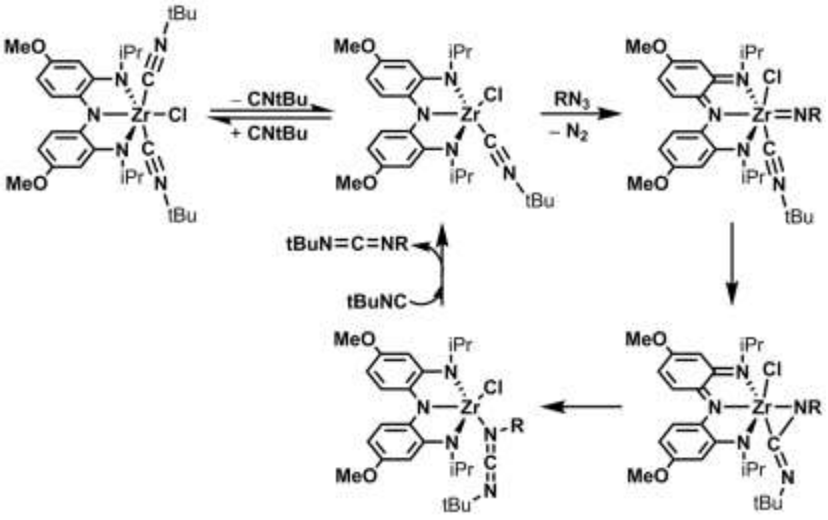

The utility of redox-active ligands extends beyond their ability to enable reactivity at d^0 transition metal centers, with mid and late transition metal centers also exhibiting ligand-enabled reactivity.[45–50] Chirik et al demonstrated this type of reactivity with the bis(imino)pyridine iron complex $(^{iPr}PDI)Fe(N_2)_2$ (where $^{iPr}PDI = (2,6\text{-}i\text{Pr}_2C_6H_3N{=}CMe)_2C_5H_3N$) (Scheme 1.6).[50–52] This complex demonstrates classical non-innocent ligand behavior, with notable contribution from both the ligand and the iron center to the frontier molecular orbitals. The best description of this complex is that of a dianionic $(^{iPr}PDI)^{2-}$ ligand coordinated to an Fe(II) center, depicted as the bottom resonance structure in Scheme 1.6.[52] Addition of an organoazide to the complex results in nitrogen extrusion and formation of a four-coordinate iron-imide $(^{iPr}PDI)Fe(=NR)$.[50] In-depth analysis of this complex by X-ray diffraction, SQUID magnetometry, and Mossbauer spectroscopy determined that an Fe(III) center was bound to a monoanionic $(^{iPr}PDI)^{-}$ ligand, indicating that the redox-active ligand and the iron center worked in concert to activate the organoazide. Exposing $(^{iPr}PDI)Fe(=NR)$ to an atmosphere of CO resulted in nitrene transfer to yield isocyanate, O=C=NR, and the Fe(II) complex $(^{iPr}PDI)Fe(CO)_2$. As with the activation of the organoazide, nitrene transfer occurs via reduction of both the iron center and the PDI ligand, demonstrating that two-electron reactivity can result from cooperative redox-events at both the metal center and a redox-active ligand.

Scheme 1.6. Nitrene transfer reactivity of (^{iPr}PDI)Fe.

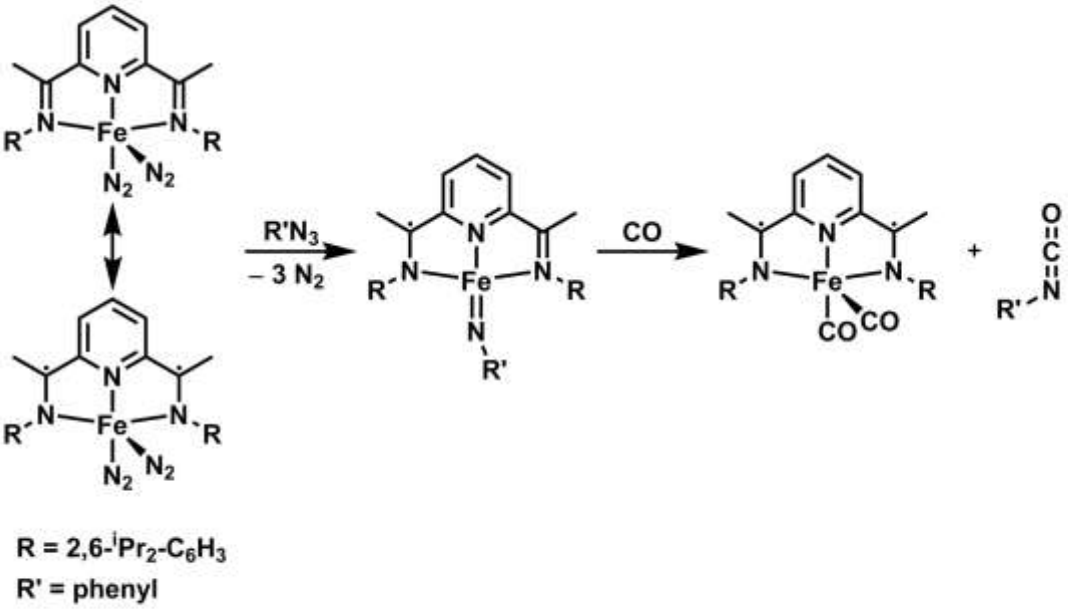

Dissertation Scope

Chapter 2 will examine the effect of ancillary donor groups in modulating the electrochemical redox potentials and electronic structure in (ONO^{sq})Ta(X)$_3$ complexes (where X = *tert*-butoxide, trifluoroethoxide, phenoxide, pentafluorophenoxide, and chloride). Chapter 3 will investigate the ability of (ONO^{cat})Ta(OR)$_2$ complexes (where R = *tert*-butyl and trifluroethyl) to activate dioxygen and probe the reactivity of the resulting metal-oxo complexes [(ONO^{q})Ta(OR)$_2$(μ-O)]$_2$. Chapter 4 will report the synthesis and characterization of chromium complexes of the ONO ligand spanning the (ONO^{cat})$^{3-}$, (ONO^{sq})$^{2-}$, and (ONO^{q})$^{-}$ redox forms. Chapter 5 investigates the reactivity of chromium complexes of the ONO ligand bearing weakly coordinating trifluoromethanesulfonate ligands and compares these complexes to analogues bearing the related DOPO ligand (where (DOPO^{q})H = 2,4,6,8-tetra(*tert*-butyl)-9-hydroxyphenoxazin-1-one). Chapter 6 reports the synthesis and characterization of ONO complexes bearing a number of first row metals, namely titanium, vanadium, manganese, and nickel.

References

(1) Jean, Y. *Molecular Orbitals of Transition Metal Complexes*; Oxford University Press, 2005.
(2) Jorgensen, C. K. *Coord. Chem. Rev.* **1966**, *1*, 164.
(3) Hendrickson, D. N.; Pierpont, C. G. *Top. Curr. Chem.* **2004**, *234*, 63.
(4) Pierpont, C. G. *Coord. Chem. Rev.* **2001**, *216-217*, 99.
(5) Kaim, W.; Schwederski, B. *Coord. Chem. Rev.* **2010**, *254*, 1580.
(6) Chirik, P. J. *Inorg. Chem.* **2011**, *50*, 9737.
(7) Schrauzer, G. N.; Mayweg, V. *J. Am. Chem. Soc.* **1962**, *84*, 3221.
(8) Gray, H. B.; Williams, R.; Bernal, I.; Billig, E. *J. Am. Chem. Soc.* **1962**, *84*, 3596.
(9) Eisenberg, R.; Gray, H. B. *Inorg. Chem.* **2011**, *50*, 9741.
(10) Davison, A.; Edelstein, N.; Holm, R. H.; Maki, A. H. *Inorg. Chem.* **1963**, *2*, 1227.
(11) Stiefel, E. I.; Waters, J. H.; Billig, E.; Gray, H. B. *J. Am. Chem. Soc.* **1965**, *87*, 3016.
(12) Gray, H. B.; Billig, E. *J. Am. Chem. Soc* **1963**, *85*, 2019.
(13) Olson, D. C.; Mayweg, V. P.; Schrauzer, G. N. *J. Am. Chem. Soc.* **1966**, *88*, 4876.
(14) Lyaskovskyy, V.; Bruin, B. De. *ACS Catal.* **2012**.
(15) Kaim, W. *Inorg. Chem.* **2011**, *50*, 9752.
(16) Scarborough, C. C.; Wieghardt, K. *Inorg. Chem.* **2011**, *50*, 9773.
(17) Tondreau, A. M.; Milsmann, C.; Lobkovsky, E.; Chirik, P. J. *Inorg. Chem.* **2011**, *50*, 9888.
(18) Chirik, P. J.; Wieghardt, K. *Science (80-.).* **2010**, *327*, 794.
(19) Milsmann, C.; Bothe, E.; Bill, E.; Weyhermüller, T.; Wieghardt, K. *Inorg. Chem.* **2009**, *48*, 6211.
(20) Banerjee, P.; Sproules, S.; Weyhermüller, T.; Debeer George, S.; Wieghardt, K. *Inorg. Chem.* **2009**, *48*, 5829.
(21) Brown, S. N. *Inorg. Chem.* **2012**, *51*, 1251.
(22) Ranis, L. G.; Werellapatha, K.; Pietrini, N. J.; Bunker, B. A.; Brown, S. N. *Inorg. Chem.* **2014**, *51*, 10203.
(23) Scarborough, C. C.; Sproules, S.; Doonan, C. J.; Hagen, K. S.; Weyhermuller, T.; Wieghardt, K. *Inorg. Chem.* **2012**, *51*, 6969.
(24) Munha, R. F.; Zarkesh, R. A.; Heyduk, A. F. *Inorg. Chem.* **2013**, *52*, 11244.
(25) Blackmore, K. J.; Sly, M. B.; Haneline, M. R.; Ziller, J. W.; Heyduk, A. F. *Inorg. Chem.* **2008**, *47*, 10522.
(26) Saito, Y.; Takemoto, J.; Hutchinson, B.; Nakamoto, K. *Inorg. Chem.* **1972**, *11*, 2003.
(27) Girgis, A.; Balch, A. *Inorg. Chem.* **1975**, *14*, 2724.
(28) Chaudhuri, P.; Hess, M.; Hildenbrand, K.; Bill, E.; Weyhermüller, T.; Wieghardt, K. *Inorg. Chem.* **1999**, *38*, 2781.
(29) Bruni, S.; Caneschi, A.; Cariati, F.; Delfs, C.; Dei, A.; Gatteschi, D. *J. Am. Chem. Soc.* **1994**, *116*, 1388.
(30) Lu, F.; Zarkesh, R. A.; Heyduk, A. F. *Eur. J. Inorg. Chem.* **2012**, *2012*, 467.
(31) Wong, J. L.; Higgins, R. F.; Bhowmick, I.; Cao, D. X.; Szigethy, G.; Ziller, J. W.; Shores, M. P.; Heyduk, A. F. *Chem. Sci.* **2015**, 1.

(32) Zarkesh, R.; Ziller, J. W.; Heyduk, A. F. *Angew. Chem. Int. Ed. Engl.* **2008**, *47*, 4715.
(33) Nguyen, A. I.; Blackmore, K. J.; Carter, S. M.; Zarkesh, R. a; Heyduk, A. F. *J. Am. Chem. Soc.* **2009**, *131*, 3307.
(34) Chun, H.; Verani, C. N.; Chaudhuri, P.; Bothe, E.; Bill, E.; Weyhermuller, T.; Wieghardt, K. *Inorg. Chem.* **2001**, *40*, 4157.
(35) Ebadi, M.; Lever, A. B. P. *Inorg. Chem.* **1999**, 467.
(36) Masui, H.; Lever, B. P.; Auburn, P. R. *Inorg. Chem.* **1991**, *30*, 2402.
(37) Munhá, R. F.; Zarkesh, R. a; Heyduk, A. F. *Dalton Trans.* **2013**, *42*, 3751.
(38) Blackmore, K. J.; Ziller, J. W.; Heyduk, A. F. *Inorg. Chem.* **2005**, *44*, 5559.
(39) Haneline, M. R.; Heyduk, A. F. *J. Am. Chem. Soc.* **2006**, *128*, 8410.
(40) Cass, M.; Pierpont, C. *Inorg. Chem.* **1986**, *25*, 122.
(41) Randolph, A. H.; Seewald, N. J.; Rickert, K.; Brown, S. N. *Inorg. Chem.* **2013**, *52*, 12587.
(42) Heyduk, A.; Zarkesh, R.; Nguyen, A. *Inorg. Chem.* **2011**, *50*, 9849.
(43) Nguyen, A. I.; Zarkesh, R. a.; Lacy, D. C.; Thorson, M. K.; Heyduk, A. F. *Chem. Sci.* **2011**, *2*, 166.
(44) Ghosh, S.; Baik, M. *Chem. Eur. J.* **2015**, *21*, 1780.
(45) Wong, J. L.; Sánchez, R. H.; Logan, J. G.; Zarkesh, R. A.; Ziller, J. W.; Heyduk, A. F. *Chem. Sci.* **2013**, *4*, 1906.
(46) Chaudhuri, P.; Hess, M.; Weyhermüller, T.; Wieghardt, K. *Angew. Chemie Int. Ed.* **1999**, *38*, 1095.
(47) Bouwkamp, M. W.; Bowman, A. C.; Lobkovsky, E.; Chirik, P. J. *J. Am. Chem. Soc.* **2006**, *128*, 13340.
(48) Broere, D. L. J.; de Bruin, B.; Reek, J. N. H.; Lutz, M.; Dechert, S.; van der Vlugt, J. I. *J. Am. Chem. Soc.* **2014**, *1*, 8.
(49) Lippert, C. A.; Arnstein, S. A.; Sherrill, C. D.; Soper, J. D. *J. Am. Chem. Soc.* **2010**, *132*, 3879.
(50) Bart, S. C.; Lobkovsky, E.; Bill, E.; Chirik, P. J. *J. Am. Chem. Soc.* **2006**, *128*, 5302.
(51) Bart, S. C.; Lobkovsky, E.; Chirik, P. J. *J. Am. Chem. Soc.* **2004**, *126*, 13794.
(52) Bart, S. C.; Chłopek, K.; Bill, E.; Bouwkamp, M. W.; Lobkovsky, E.; Neese, F.; Wieghardt, K.; Chirik, P. J. *J. Am. Chem. Soc.* **2006**, *128*, 13901.

Chapter 2

Influence of Ancillary Ligands on the Properties of a Redox-Active Ligand Bearing Complex ($(ONO^{sq})TaX_3$)

Introduction

The effects of ligand donor strength on the properties and reactivity of transition metal complexes is a fundamental aspect of coordination chemistry. A classical approach to quantifying the donor ability of ligand groups is through binding to a transition-metal-carbonyl complex and measuring the stretching frequency of the metal-bound carbonyls. This approach is typified by the complex $NiL(CO)_3$, which has been described by Tolman and used to develop the aptly named Tolman Electronic Parameter of various L-type donors (typically phosphines).[1] The carbonyl-based method has been extended to other metal centers and ligand classes both experimentally and, especially, computationally.[1–7] This approach, however, is limited to electron-rich metal centers capable of forming stable carbonyl complexes. Other classical methods to determine ligand donor strengths use electronic spectroscopy to determine *d-d* transition energies, establishing a donor strength hierarchy based on the transition energy (spectrochemical series).[8,9] A well-known example of this method was used to establish ligand donor strengths of anionic ligands bound to the Co(III) complex $[CoX(NH_3)_5]^{2+}$.

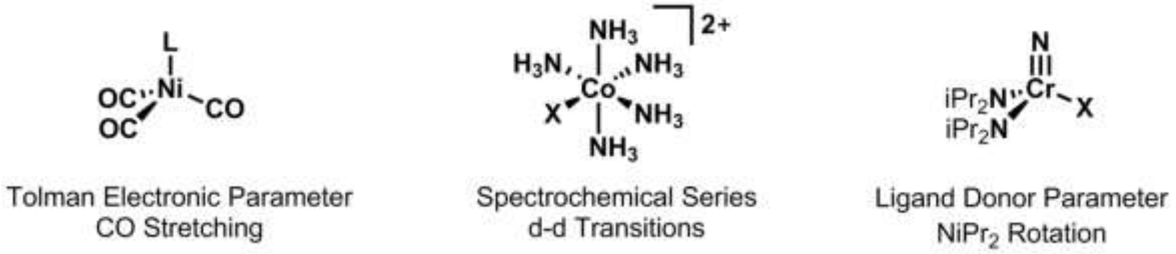

Tolman Electronic Parameter
CO Stretching

Spectrochemical Series
d-d Transitions

Ligand Donor Parameter
NiPr$_2$ Rotation

Figure 2.1. Prototypical complexes and approaches utilized to establish the donor strength of ligands.

Recently, an alternative approach was reported by Odom *et al.*, which utilized a d^0 transition metal center.[10] This method applies ^{1}H NMR analysis to estimate enthalpic barriers to rotation of diisopropylamido ligands in the complex $CrN(N^iPr_2)_2X$, values of which are then assigned as ligand donor parameters (LDP). Notably, classical carbonyl or spectrochemical methods are not amenable to establishing donor strengths to d^0 metal centers, as accomplished in this study. Moreover, metal-ligand π bonding is highly influenced by *d*-orbital population, making these results especially important for early-transition-metal complexes. The methodology reported by Odom was applicable to a wide range of donor ligands, and was in agreement with the results of other ligand-donor-based studies on low *d*-electron count metals.[11]

Similarly to controlling metal electronic structure with ligand variation, with the emergence of redox-active ligands in coordination chemistry, methods amenable to the tuning of the electronic structure of the ligand have been described. While intensive changes related to fundamental alteration of the coordinating groups have been described in Chapter 1, an alternative route which maintains the primary coordination sphere and relies on the electron donating or withdrawing effects of Hammet-substituents on the ligand backbone has been investigated. Through a series of pyridine diimine ligands with varying substituents in the 4-position, Chirik and coworkers have demonstrated a tunable redox window of 590 mV by varying the substituents from electron withdrawing (–CF_3) to electron donating (–NMe_2).[12] Similarly within our group, alteration of ligand backbone substituents on the NNN ligand revealed a tunable redox window of 270 mV by varying the substituents from electron withdrawing (–F) to electron donating (–OMe).[13]

While variation of Hammet-substituents allows for fine-tuning of the redox-active ligand, variation of ligand-backbone groups can be a labor intensive endeavor, as evidenced by the in-depth experimental protocols described in the aforementioned studies.[12,13] By extension of the variation in donor ability described by Odom, we questioned whether alteration of the ancillary ligands of a redox-active ligand-containing complex could alter the Lewis acidity of the transition metal enough to modulate significantly the redox properties of the redox-active ligand. Targeting this approach, the previously described complex $(ONO^{sq})TaCl_3$ was determined to be a suitable manifold.[14] This complex possesses three coordination sites available for ligand variation, bears little steric hindrance around the tantalum center, and is obtained from a starting material, $(ONO^{cat})TaCl_2(Et_2O)$, which demonstrates facile ligand substitution reactivity. Furthermore, $(ONO^{sq})TaCl_3$ demonstrates well-defined electrochemical behavior and exhibits hyperfine coupling to the tantalum center by electron paramagnetic resonance (EPR) spectroscopy.[14,15] We hypothesized that if ligand-substituted variants of $(ONO^{sq})TaX_3$ demonstrated significantly altered electronic structure as a function of the donor strength of X, then electrochemical and EPR analysis could benchmark and quantify the effect of the donor group X.

Results and Discussion

Synthesis and Characterization of $(ONO^{sq})TaX_3$

Our investigation on ancillary ligand effects initially targeted oxygen-based donor groups (alkoxides and phenoxides), which comprised a bulk of the ligands described by Odom.[10] While the addition of a chlorine atom surrogate was successful in the conversion of $(ONO^{cat})TaCl_2(Et_2O)$ (**1**) to $(ONO^{sq})TaCl_3$ (**3e**), we envisioned no such radical surrogate approach for the installation of alkoxide groups. Instead, anionic complexes of tantalum were targeted, such that a stepwise ligand addition and oxidation procedure could produce complexes of the formula $(ONO^{sq})TaX_3$. To this end, treatment of **1** with three equivalents of LiO^tBu resulted in the formation of $[Li(OEt_2)][(ONO^{cat})Ta(O^tBu)_3]$ ($[Li(OEt_2)]$[**2a**]) (Scheme 2.1). This complex displays two broadened ^{1}H-NMR resonances corresponding to coordinated $–O^tBu$ ligands, one appearing at 1.51 ppm as a 9H signal and another at 1.25 ppm as an 18H signal. Diethyl ether peaks appear at 2.88 and 0.85 ppm, shifted from that of free ether and supporting the presence of a lithium cation. Oxidation of complex **2a** was achieved using silver trifluoromethanesulfonate (AgOTf) which, upon addition to pale yellow ethereal solutions of **2a**, produced a deep purple solution, indicative of the formation of the highly colored $(ONO^{sq})^{2-}$ containing species. Upon workup and purification, the neutral species $(ONO^{sq})Ta(O^tBu)_3$ (**3a**) was isolated as a dark purple crystalline solid. Complex **3a** displays a UV-vis-NIR spectrum consistent with the assignment of the ligand as the semiquinonate form, with a broad NIR band at 888 nm and a visible region band at 558 nm.[14,16] Analysis of single crystals of **3a** by x-ray diffraction yielded the structure depicted in Figure 2.2.

Scheme 2.1. Synthesis of complexes **2a-d** and **3a-d**.

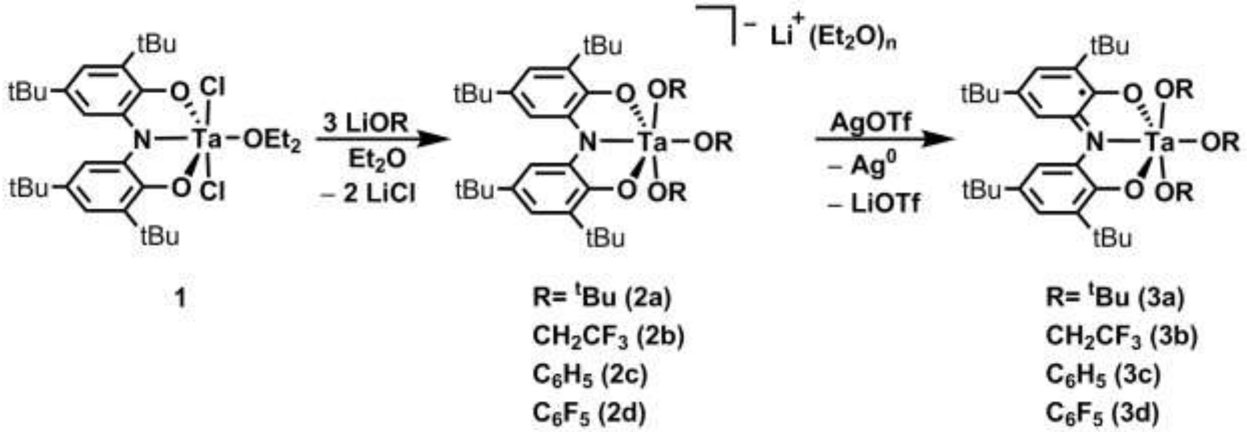

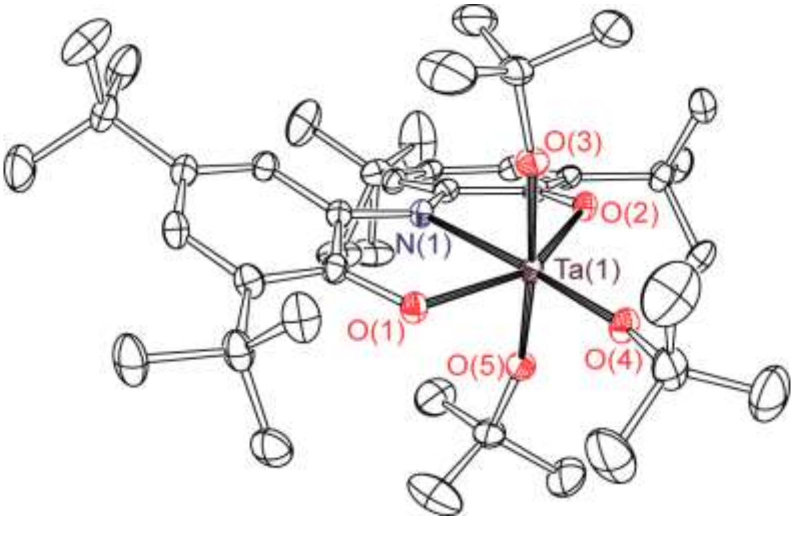

Figure 2.2. ORTEP diagram of $(ONO^{sq})Ta(O^tBu)_3$ (**3a**). Thermal ellipsoids are shown at 50% probability. Hydrogen atoms have been omitted for clarity. A second crystallographically unique but chemically identical molecule of $(ONO^{sq})Ta(O^tBu)_3$ within the asymmetric unit has also been omitted for clarity.

X-ray diffraction analysis of a single crystal of **3a** confirmed the desired pseudo-octahedral complex $(ONO^{sq})Ta(O^{t}Bu)_3$. Consistent with the spectroscopic assignment of the $(ONO^{sq})^{2-}$ form of the ligand, contracted C–O and C–N bond distances of 1.34 (avg.) and 1.36 (avg.) Å, respectively, are similar to those observed in the complex $(ONO^{sq})TaCl_3$ (**3e**) (Table 2.1) and other $(ONO^{sq})^{2-}$-supported metal complexes, supporting the assignment of the $(ONO^{sq})^{2-}$ form of the ligand in **3a**.[14,16–18] This assignment is also consistent with the observed partial localization of double bond character within the ligand backbone (Table 2.1). Application of the metrical oxidation state (MOS) calculation developed by Brown for the ONO ligand yields an MOS of −2.21 for **3a** (average of all 4 ring systems within the asymmetric unit), again, fully consistent with the $(ONO^{sq})^{2-}$ formulation.[19] A similar MOS of −2.19 is obtained for **3e**. The similar MOS between **3a** and **3e** is reflected in their observed intraligand bond distances (Table 2.1), which show no significant difference.

With a modular synthetic approach in hand, additional derivatives of the $(ONO^{sq})TaX_3$ class were pursued. Alkoxide and phenoxide derivatives were chosen utilizing the family of donors analyzed by Odom and coworkers[10] as a guide. In an identical approach used for the synthesis of **2a**, treatment of **1** with three equiv. of LiOR (R = CH_2CF_3, C_6H_5, C_6F_5) yielded the complexes $[Li(OEt_2)_n][(ONO^{cat})Ta(OR)_3]$ (R = CH_2CF_3 (**2b**), C_6H_5 (**2c**), C_6F_5 (**2d**)) detailed in Scheme 2.1. ^{1}H-NMR analysis of complex **2b** showed a single CH_2 quartet corresponding to 6H at 4.47 ppm and also displayed only one ^{19}F-NMR resonance at −77.96 ppm, suggesting fast exchange of inequivalent $–OCH_2CF_3$ ligands on the NMR time scale. Identical observations were made with **2c**, which showed three broad, overlapping resonances from 6.98-6.67 ppm arising from fast exchange of the phenoxide groups. Similarly to **2c**, complex **2d** showed three broad fluorine resonances at −158.87, −163.23 and −166.76 ppm by ^{19}F-NMR. As with **2a**, complexes **2b-d** all displayed shifted ether resonances, consistent with the presence of lithium cations. Treating salts **2b-d** with AgOTf yielded highly colored solids of **3b-d** with prototypical $(\mathrm{ONO^{sq}})^{2-}$-type absorption spectra (Figure 2.3) showing broad near-IR bands around 900 nm. Notably, a red shift in the visible region absorption band occurs with a decrease in the ligand donor parameter developed by Odom (Table 2.2).

Table 2.1. Selected bond lengths and angles for **3a** and **3e**. Computed bond lengths and angles indicated in brackets.

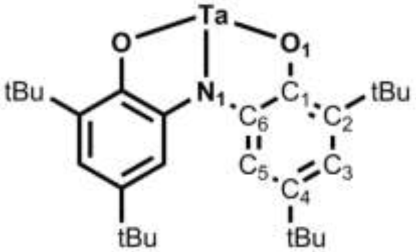

	$(\mathrm{ONO^{sq}})\mathrm{Ta(OtBu)_3}$	$(\mathrm{ONO^{sq}})\mathrm{TaCl_3}$
	3a	**3e**
	Bond Lengths (Å)	
Ta(1)–N(1)	2.2113(15) / [2.246]	2.222(13) / [2.224]
Ta(1)–O(1)	2.0137(13) / [2.012]	1.915(4) / [1.933]
O(1)–C(1)	1.335(2) / [1.315]	1.342(7) / [1.328]
N(1)–C(6)	1.366(2) / [1.357]	1.362(7) / [1.361]
C(1)–C(2)	1.408(3) / [1.410]	1.408(7) / [1.402]
C(2)–C(3)	1.390(3) / [1.383]	1.385(7) / [1.385]
C(3)–C(4)	1.414(3) / [1.408]	1.418(7) / [1.409]
C(4)–C(5)	1.377(3) / [1.375]	1.382(7) / [1.376]
C(5)–C(6)	1.413(3) / [1.408]	1.414(7) / [1.405]
C(1)–C(6)	1.429(3) / [1.431]	1.429(7) / [1.421]
Ta(1)–O(4)	1.8777(13) / [1.890]	-----
Ta(1)–Cl(1)	-----	2.312(5) / [2.326]
	Bond Angles (°)	
N(1)–Ta(1)–O(1)	73.28(6) / [72.93]	73.46(12) / [72.99]
O(3)–Ta(1)–O(5)	173.23(6) / [173.31]	-----
Cl(2)–Ta(1)–Cl(2)#	-----	176.91(18) / [175.87]
O(1)–Ta(1)–O(2)	146.67(5) / [146.01]	146.9(2) / [145.97]

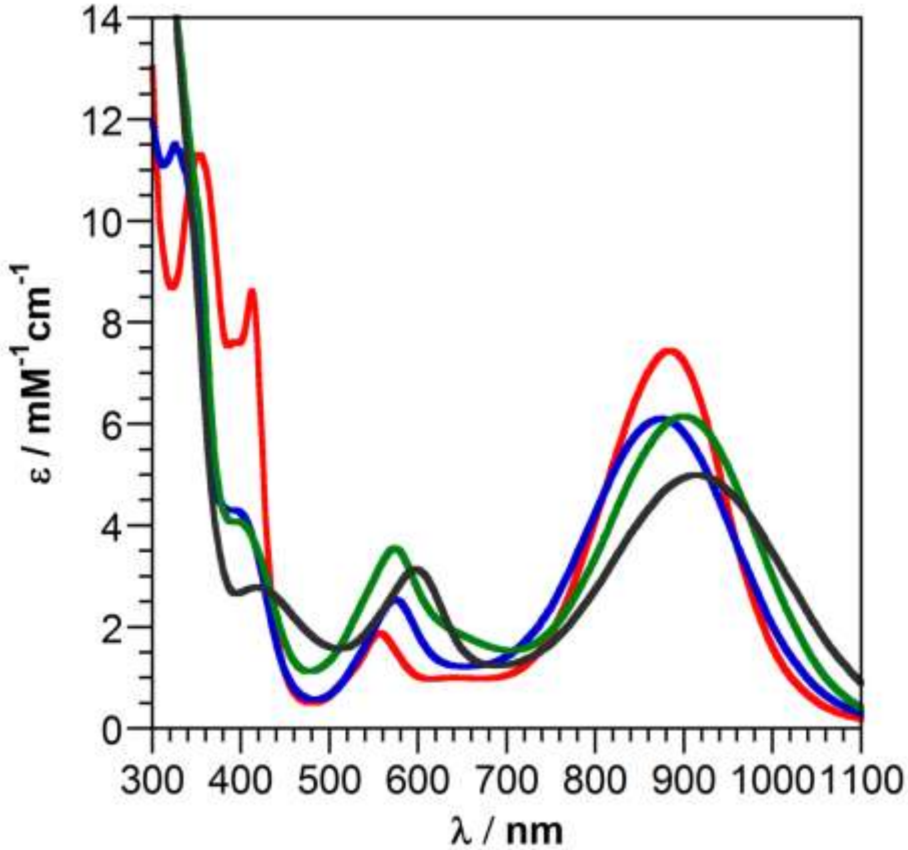

Figure 2.3. UV-vis-NIR spectra of complexes **3a-d** in toluene:**3a** (red), **3b** (blue), **3c** (green), **3d** (black).

Electrochemistry of (ONO^{sq})TaX$_3$

Electrochemical analysis revealed that complexes **3a-e** all demonstrate similar electrochemical behavior (Figure 2.4), exhibiting a reversible reduction event corresponding to the ONO$^{cat/sq}$ redox couple, and an oxidation event corresponding to the ONO$^{sq/q}$ redox couple, though the reversibility of the oxidation event shows significant dependence on the identity of the ancillary ligand. The greatest degree of reversibility was realized by incorporation of O^{t}Bu, which, as the strongest donor, is most capable of stabilizing the cationic charge on the electrochemically generated (ONO^q)Ta(O^{t}Bu)$_3^+$ species. The large steric profile of this ligand also engenders protection to the metal center from potential interaction with solvent or PF$_6^-$ upon oxidation.[20–22] The decreased donor strength and steric profiles of the ligands in complexes **3b-e** result in electrochemical irreversibility of the ONO$^{sq/q}$ redox couple.

A drastic anodic shift in redox potentials upon incorporation of ligands with lower LDPs was observed in complexes **3a-e** (Table 2.2). Incorporation of a strong donor ligand (O^{t}Bu) in **3a** yields the most negative redox potentials, shifting the ONO$^{cat/sq}$ couple to −0.985 V. Substitution of the weakest donor group investigated (Cl) in place of the strongly donating O^{t}Bu ligand results in an anodic shift of 1.13 V in the ONO$^{cat/sq}$ redox couple, which occurs at 0.151 V in **3e**. A similar, but markedly less-pronounced shift occurred in the ONO$^{sq/q}$ redox event, ranging from 0.029 V in **3a** to 0.737 V in **3e**. The redox events in complexes **3b-d** appear intermediate of these two extremes (Table 2.2).

Table 2.2. Electrochemical and spectroscopic comparison of complexes **3a-e**.

	3a X=O^{t}Bu	**3b** X=OCH$_2$CF$_3$	**3c** X=OPh	**3d** X=OC$_6$F$_5$	**3e** X=Cl
LDP (kcal/mol)	10.83	11.63	12.38	14.32	15.05
E°': ONO$^{cat/sq}$	−0.985	−0.391	−0.431	−0.107	0.151
E°': ONO$^{sq/q}$	0.029	0.423	0.388	0.572	0.737
λ_{max} (nm)	558	574	574	598	604

LDP values taken from ref. 10. LDP value for tert-butoxide was assumed as equal to the reported value of 10.83 for adamantyloxide. LDP value for trifluoroethoxide obtained through personal correspondence. E° values given in V vs. Cp$_2$Fe$^{+/0}$.

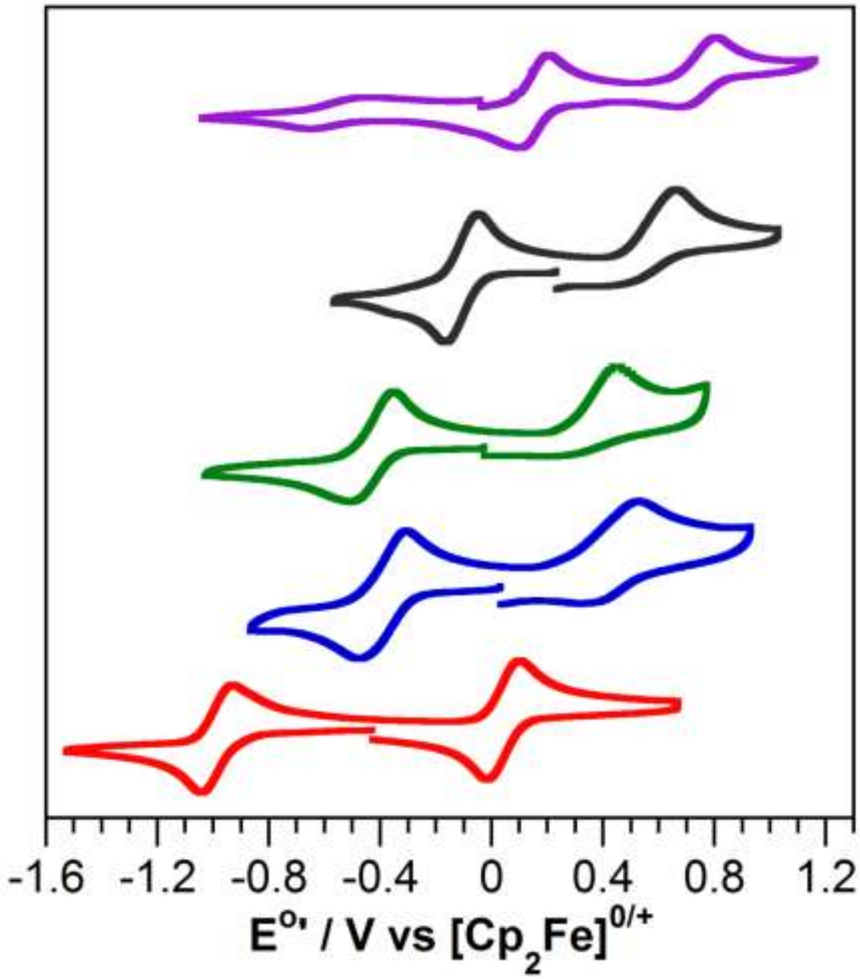

Figure 2.4. Cyclic voltammograms of complexes **3a-e**: **3a** (red), **3b** (blue), **3c** (green), **3d** (black), **3e** (purple). Voltammograms recorded in CH_2Cl_2 with 0.1 M $TBAPF_6$ and 1 mM analyte at 200 mV/s scan rate. Voltammograms referenced against an internal standard of Cp_2Co^+ PF_6^-.

Comparison of the redox potentials of complexes **3a-e** to the ligand donor parameter of their ancillary ligand revealed an obvious and drastic effect of the donor group. While the trifluoroethoxide donor appears to be a notable outlier, there is a clear linear relationship between the ligand donor parameter (LDP) of the ancillary ligand and the ONO ligand-based redox events (Figure 2.5). This linear relationship indicates a 220 mV anodic shift in the $ONO^{cat/sq}$ redox couple for every kcal/mol increase in the ligand donor parameter. The powerful tunability of the ligand-based redox events via ancillary ligand substitution is a direct result of the ability of strongly donating groups to stabilize the highly lewis acidic tantalum(V) center. By quenching this lewis acidity with strongly donating ligands, the ligand-based frontier molecular orbitals will become higher in energy and therefore undergo electrochemical redox events at more negative potentials.

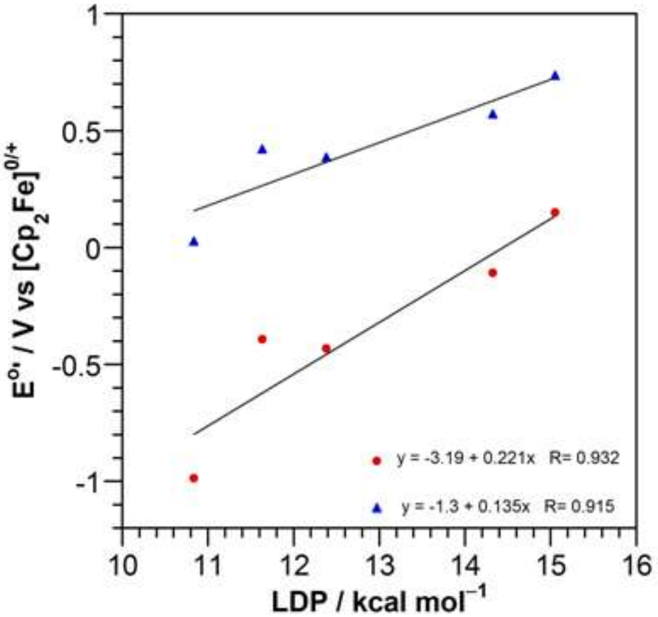

Figure 2.5. Plot of the $ONO^{cat/sq}$ couple (red dot) and $ONO^{sq/q}$ couple (blue triangle) vs the LDP of the ancillary ligand for complexes **3a-e**.

EPR Analysis of $(ONO^{sq})TaX_3$

Given the formulation of **3a-e** as open-shell radicals, analysis by EPR spectroscopy was performed on these complexes to determine if periodic trends with LDP would be observable. The previously reported complex **3e** shows well-defined hyperfine coupling to the tantalum center, exhibiting an eight-line spectrum with an isotropic hyperfine coupling constant (A_{iso}) of 20 G. This coupling has been compared to the related NNN ligand complex $(NNN^{sq})TaCl_3$, which showed an A_{iso} of 31 G. The larger value of the coupling constant was attributed to greater delocalization of the unpaired electron onto the tantalum center.[15] Consistent with the assignment of the unpaired electron residing primarily on the ligands, in both cases the isotropic hyperfine coupling was well below values observed for genuine Ta(IV) complexes with the unpaired electron localized on the metal center (61-113 G in organometallic Ta(IV) complexes, and 211 G for the inorganic coordination complex $TaCl_4(PEt_3)_2$).[23,24] By extension of the results with (ONO^{sq}TaCl$_3$ and (NNN^{sq})TaCl$_3$, we surmised that increased donor strength of the ancillary ligands would quench the Lewis acidity of the metal center and result in less delocalization of the unpaired electron onto tantalum. EPR analysis supports this hypothesis, where a clear decrease in the signal width of the derivative spectrum was observed, a result of decreased delocalization of the electron onto the tantalum center. While hyperfine coupling to the tantalum center was clear in the spectrum of **3e**, the spectra obtained for **3a-d** were not as defined. Though it is tempting to assign the splitting in **3d** as resulting from tantalum hyperfine (A_{iso} = 14 G between the inner features of the spectrum), the complexity of the spectrum apparent at the outer edges of the signal necessitates further modeling of the spectrum. Furthermore, splitting between the inner features of **3b** and **3c** provides an approximate A_{iso} = 12 G, however the expected eight-line spectrum cannot be fully resolved in these two spectra (likely a result of their narrow signal width and resulting overlap with the outer features of the derivative spectrum). The EPR spectrum of **3a** is less clear, giving a spectrum whose potential hyperfine coupling to the tantalum center is not discernible. In all cases, however, the decreasing width of the signal as the donor strength of the ancillary ligand increases is indicative of diminished tantalum character in the SOMO. All spectra show g values near 2, consistent with primarily ligand-based radicals: **3a** g = 1.999, **3b** g = 1.996, **3c** g = 1.998, **3d** g = 1.991, and **3e** g = 1.982.

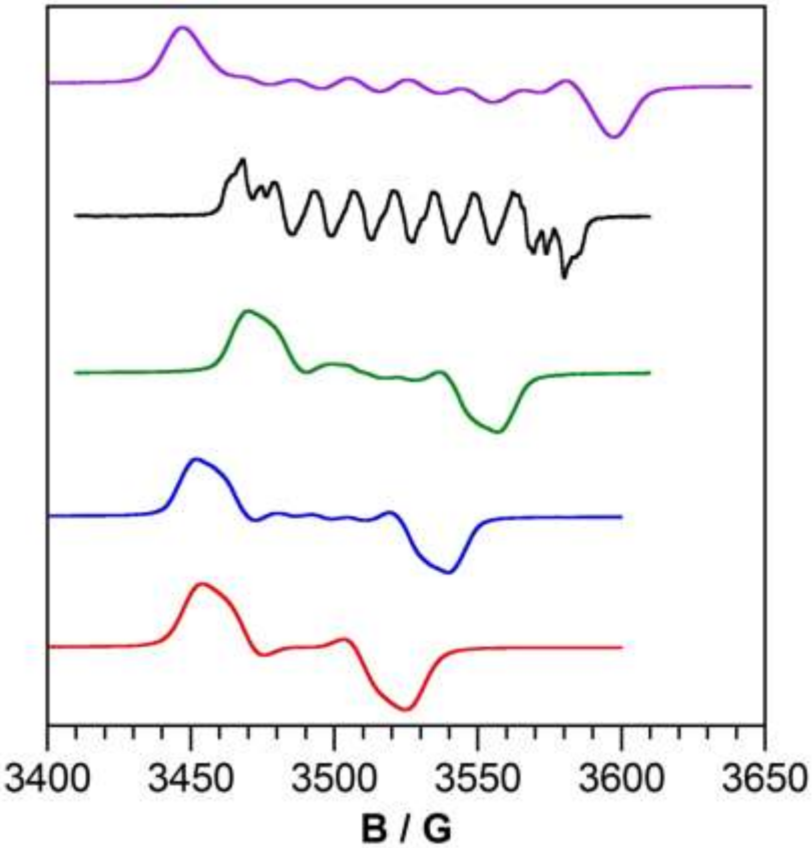

Figure 2.6. Room temperature EPR spectra of complexes **3a** (red), **3b** (blue), **3c** (green), **3d** (black), and **3e** (purple) in Et_2O.

DFT Analysis of 3a and 3e

With experimental data indicating a drastic effect of the donor ligand on the electrochemical and spectroscopic properties of complexes **3a-e**, we sought to verify our hypothesis that the donor groups modulated the metal contribution to the SOMO by interrogating **3a** and **3e** with DFT analysis. A specific selection of only **3a** and **3e** was made since these were the only species for which X-ray diffraction data were available to provide a starting point for geometry optimization. Provided in Table 2.1, computed bond lengths reproduce the structural features of the dianionic $(ONO^{sq})^{2-}$ ligand framework, showing moderate contraction of the C–O bonds and localized double-bond character within the aryl backbone. Shown in Figure 2.7, the identity of the SOMO is analogous in complexes **3a** and **3e**, being primarily ligand-based and antibonding with respect to the N–C and O–C bonds. The antibonding nature of the SOMO is reflective of the C–O and C–N bond length differences observed between the $(\mathrm{ONO}^{sq})^{2-}$ and $(\mathrm{ONO}^{q})^{1-}$ ligand forms.

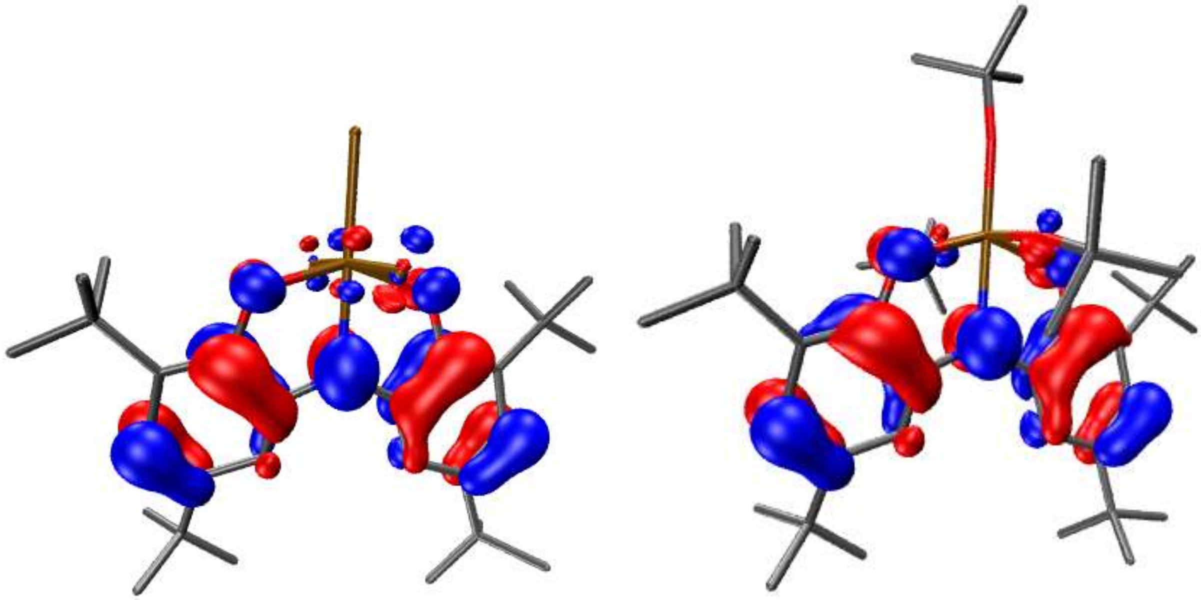

Figure 2.7. Calculated spin density plots for the SOMO of $(\mathrm{ONO}^{sq})\mathrm{TaCl}_3$ (**left**) and $(\mathrm{ONO}^{sq})\mathrm{Ta(OtBu)}_3$ (**right**).

Table 2.3. SOMO contributions from the ONO ligand, tantalum, and ancillary ligands for complexes **3a** and **3e**.

	Mullikan Population Analysis of the SOMO		
	ONO	Ta	OtBu / Cl
$(\mathrm{ONO}^{sq})\mathrm{Ta(OtBu)}_3$	96.2 %	1.6 %	2.2 %
$(\mathrm{ONO}^{sq})\mathrm{TaCl}_3$	90.9 %	4.0 %	5.0 %

The postulation that increased donor strengths effect the ligand redox-potential through decreasing the Lewis acidity of the metal center and shifting electron density to the ONO ligand was supported by DFT analysis. In complex **3a**, the SOMO is predominately ligand-based (96.2%) while in **3e**, though still predominately ligand-based, this value decreases to 90.9%. The altered ligand contribution is reflective of the cathodically shifted oxidation potential in **3a** relative to **3e**, since the decreased Lewis acidity of the tantalum center in **3a** minimizes stabilization of the ligand-based SOMO via the N–Ta π bonding interaction. Indeed, the tantalum contribution to the SOMO increases from 1.6% in **3a** to 4.0% in **3e**, consistent with the diminished Lewis acidity upon increasing the donor strength.

Summary and Conclusions

The incorporation of alkoxide and phenoxide-based donor ligands onto the (ONO)Ta framework proceeds through a conserved synthetic approach, ultimately yielding complexes of the general formula $(ONO^{sq})Ta(OR)_3$. A comparison of these complexes to the previously described complex $(ONO^{sq})TaCl_3$ demonstrates that a drastic electrochemical tunability exists as a function of the LDP of the ancillary donor group. This tunability manifests itself as a 1.13 V window for the $ONO^{cat/sq}$ redox couple, ranging from −0.985 V for complex **3a** to 0.151 V for complex **3e**. Given the LDP range reported by Odom, this range is likely near the limit of tunability for the $(ONO^{sq})TaX_3$ morphology. The donor strength may be decreased only incrementally more by substitution of chloride (LDP=15.05) for the weakest donor reported, iodide (LDP=15.80), though it remains to be seen if three large iodide groups can be accommodated by the $(ONO^{sq})Ta$ fragment. Furthermore, the donor strength cannot be extended beyond *tert*-butoxide, as attempts to incorporate the donor group dimethylamido ($–NMe_2$) (LDP=9.34) by oxidizing the anionic complex $(ONO^{cat})Ta(NMe_2)_3^{-}$ to the neutral species $(ONO^{sq})Ta(NMe_2)_3$ with the same approach as **3a-d** resulted in the formation of $(ONO^{cat})Ta(NMe_2)_2$, suggesting instability of the desired $–NMe_2$ congener towards radical expulsion.

The ability of ancillary groups to affect the redox potential of a redox-active ligand provides a straightforward and modular approach to fine-tuning the properties of redox-active ligand-containing complexes. The facile nature of this approach and the wide electrochemical potential range it enables position it as a powerful method to tuning the properties, and potentially the reactivity, of redox-active ligand-containing complexes.

Experimental

General Considerations. Manipulations were performed using standard Schlenk line techniques or in a N_2 filled glovebox. Diethyl ether, pentane, benzene, toluene, and tetrahydrofuran were sparged with argon and dried and deoxygenated by passage through activated alumina and Q5 columns, respectively. C_6D_6 was dried over NaK/benzophenone, vacuum transferred, and stored over molecular sieves. Silver trifluoromethanesulfonate (AgOTF) was dried under high vacuum prior to use. $(ONO^{cat})TaCl_2 \cdot Et_2O$ (**1**) was synthesized according to published procedures.[14] The lithium alkoxides were prepared by deprotonation of the corresponding alcohol in pentane using nBuLi.

Physical Methods. All ^1H-NMR and ^{19}F-NMR spectra were recorded on a Bruker DRX 400 MHz spectrometer. ^1H-NMR spectra were referenced to tetramethylsilane using the proteo impurity of C_6D_6 (7.16 ppm). ^{19}F-NMR spectra were referenced to trichloro-fluoromethane using an external trifluoroacetic acid standard ($\delta = -76.55$ ppm). ^{13}C-NMR spectra were recorded on a Bruker 500 MHz spectrometer equipped with a cryoprobe and referenced to tetramethylsilane using the solvent peaks of C_6D_6 (128.06 ppm). Solution UV-vis-NIR spectra were recorded in 1-cm path-length cuvettes on a Shimadzu UV-1700 spectrophotometer. Extinction coefficients were determined from Beer-Lambert Law plots. EPR spectra were collected on a Bruker EMX X-band spectrometer equipped with an ER041XG microwave bridge. EPR spectra were collected on 1 mM samples in Et_2O at room temperature. Elemental analyses were collected on a Perkin-Elmer 2400 Series II CHNS/O analyzer.

Electrochemical Methods. Electrochemical measurements were recorded with a Gamry G300 potentiostat using a standard three-electrode configuration including a 3.0 mm glassy carbon working electrode, a platinum wire auxiliary electrode, and a silver wire pseudo-reference electrode. All measurements were made on solutions that contained 1 mM analyte and 0.1 M NBu_4PF_6 in CH_2Cl_2 at an ambient temperature of ca. 21 °C in a glovebox under a N_2 atmosphere. Potentials are referenced to $Cp_2Fe^{+/0}$ using an internal standard of Cp_2Co^+ PF_6^- (E°' = −1.33 V vs $Cp_2Fe^{+/0}$ in CH_2Cl_2).[25]

Computational Methods. Calculations were performed employing the non-empirical hybrid-GGA functional PBE0.[26] For computational efficiency, initial geometry optimizations were performed using moderate split-valence plus polarization basis sets (def2-SVP).[27] Structures were refined using basis sets of triple zeta valence plus polarization (def2-TZVP) quality.[28] Crystal structures obtained from X-ray diffraction experiments were used as starting points for the geometry optimization; no molecular symmetry was imposed. All calculations were performed using the quantum chemistry program package TURBOMOLE.[30,31]

Crystallographic Methods. X-ray diffraction data were collected on single crystals mounted on a glass fiber using a Bruker SMART APEX II diffractometer. Measurements were carried out using Mo Kα (λ = 0.71073 Å) radiation, wavelength selected with a single-crystal graphite monochromator. A full sphere of data was collected for each crystal structure. The APEX[32] program package was used to determine the unit cell parameters and for data collection. The raw frame data was processed using SAINT[33] and SADABS[34] to yield the reflection data files. Subsequent calculations were carried out using the SHELXTL[35] program. The structures were solved by direct methods and refined on F^2 by full matrix least-squares techniques. The analytical scattering factors[36] for neutral atoms were used throughout the analysis. Hydrogen atoms were included using a riding model. ORTEP diagrams were generated using ORTEP-3 for Windows.

Table 2.4 Data collection and refinement parameters for **3a**.

	3a
Empirical Formula	2 ● $C_{40}H_{67}NO_5Ta$
Formula Weight (g/mol)	1645.78
Crystal System	Triclinic
Space Group	$P\bar{1}$
a (Å)	9.5735(6)
b (Å)	21.2731(12)
c (Å)	23.1516(13)
α (°)	68.6581(6)
β (°)	85.1750(7)
γ (°)	77.3528(7)
Volume (Å^3)	4285.1(4)
Z	4
F(000)	1708
Reflections collected	51388
Independent reflections (R_{int})	20249 (0.0131)
GOF	1.033
R1 [I > 2σ(I)][a]	0.0200
wR2 (all data)[a]	0.0496

[a] $R1 = \Sigma||F_o|-|F_c|| / \Sigma|F_o|$; $wR2 = [\Sigma[w(F_o^2-F_c^2)^2] / \Sigma[w(F_o^2)^2]]^{1/2}$; $GOF = S = [\Sigma[w(F_o^2-F_c^2)^2] / (n-p)]^{1/2}$

[Li(OEt$_2$)][(ONO^{cat})Ta(O^{t}Bu)$_3$] ([Li(OEt$_2$)][2a]). A vial was charged with (ONO^{cat})TaCl$_2$·Et$_2$O (0.124 g, 0.166 mmol) and dissolved in 5 mL of Et$_2$O. In a separate vial, LiO^{t}Bu (0.040 g, 0.500 mmol) was dissolved in 5 mL of Et$_2$O. The solution of LiO^{t}Bu was added to the solution of (ONO^{cat})TaCl$_2$·Et$_2$O at room temperature and stirred for 3 hours. The reaction was dried under vacuum and the resulting crude was extracted with pentane and filtered through celite. Removal of solvent under vacuum yielded the product as a yellow solid (0.119 g, 79 %). ^{1}H-NMR (400 MHz, C_6D_6) δ/ppm: 7.82 (s, 2H, aryl-H), 7.07 (s, 2H, aryl-H), 2.88 (q, *J*=7 Hz, 4H, Et$_2$O), 1.71

(s, 18H, ^{t}Bu), 1.56 (s, 18H, ^{t}Bu), 1.51 (s, 9H, O^{t}Bu), 1.25 (s, 18H, O^{t}Bu), 0.85 (t, *J*=7 Hz, 6H, Et_2O). ^{13}C {^1H}-NMR (125 MHz, C_6D_6) δ/ppm: 157.0, 145.8, 142.1, 133.0, 114.4, 110.2, 75.6, 66.4, 35.4, 35.1, 33.1, 32.9, 32.8, 30.6, 14.8. Anal. Calcd. for $C_{44}H_{77}NO_6LiTa$: C, 58.46; H, 8.59; N, 1.55. Found: C, 58.28; H, 8.24; N, 1.40. UV-vis-NIR (toluene) λ_{max}/nm (ε/M^{-1} cm^{-1}): 322 (14,500), 376 sh. (3910).

[Li(OEt$_2$)][(ONO^{cat})Ta(OCH$_2$CF$_3$)$_3$] ([Li(OEt$_2$)][2b]). A vial was charged with (ONO^{cat})TaCl$_2$·Et$_2$O (0.071 g, 0.094 mmol) and was dissolved in 5 mL of Et_2O. In a separate vial, $LiOCH_2CF_3$ (0.030 g, 0.280 mmol) was dissolved in 5 mL of Et_2O. Both solutions were frozen in a cold well, and upon thawing, the solution of $LiOCH_2CF_3$ was added to the solution of (ONO^{cat})TaCl$_2$·Et$_2$O. After stirring for 5 hours the mixture was filtered through celite and dried under vacuum. The crude material was co-evaporated with pentane, then slurried in 1 mL of pentane and chilled at −35 °C overnight. Subsequently, the solid was separated from the pentane and dried under vacuum to yield the product as a yellow solid (0.066 g, 71 %). ^1H-NMR (400 MHz, C_6D_6) δ/ppm: 7.88 (d, *J*=2 Hz, 2H, aryl-H), 7.12 (d, *J*=2 Hz, 2H, aryl-H), 4.47 (q, *J*=9 Hz, 6H, CH_2), 2.90 (q, *J*=7 Hz, 4H, Et_2O), 1.59 (s, 18H, ^{t}Bu), 1.48 (s, 18H, ^{t}Bu), 0.83 (t, *J*=7 Hz, 6H, Et_2O). ^{19}F {^1H}-NMR (376 MHz, C_6D_6) δ/ppm: −77.96. ^{13}C {^1H}-NMR (125 MHz, C_6D_6) δ/ppm: 156.5, 144.4, 144.1, 134.5, 117.0, 111.3, 66.5, 35.4, 35.1, 32.5, 30.3, 14.2. Anal. Calcd. for $C_{38}H_{56}F_9NO_6LiTa$: C, 46.49; H, 5.75; N, 1.43. Found: C, 46.31; H, 5.32; N, 1.18. UV-vis-NIR (toluene) λ_{max}/nm (ε/M^{-1} cm^{-1}): 408 (3360).

[Li(OEt$_2$)$_2$][(ONO^{cat})Ta(OPh)$_3$] ([Li(OEt$_2$)$_2$][2c]). (ONO^{cat})TaCl$_2$(Et$_2$O) (0.116 g, 0.155 mmol) was dissolved in 8 mL of Et_2O and frozen in a cold well. Upon thawing, LiOPh (0.046 g, 0.460 mmol) was added to the solution of (ONO^{cat})TaCl$_2$(Et$_2$O) as a 2 mL solution in Et_2O. An addition 2 mL of Et_2O was used to wash the vial and aid transfer. After 4 hours the mixture was chilled overnight in a freezer. After sitting overnight, the reaction was filtered, dried, and pentane cooevaporated. The crude material was slurried in *ca.* 2 mL of pentane and stored overnight in a freezer at −35 °C. Yellow solids of **2c** were collected and dried under vacuum (0.130 g, 82 %). ^{1}H-NMR (400 MHz, C_6D_6) δ/ppm: 7.38 (s, 2H, aryl-H), 7.00 (s, 2H, aryl-H), 6.97-6.88 (br. overlapping, 12H, O-aryl-H), 6.67 (br, 3H, O-aryl-H), 3.05 (q, J=7 Hz, 8H, Et_2O), 1.68 (s, 18H, ^{t}Bu), 1.44 (s, 18H, ^{t}Bu), 0.87 (t, J=7 Hz, 12H, Et_2O).

$[Li(OEt_2)_{1.5}][(ONO^{cat})Ta(OC_6F_5)_3]$ ($[Li(OEt_2)_{1.5}]$[2d]). $(ONO^{cat})TaCl_2(Et_2O)$ (0.131 g, 0.175 mmol) was dissolved in 5 mL of Et_2O. To this solution was added $LiOC_6F_5$ (0.100 g, 0.526 mmol) as a 3 mL solution in Et_2O. After 2 hours the mixture was filtered, dried, and pentane coevaporated. The crude material was slurried in *ca.* 4 mL of pentane and chilled in a freezer at −35 °C overnight. The solids were collected, redissolved in 4 mL of toluene and dried to yield the product as a yellow solid (0.182 g, 82 %). ^{1}H-NMR (400 MHz, C_6D_6) δ/ppm: 7.44 (d, J=2 Hz, 2H, aryl-H), 6.95 (d, J=2 Hz, 2H, aryl-H), 2.93 (q, J=7 Hz, 6H, Et_2O), 1.56 (s, 18H, ^{t}Bu), 1.33 (s, 18H, ^{t}Bu), 0.80 (t, J=7 Hz, 9H, Et_2O). ^{19}F {^{1}H}-NMR (376 MHz, C_6D_6) δ/ppm: −158.87 (d, J=22.6 Hz), −163.23, −166.76.

$(ONO^{sq})Ta(O^tBu)_3$ (3a). ($[Li(OEt_2)]$[2a]) (0.054 g, 0.060 mmol) was dissolved in 5 mL of Et_2O and chilled at −35 °C for 1 hour. AgOTf (0.015 g, 0.060 mmol) was dissolved in 5 mL of Et_2O and added dropwise to the solution of ($[Li(OEt_2)]$[2a]). The reaction was stirred for 1 hour and then dried under vacuum. The resulting solid was extracted with pentane and filtered through celite. Removal of solvent under vacuum yielded the product as a dark purple solid (0.046 g, 94 %). Crystalline material is obtained by layering a saturated THF solution of **5a** with acetonitrile. Anal. Calcd. for $C_{40}H_{67}NO_5Ta$: C, 58.38; H, 8.21; N, 1.70. Found: C, 58.21; H, 8.16; N, 1.57. UV-vis-NIR (toluene) λ_{max}/nm (ε/M^{-1} cm^{-1}): 348 (10430), 412 (8330), 558 (1780), 888 (7200).

(ONO^{sq})Ta(OCH$_2$CF$_3$)$_3$ (3b). ([Li(OEt$_2$)][2b]) (0.043 g, .044 mmol) was dissolved in 4 mL of Et$_2$O and AgOTf (0.011 g, .044 mmol) was also dissolved in 4 mL of Et$_2$O. Both solutions were chilled, whereupon the solution of AgOTf was added to the solution of ([Li(OEt$_2$)][2b]). After stirring for 2 hours the reaction was dried under vacuum, extracted with pentane and filtered through celite. The solution was dried under vacuum to yield the product as a purple/blue solid (0.036 g, 92 %). UV-vis-NIR (toluene) λ_{max}/nm (ε/M^{-1} cm^{-1}): 324 (11800), 392 (4210), 574 (2480), 876 (5910). Anal. Calcd. for $C_{34}H_{46}F_9NO_5Ta$: C, 45.34; H, 5.15; N, 1.56. Found: C, 45.83; H, 5.21; N, 1.47.

(ONO^{sq})Ta(OPh)$_3$ (3c). ([Li(OEt$_2$)$_2$][2c]) (0.130 g, 0.125 mmol) was dissolved in 12 mL of Et$_2$O and briefly chilled in a −35 °C freezer. To this cold solution was added AgOTf (0.032 g, 0.124 mmol) as a 2 mL solution in THF. After stirring for one hour the mixture was dried under vacuum and then extracted with pentane, filtered, and dried. The crude purple solids were slurried in *ca.* 1 mL of acetonitrile and chilled for 2 days in a freezer. Dark purple solids were collected and washed with two 0.5 mL portions of acetonitrile to yield the product as a dark purple solid (0.054 g, 50 %). UV-vis-NIR (toluene) λ_{max}/nm (ε/M^{-1} cm^{-1}): 397 (4030), 574 (3550), 899 (6070). Anal. Calcd. for $C_{46}H_{55}NO_5Ta$: C, 62.58; H, 6.28; N, 1.59. Found: C, 62.46; H, 6.41; N, 1.75.

(ONO^{sq})Ta(OC$_6$F$_5$)$_3$ (3d). ([Li(OEt$_2$)$_{1.5}$][2d]) (0.123 g, 0.097 mmol) was dissolved in 5 mL of Et$_2$O and briefly chilled in a −35 °C freezer. To this cold solution was added AgOTf (0.025 g, 0.097 mmol) as a 3 mL solution in Et$_2$O. After stirring for one hour the mixture was dried under vacuum and then extracted with pentane, filterd, and dried. The crude material was dissolved in a minimum of toluene and layered with acetonitrile. After mixing of the layers the solution was transferred to a freezer. After sitting overnight in a freezer at −35 °C, dark teal solids were collected and dried under vacuum (0.055 g, 49 %). UV-vis-NIR (toluene) λ_{max}/nm (ε/M^{-1} cm^{-1}): 418 (2760), 598 (3140), 912 (4960). Anal. Calcd. for $C_{46}H_{40}F_{15}NO_5Ta$: C, 47.93; H, 3.50; N, 1.22. Found: C, 48.22; H, 3.45; N, 1.03.

References

(1) Tolman, C. A. *Chem. Rev.* **1977**, *77*, 313.
(2) Abel, E. W.; Bennett, M. A.; Wilkinson, G. *J. Chem. Soc.* **1959**, 2323.
(3) Cotton, F. A. *Inorg. Chem.* **1963**, *3*, 702.
(4) Magee, T. A.; Matthews, C. N.; Wang, T. S.; Wotiz, J. H. *J. Am. Chem. Soc.* **1961**, *83*, 3200.
(5) Strohmeier, W.; Muller, F. J. *Naturforsch., B J. Chem. Sci.* **1967**, *22B*, 451.
(6) Taylor, R. C.; Horrocks, D. *Inorg. Chem.* **1963**, *2*, 723.
(7) Setiawan, D.; Kalescky, R.; Kraka, E.; Cremer, D. *Inorg. Chem.* **2016**, *55*, 2332.
(8) Shimura, Y.; Tsuchida, R. *Bull. Chem. Soc. Jpn.* **1956**, *29*, 311.
(9) Hoggard, P. *Struct. Bond.* **2004**, *106*, 37.
(10) DiFranco, S.; Maciulis, N.; Staples, R. J.; Batrice, R. J.; Odom, A. L. *Inorg. Chem.* **2012**, *51*, 1187.
(11) Lukens, W. W.; Smith, M. R.; Andersen, R. A. *J. Am. Chem. Soc.* **1996**, *118*, 1719.
(12) Darmon, J.; Turner, Z.; Lobkovsky, E.; Chirik, P. *Organometallics* **2012**, *31*, 2275.
(13) Munha, R. F.; Zarkesh, R. A.; Heyduk, A. F. *Inorg. Chem.* **2013**, *52*, 11244.
(14) Zarkesh, R.; Ziller, J. W.; Heyduk, A. F. *Angew. Chem. Int. Ed. Engl.* **2008**, *47*, 4715.
(15) Heyduk, A.; Zarkesh, R.; Nguyen, A. *Inorg. Chem.* **2011**, *50*, 9849.
(16) Bruni, S.; Caneschi, A.; Cariati, F.; Delfs, C.; Dei, A.; Gatteschi, D. *J. Am. Chem. Soc.* **1994**, *116*, 1388.
(17) Larsen, S.; Pierpont, C. *J. Am. Chem. Soc.* **1988**, *110*, 1827.
(18) Chaudhuri, P.; Hess, M.; Hildenbrand, K.; Bill, E.; Weyhermüller, T.; Wieghardt, K. *Inorg. Chem.* **1999**, *38*, 2781.
(19) Ranis, L. G.; Werellapatha, K.; Pietrini, N. J.; Bunker, B. A.; Brown, S. N. *Inorg. Chem.* **2014**, *53*, 10203.
(20) Uhrhammer, R.; Su, Y.; Swenson, D. C.; Jordan, R. F. *Inorg. Chem.* **1994**, *1*, 4398.
(21) Murphy, E. F.; Murugavel, R.; Roesky, H. W. *Chem. Rev.* **1997**, *97*, 3425.
(22) Jordan, R. F.; Dasher, W. E.; Echols, S. F. *J. Am. Chem. Soc.* **1986**, 1718.
(23) Noh, W.; Girolami, G. S. *Inorg. Chem.* **2008**, *47*, 535.
(24) Labauze, G.; Samuel, E.; Livage, J. *Inorg. Chem.* **1980**, *19*, 1384.
(25) Connelly, N. G.; Geiger, W. E. *Chem. Rev.* **1996**, *96*, 877.
(26) Perdew, J. P.; Ernzerhof, M.; Burke, K. *J. Chem. Phys.* **1996**, *105*, 9982.
(27) Schäfer, A.; Horn, H.; Ahlrichs, R. *J. Chem. Phys.* **1992**, *97*, 2571.
(28) Schäfer, A.; Huber, C.; Ahlrichs, R. *J. Chem. Phys.* **1994**, *100*, 5829.
(29) Andrae, D.; Häußermann, U.; Dolg, M.; Stoll, H.; Preuß, H. *Theor. Chim. Acta* **1990**, *77*, 123.
(30) Furche, F.; Ahlrichs, R.; Hättig, C.; Klopper, W.; Sierka, M.; Weigend, F. *Wiley Interdiscip. Rev. Comput. Mol. Sci.* **2014**, *4*, 91.
(31) TURBOMOLE V6.3, Turbomole GmbH, Karlsruhe, 2011. http://www.turbomole.com.

(32) APEX2, Version 2014.11-0, Bruker AXS, Inc.; Madison, WI 2014.
(33) SAINT, Version 8.34a, Bruker AXS, Inc.; Madison, WI 2013.
(34) Sheldrick, G. M. SADABS, Version 2014/5, Bruker AXS Inc.; Madison, WI 2014.
(35) Sheldrick, G. M. SHELXTL, Version 2014/7, Bruker AXS Inc.; Madison, WI 2014.
(36) International Tables for Crystallography 1992, Vol C., Dordrecht: Kluwer Academic Publishers.

Chapter 3

Synthesis and Reactivity of Tantalum–Oxo Complexes Supported by the Redox-Active ONO Ligand

Introduction

Extensive research on the reactivity of early transition metal complexes featuring metal-ligand multiple bonds (M=NR, M=O) has uncovered a number of powerful transformations affected by this moiety, including C–H bond activation and [2+2] cycloaddition reactions involving unsaturated organic substrates.[1–10] These reactions are typically limited to stoichiometric transformations and ligand-exchange processes, owing to the low propensity of early transition metals to access low-valent states through group transfer or reductive elimination processes.[11] Enabling multi-electron reactivity at these reactive fragments could open new avenues for their application in catalytic bond transformations. The incorporation of a redox-active ligand into the coordination sphere of early transition metals has been identified as a potential method to enable these multi-electron transformations.[11]

Previous reactivity studies utilizing redox-active ligands have demonstrated that coordination of a redox-active ligand to a d^0 metal center enables multi-electron reactivity to occur at the metal center.[12–21] Specifically, the complexes $(ONO^{cat})TaCl_2(Et_2O)$ and $(ONO^{cat})Ta(O^tBu)_2$ have demonstrated multi-electron reactivity with organic azides.[15] Upon reaction with excess phenylazide, $(ONO^{cat})Ta(O^tBu)_2$ catalyzes the production of azobenzene without consumption of the tantalum complex, while $(ONO^{cat})TaCl_2(Et_2O)$ undergoes significant decomposition in the course of the same reaction (Scheme 3.1). This transformation is thought to proceed through the initial formation of the putative species $(ONO^q)Ta(X)_2(=NPh)$ (X = Cl or O^tBu), whose formation is enabled by a two electron, ligand-based oxidation. Subsequent elimination of azobenzene through homocoupling of two tantalum imido species closes the cycle and reduces the tantalum complex back to its starting oxidation state.[15] Utilizing the related redox-active NNN ligand (where $(NNN^{cat})^{3-}$ = bis(2-isopropylamido-4-methoxyphenyl)amide) and a zirconium center yielded similar imido reactivity; the reaction of (NNN^{cat})ZrCl(CN^{t}Bu)$_2$ with alkylazides in the presence of excess *tert*-butylisocyanide produced carbodiimide catalytically via nucleophilic attack of the titanium-imide moiety on a coordinated isocyanide ligand, with subsequent reductive elimination, a ligand-enabled process, yielding the carbodiimide product (as described in Chapter 1).[13]

Scheme 3.1. **A**)Reactivity of (ONO^{cat})Ta(O^{t}Bu)$_2$ with azides. **B**) Putative equilibrium process between (ONO^{cat})TaCl$_2$(Et$_2$O) and azobenzene.

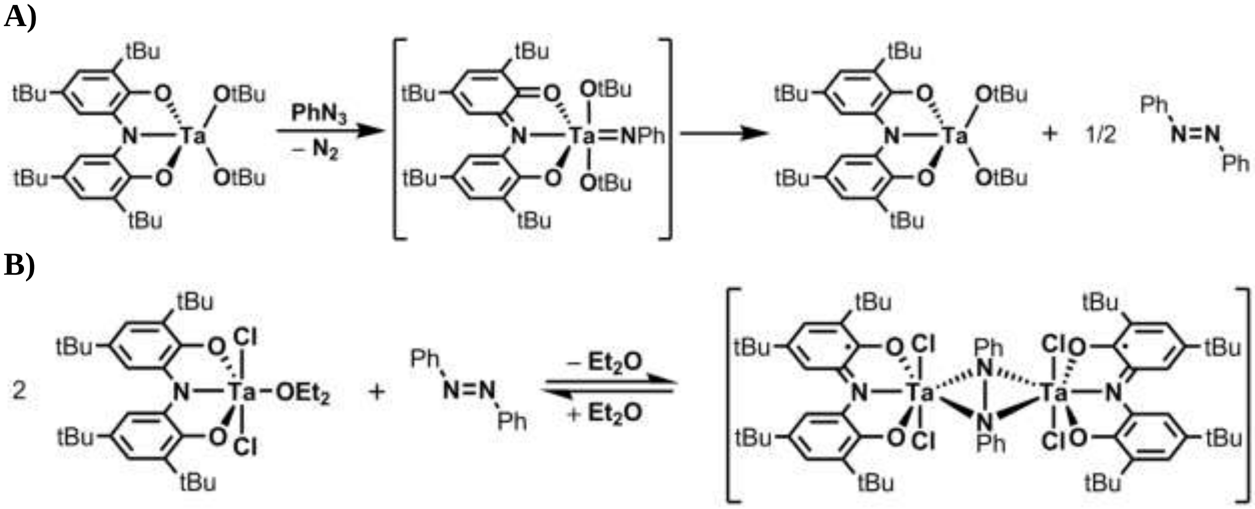

Though (ONO^{cat})Ta(O^{t}Bu)$_2$ favors expulsion of azobenzene from the putative tantalum-imido intermediate, the increased oxidizing power of dioxygen and smaller steric profile as compared to azobenzene, coupled with the oxophilicity of tantalum, suggests that the final azobenzene expulsion step in Scheme 3.1.A could be reversed when utilizing dioxygen. As evidence for potential dioxygen activation by (ONO^{cat})Ta(O^{t}Bu)$_2$, partial reduction of azobenzene was observed in studies utilizing the complex (ONO^{cat})TaCl$_2$(Et$_2$O) which, upon treatment with azobenzene, yielded an intermediate consistent with the formulation [(ONO^{sq})TaCl$_2$(η^2:μ^2-PhNNPh)]$_2$ (Scheme 3.1.B).[15]

Utilizing redox-active ligands to enable dioxygen activation at early-transition-metal centers has been a topic of previous investigations. Treatment of (ONHO^{cat})ZrCl$_2$(THF) with one half of an equivalent of dioxygen produced bimetallic $[(ONO^{q})ZrCl_2(\mu\text{-}OH)]_2$,[20] resulting from reduction and protonation of the O_2 substrate. In another example, Abu-Omar and coworkers reported the ability of a redox-active ligand supported zirconium complex to partially reduce dioxygen by two electrons, yielding an η^2-peroxo moeity.[21] Moreover, the Soper group has reported the use of redox-active catecholate complexes of rhenium, whereby ligand-based redox events allow for facile dioxygen activation.[22] Similarly, a catecholate supported molybdenum complex has been reported to affect complete reduction of dioxygen into molybdenum-oxo groups, with the reducing equivalents originating from two catecholate ligands.[23]

Expanding upon the limited field of O_2 activation with early-metal redox-active ligand complexes, the reactivity of complexes of the formula $(ONO^{cat})Ta(OR)_2$ with O_2 has been explored. The effects of alkoxide ligands of varying donor abilities on the properties and reactivity of these species has also been investigated to determine if a simple alteration of the alkoxide could result in significant changes in redox properties and reactivity.

Results and Discussion

Synthesis and Characterization of $[(ONO)Ta(OCH_2CF_3)]_2$

The drastic effect of ancillary alkoxide on the redox properties of $(ONO^{sq})Ta(OR)_3$ complexes discussed in Chapter 2 provided motivation to pursue coordinatively unsaturated variants, therefore synthesis of the new complex $(ONO^{cat})Ta(OCH_2CF_3)_2$ was pursued for comparison with the previously reported complex $(ONO^{cat})Ta(O^tBu)_2$ (**4a**). Initial attempts to synthesize this complex followed the method used for **4a**, whereby treatment of $(ONO^{cat})TaMe_2$ with two equivalents of ^tBuOH yielded **4a**.[15] Using trifluoroethanol ($HOCH_2CF_3$) as the alcohol, thermolysis of the reaction was necessary to affect reaction completion. Alternatively, the synthesis of this complex was readily achieved under mild conditions by treatment of

$(ONO^{cat})TaCl_2 \cdot Et_2O$ with two equivalents of $LiOCH_2CF_3$ in diethyl ether. Purification of the crude material via chilling of a pentane slurry yielded the complex as an orange/yellow solid. Both ^1H and ^{19}F-NMR in C_6D_6 displayed two sets of resonances for the $–OCH_2CF_3$ groups, attributed to a dimeric structure of the complex where a bridging $–OCH_2CF_3$ group and a monocoordinate $–OCH_2CF_3$ group exist as discrete, non-exchanging ligands on the NMR timescale.

Analysis of a single crystal of this product by X-ray diffraction confirmed the expected dimeric formulation of $[(ONO^{cat})Ta(OCH_2CF_3)_2]_2$ **(4b)**. The solid-state structure of **4b** is depicted in Figure 3.1 with selected bond lengths provided in Table 3.1. Each tantalum center exhibits a slightly distorted octahedral geometry, with two $–OCH_2CF_3$ ligands bridging the metal centers. Notable structural distortions from octahedral geometry are observed in the O(3)–Ta(1)–O(4) bond angle of 151.04(10)°, as well as the N(1)–Ta(1)–O(1) bond angle of 74.84(11)°. Expectedly, the O(3)–Ta(1) and O(3)#–Ta(1) bond lengths of the bridging $–OCH_2CF_3$ groups, 2.105(2) and 2.154(2) Å, respectively, are longer than that of the monocoordinate $–OCH_2CF_3$ O(4)–Ta(1) bond length of 1.902(2) Å. Bond lengths within the ligand aryl backbone vary by only 0.03 Å, consistent with a delocalized aromatic ring and the assignment of the ligand as the $(ONO^{cat})^{3-}$ form.[15,20,24,25] Application of Brown's MOS calculation yields a value of −3.22, supporting the fully reduced $(ONO^{cat})^{3-}$ assignment.[26] The Ta–O(4) bond length of 1.902(2) Å observed for the monocoordinate alkoxide in **4b** is longer than the Ta-alkoxide distance observed in **4a** (1.86 Å, avg.), consistent with the weaker donor strength of $–OCH_2CF_3$ compared to $–O^tBu$. This is also apparent from the Ta(1)–O(4)–C bond angle of 135.1(3)° (or 133.3(9)°, considering the disordered trifluoroethyl group) in the $–OCH_2CF_3$ ligand, which shows less linearization, and thus less π-donation, than the corresponding $–O^tBu$ bond angles of 144.8(2)°

and 146.5(2)° observed in **4a**. The gross structural differences between **4a** and **4b** can be attributed to the increased steric profile of the –O^{t}Bu groups compared to that of the –OCH$_2$CF$_3$ groups, preventing dimerization and maintaining **4a** as monomeric.

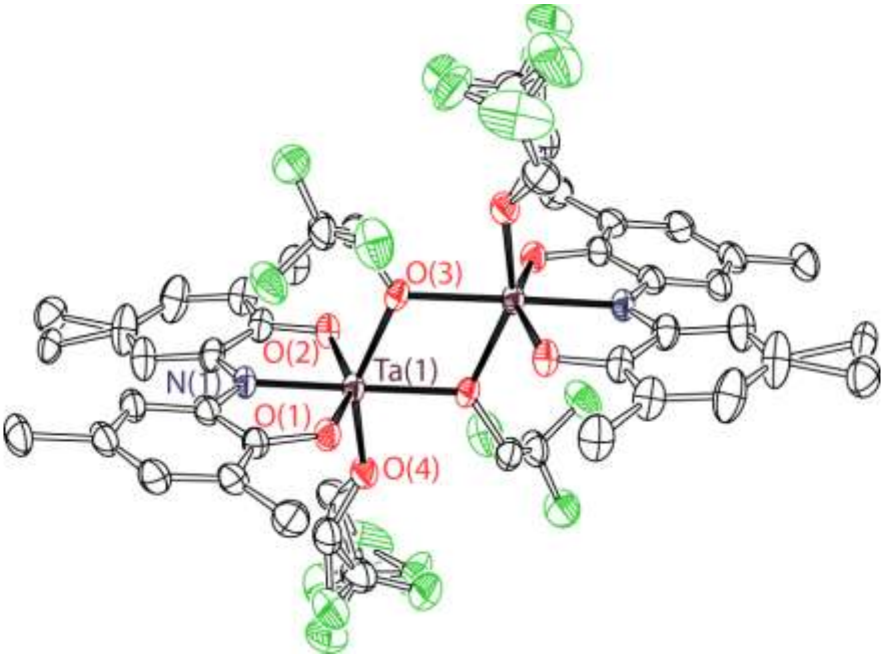

Figure 3.1. ORTEP diagram of [(ONO^{cat})Ta(OCH$_2$CF$_3$)$_2$]$_2$ **(4b)**. Thermal ellipsoids are shown at 50% probability. Hydrogen atoms and the tert-butyl groups of the ONO ligand backbone have been omitted for clarity. Three molecules of co-crystallized toluene were also omitted for clarity.

Table 3.1. Selected bond distances (Å) and angles (°) for **4a** and **4b**.

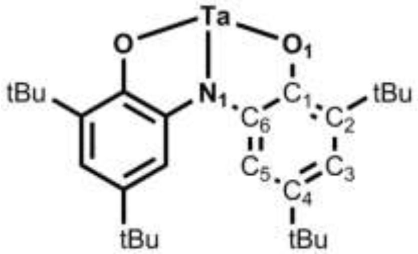

	$(ONO^{cat})Ta(O^tBu)_2$ **4a**	$[(ONO^{cat})Ta(OCH_2CF_3)_2]_2$ **4b**
	Bond Lengths (Å)	
N(1)–Ta(1)	2.067(3)	2.045(3)
O(1)–Ta(1)	1.931(2)	1.914(2)
C(6) –N(1)	1.419(5)	1.416(5)
C(1) –O(1)	1.374(4)	1.378(4)
C(1) –C(2)	1.387(5)	1.388(5)
C(2) –C(3)	1.403(5)	1.401(5)
C(3) –C(4)	1.394(5)	1.396(6)
C(4) –C(5)	1.394(5)	1.396(5)
C(5) –C(6)	1.390(5)	1.391(5)
C(6) –C(1)	1.404(5)	1.392(5)
O(3)–Ta(1)	1.855(2)	2.105(2)
O(3)#–Ta(1)	-----	2.154(2)
O(4)–Ta(1)	1.860(2)	1.902(2)
	Bond Angles (°)	
N(1)–Ta(1)–O(1)	75.09(11)	74.84(11)
O(3)–Ta(1)–O(3)#	-----	67.86(10)
O(3)–Ta(1)–O(4)	107.99(11)	151.04(10)

Synthesis and Characterization of Tantalum-Oxo Trimers

An initial attempt at pursuing tantalum-oxo species was undertaken via treatment of **4a** with KOH in THF, which yielded a new diamagnetic species (Scheme 3.2). The ^{1}H-NMR spectrum displayed a $–O^tBu$ resonance that was shifted from 1.14 ppm in the starting material to 0.96 ppm in the product. The integration of this peak relative to the ligand ^{t}Bu resonances was also reduced from 1:1 in the starting material to 1:2 in the product, indicating the loss of a $–O^tBu$ ligand. This loss was attributed to expulsion of ^{t}BuOH, as drying the crude reaction mixture and extracting with pentane did not result in precipitation of the other potential by-product KO^{t}Bu. A tentative formulation of the product as ([(ONO^{cat})Ta(O^{t}Bu)(μ-O)]$_n^{n-}$ nK$^+$ (**5**) was therefore consistent with the spectroscopic data. Furthermore, treatment of **5** with 18-crown-6 resulted in a downfield shift of the –O^{t}Bu resonance from 0.96 ppm to 1.42 ppm, consistent with an altered coordination environment of the putative potassium counterion and suggesting the tentative formation of [(ONO^{cat})Ta(O^{t}Bu)(μ-O)]$_n^{n-}$ n[K(18-crown-6)]$^+$ (**6**). This synthetic path utilizing KOH was not amenable to **4b**, which yielded a complex mixture of intractable products.

Scheme 3.2. Synthesis of complexes **5** and **7**.

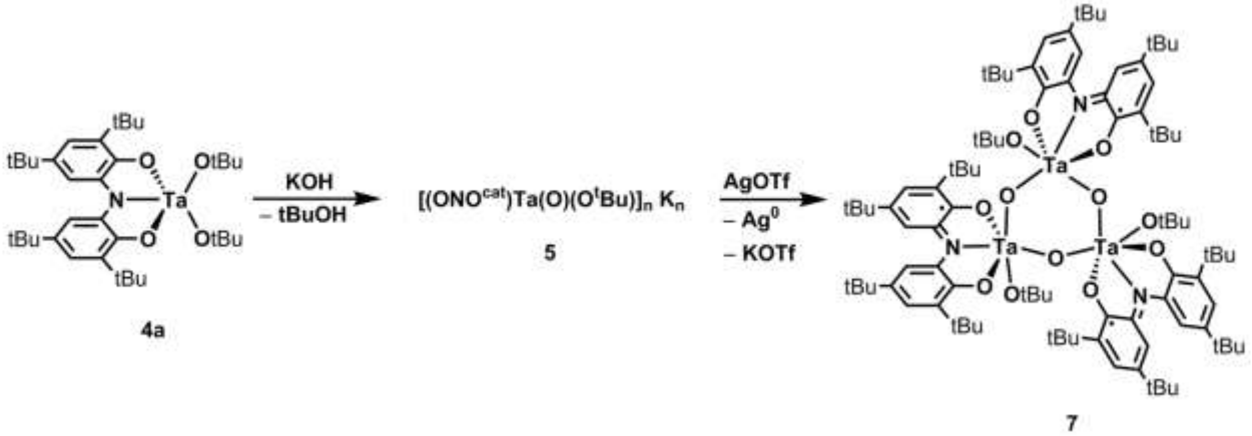

Oxidation of **5** was achieved with silver triflate to afford [(ONO^{sq})Ta(O^{t}Bu)(μ-O)]$_3$ (**7**) as a deep purple solid. Single crystal X-ray diffraction analysis of **7** yielded the structure in Figure 3.2. Complex **7** exists as a trimer in the solid state and possesses bond lengths provided in Table 3.2. The metal center has a distorted octahedral coordination geometry, with an O(1)–Ta–O(2) bond angle of 144.90°. The bridging oxo groups display inequivalent Ta–O bond distances of 1.8740(19) Å and 1.9903(19) Å which are consistent with Ta–(μ^2-O) bond lengths.[27,28] The six-membered Ta$_3$O$_3$ core formed from the bridging oxo units is essentially planar. Partial cyclohexadienyl bond character within the aryl backbone and contracted C–O and C–N bond lengths (avg.) of 1.34 Å and 1.36 Å, respectively, are similar to those observed in the complex (ONO^{sq})TaCl$_3$ and other (ONO^{sq})$^{2-}$ supported metal complexes, supporting the assignment of the

$(ONO^{sq})^{2-}$ form of the ligand in **7**.[14,29–31] This assignment is further validated by metrical oxidation state calculations, which yield a value of −2.23.

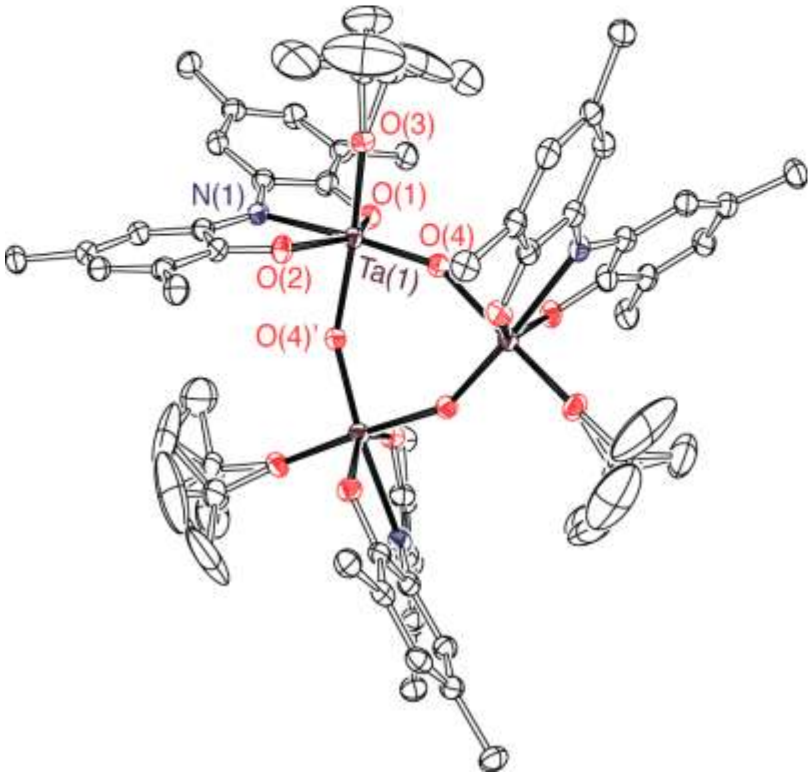

Figure 3.2. ORTEP diagram of $[(ONO^{sq})Ta(O^{t}Bu)(\mu\text{-}O)]_3$ (**7**). Thermal ellipsoids are shown at 50% probability. Hydrogen atoms and the tert-butyl groups of the ONO ligand backbone have been omitted for clarity.

Complex **7** is NMR silent and displays a UV-vis-NIR spectrum indicative of the semiquinone oxidation state of the ligand (Figure 3.3), with λ_{max} values of 930 nm and 558 nm. Analysis by EPR spectroscopy revealed an isotropic signal with a single g value of 1.99, suggesting an organic based radical. Evans method analysis determined a μ_{eff} of 1.67 μB (considering each monomeric unit as independent for the concentration term in the calculation), consistent with an S=1/2 system and suggesting each $(ONO^{sq})Ta$ fragment has a non-interacting, ligand-based radical. This result unequivocally rules out strong antiferromagnetic coupling between the ligand based radicals to yield an overall S=1/2 trimeric species, since attempts at calculating the effective magnetic moment using the concentration of the trimer yielded a μ_{eff} of 2.90 μB.

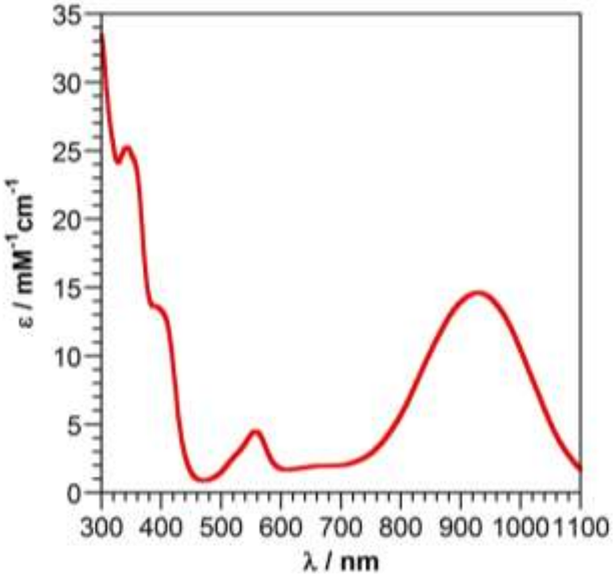

Figure 3.3. UV-vis-NIR spectrum of **7** recorded in toluene.

The trimeric structure obtained in complex **7** prompted a revisit of the use of KOH in accessing tantalum-oxo groups. Whereas the treatment of $(\mathrm{ONO^{cat}})\mathrm{Ta(O^tBu)_2}$ with KOH resulted in loss of a single unit of alcohol and retention of the potassium ion, the inclusion of a halide into the tantalum precursor could provide a driving force for the loss of potassium as well. With this goal, $(\mathrm{ONO^{cat}})\mathrm{TaMeCl(Et_2O)}$ was treated with one equivalent of KOH in THF. An orange product was separated from a white precipitate of, presumably, KCl and analysis by ^{1}H-NMR revealed the loss of the tantalum-methyl group and the appearance of a single coordinated THF molecule with resonances shifted from free THF. Single crystal analysis confirmed the loss of chloride and methyl ligands as well as the coordination of THF, revealing the product as $[(\mathrm{ONO^{cat}})\mathrm{Ta(THF)}(\mu\text{-O})]_3$ (**8**) (Figure 3.4). Bond lengths within the ligand backbone are consistent with the presence of a fully reduced $(\mathrm{ONO^{cat}})^{3-}$ ligand, showing no notable localized double-bond character within the aryl ring and possessing a long C(1)–O(1) bond of 1.375(3) Å. As with **7**, complex **8** exhibits inequivalent bridging tantalum-oxo bond distances of 1.9564(16) and 1.8843(16) Å. The trend in bridging oxo bond length is, however, opposite between **7** and **8**. Whereas in **7** the longer bridging tantalum-oxo (1.9903(19) Å) is trans to the *tert*-butoxide ligand and the shorter tantalum-oxo (1.8740(19) Å) is trans to the ONO nitrogen, in **8**, the longer bridging tantalum-oxo (1.9564(16) Å) is trans to the ONO nitrogen and the shorter tantalum-oxo is trans to the THF ligand (1.8843(16) Å). This trend is consistent with both the stronger donor ability of *tert*-butoxide relative to THF, and also with the decreased donor ability of the ONO ligand upon oxidation from the $(\mathrm{ONO^{cat}})^{3-}$ form in **8** to the $\mathrm{ONO^{sq}}$ form in **7**. As with **7**, the six-membered Ta_3O_3 core in **8** is essentially planar.

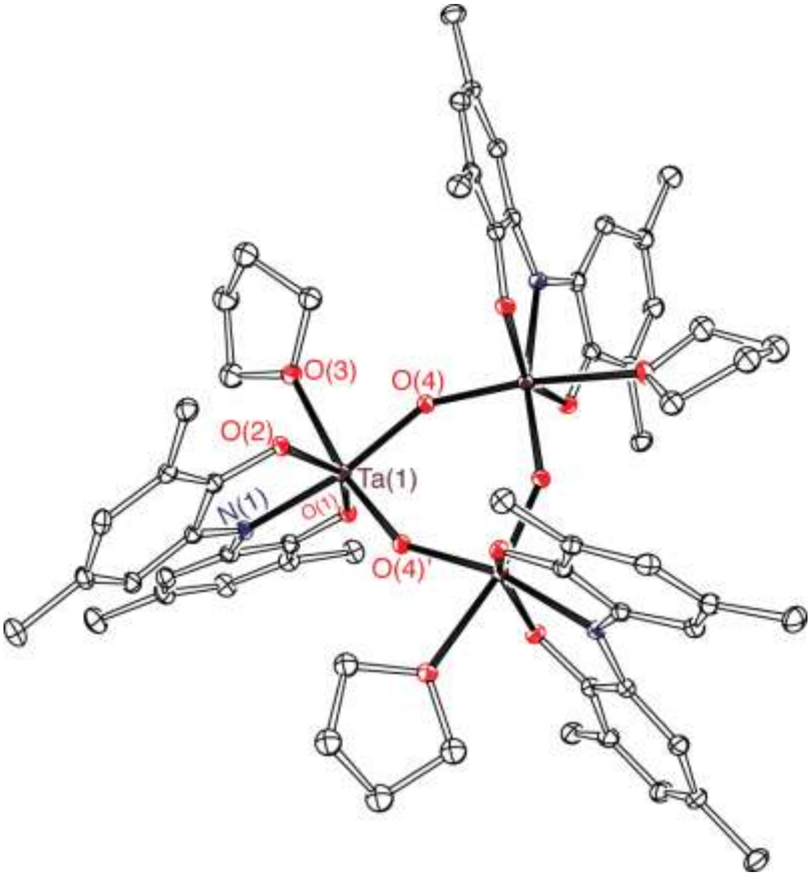

Figure 3.4. ORTEP diagram of $[(\mathrm{ONO^{cat}})\mathrm{Ta(THF)}(\mu\text{-O})]_3$ (**8**). Thermal ellipsoids are shown at 50% probability. Hydrogen atoms and the tert-butyl groups of the ONO ligand backbone have been omitted for clarity.

Table 3.2. Selected bond distances (Å) and angles (°) for **7** and **8**.

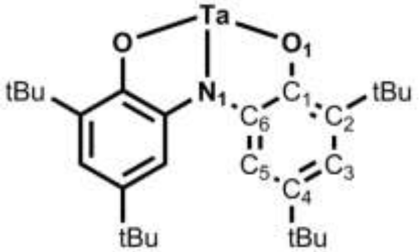

	$[(\text{ONO}^{sq})\text{Ta}(\text{O}^t\text{Bu})(\mu\text{-O})]_3$ **7**	$[(\text{ONO}^{cat})\text{Ta}(\text{THF})(\mu\text{-O})]_3$ **8**
	Bond Lengths (Å)	
N(1)–Ta(1)	2.236(2)	2.0886(19)
O(1)–Ta(1)	1.982(2)	1.9379(16)
C(6) –N(1)	1.359(4)	1.403(3)
C(1) –O(1)	1.345(4)	1.375(3)
C(1) –C(2)	1.403(4)	1.390(3)
C(2) –C(3)	1.385(4)	1.408(4)
C(3) –C(4)	1.412(4)	1.388(4)
C(4) –C(5)	1.375(4)	1.401(4)
C(5) –C(6)	1.406(4)	1.391(3)
C(6) –C(1)	1.429(4)	1.409(3)
O(3)–Ta(1)	1.875(2)	2.2370(17)
O(4)–Ta(1)	1.8740(19)	1.9564(16)
O(4)#–Ta(1)	1.9903(19)	1.8843(16)
	Bond Angles (°)	
N(1)–Ta(1)–O(1)	72.61(8)	74.71(7)
O(4)–Ta(1)–O(4)#	87.84(12)	91.47(9)
N(1)–Ta(1)–O(4)	171.87(8)	166.42(7)
Ta(1)–O(4)–Ta(1)#	152.17(12)	148.53(9)

O_2 Reactivity of $(\text{ONO}^{cat})\text{Ta}(\text{OR})_2$ Complexes

With **4a** and **4b** both possessing fully-reduced catecholate forms of the ligand, and expected to display significant electronic differences as demonstrated by the model complexes **3a** and **3b**, their ability to activate O_2 was investigated. Exposing a cold pentane solution of **4a** to half an equivalent of O_2 (Scheme 3.3) produced a burgundy-colored solution which, upon warming, became dark green/purple. The dark green product $[(\text{ONO}^{q})\text{Ta}(\text{O}^t\text{Bu})_2(\mu\text{-O})]_2$ (**9a**) was isolated from the crude reaction solids in 31% yield after removing impurities via cold pentane washing. Analogously, treatment of **4b** with one equivalent of O_2 in a cold pentane/benzene solution yielded a dark green crude product which, upon washing with cold pentane, afforded pure $[(ONO^q)Ta(OCH_2CF_3)_2(\mu\text{-}O)]_2$ (**9b**) in 39% yield.

Scheme 3.3. Synthesis of complexes **9a** and **9b**.

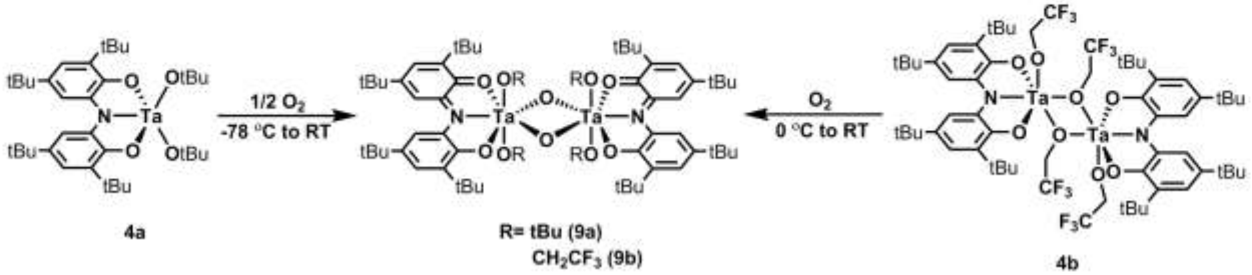

X-ray diffraction analysis on single crystals of **9a** yielded the structure depicted in Figure 3.5, with selected bond distances provided in Table 3.3. The coordination environment around the metal center is distorted pentagonal bipyramidal, with an O(3)–Ta(1)–O(4) bond angle of 158.53(13)°. The Ta(1)–O(5) and Ta(1)–O(6) bond lengths of 1.959(3) Å and 1.957(3) Å are consistent with previously characterized tantalum(V) μ-O bond lengths.[27,28] The distance between O(5) and O(6) is 2.40 Å, outside of the range of typical O–O bonds present in μ-η^2:η^2-O_2 ligands (typically 1.4-1.5 Å),[32] indicating the complete scission of the O=O bond and formation of two independent μ-O groups. The Ta(1)–O(3)–C and Ta(1)–O(4)–C bond angles of the tert-butoxide ligands are 155.0(3)° and 154.8(3)° respectively. The aryl backbone exhibits localized double bond character, with short bond lengths of 1.36 Å and lengthening of the other bonds up to 1.45 Å (See Table 3.3). This cyclohexadienyl-type character in addition to the short C–O and C–N bond lengths of 1.28-1.29 and 1.34 Å, respectively, indicates the presence of the $(ONO^q)^{1-}$ form of the ligand.[14,20,30,33,34]

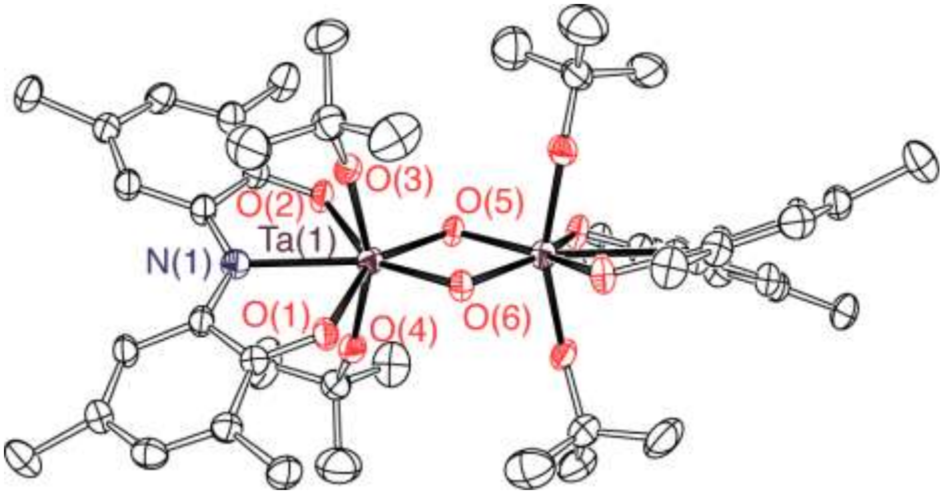

Figure 3.5. ORTEP diagram of $[(ONO^{q})Ta(O^{t}Bu)_2(\mu^2\text{-}O)]_2$ (**9a**). Thermal ellipsoids are shown at 50% probability. Hydrogen atoms and the tert-butyl groups of the ONO ligand backbone have been omitted for clarity.

Structural characterization of **9b** revealed this complex to be isostructural with **9a** (Figure 3.6). Similarly to **9a**, the shortening of the C–N and C–O bonds within the ligand and the cyclohexadienyl bond character in the aryl backbone suggests the quinonate form of the ligand. The Ta(1)–O(5) and Ta(1)–O(6) bond lengths of 1.9294(18) and 1.9565(18) Å, respectively, are comparable those observed in **9a**. Furthermore, the distance of 2.39 Å between O(5) and O(6) indicates the presence of two, independent μ-O groups. Analogous differences in the Ta–alkoxide bond lengths were observed between **9a** and **9b** (*ca.* 0.04 Å) as were observed between **4a** and **4b** (0.04 Å). The bond angles for Ta(1)–O(3)–C and Ta(1)–O(4)–C are 130.64(18)° and 144.21(18)°, respectively, reflecting the decreased donor strength of trifluoroethoxide relative to *tert*-butoxide. Metrical oxidation state calculations of **9a** and **9b** yielded values of −1.24 and −1.06, respectively, indicative of the monoanionic $(ONO^{q})^{1-}$ assignment for the ligand in each of these complexes.[26]

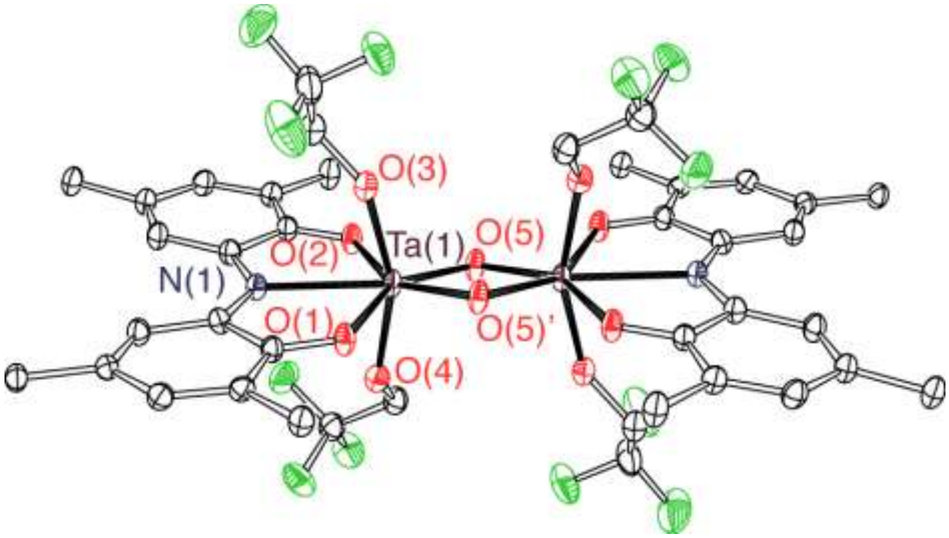

Figure 3.6. ORTEP diagram of $[(ONO^q)Ta(OCH_2CF_3)_2(\mu^2\text{-}O)]_2$ (**9a**). Thermal ellipsoids are shown at 50% probability. Hydrogen atoms and the tert-butyl groups of the ONO ligand backbone have been omitted for clarity. Cocrystallized and disordered benzene and toluene have also been omitted for clarity.

Complexes **9a** and **9b** are diamagnetic, allowing characterization by NMR spectroscopy. Complex **9a** displayed a single $–O^tBu$ resonance with equal intensity to the ligand tert-butyl resonances while **9b** displayed a single unique $–CH_2–$ quartet and a single resonance in the ^{19}F-NMR spectrum. The UV-vis-NIR spectrum of **9a** exhibits intense absorption bands in the near IR region, with λ_{max} at 822 and 760 nm, and a visible region band at λ_{max} of 440 nm. Complex **9b** exhibits similar NIR absorption bands at 810 and 770 nm, and a visible region band at 468 nm (Figure 3.7). These bands are indicative of $(ONO^q)^{1-}$ supported metal complexes, with the NIR bands arising from intraligand π-π^* transitions.[35,36]

Table 3.3. Selected bond distances (Å) and angles (°) for **9a** and **9b**.

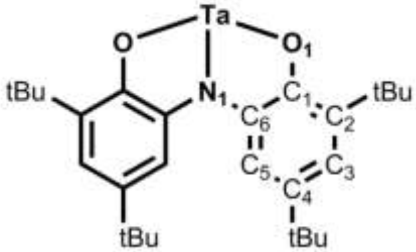

	$[(ONO^{q})Ta(O^{t}Bu)_2(\mu^2\text{-O})]_2$ **9a**	$[(ONO^{q})Ta(OCH_2CF_3)_2(\mu^2\text{-O})]_2$ **9b**
	Bond Lengths (Å)	
N(1)–Ta(1)	2.386(4)	2.461(2)
O(1)–Ta(1)	2.193(3)	2.1163(18)
O(2)–Ta(1)	2.184(3)	2.1238(19)
C(6) –N(1)	1.345(6)	1.346(3)
C(1) –O(1)	1.278(5)	1.281(3)
C(1) –C(2)	1.433(6)	1.441(4)
C(2) –C(3)	1.362(6)	1.364(4)
C(3) –C(4)	1.437(6)	1.439(4)
C(4) –C(5)	1.362(6)	1.361(4)
C(5) –C(6)	1.420(6)	1.434(4)
C(6) –C(1)	1.447(6)	1.452(4)
O(3)–Ta(1)	1.905(3)	1.948(2)
O(4)–Ta(1)	1.898(3)	1.944(2)
O(5)–Ta(1)	1.957(3)	1.9294(18)
O(6)/O(5)#–Ta(1)	1.959(3)	1.9565(18)
	Bond Angles (°)	
N(1)–Ta(1)–O(1)	67.75(12)	68.11(7)
O(3)–Ta(1)–O(4)	158.53(13)	157.92(8)
O(5)–Ta(1)–O(6)/O(5)#	75.60(13)	75.88(8)

Analysis of **9a** by cyclic voltammetry revealed partially reversible reductions at −1.05 and −1.42 V, with daughter peaks at *ca.* −0.5 V appearing when the voltage window was scanned past the second reduction event (Figure 3.7). Consistent with the results from the electrochemical data presented in Chapter 1, a significant anodic shift was observed for these reduction events in **9b**. Cyclic voltammetry performed on **9b** revealed reduction events at −0.58 and −0.94 V, with slightly increased reversibility of the second reduction event as compared to

9a. Anodic shifts of 470 and 480 mV for the first and second reduction, respectively, were observed between **9a** and **9b**, consistent with the results observed between model complexes **3a** and **3b**. Considering the small separation between the first and second reduction events for **9a** and **9b** (0.37 and 0.36 V, respectively), the reduction events likely correspond to stepwise one-electron reduction of each of the ONO ligands present in the complex.

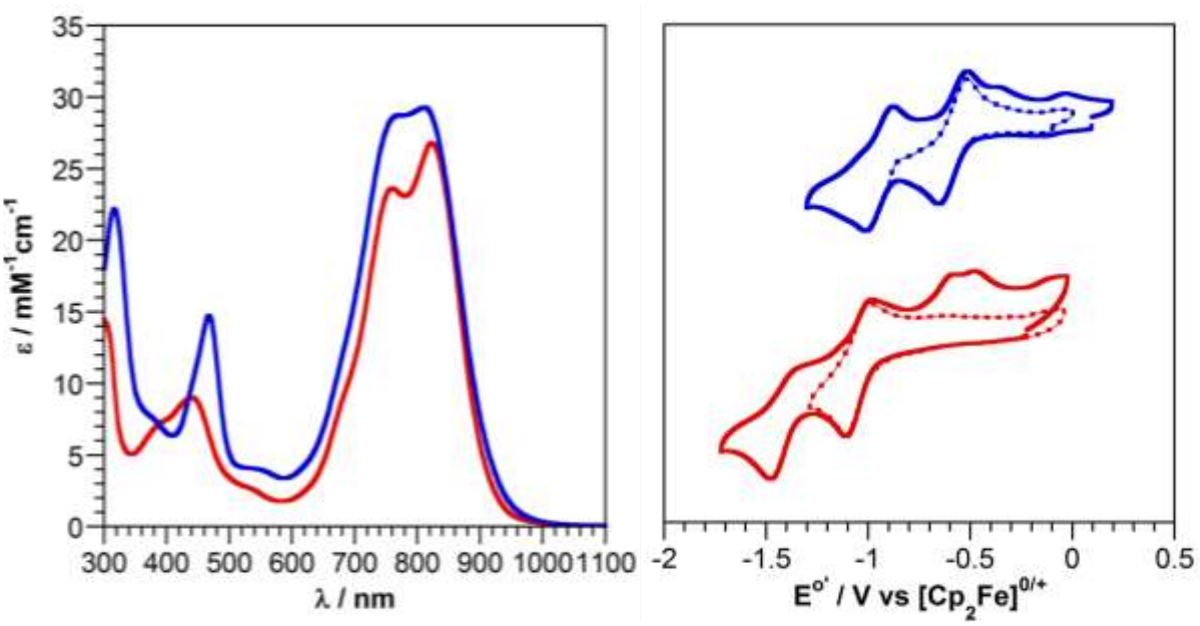

Figure 3.7. Left. UV-vis-NIR spectrum of **9a (red)** and **9b (blue)** recorded in toluene. **Right.** Cyclic voltammograms of **6a (red)** and **6b (blue)** recorded in CH_2Cl_2 at a 200 mV/s scan rate at 1mM concentrations with 0.1 M $TBAPF_6$ as the supporting electrolyte.

*Reactivity of **9a** and **9b***

Prototypical reagents for hydrogen-atom abstraction and C–H bond activation studies were used to probe the reactivity of **9a** and **9b**. Complex **9a** reacts with one equivalent of diphenylhydrazine in C_6D_6 over the course of 2 days to produce azobenzene and one equivalent of ^{t}BuOH (as determined by comparison of the azobenzene and ^{t}BuOH peak integrations). During the course of the reaction the green color of **9a** gives way to purple, reminiscent of the color of **7**. Heating this mixture to 70 °C continues ^{t}BuOH formation, though this production slows before generating a full second equivalent of ^{t}BuOH. Removal of the reaction volatiles under vacuum, redissolving in C_6D_6, and continued heating at 70 °C resumes slow ^{t}BuOH formation until, nominally, the second equivalent of ^{t}BuOH is produced. While ^{1}H-NMR suggests the loss of *ca.* two equivalents of ^{t}BuOH, the presence of an IR band at 3649 cm^{-1} is consistent with the persistence of a hydroxyl containing species. The final product displays a UV-vis-NIR spectrum indicative of an $(ONO^{sq})^{2-}$ supported complex (Figure 3.8) that, along with the ^{1}H-NMR observations, suggests the formation of **7**. Treatment of **9b** with one equivalent of diphenylhydrazine under the same conditions resulted in complete consumption of diphenylhydrazine and formation of azobenzene on the timescale of minutes, with a similar green to purple color change occurring immediately upon mixing. The formation of trifluoroethanol follows the same trend observed with ^{t}BuOH, producing one equivalent at room temperature and requiring the same heat, vacuum, heat cycle to promote the loss of the second equivalent of trifluoroethanol. Again, an IR band at 3653 cm^{-1} suggests the persistence of a hydroxyl containing species. The UV-vis-NIR spectrum of the product is consistent with the presence on an ONO^{sq} fragment, suggesting the formation of the trifluoroethoxide containing congener to **7**. A potential reactivity pattern consistent with the observed formation of azobenzene and alcohol is provided in Scheme 3.4.

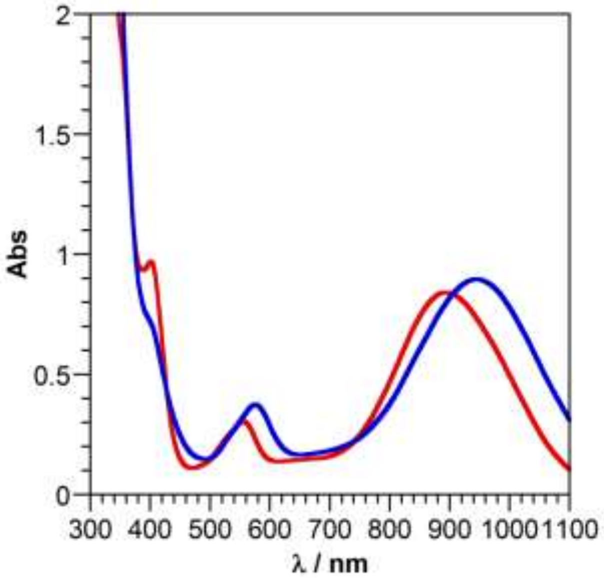

Figure 3.8. UV-vis-NIR spectra of the crude products obtained from treatment of **9a (red)** and **9b (blue)** with one equivalent of diphenylhydrazine and subsequent heating.

Scheme 3.4. Possible reaction intermediate obtained by treating **9a** and **9b** with one equivalent of diphenylhydrazine and subsequent heating.

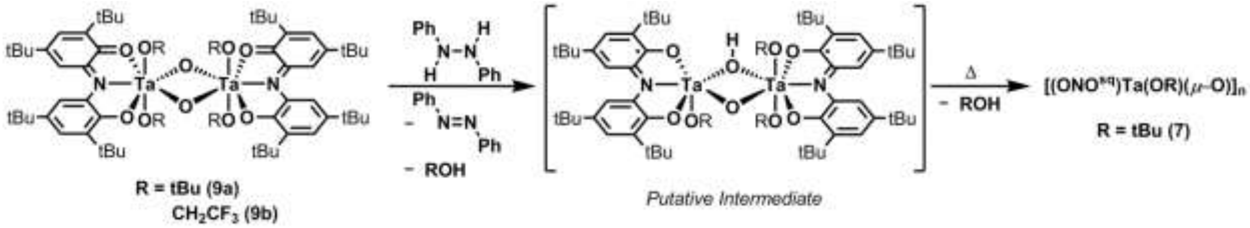

After establishing preliminary reactivity with the strong hydrogen-atom donor diphenylhydrazine, the reactivity of **9a** and **9b** was investigated with 9,10-dihydroanthracene (9,10-DHA). Treatment of **9a** and **9b** with >10 equivalents of 9,10-DHA in a sealed J. Young tube and heating at 70 °C resulted in the production of ^{t}BuOH and CF_3CH_2OH, respectively, accompanied by the disappearance of the diamagnetic starting material and the formation of anthracene as indicated by ^{1}H-NMR spectroscopy. Two equivalents of alcohol were produced per equivalent of anthracene, consistent with the reactivity established with diphenylhydrazine.

Analysis of the crude 9,10-DHA reaction mixtures by UV-vis-NIR spectroscopy yielded the spectra in Figure 3.9. The reaction product from **9a** with 9,10-DHA displays absorption bands consistent with (ONO^{sq})$^{2-}$ supported complexes, with λ_{max} values at 926 and 552 nm, respectively. Analogous results were obtained from the reaction of **9b** with 9,10-DHA, where the crude reaction product yielded a spectrum with λ_{max} values at 946 and 574 nm. The assignment of the reaction product from **9a** and 9,10-DHA as **7** is consistent with the UV-vis-NIR spectrum and the observed ^{t}BuOH formation. Considering their similar reactivity patterns, a similar formulation for the reaction product obtained from **9b** is likely. Taken together, these results suggest that complexes **9a** and **9b** are capable of affecting hydrogen-atom abstraction from substrates with C–H bond strengths up to 76 kcal/mol,[37] though the ability to abstract a hydrogen atom from 9,10-DHA appears to stop upon formation of **7** (and its putative trifluoroethoxide congener) under these experimental conditions.

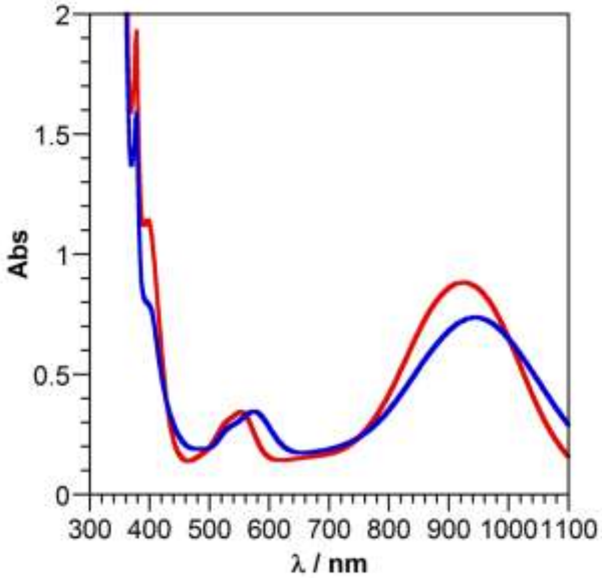

Figure 3.9. UV-vis-NIR spectra of the crude reaction product obtained by treatment of **9a (red)** and **9b (blue)** with excess 9,10-DHA and subsequent heating.

To compare the effects of donor ligand on reactivity, **9a** and **9b** were subjected to kinetic analysis for the aforementioned oxidation of 9,10-DHA. Solutions of **9a** and **9b** were prepared in C_6D_6 in J. Young tubes, treated with an excess of 9,10-DHA and an internal standard, then heated at 70 °C with intermittent analysis by ^{1}H-NMR. Under these pseudo-first order conditions, consumption of **9a** occurs with a rate constant of k_{obs} = 8.3x10^{-5} sec^{-1}, while **9b** consumption occurs with a rate constant of $k_{obs} = 2.5x10^{-5}$ sec^{-1} (excluding non-linear data points beyond 11 hours). Furthermore, initial rate analysis of anthracene formation over approximately the first 30% of the reaction indicates **9a** forms anthracene at $3.2x10^{-9}$ M sec^{-1}, while **9b** proceeds at $9.4x10^{-10}$ M sec^{-1}. While the formation of anthracene tracks moderately well with consumption of **9a**, anthracene formation appears delayed relative to consumption of **9b** (Figure 3.10). In the case of **9b**, this seems to suggest the initial formation of a paramagnetic intermediate that still possesses the oxidizing capacity to convert 9,10-DHA to anthracene. Furthermore, the formation of anthracene from **9a** clearly shows two-step behavior, with the first half of anthracene forming much faster than the second half. This is consistent with the rate of substrate oxidation slowing upon stepwise reduction of **9a**, whose reactivity is proposed in Scheme 3.5. This two-step behavior is not indicated by monitoring anthracene formation from **9b**. Yields of anthracene for **9a** and **9b** were both ≥ 80 %.

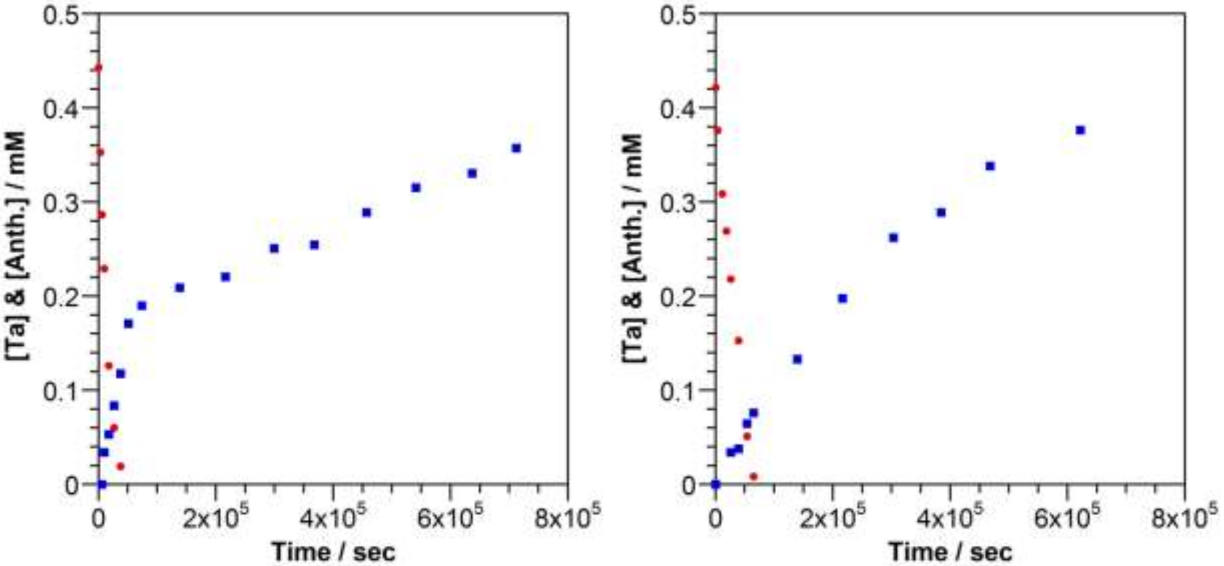

Figure 3.10. Left. Time profile for the reaction of **9a** with 9,10-dihydroanthracene at 70 °C. Consumption of **9a** (red dots) and formation of anthracene (blue squares) plotted against time. **Right.** Time profile for the reaction of **9b** with 9,10-dihydroanthracene. Consumption of **9b** (red dots) and formation of anthracene (blue squares) plotted against time.

Scheme 3.5. Reactivity of **9a** and **9b** with trimethylphosphine and 9,10-DHA.

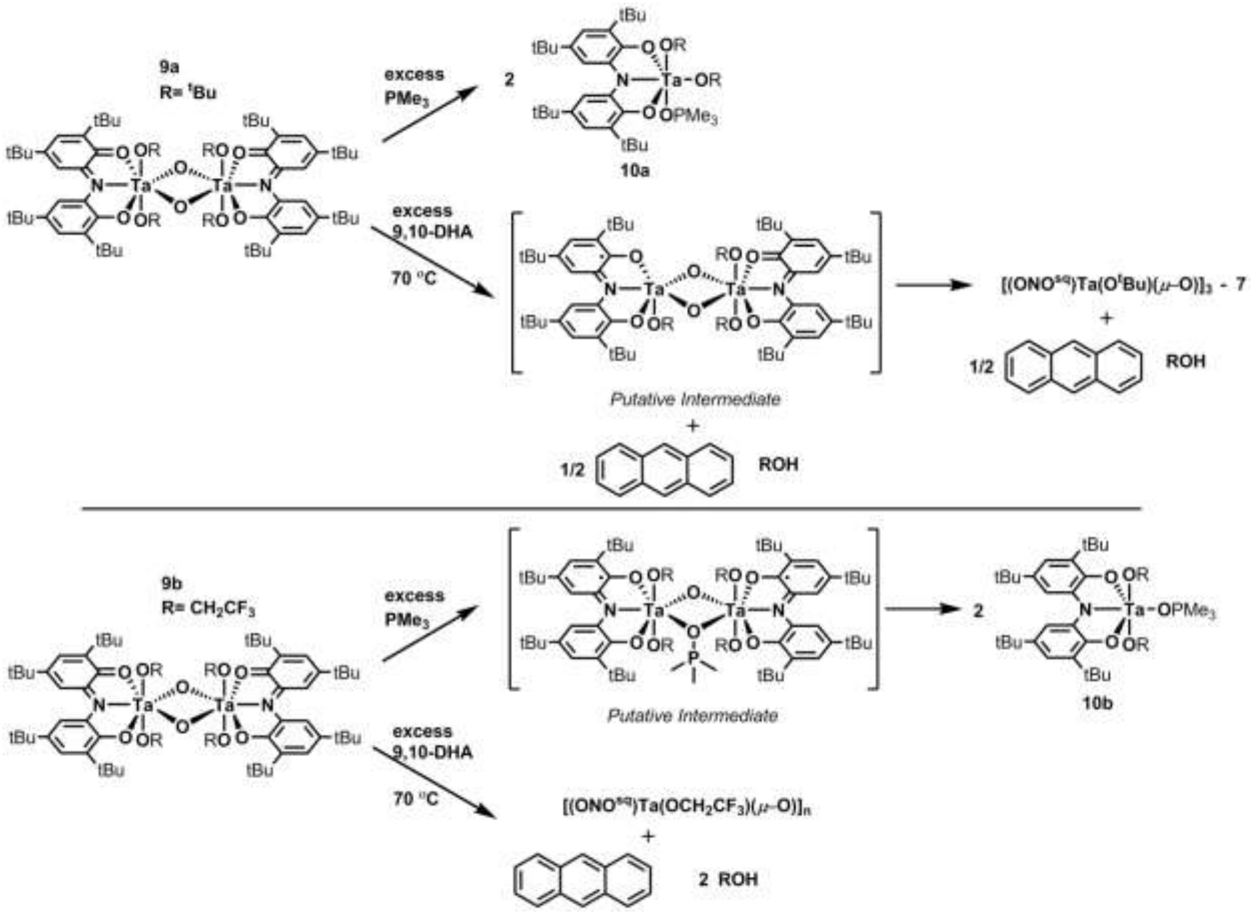

Complexes **9a** and **9b** also demonstrate mild oxygen-atom transfer ability. When treated with excess (10 equivalents) trimethylphosphine (PMe_3) in benzene and heated overnight at 70 °C, **9a** and **9b** each produce a new diamagnetic product. In both products a new doublet was observed by ^{1}H-NMR spectroscopy at *ca.* 0.5 ppm which integrated to 9H, consistent with the presence of a PMe_3 fragment, with the doublet arising through coupling with the S = 1/2 phosphorus nucleus. A single resonance was also observed by ^{31}P-NMR spectroscopy for the reaction product from both **9a** and **9b**. The product from complex **9a** exhibits two ^{1}H-NMR resonances for the $^{-}O^{t}Bu$ ligands, each appearing as a broadened singlet integrating to 9H. The reaction product from complex **9b** had a single CH_2 quartet integrating to 4H and a single ^{19}F-NMR resonance. These observations are consistent with oxygen-atom transfer to PMe_3, confirmed through the reaction of **4a** and **4b** with stoichiometric trimethylphosphine oxide ($O{=}PMe_3$) to form the corresponding adducts ($(ONO^{cat})Ta(O^tBu)_2(O{=}PMe_3)$) (**10a**) and $(ONO^{cat})Ta(OCH_2CF_3)_2(O{=}PMe_3)$ (**10b**). NMR spectroscopy confirmed that the independently prepared complexes **10a** and **10b** are identical to those obtained by the reaction of **9a** and **9b** with PMe_3.

Kinetic analysis of the oxidation of PMe_3 by **9a** and **9b** was performed under pseudo-first order conditions in C_6D_6 in sealed J. Young tubes at room temperature. Compared to the results of 9,10-DHA oxidation, divergent results were obtained for PMe_3 oxidation; **9b** consumption occurs orders of magnitude faster than **9a**. Under these pseudo-first order conditions, consumption of **9b** occurs with a rate constant of $k_{\text{obs}} = 3.3\text{x}10^{-3}\ \text{sec}^{-1}$, while **9a** lags at $k_{\text{obs}} = 2.8\text{x}10^{-6}\ \text{sec}^{-1}$. This reaction proceeds in two distinct steps for **9b**, with starting material consumption and formation of a paramagnetic $(ONO^{sq})^{2-}$ containing intermediate occurring orders of magnitude faster than formation of **10b**. The presence of an $(ONO^{sq})^{2-}$ ligand in this intermediate is evidenced through UV-vis spectroscopy (Figure 3.12). However, consumption of **9a** and formation of **10a** occur nearly concomitantly (Figure 3.11) and do not exhibit the same obvious two-step process observed with **9b**. Notably, formation of **10b** occurs only slightly faster than formation of **10a**; over the course of the formation of the first 0.1 mM of **10**, the initial rate of formation is $9.9\text{x}10^{-10}\ \text{M sec}^{-1}$ for **10a** and $3.3\text{x}10^{-9}\ \text{M sec}^{-1}$ for **10b**. Yields of both **10a** and **10b** under these reaction conditions are *ca* 58%, with unidentified side products comprising the remainder of the material.

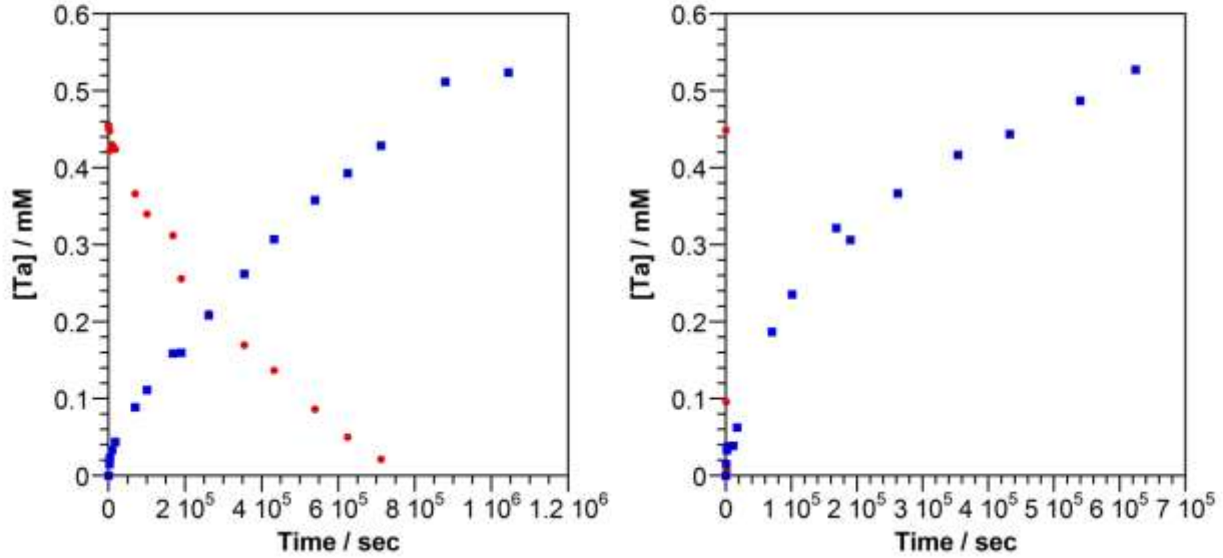

Figure 3.11. Left. Time profile for the reaction of **9a** with trimethylphosphine. Consumption of **9a** (red dots) and formation of **10a** (blue squares) plotted against time. **Right.** Time profile for the reaction of **9b** with trimethlyphophine. Consumption of **9b** (red dots) and formation of **10b** (blue squares) plotted against time.

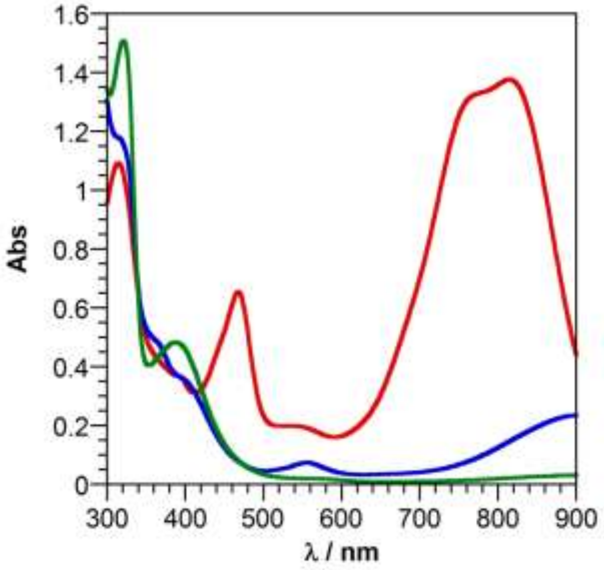

Figure 3.12. UV-vis spectra of **9b** (red), the ONO^{sq} intermediate (blue) observed upon reaction with trimethylphosphine, and the final reaction product **10b** (green).

The yields indicate significant side reactions are occurring in the reaction of **9a** and **9b** with PMe$_3$. In the case of **9a**, this could be linked to rapid deleterious side reactions upon reduction of **9a** with the first equivalent of PMe$_3$, consistent with the clear link between **9a** consumption and **10a** formation. This situation is less defined in the case of **9b**, which undergoes an immediate and rapid reduction to an unknown intermediate. If this step is linked to formation of O=PMe_3 (as suggested in Scheme 3.4) then the observation of **10b**, whose formation occurs much slower than consumption of **9a**, occurs only after another low-yielding reaction step.

Summary and Conclusions

Through disparate synthetic pathways, tantalum-oxo complexes of the ONO ligand have been prepared in all three ligand oxidation states. Notable are the bridging oxo species $[(ONO^q)Ta(OR)_2(\mu\text{-}O)]_2$ which show significant differences in their electrochemical redox potentials, an outcome consistent with the results described in Chapter 2. These results support the assertion that ancillary ligand effects can be extended to more complicated and differentially functionalized complexes and still exert a powerful influence over redox properties of the redox-active ligand. In complexes **9a** and **9b**, C–H activation of 9,10-DHA was demonstrated at elevated temperatures. Oxygen-atom transfer reactivity was also demonstrated by **9a** and **9b**, which both underwent formal transfer of the tantalum-oxo to trimethylphosphine. Kinetic analysis revealed unexpected contrasting results. While **9a** performed C–H activation at a faster rate than **9b**, **9b** proved more kinetically competent than **9a** at affecting oxygen-atom transfer to trimethylphosphine. These results indicate that altering the redox properties of substituted complexes of the formula $[(ONO^q)Ta(OR)_2(\mu\text{-}O)]_2$ through alkoxide variation will not broadly improve or diminish reactivity, but reactivity differences will be dependent on the specific reaction (C–H activation vs oxygen-atom transfer). Such differences could be rooted in pKa effects upon alkoxide variation.

Experimental

General Considerations. Manipulations were performed using standard Schlenk line techniques or in a N_2 filled glovebox. Diethyl ether, pentane, benzene, toluene, and tetrahydrofuran were sparged with argon and then dried and deoxygenated by passage through activated alumina and

Q5 columns, respectively. C_6D_6 and THF-*d^8* were dried over NaK/benzophenone, vacuum transferred, then stored over molecular sieves and sodium, respectively. Silver trifluoromethanesulfonate (AgOTF) was dried under high vacuum prior to use. $(ONO^{cat})TaCl_2 \cdot Et_2O$ (**1**) and $(ONO^{cat})Ta(O^tBu)_2$ (**4a**) were synthesized according to published procedures.[14,15] KOH was purified using the method described for the purification of NaOH.[38] Iodosobenzene (PhIO) was prepared according to published procedures and dried under high vacuum.[39] Technical grade diphenylhydrazine was recrystallized from concentrated pentane solutions prior to use. The reagents LiO^tBu and $LiOCH_2CF_3$ were prepared by treating pentane solutions of the corresponding alcohol with nBuLi. Ultra-high purity oxygen was dried through a column of drierite during use.

Physical Methods. All ^{1}H-NMR, ^{19}F-NMR, and ^{31}P-NMR spectra were recorded on a Bruker DRX 400 MHz spectrometer. ^{1}H-NMR spectra were referenced to tetramethylsilane using the proteo impurity of C_6D_6 (7.16 ppm). ^{19}F-NMR spectra were referenced to trichloro-fluoromethane using an external trifluoroacetic acid standard ($\delta = -76.55$ ppm). ^{31}P-NMR spectra were referenced using an external phosphoric acid (H_3PO_4) standard ($\delta = 0.00$ ppm). ^{13}C-NMR spectra were recorded on a Bruker 500 MHz spectrometer equipped with a cryoprobe and referenced to tetramethylsilane using the solvent peaks of C_6D_6 (128.06 ppm) or THF-*d^8* (67.21, 25.31 ppm). Solution UV-vis-NIR spectra were recorded in 1-cm path-length cuvettes on a Shimadzu UV-1700 spectrophotometer. Extinction coefficients were determined from Beer-Lambert Law plots. IR spectra were obtained under a nitrogen atmosphere in a glovebox using a Thermo Scientific Nicolet iS5 with an iD5 ATR attachment. EPR spectra were collected on a Bruker EMX X-band spectrometer equipped with an ER041XG microwave bridge. Elemental analyses were collected on a Perkin-Elmer 2400 Series II CHNS/O analyzer.

Electrochemical Methods. Electrochemical measurements were recorded with a Gamry G300 potentiostat using a standard three-electrode configuration including a 3.0 mm glassy carbon working electrode, a platinum wire auxiliary electrode, and a silver wire pseudo-reference electrode. All measurements were made on solutions that contained 1 mM analyte and 0.1 M NBu_4PF_6 in CH_2Cl_2 at an ambient temperature of *ca*. 21 °C in a glovebox under a N_2 atmosphere. Potentials are referenced to $Cp_2Fe^{+/0}$ using an internal standard of ferrocene.

Crystallographic Methods. X-ray diffraction data were collected on single crystals mounted on a glass fiber using a Bruker SMART APEX II diffractometer. Measurements were carried out using Mo Kα (λ = 0.71073 Å) radiation, wavelength selected with a single-crystal graphite monochromator. A full sphere of data was collected for each crystal structure. The APEX[40] program package was used to determine the unit cell parameters and for data collection. The raw frame data was processed using SAINT[41] and SADABS[42] to yield the reflection data files. Subsequent calculations were carried out using the SHELXTL[43] program. The structures were solved by direct methods and refined on F^2 by full matrix least-squares techniques. The analytical scattering factors[44] for neutral atoms were used throughout the analysis. Hydrogen atoms were included using a riding model. ORTEP diagrams were generated using ORTEP-3 for Windows.

Table 3.4. Data collection and refinement parameters for **4**, **7**, **8**, **9a**, and **9b**.

	4b	**7**	**8**	**9a**	**9b**
Empirical Formula (g/mol)	$C_{64}H_{88}F_{12}N_2O_8Ta_2{\bullet}3(C_7H_8)$	$C_{96}H_{147}N_3O_{12}Ta_3$	$C_{96}H_{144}N_3O_{12}Ta_3$	$C_{72}H_{116}N_2O_{10}Ta_2$	$C_{64}H_{88}F_{12}N_2O_{10}Ta_2{\bullet}½(C_6H_6){\bullet}½(C_7H_8)$
Formula Weight	1879.66	2078.01	2074.99	1531.56	1805.50
Crystal System	Monoclinic	Trigonal	Trigonal	Monoclinic	Monoclinic
Space Group	*C*2/*c*	$R\bar{3}$	*R*3	*C*2/*c*	*C*2/*c*
a (Å)	35.837(2)	22.7060(13)	22.1958(9)	15.332(2)	25.5162(19)
b (Å)	10.1645(7)	22.7060(13)	22.1958(9)	25.393(4)	18.0868(14)
c (Å)	25.3742(17)	37.892(2)	40.0402(16)	21.142(4)	18.7858(14)
α (°)	90	90	90.00	90	90
β (°)	112.5130(7)	90	90.00	111.2547(16)	114.8860(10)
γ (°)	90	120	120.00	90	90
Volume ($Å^3$)	8538.5(10)	16918(2)	17083.2(12)	7671(2)	7864.7(10)
Z	4	6	6	4	4
F(000)	3816	6354	6336	3152	3648
Rflns. collected	47027	66973	68143	41054	43612
Ind. rflns. (R_{int})	9401 (0.0246)	8622 (0.0437)	9374 (0.0222)	7854 (0.0497)	8660 (0.0249)
GOF	1.060	1.036	1.093	1.070	1.059
R1 [I > 2σ(I)][a]	0.0323	0.0261	0.0251	0.0344	0.0240
wR2 (all data)[a]	0.0896	0.0682	0.0672	0.0763	0.0656

[a] $R1 = \Sigma||F_o|-|F_c|| / \Sigma|F_o|$; $wR2 = [\Sigma[w(F_o^2-F_c^2)^2] / \Sigma[w(F_o^2)^2]\ ]^{1/2}$; $GOF= S = [\Sigma[w(F_o^2-F_c^2)^2] / (n-p)]^{1/2}$

$[(ONO^{cat})Ta(OCH_2CF_3)_2]_2$ (4b). $(ONO^{cat})TaCl_2{\cdot}Et_2O$ (0.636 g, 0.850 mmol) was dissolved in 60 mL of Et_2O in a round-bottom flask. In a vial, $LiOCH_2CF_3$ (0.180 g, 1.70 mmol) was dissolved in 15 mL of Et_2O. Both solutions were chilled in a cold well, then the solution of $LiOCH_2CF_3$ was added to the solution of $(ONO^{cat})TaCl_2{\cdot}Et_2O$. After 3.5 hours the solution was filtered through celite and dried under vacuum. The resulting solid was slurried in 3 mL of pentane and chilled at −35 °C overnight. The solids were then separated and dried under vacuum to yield the product as a light orange solid (0.595 g, 87 %). ^{1}H-NMR (400 MHz, C_6D_6) δ/ppm: 7.81 (d, *J*=2 Hz, 4H, aryl-H), 7.15 (d, *J*=2 Hz, 4H, aryl-H), 5.04 (q, *J*=8 Hz, 4H, CH_2), 4.16 (q, *J*=8 Hz, 4H, CH_2), 1.57 (s, 36H, ^{t}Bu), 1.41 (s, 36H, ^{t}Bu). ^{19}F{^{1}H}-NMR (376 MHz, C_6D_6) δ/ppm: −75.67, −78.01. ^{13}C {^{1}H}-NMR (125 MHz, C_6D_6) δ/ppm: 157.0, 146.2, 143.5, 135.7, 119.3, 111.9, 35.4, 35.2, 32.3, 30.6. Anal. Calcd. for $C_{32}H_{44}F_6NO_4Ta$: C, 47.95; H, 5.53; N, 1.75. Found: C, 47.50; H, 5.60; N, 1.60. UV-vis-NIR (toluene) λ_{max}/nm (ε/M^{-1} cm^{-1}): 400 (4910). IR ῡ/cm^{-1}: 2958, 2902, 2870, 1419, 1282, 1164, 1117, 1033, 963, 840, 700, 652.

[(ONO^{cat})Ta(O^{t}Bu)(μ-O)]$_n^-$ nK$^+$ (5). (ONO^{cat})Ta(O^{t}Bu)$_2$ (0.409 g, 0.545 mmol) was dissolved in 15 mL of THF and added to a vial of solid KOH (0.030 g, 0.535 mmol). After stirring overnight, the reaction was dried under vacuum. The resulting solid was dissolved in toluene, filtered through celite, and dried. The yellow solid was then slurried in *ca.* 2 mL of pentane and chilled at −35 °C overnight. The resulting solids were isolated and dried under vacuum to yield the product as a yellow solid (0.317 g, 80 %). ^{1}H-NMR (400 MHz, C_6D_6) δ/ppm: 7.80 (s, 2H, aryl-H), 6.97 (s, 2H, aryl-H), 1.70 (s, 18H, ^{t}Bu), 1.53 (s, 18H, ^{t}Bu), 0.96 (s, 9H, O^{t}Bu). ^{13}C {^{1}H}-NMR (125 MHz, C_6D_6) δ/ppm: 156.8, 145.6, 141.3, 134.0, 112.7, 109.4, 77.1, 35.4, 35.3, 33.3, 32.8, 31.0. Anal. Calcd. for $C_{32}H_{49}KNO_4Ta$: C, 52.52; H, 6.75; N, 1.91. Found: C, 52.22; H, 6.77; N, 1.84.

[(ONO^{cat})Ta(O^{t}Bu)(μ-O)]$_n^-$ n[K(18-crown-6)]$^+$ (6). To a cold solution of [(ONO^{cat})Ta(O^{t}Bu)(μ-O)]$_n^-$ nK$^+$ (0.050 g, 0.069 mmol) in 7 mL of Et_2O was added a solution of 18-crown-6 (0.018 g, 0.068 mmol) in 4 mL of Et_2O. After stirring overnight the solution was filtered away from a yellow precipitate, which was further extracted with 2 mL of Et_2O. Removal of the solvent yielded the product as a pale yellow solid (0.049 g, 72 %). ^{1}H-NMR (400 MHz, C_6D_6) δ/ppm: 7.77 (s, 2H, aryl-H), 6.99 (s, 2H, aryl-H), 3.02 (s, 24H, -O(CH_2)$_2$O-), 1.84 (s, 18H, ^{t}Bu), 1.57 (s, 18H, ^{t}Bu), 1.42 (s, 9H, O^{t}Bu). Anal. Calcd. for $C_{44}H_{73}KNO_{10}Ta$: C, 53.05; H, 7.39; N, 1.41. Found: C, 52.96; H, 7.46; N, 1.49.

[(ONO^{sq})Ta(O^{t}Bu)(μ-O)]$_3$ (7). [(ONO^{cat})Ta(O^{t}Bu)(μ-O)]$_n^-$ nK$^+$ (0.052 g, 0.071 mmol) and AgOTf (0.018 g, 0.070 mmol) were combined in 10 mL of Et_2O. After stirring overnight, the reaction was dried and then extracted with pentane. The pentane solution was filtered and subsequent removal of the solvent yielded the product as a purple solid (0.047 g, 94 %). UV-vis-NIR (toluene) λ_{max}/nm (ε/M^{-1} cm^{-1}): 558 (4330), 930 (13900). Anal. Calcd. for $C_{96}H_{147}N_3O_{12}Ta_3$: C, 55.49; H, 7.13; N, 2.02. Found: C, 55.49; H, 7.31; N, 2.06. IR $\bar{\upsilon}$/cm^{-1}: 2956, 2905, 2868, 1468, 1413, 1360, 1309, 1237, 1172, 1047, 848, 813, 778, 619.

[(ONO^{cat})Ta(THF)(μ-O)]$_3$ (8). (ONO)TaMeCl·Et_2O (0.230 g, 0.316 mmol) and KOH (0.018 g, 0.320 mmol) were combined in 18 mL of THF and stirred for 3 days. The reaction was dried, extracted with pentane, and filtered. Removal of solvent yielded the product as an orange/red solid (0.206 g, 94%). ^{1}H-NMR (400 MHz, C_6D_6) δ/ppm: 7.62 (s, 2H, aryl-H), 6.96 (s, 2H, aryl-H), 3.81 (br, 4H, THF), 1.73 (s, 18H, ^{t}Bu), 1.40 (s, 18H, ^{t}Bu), 0.76 (br, 4H, THF). ^{13}C {^{1}H}-NMR (125 MHz, C_6D_6) δ/ppm: 156.9, 144.5, 143.7, 134.6, 114.7, 109.8, 73.4, 34.9, 34.9, 32.3, 31.4, 24.9. Anal. Calcd. for $C_{96}H_{144}N_3O_{12}Ta_3$: C, 55.57; H, 6.99; N, 2.03. Found: C, 55.66; H, 7.34; N, 2.11.

[(ONO^q)Ta(O^{t}Bu)$_2$(μ-O)]$_2$ (9a). In a glovebox, (ONO^{cat})Ta(O^{t}Bu)$_2$ (0.312 g, 0.416 mmol) was dissolved in 90 mL of pentane in a round bottom flask. A gas addition bulb was attached and the apparatus was moved to a schlenk line and attached to a Drierite filled column. After evacuating and refilling the system with O_2 three times, O_2 was trapped inside the bulb (32.2 mL, 120 mmHg, 0.208 mmol). The reaction mixture was chilled to −78 °C and then exposed to the bulb of O_2. After stirring for 2.5 hours, the maroon colored solution was removed from the cold bath. After another 2.5 hours, the reaction was dried under reduced pressure and returned to a glovebox. The crude product was slurried in pentane and chilled for 2 days at −35 °C. The pentane was removed to yield the product as a dark green solid (0.100 g, 31 %). ^{1}H-NMR (400 MHz, C_6D_6) δ/ppm: 7.50 (s, 4H, aryl-H), 7.47 (s, 4H, aryl-H), 1.79 (s, 36H, ^{t}Bu), 1.38 (s, 36H, ^{t}Bu), 1.18 (s, 36H, O^{t}Bu). ^{13}C {^{1}H}-NMR (125 MHz, THF-d^8) δ/ppm: 183.5, 147.3, 147.0, 143.0, 134.8, 118.1, 78.6, 36.2, 35.9, 32.1, 30.6, 29.9. UV-vis-NIR (toluene) λ_{max}/nm (ε/M^{-1} cm^{-1}): 440 (8310), 760 (22500), 822 (25500). Anal. Calcd. for $C_{72}H_{116}N_2O_{10}Ta_2$: C, 56.46; H, 7.63; N, 1.83. Found: C, 55.97; H, 7.76; N, 1.69. IR $\bar{\upsilon}$/cm^{-1}: 2960, 2906, 2868, 1518, 1348, 1318, 1279, 1261, 1185, 1095, 993, 902, 672.

$[(ONO^q)Ta(OCH_2CF_3)_2(\mu\text{-}O)]_2$ (9b). ***Method A***. In a glovebox, $[(ONO^{cat})Ta(OCH_2CF_3)_2]_2$ (0.151 g, 0.094 mmol) was dissolved in 30 mL of a 2:1 solution of benzene/pentane in a round bottom flask. A gas addition bulb was attached and the apparatus was moved to a schlenk line and attached to a Drierite filled column. After evacuating and refilling the system with O_2 three times, O_2 was trapped inside the bulb (9.6 mL, 180 mmHg, 0.093 mmol). The reaction mixture was chilled in an ice bath and then exposed to the bulb of O_2. The ice was allowed to melt over the course of the reaction, and after stirring for 4.5 hours the dark green reaction was dried under reduced pressure and returned to a glovebox. The crude product was slurried in pentane and chilled overnight at −35 °C. The pentane was removed to yield the product as a dark green solid (0.060 g, 39 %). ^{1}H-NMR (400 MHz, C_6D_6) δ/ppm: 7.49 (d, J=2 Hz, 4H, aryl-H), 7.37 (d, J=2 Hz, 4H, aryl-H), 4.78 (q, J=9 Hz, 8H, CH_2), 1.70 (s, 36H, ^{t}Bu), 1.10 (s, 36H, ^{t}Bu). ^{19}F {^{1}H}-NMR (376 MHz, C_6D_6) δ/ppm: −77.80. ^{13}C {^{1}H}-NMR (125 MHz, C_6D_6) δ/ppm: 184.2, 149.6, 146.5, 143.1, 137.0, 118.0, 70.1 (q, J=35 Hz), 36.1, 35.6, 30.2, 29.7. UV-vis-NIR (toluene) λ_{max}/nm (ε/M^{-1} cm^{-1}): 316 (21000), 468 (14300), 770 (27500), 810 (27900). Anal. Calcd. for $C_{64}H_{88}F_{12}N_2O_{10}Ta_2$: C, 47.01; H, 5.42; N, 1.71. Found: C, 46.78; H, 5.38; N, 1.55. IR $\bar{\upsilon}$/cm^{-1}: 2964, 2908, 2870, 1510, 1281, 1257, 1200, 1147, 1092, 1000, 902, 666.

Method B. $[(ONO^{cat})Ta(OCH_2CF_3)_2]_2$ (0.258 g, 0.161 mmol) and PhIO (0.071 g, 0.321 mmol) were combined in 12 mL of benzene and stirred for 13 hours. The dark green solution was dried, extracted with Et_2O, filtered through celite, and then dried under vacuum. The crude product was slurried in 2 mL of pentane and chilled overnight at −35 °C. The solid was separated from the pentane and dried under vacuum to yield the product as a dark green solid (0.112 g., 43 %). The NMR spectra matched that of Method A.

General Procedure for the Reactivity of 9a and 9b with Diphenylhydrazine

9a (3.8 mg, 2.5 µmol) was combined with diphenylhydrazine (30 µL of 0.079 M stock solution in C_6D_6, 1 equiv.) in C_6D_6 in a J. Young style NMR tube. The mixture was sonicated for an hour and allowed to sit at room temperature for two days, yielding a purple solution with no remaining **9a** or diphenylhydrazine, as determined by ^{1}H-NMR. The mixture was then heated to 70 °C and monitored intermittently by ^{1}H-NMR. After a total of 3.5 hours of heating, the mixture was brought into a glovebox and dried under vacuum. The mixture was then redissolved in C_6D_6 and added to a J. Young style NMR tube. The mixture was again heated to 70 °C and monitored intermittently by ^{1}H-NMR over the course of 28 hours, at which point it was brought into a glovebox and dried under vacuum. UV-vis-NIR (toluene) λ_{max}/nm: 402, 556, 894. IR $\bar{\upsilon}$/cm^{-1}: 3649, 2959, 2906, 2868, 1537, 1468, 1414, 1360, 1309, 1237, 1173, 1047, 1011, 850, 812, 776.

9b (4 mg, 2.4 µmol) was combined with diphenylhydrazine (30 µL of 0.079 M stock solution in C_6D_6, 1 equiv.) in C_6D_6 in a J. Young style NMR tube and quickly shaken to afford mixing, yielding a purple solution with no remaining **9b** or diphenylhydrazine, as determined by ^{1}H-NMR. The mixture was then heated to 70 °C and monitored intermittently by ^{1}H-NMR. After a total of 7.5 hours of heating, the mixture was brought into a glovebox and dried under vacuum. The mixture was then redissolved in C_6D_6 and added to a J. Young style NMR tube. The mixture was again heated to 70 °C and monitored intermittently by ^{1}H-NMR over the course of 28 hours, at which point it was brought into a glovebox and dried under vacuum. UV-vis-NIR (toluene) λ_{max}/nm: 576, 946. IR $\bar{\upsilon}$/cm^{-1}: 3653, 2955, 2907, 2869, 1539, 1469, 1413, 1361, 1284, 1236, 1150, 1106, 1049, 850, 686.

General Procedure for the Reactivity of 9a and 9b with 9,10-DHA

9a (2 mg, 1.3 µmol) was combined with 9,10-DHA (3 mg, 17 µmol) and an internal standard of mesitylene (10 µL of a 10% by volume solution in C_6D_6) in C_6D_6 in a J. Young style NMR tube. The mixture was heated to 70 °C and monitored intermittently by ^{1}H-NMR. After a total of 85 hours of heat, *ca*. 0.78 equivalents of anthracene were produced. UV-vis-NIR (toluene) λ_{max}/nm: 398, 552, 926.

9b (2 mg, 1.2 µmol) was combined with 9,10-DHA (3 mg, 17 µmol) and an internal standard of mesitylene (10 µL of a 10% by volume solution in C_6D_6) in C_6D_6 in a J. Young style NMR tube. The mixture was heated to 70 °C and monitored intermittently by ^{1}H-NMR. After a total of 61 hours of heat, *ca*. 0.95 equivalents of anthracene were produced. UV-vis-NIR (toluene) λ_{max}/nm: 574, 946.

Kinetic Analysis of 9a and 9b with 9,10-DHA

A saturated solution of **9a** in C_6D_6 was formed by stirring **9a** in *ca*. 2 mL of C_6D_6 for at least 15 minutes. This solution was then filtered and 0.6-0.8 mL was added to a J. Young tube. An internal standard of bromomesitylene (10 μL, 6.5 mM in C_6D_6, $6.5\text{x}10^{-7}$ mol) was then added. After determining the concentration of **9a** by ^{1}H-NMR, the reaction volume was brought to 0.810 mL, and then an equal molar amount of a stock solution of **9b** was added to another J. Young tube and the volume brought to 0.8 mL. An internal standard of bromomesitylene (10 μL, 6.5 mM in C_6D_6, $6.5\text{x}10^{-7}$ mol) was then added. After confirming the concentration of **9b** by ^{1}H-

NMR, 9,10-DHA (45 μL, 0.166 M, 20 equiv.) was added to each reaction. The reactions were then heated at 70 °C and monitored intermittently by ^{1}H-NMR until completion.

General Procedure for the Reactivity of 9a and 9b with PMe_3. 9a (0.015 g, 0.010 mmol) was added to a Strauss tube with benzene. PMe_3 was then added (133 µL, 0.735 M in toluene, 0.098 mmol). The strauss tube was sealed, removed from the glovebox and heated outside in an oil bath at 70 °C overnight. The reaction was dried under vacuum and returned to a glovebox. The product was removed with pentane and dried under vacuum. Analysis by NMR showed the major diamagnetic species was a spectroscopic match to **10a** described herein. Application of these reaction conditions to **9b** showed the major diamagnetic species was a spectroscopic match to **10b**.

Kinetic Analysis of 9a and 9b with PMe_3

A saturated solution of **9a** in C_6D_6 was formed by stirring in *ca*. 2 mL of C_6D_6 for at least 15 minutes. This solution was then filtered and 0.6-0.8 mL was added to a J. Young tube. An internal standard of bromomesitylene (10 μL, 6.5 mM in C_6D_6, 6.5×10^{-7} mol) was then added. After determining the concentration of **9a** by ^{1}H-NMR, the reaction volume was brought to 0.810 mL, and then an equal molar amount of a stock solution of **9b** was added to another J. Young tube and the volume brought to 0.8 mL. An internal standard of bromomesitylene (10 μL, 6.5 mM in C_6D_6, 6.5×10^{-7} mol) was then added. After confirming the concentration of **9b** by ^{1}H-NMR, PMe_3 (10 μL, 0.735 M in toluene, 20 equiv.) was added to each reaction. The reactions proceeded at room temperature and were monitored intermittently by ^{1}H-NMR.

(ONO^{cat})Ta(OtBu)2(O=PMe3) (10a). A J. Young tube was charged with trimethylphosphine oxide (3.1 mg, 34 µmol). A C_6D_6 solution of (ONO^{cat})Ta(O^tBu)$_2$ (25 mg, 33 µmol) was added, the tube sealed, and the reaction shaken to afford mixing. The yellow reaction mixture lightened and NMR spectroscopy confirmed the formation of the desired product **10a**. ^{1}H-NMR (400 MHz, C_6D_6) δ/ppm: 7.58 (s, 2H, aryl-H), 6.94 (s, 2H, aryl-H), 1.68 (s, 18H, ^{t}Bu), 1.51 (s, 18H, ^{t}Bu), 1.48 (s, 9H, O^{t}Bu), 1.34 (s, 9H, O^{t}Bu), 0.54 (d, *J*=13 Hz, 9H, $OPMe_3$). ^{31}P {^{1}H}-NMR (162 MHz, C_6D_6) δ/ppm: 54.49. UV-vis-NIR (toluene) λ_{max}/nm (ε/M^{-1} cm^{-1}): 326 (14500), 372 sh (3340). IR ῡ/cm^{-1}: 2953, 2910, 2863, 1559, 1442, 1358, 1279, 1197, 1144, 1047, 1009, 942, 868, 839, 747, 637.

(ONO^{cat})Ta(OCH2CF3)2(O=PMe3) (10b). A J. Young tube was charged with trimethylphosphine oxide (2.5 mg, 27 µmol). A C_6D_6 solution of [(ONO^{cat})Ta(OCH_2CF_3)$_2$]$_2$ (22 mg, 14 µmol) was added, the tube sealed, and the reaction shaken to afford mixing. The reaction mixture turned yellow and NMR spectroscopy confirmed the formation of the desired product. ^{1}H-NMR (400 MHz, C_6D_6) δ/ppm: 7.60 (s, 2H, aryl-H), 6.97 (s, 2H, aryl-H), 4.60 (q, *J*=9 Hz, 4H, CH_2CF_3), 1.59 (s, 18H, ^{t}Bu), 1.46 (s, 18H, ^{t}Bu), 0.55 (d, *J*=13 Hz, 9H, $OPMe_3$). ^{19}F {^{1}H}-NMR (376 MHz, C_6D_6) δ/ppm: −74.95. ^{31}P {^{1}H}-NMR (162 MHz, C_6D_6) δ/ppm: 63.33. ^{13}C {^{1}H}-NMR (125 MHz, C_6D_6) δ/ppm: 156.4, 144.9, 144.1, 134.4, 115.2, 110.3, 35.3, 35.1, 32.5, 30.3, 15.2 (d, *J*=70 Hz). UV-vis-NIR (toluene) λ_{max}/nm (ε/M^{-1} cm^{-1}): 322 (13700), 386 (3290). IR ῡ/cm^{-1}: 2953, 2913, 2870, 1562, 1435, 1279, 1159, 1138, 1093, 1048, 948, 870, 832, 750, 643.

References

(1) Duncan, A.; Bergman, R. *Chem. Rec.* **2002**, *2*, 431.
(2) Hazari, N.; Mountford, P. *Acc. Chem. Res.* **2005**, *38*, 839.
(3) Walsh, P.; Hollander, F.; Bergman, R. *Organometallics* **1993**, *12*, 3705.
(4) Cummins, C.; Baxter, S.; Wolczanski, P. *J. Am. Chem. Soc.* **1988**, *110*, 8731.
(5) Schaller, C.; Cummins, C.; Wolczanski, P. *J. Am. Chem. Soc.* **1996**, *118*, 591.
(6) Bennett, J.; Wolczanski, P. *J. Am. Chem. Soc.* **1997**, *119*, 10696.
(7) Schaller, C. P.; Wolczanski, P. T. *Inorg. Chem.* **1993**, *32*, 131.
(8) Carney, M.; Walsh, P.; Hollander, F.; Bergman, R. *Organometallics* **1992**, *11*, 761.
(9) Howard, W.; Waters, M.; Parkin, G. *J. Am. Chem. Soc.* **1993**, *115*, 4917.
(10) Polse, J.; Andersen, R.; Bergman, R. *J. Am. Chem. Soc.* **1995**, *117*, 5393.
(11) Munhá, R. F.; Zarkesh, R. A.; Heyduk, A. F. *Dalton Trans.* **2013**, *42*, 3751.

(12) Haneline, M. R.; Heyduk, A. F. *J. Am. Chem. Soc.* **2006**, *128*, 8410.

(13) Nguyen, A. I.; Zarkesh, R. A.; Lacy, D. C.; Thorson, M. K.; Heyduk, A. F. *Chem. Sci.* **2011**, *2*, 166.

(14) Zarkesh, R.; Ziller, J. W.; Heyduk, A. F. *Angew. Chem. Int. Ed. Engl.* **2008**, *47*, 4715.

(15) Heyduk, A.; Zarkesh, R.; Nguyen, A. *Inorg. Chem.* **2011**, *50*, 9849.

(16) Blackmore, K. J.; Ziller, J. W.; Heyduk, A. F. *Inorg. Chem.* **2005**, *44*, 5559.

(17) Blackmore, K. J.; Lal, N.; Ziller, J. W.; Heyduk, A. F. *J. Am. Chem. Soc.* **2008**, *130*, 2728.

(18) Ketterer, N. A.; Fan, H.; Blackmore, K. J.; Yang, X.; Ziller, J. W.; Baik, M. H.; Heyduk, A. F. *J. Am. Chem. Soc.* **2008**, *130*, 4364.

(19) Blackmore, K. J.; Sly, M. B.; Haneline, M. R.; Ziller, J. W.; Heyduk, A. F. *Inorg. Chem.* **2008**, *47*, 10522.

(20) Lu, F.; Zarkesh, R. A.; Heyduk, A. F. *Eur. J. Inorg. Chem.* **2012**, *2012*, 467.

(21) Stanciu, C.; Jones, M.; Fanwick, P.; Abu-Omar, M. *J. Am. Chem. Soc.* **2007**, *129*, 12400.

(22) Lippert, C. A.; Arnstein, S. A.; Sherrill, C. D.; Soper, J. D. *J. Am. Chem. Soc.* **2010**, *132*, 3879.

(23) Cass, M.; Pierpont, C. *Inorg. Chem.* **1986**, *25*, 122.

(24) Wright, D. D.; Brown, S. N. *Inorg. Chem.* **2013**, *52*, 7831.

(25) Wong, J. L.; Sánchez, R. H.; Logan, J. G.; Zarkesh, R. A.; Ziller, J. W.; Heyduk, A. F. *Chem. Sci.* **2013**, *4*, 1906.

(26) Ranis, L. G.; Werellapatha, K.; Pietrini, N. J.; Bunker, B. A.; Brown, S. N. *Inorg. Chem.* **2014**, *53*, 10203.

(27) Abbenhuis, H.; Feiken, N.; Grove, D.; Jastrzebski, J.; Kooijman, H.; Sluis, P.; Smeets, W.; Spek, A.; van Koten, G. *J. Am. Chem. Soc.* **1992**, *114*, 9773.

(28) Chen, S.-J.; Zhang, X.-H.; Yu, X.; Qiu, H.; Yap, G.; Guzei, I.; Lin, Z.; Wu, Y.-D.; Xue, Z.-L. *J. Am. Chem. Soc.* **2007**, *129*, 14408.

(29) Bruni, S.; Caneschi, A.; Cariati, F.; Delfs, C.; Dei, A.; Gatteschi, D. *J. Am. Chem. Soc.* **1994**, *116*, 1388.

(30) Chaudhuri, P.; Hess, M.; Hildenbrand, K.; Bill, E.; Weyhermüller, T.; Wieghardt, K. *Inorg. Chem.* **1999**, *38*, 2781.

(31) Larsen, S.; Pierpont, C. *J. Am. Chem. Soc.* **1988**, *110*, 1827.

(32) Farnaby, J.; Fang, M.; Ziller, J.; Evans, W. *Inorg. Chem.* **2012**, *51*, 11168.

(33) Simpson, C.; Boone, S.; Pierpont, C. *Inorg. Chem.* **1989**, *28*, 4379.

(34) Szigethy, G.; Heyduk, A. *Dalt. Trans.* **2012**, *41*, 8144.

(35) Caneschi, A.; Cornia, A.; Dei, A. **1998**, *1669*, 3419.

(36) Girgis, A.; Balch, A. *Inorg. Chem.* **1975**, *14*, 2724.

(37) Warren, J. J.; Tronic, T. a; Mayer, J. M. *Chem. Rev.* **2010**, *110*, 6961.

(38) Kelly, J.; Snyder, P. *J. Am. Chem. Soc.* **1951**, *73*, 4114.

(39) Saltzman, H.; Sharefkin, J. *Org. Synth.* **1963**, *43*, 60.

(40) APEX2, Version 2014.11-0, Bruker AXS, Inc.; Madison, WI 2014.

(41) SAINT, Version 8.34a, Bruker AXS, Inc.; Madison, WI 2013.

(42) Sheldrick, G. M. SADABS, Version 2014/5, Bruker AXS Inc.; Madison, WI 2014.

(43) Sheldrick, G. M. SHELXTL, Version 2014/7, Bruker AXS Inc.; Madison, WI 2014.

(44) International Tables for Crystallography 1992, Vol C., Dordrecht: Kluwer Academic Publishers.

Chapter 4

Synthesis and Characterization of Chromium Complexes of the Redox-Active ONO Ligand

Introduction

Research on chromium complexes of redox-active ligands has a rich history, dating almost as far back as the original discovery of ligand non-innocence. In 1964, only two years after the discovery of non-innocent dithiolene ligands, the first reports of chromium dithiolene complexes were published by Holm et al.[1] Subsequent reports detailed a broad family of substituted tris(dithiolene)chromium complexes and their electron transfer series', with the data supporting the presence of Cr(III) metal centers.[2–11]

The stability of these complexes and their rich electrochemical and magnetic properties initiated intense research into the coordination chemistry of chromium with redox-active ligands, resulting in reports of chromium complexes with all major classes of redox-active ligands. These studies have detailed electrochemical, magnetic, structural, and computational data on bipyridine,[12–14] phenanthrene,[12,15–17] α-diimine,[18] catechol,[10,19–22] amidophenol,[23] and o-phenylenediamine[24] complexes of chromium. In all cases of homoleptic CrL_3 complexes, the Cr(III) oxidation state is observed.

Despite the interest in chromium complexes of redox-active ligands, the first row series of homoleptic $M(ONO)_2$ complexes remained void of the chromium complex until 2014, when Brown et al. reported the synthesis and characterization of $Cr(ONO)_2$.[25] As expected, the chromium center was found to adopt the Cr(III) oxidation state in solution (though solid state data were consistent with a Cr(IV) assignment of the metal center). Our own research interests lie in the intersection of characterization and reactivity; whereas coordinatively saturated complexes common to those reported for chromium preclude reactivity, our lab pursues complexes in which a single ONO ligand has been coordinated leaving the remaining coordination sites available for further substitution. To this end, chromium complexes have been prepared and fully characterized with a single ONO ligand coordinated.

Results and Discussion

Synthesis, Characterization, and Reactivity

As reported by Brown, the ONO ligand can be installed onto a chromium metal center utilizing the main group complex Pb(ONO^q)$_2$. While this approach proved successful for the installation of two ligands and formation of the homoleptic complex Cr(ONO)$_2$, the doubly-ligated nature of the ONO source suggested that it may not be non-amenable to the controlled installation of a single ONO ligand. Our approach therefore utilized the ligand source (ONO^q)K, which has proven in our lab to be a mild metalating reagent.[26] The reaction of this salt with the soluble chromium source $CrCl_3(THF)_3$ proved effective at affording the complex (ONO^q)$CrCl_2$(THF) (**11**) (Scheme 4.1).

Scheme 4.1. Synthetic methods for the synthesis of complexes **11**, **12**, **14**, and **15**.

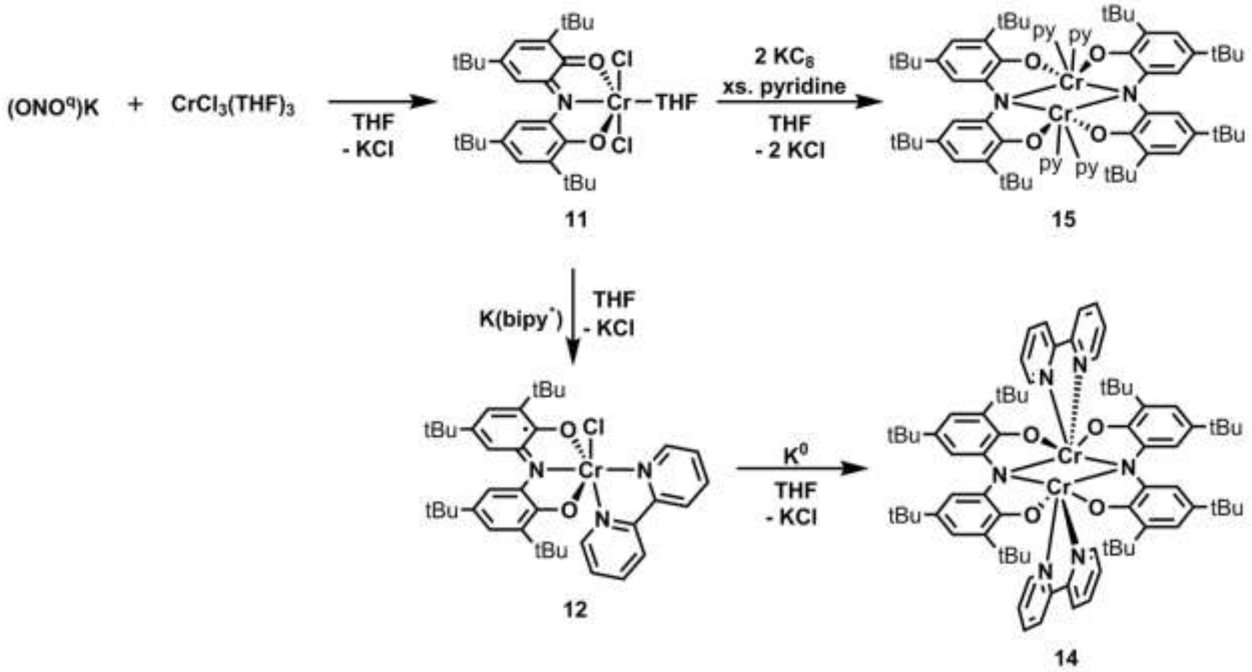

The identity of **11** was confirmed crystallographically (Figure 4.1), revealing a pseudo-octahedral complex with *trans*-coordinated chlorides. Analysis of the intraligand bond lengths revealed contracted C–O bond distances of 1.28 Å (avg.) and highly localized double-bond character within the aryl backbone, indicative of the monoanionic quinonate form of the ligand (Table 4.1).[27–31] Application of Browns MOS calculation yields a value of −1.14, consistent with a monoanionic $(ONO^{q})^{1-}$ ligand. Compared to chromium complexes in the di- and trianionic form of the ONO ligand (Table 4.1), the N(1)–Cr(1) distance of 1.998(3) Å is notably lengthened, and resultingly, the O(1)–Cr(1)–O(2) angle is reduced to 162.63(13)°. This movement of the metal center out of the binding pocket of the ONO ligand upon oxidation from $ONO^{cat} \rightarrow ONO^{sq} \rightarrow ONO^{q}$ is common and a direct reflection of the decreased donor ability of lesser charged forms of the ONO ligand.

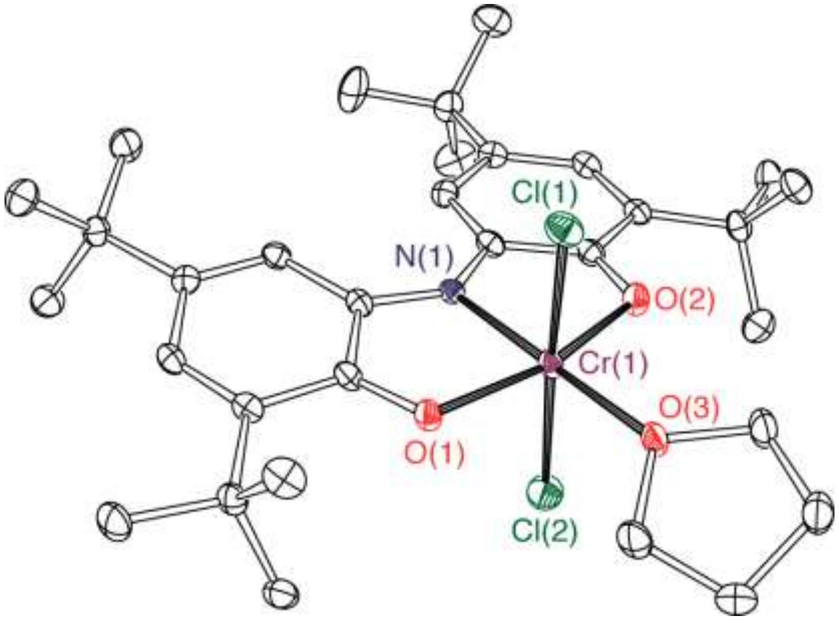

Figure 4.1. ORTEP diagram of $(ONO^{q})CrCl_2(THF)$ (**11**). Thermal ellipsoids are shown at 50% probability. Hydrogen atoms have been omitted for clarity. A cocrystallized molecule of THF has been omitted for clarity.

Table 4.1. Selected bond distances (Å) and angles (°) for **11**, **12**, and **13**.

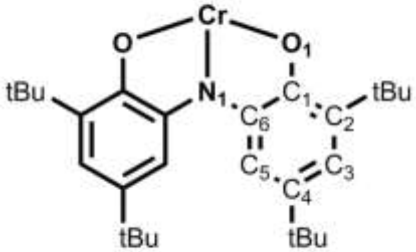

	(ONO^{q})CrCl$_2$(THF) **11**	(ONO^{sq})CrCl(bipy) **12**	(ONO^{cat})Cr(py)$_3$ **13**
		Bond Lengths (Å)	
N(1)–Cr(1)	1.998(3)	1.9263(15)	1.923(2)
O(1)–Cr(1)	1.962(3)	1.9413(14)	1.939(2)
N(1)–C(6)	1.355(5)	1.380(2)	1.389(4)
O(1)–C(1)	1.280(5)	1.314(2)	1.356(3)
C(1)–C(2)	1.449(6)	1.424(3)	1.396(4)
C(2)–C(3)	1.373(6)	1.388(3)	1.411(4)
C(3)–C(4)	1.430(6)	1.417(3)	1.388(4)
C(4)–C(5)	1.378(6)	1.379(3)	1.402(4)
C(5)–C(6)	1.419(6)	1.410(2)	1.385(4)
C(1)–C(6)	1.455(6)	1.430(2)	1.432(4)
Cr(1)–Cl(1)	2.3188(14)	2.3175(6)	-----
Cr(1)–O(3)	2.003(3)	-----	-----
Cr(1)–N(2)	-----	2.1025(16)	2.123(3)
Cr(1)–N(3)	-----	2.0705(18)	2.093(3)
		Bond Angles (°)	
N(1)–Cr(1)–O(1)	81.32(13)	82.27(6)	83.45(9)
N(1)–Cr(1)–Cl(1)	93.07(11)	91.61(5)	-----
N(1)–Cr(1)–N(2)	-----	167.04(7)	92.30(10)
O(1)–Cr(1)–O(2)	162.63(13)	163.56(6)	166.48(9)
N(2)–Cr(1)–N(3)	-----	77.01(7)	87.35(10)

This assertion was further supported by UV-vis-NIR spectroscopy, which revealed near-IR bands at 927 and 827 nm, characteristic of metal complexes containing the monoanionic quinonate form of the ligand.[27,29,32] Electrochemical characterization of **11** revealed multiple redox events (Figure 4.2). A reversible reduction event occurred at −0.49 V, corresponding, nominally, to the reduction of the ONO ligand from the quinonate to the semiquinonate form.

Scanning further negative revealed an additional irreversible reduction event at −1.53 V (E_{pc}) which produced multiple daughter species, likely due to the dissociation of chloride from the doubly reduced, dianionic species. Furthermore, a reversible oxidation event was observed at 0.91 V, though this event has not been identified as being either metal (Cr(III)→ Cr(IV)) or ligand ($ONO^{q} \rightarrow ONO^{\bullet}$) based. The assignment of the complex as containing the $(ONO^{q})^{1-}$ form of the ligand and a high spin Cr(III) center was confirmed by Evans method analysis, providing a μ_{eff} value of 3.55 μB.

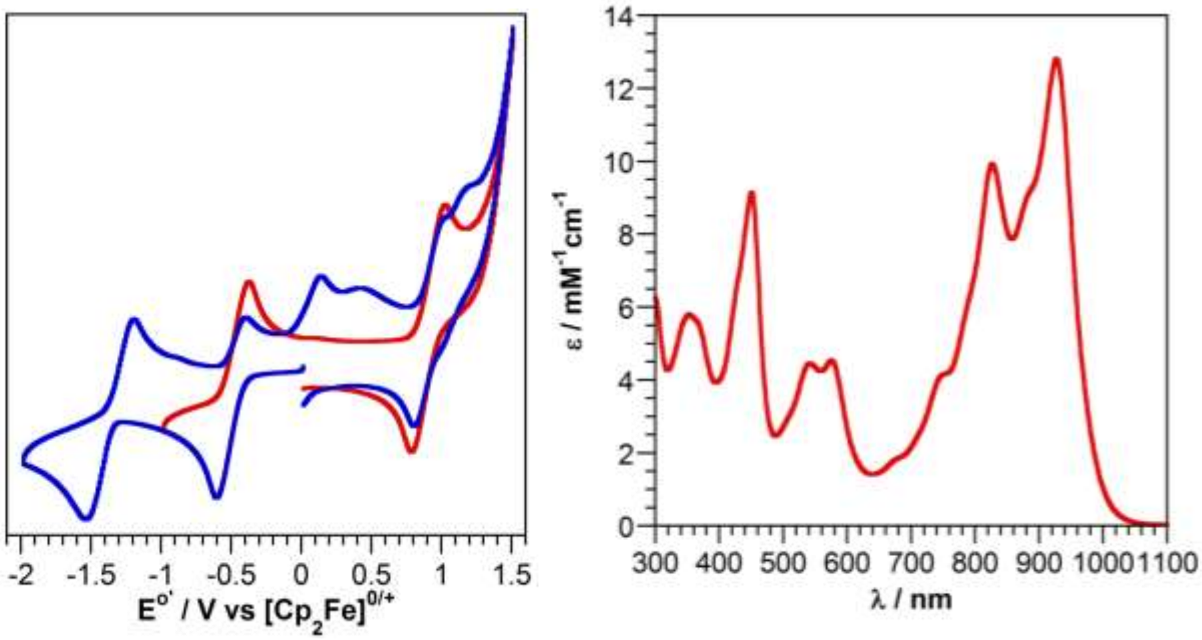

Figure 4.2. Left. Cyclic voltammogram of **11** obtained in THF with 0.1 M $TBAPF_6$ and 1 mM analyte at scan rates of 200 mV/s. **Right.** UV-vis-NIR spectrum of **11** obtained in toluene.

The ligand-based assignment of the reduction event at −0.49 V was tested synthetically by treating **11** with an equivalent of *in situ* prepared bipyridine radical anion K(bipy$^{\cdot}$). This reaction yielded (ONO^{sq})CrCl(bipy) (**12**), which has been characterized crystallographically (Figure 4.3). Solid state characterization yielded the expected octahedral coordination geometry around the chromium center, with the multidentate ONO and bipy ligands aligning perpendicular to one another and the chloride ligand occupying the remaining coordination site. Bond metrics within the ligand framework are indicative of the (ONO^{sq})$^{2-}$ formulation, with contracted C–O bond distances of 1.31 Å (avg.) and localized double bond character within the aryl backbone on the ONO ligand (Table 4.1), though these bond length contractions are not as pronounced as the fully oxidized (ONO^{q})$^{1-}$ form of the ligand.[28,33–35] Bond lengths within the bipy ligand framework indicate neutral bipy, confirming that electron transfer has occurred from the reduced K(bipy$^{\cdot}$) starting material to the (ONO^{q})$^{1-}$ ligand present in **11**, yielding the (ONO^{sq})$^{2-}$ fragment in **12**. MOS calculations confirm the (ONO^{sq})$^{2-}$ assignment, yielding a value of −2.04.

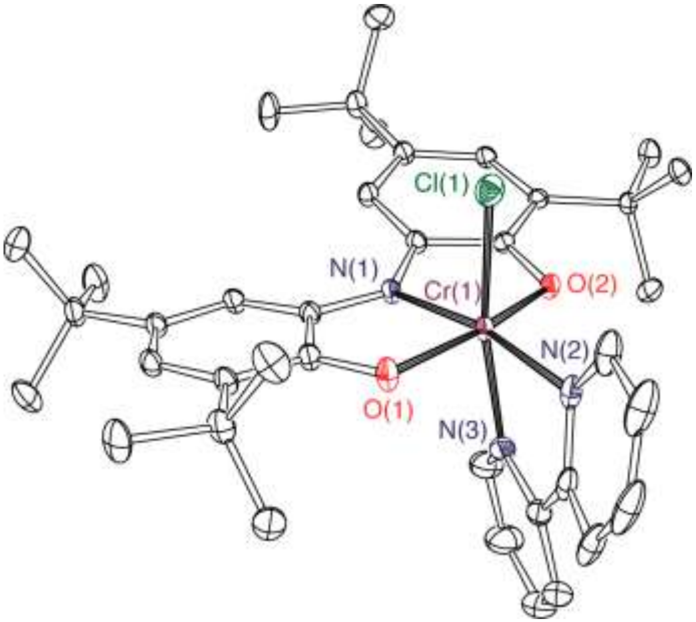

Figure 4.3. ORTEP diagram of (ONO^{sq})CrCl(bipy) (**12**). Thermal ellipsoids are shown at 50% probability. Hydrogen atoms have been omitted for clarity.

The formulation of (ONO^{sq})$^{2-}$ is further supported by UV-vis-NIR spectroscopy which reveals a broad NIR band centered at 1187 nm, characteristic of this ligand oxidation state.[28,33] Evans method analysis yielded a μ_{eff} of 2.76 μB, consistent with an S=1 ground state resulting from antiferromagnetic coupling of the (ONO^{sq})$^{2-}$ radical with an electron on a high spin S=3/2 chromium center. Electrochemical analysis of **12** revealed multiple redox events, resulting from the inclusion of two redox-active ligands in the chromium coordination sphere. A reversible oxidation of **12** occurs at −0.10 V, corresponding to a ligand-based oxidation. This assignment is supported by the reaction in Scheme 4.1, whereby the $(\mathrm{ONO^{q}})^{1-}$ ligand in **11** was reduced to $(\mathrm{ONO^{sq}})^{2-}$ in **12** (also supported by further syntheses described in Chapter 5). Multiple reduction events are observed in **12**, with the first reduction occurring at −1.43 V (E_{pc}) and displaying irreversibility, nominally resulting from Cl^{-} loss upon reduction and subsequent *in situ* formation of $(\mathrm{ONO^{cat}})$Cr(bipy)(THF). This initial reduction event is assigned as ligand-based, corresponding to the reduction of $(\mathrm{ONO^{sq}})^{2-}$ to $(\mathrm{ONO^{cat}})^{3-}$ (this assignment is corroborated by syntheses described herein). A further reversible reduction of **12** occurs at −1.98 V, assigned as a bipy-based reduction owing to the proclivity of bipy-based reductions to occur before Cr(III) reduction in $\mathrm{Cr(bipy)_3}$ complexes.[13] The reduction event at −2.73 V has not been investigated further, and it is therefore not explicitly assigned. The daughter species formed upon reduction of **12** can be observed on multiple cycles of the voltammogram, with re-oxidation occurring at −0.96 V and further oxidation occurring at *ca*. 0.24 V (though this event is difficult to fully resolve).

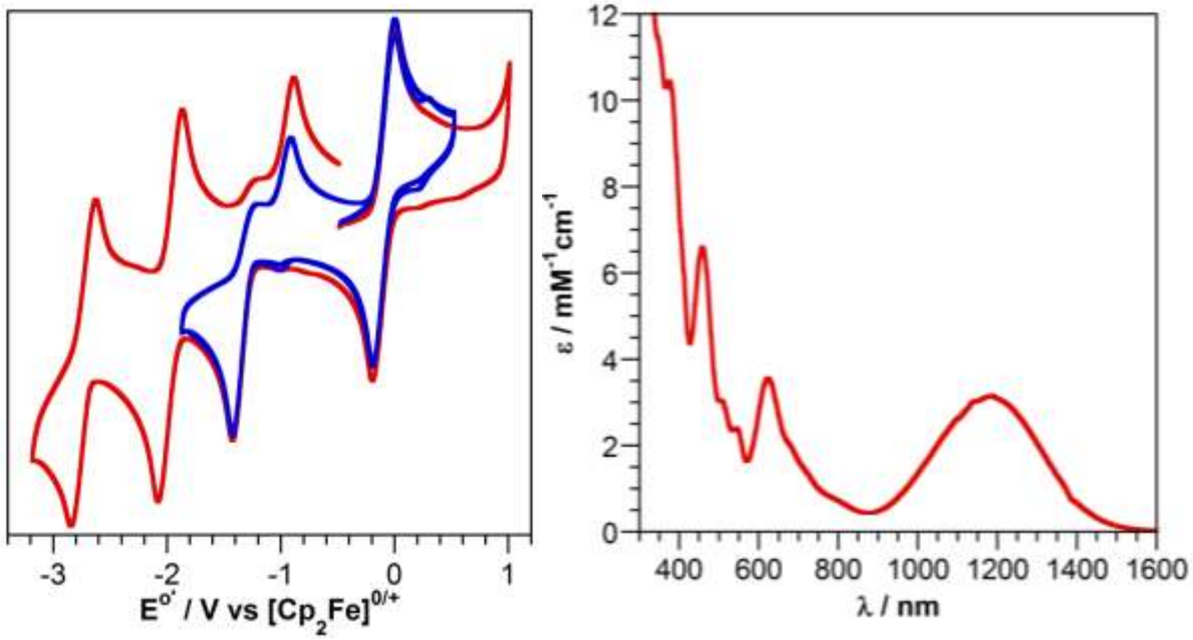

Figure 4.4. Left. Cyclic voltammogram of **12** in THF with 0.1 M $\mathrm{TBAPF_6}$ and 1 mM analyte at 200 mV/s. Muliti-scan voltammogram showing the daughter species (**blue**) and single scan voltammogram of **12** (**red**). **Right.** UV-vis-NIR spectrum of **12** obtained in toluene.

To complete the series of (ONO)Cr complexes with a fully-reduced, trianionic $(ONO^{cat})^{3-}$ supported complex, an *in situ* formed solution of $(ONO^{cat})Li_3$ was added to a vigorously stirred mixture of $CrCl_3(py)_3$ (also formed *in situ* from $CrCl_3(THF)_3$), yielding a dark green product. Analysis by single crystal x-ray diffraction determined this product to be $(ONO^{cat})Cr(py)_3$ (**13**) (Figure 4.5). Solid state analysis confirmed the coordination of three pyridine ligands to **13**, yielding a chromium center in a pseudo-octahedral coordination geometry. Bond metrics within the aryl backbone of the ONO ligand showed no notable localized double bond character, and the C–O and C–N bond distances of 1.36 and 1.39 Å (avg.), respectively, are consistent with a fully reduced $(ONO^{cat})^{3-}$ ligand.[25–28,36–39] Metrical oxidation state calculations yielded a value of −2.76 (average of both molecules in the asymmetric unit), indicative of the trianionic $(ONO^{cat})^{3-}$ assignment in **13**.[25]

Scheme 4.2. Synthesis of complex **13**.

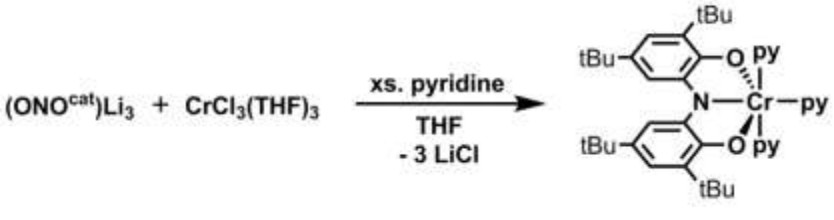

13

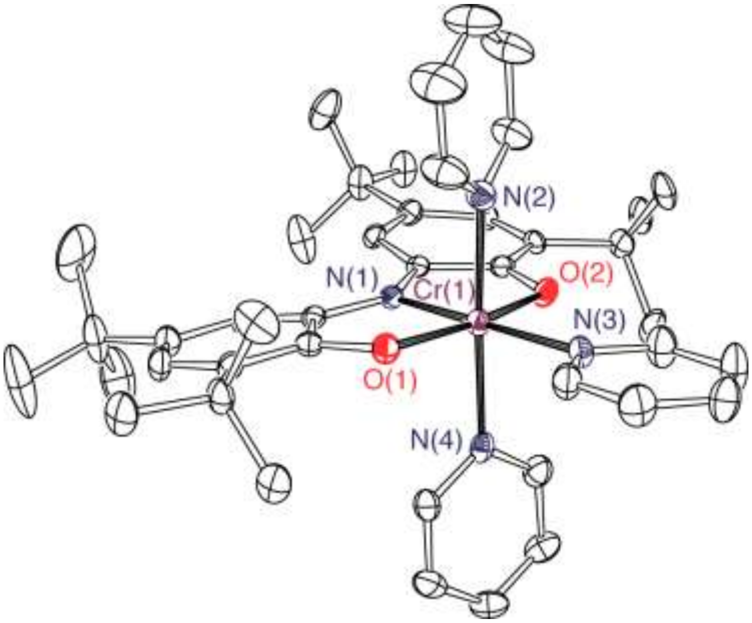

Figure 4.5. ORTEP diagram of $(ONO^{cat})Cr(py)_3$ (**13**). Thermal ellipsoids are shown at 50% probability. Hydrogen atoms have been omitted for clarity. Another molecule of **13** and three cocrystallized THF molecules have been omitted for clarity.

Cyclic voltammetric analysis of **13** revealed two reversible oxidations at −0.97 and 0.32 V, corresponding to the $ONO^{cat/sq}$ and $ONO^{sq/q}$ redox couples, respectively, while an additional irreversible oxidation could be resolved just prior to the edge of the solvent window. An irreversible reduction occurs at −2.62 V (E_{pc}), which is tentatively assigned as a chromium-based reduction from Cr(III)→Cr(II). The irreversibility is likely caused by pyridine dissociation upon reduction of kinetically inert Cr(III) to kinetically labile Cr(II). Further cathodic scanning reveals a reversible reduction event at −2.80 V. The electrochemical behavior of **13** is strikingly similar to that of its rhodium analogue $(ONO^{cat})Rh(py)_3$, which shows two reversible oxidations at −0.91 and 0.12 V and an irreversible reduction event at −2.87 V.[26] Analysis by UV-vis spectroscopy revealed a broad visible region band at 730 nm and additional high energy bands at 408 and 352 nm. While the broad band at 730 nm may appear similar to the broad, low energy NIR bands observed in $(ONO^{sq})^{2-}$ containing complexes, the significant blue shift, along with the solid state bond metrics, suggest the $(ONO^{cat})^{3-}$ assignment. Notably, the rhodium congener

(ONO^{cat})Rh(py)$_3$ shows an absorption spectrum bearing similar features, with an intense band at 380 nm and a broad visible region band at 585 nm.[26]

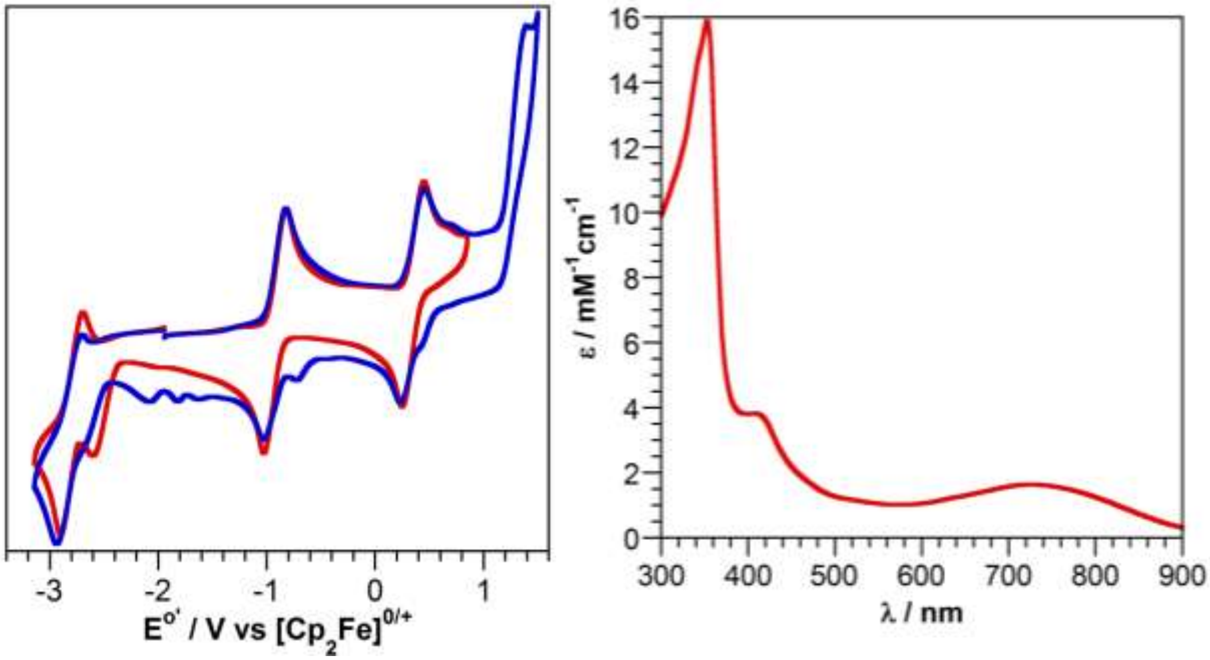

Figure 4.6. Left. Cyclic voltammogram of **13** in THF with 0.1 M TBAPF$_6$ and 1 mM analyte at 200 mV/s. Voltammogram showing two reversible oxidations (**red**) and also showing the third, irreversible oxidation event (**blue**). **Right.** UV-vis spectrum of **13** obtained in toluene.

Given the electrochemically accessible reduction of **12**, this process was pursued synthetically to yield a fully reduced (ONO^{cat})$^{3-}$ coordinated complex. With the proposed loss of chloride upon its reduction, this process was expected to result in the binding of solvent and provide a single readily substituted coordination site. Reduction of **12** with K^0 produced a new product with no notable absorption bands in the NIR range and only a broad, low intensity band at 604 nm. This lack of NIR bands suggests ligand based reduction to (ONO^{cat})$^{3-}$. Instead of the expected structure (ONO^{cat})Cr(bipy)(THF), single crystals of this product revealed an unusual bimetallic complex with the formula [(ONO^{cat})Cr(bipy)]$_2$ (**14**) (Figure 4.7).

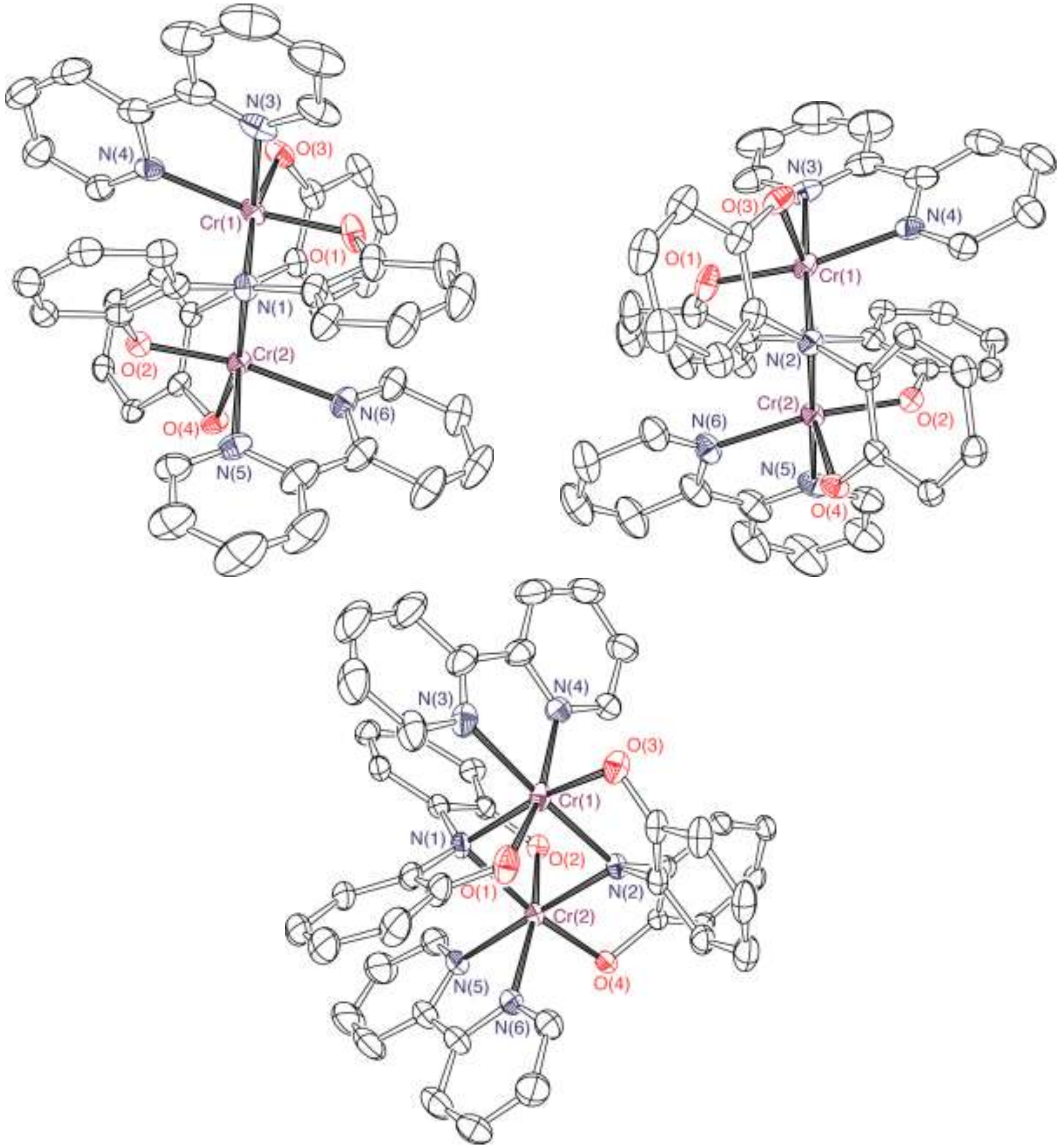

Figure 4.7. ORTEP diagram of $[(\mathrm{ONO^{cat}})\mathrm{Cr(bipy)}]_2$ (**14**). Thermal ellipsoids are shown at 50% probability. Hydrogen atoms and the $-^{t}$Bu groups of the ONO ligand have been omitted for clarity. **Top Left**. View down the N(1)---N(2) axis. **Top Right**. View down the N(2)---N(1) axis. **Bottom**. Side-on view perpendicular to the N_2Cr_2 core.

While this structure is formally a dimer of two $(\mathrm{ONO^{cat}})$Cr(bipy) units, the coordination mode of the two ONO units within **14** are dissimilar. Coordination of the oxygen donors O(1) and O(2) of ONO-1 to the Cr---Cr group occurs on opposite faces of the plane defined by the

N(1)–Cr(1)–Cr(2) plane (Figure 4.7, Top Left), resulting in *trans* coordination of O(1) and O(2) to the bipy ligands. Alternatively, within ONO-2 the oxygen donors O(3) and O(4) coordinate to the Cr---Cr group in a nearly co-planar fashion to the N(2)–Cr(1)–Cr(2) plane (Figure 4.7, Top Right), resulting in *trans* coordination of O(3) and O(4) to the bridging amide N(1) of ONO-1. Both chromium centers adopt pseudo-octahedral geometry. While bond length analysis of the C–O and C–N bonds in ONO and amidophenolate (included in the comparision due to the highly non-planar conformation of the ONO ligand in **14**) complexes is an effective method for the determination of the ligand charge, the structural effects of the bridging mode of the central nitrogen preclude direct comparison to literature values. This effect is notable for the bond lengths of the central nitrogen to the aryl rings, which average 1.43 and 1.46 Å for ONO-1 and ONO-2, respectively. In simple, non-bridging complexes of amidophenolates and ONO the average distance for the N–C(aryl) bond is 1.40 Å for the fully reduced form of the ligand.[25,40] The lengthening of this bond in **14** is caused by the donation of both nitrogen lone pairs to the chromium metal centers, preventing π-donation into the aryl ring and lengthening the bond from the typical 1.40 Å average. This lack of π-donation from the nitrogen atom would also affect the O–C(aryl) bond; as there is now only a single heteroatom capable of π-donation into the aryl ring, the extent of this donation will increase and shorten the O–C(aryl) bond. This effect, and not ligand-based oxidation, is the reason for the slightly contracted lengths of the C–O bonds (1.34 Å avg.) in **14**. Bearing these structural features in mind, MOS calculations still yield a value of −2.94, consistent with the trianionic $(\mathrm{ONO}^{\mathrm{cat}})^{3-}$ ligand.[25]

The Cr---Cr distance in **14** is 2.8657(6) Å, which is just outside of bonding distance based on the reported 1.39 Å covalent radius of chromium.[41] Evans method analysis determined a μ_{eff} of 2.97 μB, clearly indicating that bridging amide mediated antiferromagnetic coupling is resulting in a reduced effective magnetic moment, or, that there is indeed a bonding interaction between the chromium centers. Supporting the presence of a formal bond, a long Cr–Cr single bond distance of 3.281(1) Å has been reported for $[CpCr(CO)_3]_2$, indicating that a reliance on the average covalent radius of 1.39 Å may be unreliable.[42] The observed Cr---Cr distance in **14** is similar to distances observed in other bridging amide complexes of chromium, which also demonstrate diminished effective magnetic moments resulting from antiferromagnetic coupling or, potentially, a direct bonding interaction (though these reports do not go so far as to explicitly assign a Cr–Cr bond, and are typically quite careful in their descriptions of the nature of the Cr---Cr interaction).[43–52] For this reason a formal bond is not drawn or presented in the ORTEP diagram, though it is not explicitly ruled out.

Table 4.2. Selected bond distances (Å) and angles (°) for **14** and **15**.

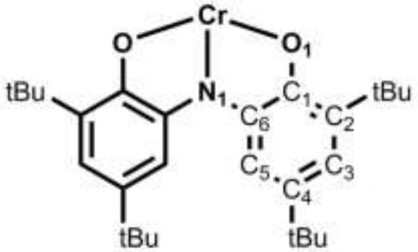

	14 **ONO-1**	**14** **ONO-2**	**15** **ONO-1**	**15** **ONO-2**
		Bond Lengths (Å)		
N(1)/N(2)–Cr(1)	2.078(2)	2.109(2)	2.0745(15)	2.0573(15)
N(1)/N(2)–Cr(2)	2.084(2)	2.094(2)	2.0559(15)	2.0882(15)
O(1)/O(3)–Cr(1)	1.939(2)	1.934(2)	1.9384(13)	1.9360(13)
O(2)/O(4)–Cr(2)	1.9362(19)	1.9295(19)	1.9461(12)	1.9263(12)
C(6)–N(1)/N(2)	1.433(3)	1.453(3)	1.448(2)	1.438(2)
C(1)–O(1)/O(3)	1.342(4)	1.344(4)	1.349(2)	1.346(2)
C(1)–C(2)	1.405(4)	1.421(4)	1.418(2)	1.405(2)
C(2)–C(3)	1.404(6)	1.398(5)	1.397(3)	1.407(3)
C(3)–C(4)	1.375(6)	1.392(5)	1.404(3)	1.397(3)
C(4)–C(5)	1.402(4)	1.387(4)	1.395(3)	1.401(3)
C(5)–C(6)	1.385(4)	1.398(4)	1.391(2)	1.383(2)
C(6)–C(1)	1.412(4)	1.401(4)	1.403(2)	1.410(2)
N(3)–Cr(1)	2.126(3)	-----	2.1351(16)	-----
N(4)–Cr(1)	2.122(3)	-----	2.1798(16)	-----
Cr(1)---Cr(2)	2.8657(6)	-----	2.9523(4)	-----
		Bond Angles (°)		
Cr(1)–N(1)–Cr(2)	87.05(8)	-----	91.25(6)	-----
Cr(1)–N(2)–Cr(2)	-----	85.96(8)	-----	90.82(6)
O(1)–Cr(1)–O(3)	88.83(9)	-----	176.10(5)	-----
O(1)–Cr(1)–N(1)	79.29(9)	-----	82.18(5)	-----
O(3)–Cr(1)–N(2)	-----	83.65(8)	-----	81.21(6)
N(3)–Cr(1)–N(4)	75.99(10)	-----	87.36(6)	-----

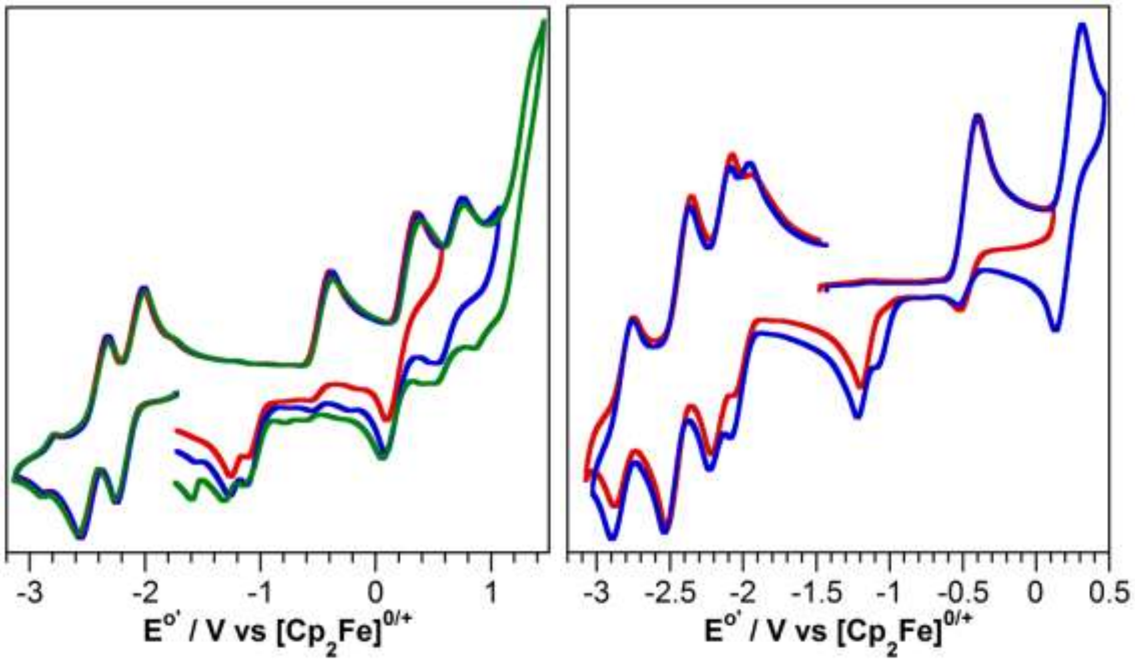

Figure 4.8. Left. Cyclic voltammogram of **14** with initial cathodic scanning and varying anodic scan windows. **Right.** Cyclic voltammogram of **14** with initial anodic scanning, with varying anodic scan windows. Voltammograms collected in THF with 0.1 M TBAPF$_6$ and 1 mM analyte at a scan rate of 200 mV/s.

Electrochemical analysis of **14** suggests the dimeric formula is maintained in solution but is unstable upon oxidation, with an irreversible oxidation event occurring at −0.48 V and generating a new daughter peak at −1.20 V (E$_{pc}$). This irreversibility was assumedly caused through monomerization of the dimer, since oxidation of the ligand backbone would significantly diminish the ability of the central nitrogen of ONO to bridge the two chromium centers. However, further anodic scanning revealed a second oxidation event at 0.22 V that produced two daughter peaks at −1.08 (E$_{pc}$) and −1.20 V, suggesting the nature of the daughter species' is more complicated. Compared to the electrochemical behavior of **12**, the minor daughter species at −1.08 V observed in **14** is a close match to that of the daughter species generated in **12** (E$_{pc}$ = −1.01 V), with the differing relative concentration of these daughter species likely causing the small difference in E$_{pc}$ (Figure 4.4). This seems to suggest that the anodically shifted daughter species at −1.20 V could represent a reorganized dimer, while the minor daughter species at −1.08 V could correspond to monomeric [(ONO^{sq})Cr(bipy)(THF)]$^+$

generated in small amounts. Scanning even further anodically revealed two additional oxidation events, a semi-reversible oxidation at 0.64 V and, what appears to be, another oxidation event juxtaposed onto the solvent oxidation edge. An additional daughter peak is observed at −1.60 V (E_{pc}) when these furthest oxidations are included in the voltammogram. In the cathodic region, reversible reductions occur at −2.11 and −2.40 V which, considering the $(ONO^{cat})^{3-}$ formulation of the ligands, likely correspond to reduction of each of the bipy ligands. If anodic scans are first performed, daughter species (which are already present in minute amounts) are observed at −2.02 and −2.82 V. While similar to the reduction events observed in **12** (−1.98 and −2.73 V), the notable difference in the second reduction suggests these daughter peaks are not related to those observed in **12**, but are instead related to the major, initial daughter species whose first reduction is observed at −1.20 V.

The reduction-based synthetic strategy utilized to obtain **14** was extended in an attempt at accessing complex **13** via reduction of **11** in the presence of excess pyridine. This strategy instead yielded a product with a UV-vis-NIR spectrum similar to that of **14**, with low intensity visible region bands at 514 and 610 nm. Single crystal X-ray diffraction analysis determined the product to be a pyridine substituted analogue of **14**, $[(ONO^{cat})Cr(py)_2]_2$ (**15**) shown in Figure 4.9.

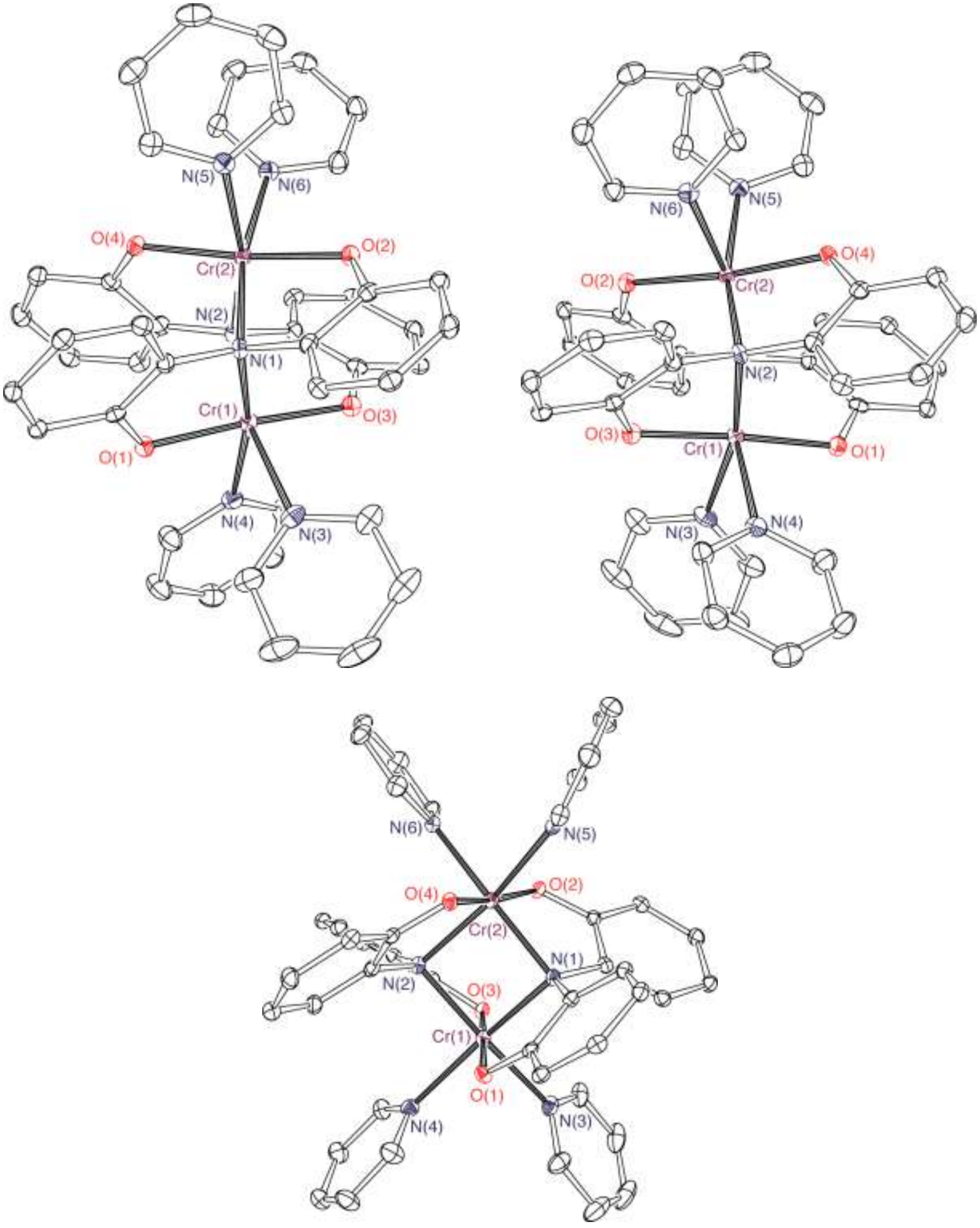

Figure 4.9. ORTEP diagram of $[(ONO^{cat})Cr(py)_2]_2$ (**15**). Thermal ellipsoids are shown at 50% probability. Hydrogen atoms and the $-^{t}Bu$ groups of the ONO ligand have been omitted for clarity. Another molecule of **15** within the asymmetric unit has also been omitted. **Top Left**. View down the N(1)---N(2) axis. **Top Right**. View down the N(2)---N(1) axis. **Bottom**. Side-on view perpendicular to the N_2Cr_2 core.

The most notable difference between **15** and **14** is the symmetric nature of the dimer observed in **15**; whereas in **14** the two ONO units coordinate to the Cr_2 core in an asymmetric fashion, both ONO units in **15** coordinate to the Cr_2 core in an identical coordination mode (note Figure 4.9 top left vs top right views). All of the phenoxide donor groups in **15** coordinate *trans* to the phenoxides of the opposing ONO ligand, while the capping pyridine groups all coordinate *trans* to the bridging amides. This is in stark contrast to the structural features of **14**, where the phenoxide groups of ONO-1 coordinate *trans* to bipy nitrogens, and the phenoxide groups of ONO-2 coordinate *trans* to the bridging amide. As in **14**, both chromium centers adopt pseudo-octrahedral coordination geometry. Close inspection of the bipy and pyridine coordination environments do not reveal any obvious reason for the structural disparity; hypothetical substitution of bipy for the two pyridines in **15** does not appear to confer any detrimental steric interactions, nor does pyridine substitution for bipy in **14**. The disparity could be rooted in subtle electronic changes conferred by the slightly altered coordination of a bipy ligand vs two pyridine ligands; the average N–Cr–N bond angle in **15** is 87.7°, while in **14** the average angle is 76.2°, contracted due to the bidentate nature of bipy. Alternatively, the difference could simply be a consequence of the bipy ligand preventing a structural rearrangement step that can occur with monodentate pyridine ligands, making the difference one of kinetics and not necessarily thermodynamics.

The average C–O bond distance in **15** is 1.34 Å, identical to those observed in **14**, while the average C–N bond distance in **15** is 1.44 Å, similar to those observed in the ONO ligands of **14**. Again, as described for complex **14**, MOS calculations should be viewed with the gross structural effects of the bridging amide in mind; metrical oxidation state calculations yield a value of −2.93, consistent with the $(ONO^{cat})^{3-}$ assignment of the ligand. The Cr---Cr distance in

15 is 2.9523(4) and 2.8991(4) Å in the two molecules within the asymmetric unit, similar to that of **14**. For the same rationale used in complex **14**, no explicit bond between the chromium centers is presented. Evans method analysis determined a μ_{eff} of 3.08 μB, analogous to the results obtained with **15** and indicative of antiferromagnetic coupling between the chromium centers.

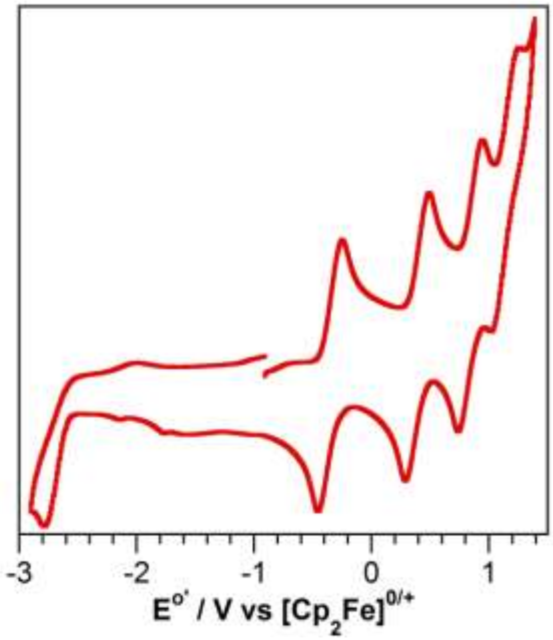

Figure 4.10. Cyclic voltammogram of **15** recorded in THF with 0.1 M $TBAPF_6$ and 1 mM analyte at a scan rate of 200 mV/s.

Electrochemical analysis of **15** revealed another significant deviation from the behavior of **14**. Cyclic voltammetry revealed that the first oxidation event in **15** (whose onset potential is similar to that observed in **14**) is reversible, contrasting the irreversible nature of the first oxidation in **14**. While this would seem to suggest that **15** might not retain its dimeric structure in THF, the presence of a total of 4 oxidative events is in stark contrast to that seen in the electrochemistry of $(ONO^{cat})Cr(py)_3$ (**13**), which only shows a (barely discernible) third, irreversible oxidation event in the electrochemical window of THF. If **15** existed as a monomer of hypothetical formulation $(ONO^{cat})Cr(py)_2(THF)$ in solution then it would likely possess analogous electrochemistry to that of **13**. Notably, the peak separation between the 1st and 2nd oxidation events (−0.97 and 0.32 V, respectively) in **13** is 1.29 V, while this decreases to 0.74 V in **15**, owing to a significant anodic shift in the 1st oxidation event (also observed in **14**). This separation and the accessibility of four reversible oxidation events at −0.35, 0.39, 0.84, and 1.14 V is consistent with **15** remaining a dimer in solution and undergoing multiple one-electron events. This assertion necessitates that oxidation of the ligand removes electron density primarily at the oxygen and phenyl groups (Chart 4.1) to maintain the bridging ability of the central amide. While not typically presented in this form within our group, this resonance structure has been preferred by others[35], and is consistent with the relatively minimal contraction of the N–C bond upon $(\mathrm{ONO^{cat}})^{3-} \rightarrow (\mathrm{ONO^{sq}})^{2-}$ oxidation and the notable contraction of the C–O bond upon this oxidation (see Table 4.1). This is also consistent with maintaining the bridging ability of the central nitrogen upon the first oxidation event of each ONO ligand. Coordination of the central nitrogen to two lewis acids could also stabilize the nitrogen based lone pairs and result in the second ONO-based oxidation event being primarily based on the other aryl–O moiety, allowing the central nitrogen to maintain the dimeric formula upon the 3rd and 4th oxidation events at 0.84 and 1.14 V.

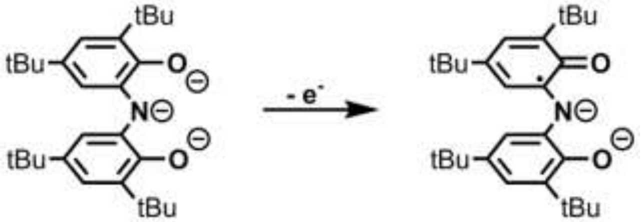

Chart 4.1. Alternative electronic structure of the ONO ligand upon oxidation to the $(\mathrm{ONO^{sq}})^{2-}$ form.

Organometallic (ONO)Cr Chemistry

In an attempt to synthesize new (ONO)Cr derivatives with organic X-type ligands, the synthesis of $(\mathrm{ONO^{q}})\mathrm{Cr(Ph)_2}$ was pursued. This venture was inspired by the organometallic chemistry of the simple complex $\mathrm{CrCl_3THF_3}$ which, upon treatment with 3 equiv. PhMgBr in THF, yields $\mathrm{CrPh_3THF_3}$.[53] While this complex is stable in THF, application of extended vacuum or dissolution in weakly coordinating solvents causes this complex to produce *ca.* 0.5 equiv. of biphenyl. Similar formation of biphenyl is observed when $CrCl_3$ is treated with PhMgBr in weakly coordinating diethyl ether.[54] The stability of $CrPh_3THF_3$ in the presence of strong ligands suggested that ONO coordinated chromium might form stable Cr–Ph groups. If this was not the case, then the coordination of an $(ONO^q)^{1-}$ moiety would provide a path to two-electron reactivity, whereas the reports with simple $CrCl_3$ only yielded one-electron reduction of the chromium center.

To this end, a freshly thawed THF solution of **11** was treated with two equiv. of PhLi in THF. A product showing broad visible region bands and lacking near-IR bands was obtained, indicating the ONO ligand was in the fully reduced catecholate form. NMR analysis of the crude product revealed biphenyl in the reaction mixture, suggesting reductive elimination of the putative intermediate "$(ONO^q)Cr(Ph)_2$" had occurred, yielding the $(ONO^{cat})^{3-}$ containing product. To quantify the amount of biphenyl formed, the reaction was repeated and the reaction mixture analyzed by gas chromatography. Gas chromatographic analysis revealed a 26% yield of biphenyl and an 18% yield of benzene, though the remaining equivalents could not be accounted for. Identical yields were obtained when performed in a reaction volume of 6 mL or 11 mL, suggesting biphenyl formation was not a result of phenyl radical expulsion and subsequent radical coupling. However, expulsion of phenyl radical and abstraction of $H^{\cdot}$ from the solvent, THF, is the likely source of benzene. Given that benzene is present in sub-millimole amounts, evaporative losses might result in an underreported yield.

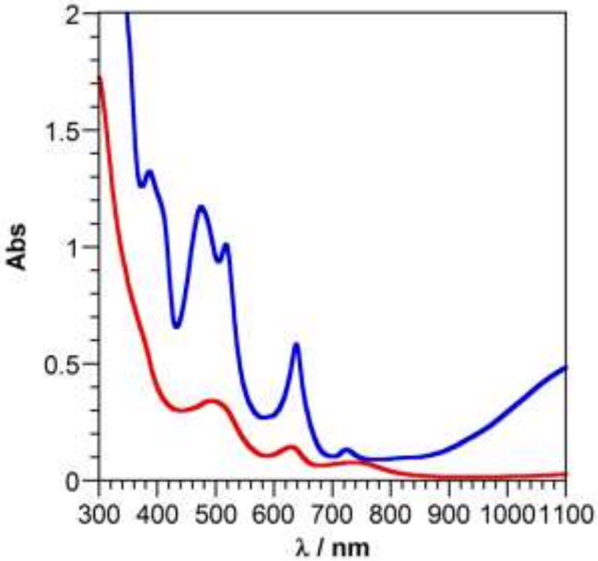

Figure 4.11. UV-vis-NIR spectra of reaction products obtained from treatment of **11** with 2 equiv. of PhLi (**red**) and 1 equiv. PhLi (**blue**).

Addition of a single equivalent of PhLi to **11** resulted in reduction of the starting material to an $(\mathrm{ONO}^{\mathrm{sq}})^{2-}$ containing product (Scheme 4.3) and yielded 7% biphenyl and 24% benzene. Addition of another equivalent of PhLi to the resulting reaction mixture reproduced the results obtained when both equivalents were added as one portion, yielding 25% biphenyl and 18% benzene. The proposed reaction intermediate, "$(\mathrm{ONO}^{\mathrm{sq}})\mathrm{CrCl(THF)}_2$" therefore seems to be responsible for the majority of the observed biphenyl. Biphenyl yields are, however, lower than those reported for simple CrCl_3.

Scheme 4.3. Reactivity and putative reaction products obtained by reduction of **11** with PhLi.

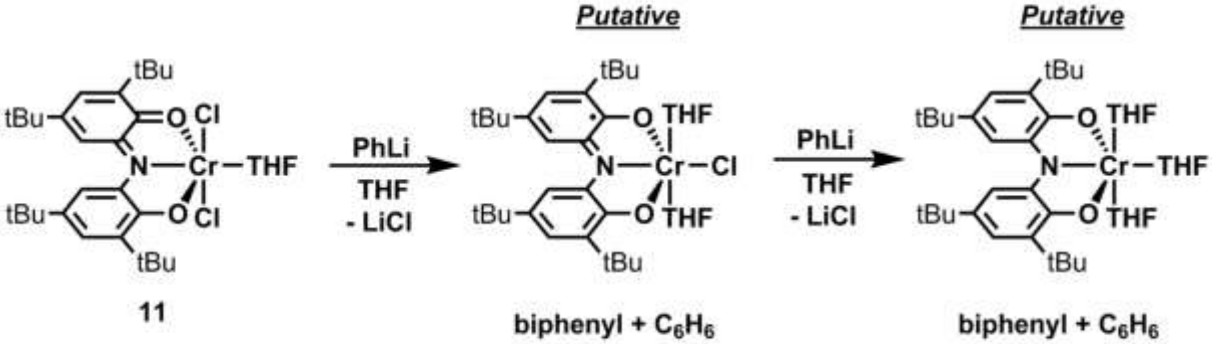

To confirm the yields determined by gas chromatography, the reaction of $(\mathrm{ONO}^{\mathrm{q}})\mathrm{CrCl}_2\mathrm{(THF)}$ with two equivalents of 4-*tert*-butylphenyllithium was performed on a preparative scale and the product 4,4’-di-tert-butylbiphenyl isolated from the reaction mixture (the substitution of the *tert*-butyl variant was necessary to avoid sublimation of biphenyl upon reaction workup). After beginning the reaction under the same temperature conditions as before, the reaction mixture was allowed to stir overnight at which point the reaction was dried under vacuum. The residue was extracted with pentane, filtered and washed through a pipette-plug of silica, and the extract dried under vacuum. The product 4,4’-di-*tert*-butylbiphenyl was isolated in 20% yield, analogous to the results obtained chromatographically with biphenyl.

Summary and Conclusions

Heteroleptic complexes of the general formula (ONO)CrX_nL_m have been prepared in all three oxidation states of the ONO ligand, with the chromium center showing a strong proclivity for the Cr(III) oxidation state. This preference manifests itself by adjusting the charge on the ONO ligand as a function of the number of X-type ligands bound to the chromium center. Throughout the series, bond lengths within the ONO ligand are reflective of the ligand charge and consistent with metrical oxidation state calculations. Moreover, electronic absorption spectroscopy yields spectra with diagnostic features in the near-IR region, showing a strongly absorbing pair of bands at 827 and 927 nm in (ONO^q)Cr, a broad near-IR band in the 1200 nm region in (ONO^{sq})Cr, and lacking near-IR bands in (ONO^{cat})Cr complexes. This trait confers a rapid and powerful method for the determination of the ligand oxidation state in (ONO)Cr complexes, the generality of which is confirmed and extended in proceeding chapters.

The isolation of dimeric complexes $[(ONO^{cat})Cr(bipy)]_2$ and $[(ONO^{cat})Cr(py)_2]_2$ demonstrates that the sterically non-encumbering nature of the ONO ligand makes it susceptible to forming higher order structures when coordination sites are not strictly controlled through ligand binding. These bimetallic structures do however yield complexes with rich electrochemical properties, each displaying four accessible oxidation events within the THF solvent window.

The pursuit of chromium–phenyl complexes demonstrated that the (ONO)Cr fragment is likely not amenable to the synthesis of stable organometallic complexes, undergoing apparent reductive elimination of biphenyl and radical expulsion of phenyl radicals upon formation of putative $(ONO^q)CrPh_2$ and (ONO^q)CrPhCl intermediates. Though low yielding with respect to the homocoupled organic product, this result demonstrates potential applications of the (ONO)Cr fragment to carbon-carbon bond forming transformations.

Experimental

General Considerations. Manipulations were performed using standard Schlenk line techniques or in a N_2 filled glovebox. Diethyl ether, pentane, benzene, toluene, and tetrahydrofuran were sparged with argon and then dried and deoxygenated by passage through activated alumina and Q5 columns. Pyridine was dried over elemental sodium, vacuum transferred, and stored over molecular sieves. Silver trifluoromethanesulfonate (AgOTF) was dried under high vacuum prior to use. (ONO^q)K was prepared according to literature procedures.[26]

Physical Methods. Solution UV-vis-NIR spectra were recorded in 1-cm path-length cuvettes on a Shimadzu UV-1700 spectrophotometer. Extinction coefficients were determined from Beer-Lambert Law plots. EPR spectra were collected on a Bruker EMX X-band spectrometer equipped with an ER041XG microwave bridge. Solution magnetic moments (μ_{eff}) were determined using Evans Method.[55–57] Electrospray ionization mass spectrometry (ESI-MS) data were collected on a Waters LCT Premier mass spectrometer. Elemental analyses were collected on a Perkin-Elmer 2400 Series II CHNS/O analyzer. Stock solutions of biphenyl were used to generate a five point calibration curve for quantification of biphenyl from reaction mixtures.

Electrochemical Methods. Electrochemical measurements were recorded with a Gamry G300 potentiostat using a standard three-electrode configuration including a 3.0 mm glassy carbon working electrode, a platinum wire auxiliary electrode, and a silver wire reference electrode. All measurements were made on solutions that contained 1 mM analyte and 0.1 M NBu_4PF_6 in THF at an ambient temperature of ca. 21 °C in a glovebox under a N_2 atmosphere. Potentials are referenced to $Cp_2Fe^{+/0}$ using an internal standard of ferrocene or decamethylferrocene ($E°'$ = -0.440 V vs $Cp_2Fe^{+/0}$ in THF).[58]

Crystallographic Methods. X-ray diffraction data were collected on single crystals mounted on a glass fiber using a Bruker SMART APEX II diffractometer. Measurements were carried out using Mo Kα (λ = 0.71073 Å) radiation, wavelength selected with a single-crystal graphite monochromator. A full sphere of data was collected for each crystal structure. The APEX[59] program package was used to determine the unit cell parameters and for data collection. The raw frame data was processed using SAINT[60] and SADABS[61] to yield the reflection data files. Subsequent calculations were carried out using the SHELXTL[62] program. The structures were solved by direct methods and refined on F^2 by full matrix least-squares techniques. The analytical scattering factors[63] for neutral atoms were used throughout the analysis. Hydrogen atoms were included using a riding model. ORTEP diagrams were generated using ORTEP-3 for Windows.

Table 4.3. Data collection and refinement parameters for complexes **11-15**.

	11	**12**	**13**	**14**	**15**
Empirical Formula	$C_{32}H_{48}Cl_2CrNO_3 \bullet C_4H_8O$	$2\ C_{38}H_{48}ClCrN_3O_2 \bullet C_{24}H_{27}$	$2\ C_{43}H_{53}CrN_4O_2 \bullet 3\ C_4H_8O$	$C_{81}H_{107}Cr_2N_6O_4$	$2\ C_{76}H_{100}Cr_2N_6O_4 \bullet C_{7.5}H_{10}N_3$
Formula Weight	689.71	1647.94	1636.09	1332.72	2673.41
Crystal System	Monoclinic	Monoclinic	Orthorhombic	Monoclinic	Monoclinic
Space Group	$P2_1/c$	C2/c	*Pbca*	$P2_1/n$	$P2_1/c$
a (Å)	10.717(2)	33.8563(13)	22.490(2)	14.7312(14)	24.5442(11)
b (Å)	16.799(4)	14.6946(6)	28.684(3)	25.662(2)	26.7900(12)
c (Å)	20.447(4)	41.1127(16)	32.067(3)	20.964(2)	25.4091(12)
α (°)	90	90	90	90	90
β (°)	92.521(3)	114.3130(4)	90	109.4763(12)	117.0027(6)
γ (°)	90	90	90	90	90
Volume ($Å^3$)	3677.5(14)	18639.7(13)	20686(4)	7471.6(12)	14886.1(12)
Z	4	8	8	4	4
F(000)	1476	7032	7024	2860	5728
Rflns. collected	39903	112980	227326	80909	183863
Ind. rflns. (R_{int})	8763 (0.0438)	23464 (0.0231)	25100 (0.1226)	15286 (0.0233)	37469 (0.0553)
GOF	1.113	1.032	1.053	1.025	1.039
R1 [I > 2σ(I)][a]	0.0855	0.0549	0.0754	0.0684	0.0455
wR2 (all data)[a]	0.2374	0.1528	0.1928	0.1913	0.1196

[a] $R1 = \Sigma||F_o|-|F_c|| / \Sigma|F_o|$; $wR2 = [\Sigma[w(F_o^2-F_c^2)^2] / \Sigma[w(F_o^2)^2]\ ]^{1/2}$; $GOF = S = [\Sigma[w(F_o^2-F_c^2)^2] / (n-p)]^{1/2}$

(ONO^q)$CrCl_2$(THF) (11). A vial was charged with $CrCl_3(THF)_3$ (0.106 g, 0.283 mmol) and 3 mL of THF. This mixture was stirred vigorously and a 12 mL solution of (ONO^q)K (0.130 g, 0.281 mmol) in THF was added dropwise over the course of 15 minutes to the slurry of $CrCl_3(THF)_3$. After stirring for 3 hours the reaction was dried under vacuum, extracted with toluene, filtered, and dried under vacuum. The crude material was dissolved in THF and layered with pentane. After mixing of the layers overnight, the solution was placed in a −35 °C freezer for a day. Crystalline material was collected, redissolved in toluene, filtered, and dried to yield the product as a dark maroon/brown solid (0.071 g, 41%). Anal. Calcd. for $C_{32}H_{47}NO_3Cl_2Cr$: C, 62.23; H, 7.68; N, 2.27. Found: C, 61.92; H, 8.10; N, 1.87. UV-vis-NIR (toluene) λ_{max}/nm (ε/M^{-1} cm^{-1}): 352 (5830), 450 (9110), 542 (4460), 575 (4540), 827 (9880), 927 (12700).

(ONO^{sq})CrCl(bipy) (12). A vial was charged with KC_8 (0.072 g, 0.533 mmol) and 1 mL of THF and then frozen in a cold well. To another vial was added 2,2'-bipyridine (0.076 g, 0.486 mmol) which was dissolved in 4 mL of THF and then frozen in a cold well. Upon thawing, the solution of bipy was added to the slurry of KC_8. After stirring for 20 minutes, this slurry was added to a freshly thawed solution of (ONO^{q})CrCl$_2$(THF) (0.300 g, 0.486 mmol) in 10 mL of THF. After stirring for 3.5 hours the mixture was filtered and dried. The crude material was dissolved in THF and layered with pentane, yielding the product as a dark green solid (0.314 g, 97%). Anal. Calcd. for $C_{38}H_{48}N_3O_2ClCr$: C, 68.50; H, 7.26; N, 6.31. Found: C, 68.16; H, 7.25; N, 5.97. UV-vis-NIR (toluene) λ_{max}/nm (ε/M^{-1} cm^{-1}): 375 (10500), 458 (6750), 506 (3030), 544 (2400), 623 (3550), 1187 (3150).

(ONO^{cat})Cr(py)$_3$ (13). A vial was charged with (ONO^{cat})H$_3$ (0.294 g,0.691 mmol) which was dissolved in 5 mL of THF and frozen in a cold well. Upon thawing, *n*-BuLi (0.77 mL, 2.7 M in hexanes, 2.08 mmol) was added to the solution of (ONO^{cat})H$_3$. Concurrently, a separate vial was charged with $CrCl_3(THF)_3$ (0.264 g, 0.704 mmol) which was slurried in 2 mL of THF. To the vigorously stirred slurry of $CrCl_3(THF)_3$ was added 4 mL of pyridine. After each of the separate mixtures had stirred for 20 minutes, the *in situ* formed solution of (ONO^{cat})Li$_3$ was added to the slurry of *in situ* formed $CrCl_3(py)_3$. After stirring overnight the reaction mixture was concentrated to a volume of 2 mL under vacuum and then diluted into 100 mL of a 1:1 benzene/toluene solution and stirred. The mixture was filtered and 5 mL of pyridine was added to the filtrate, which was subsequently dried under vacuum. The crude solid was washed copiously with 10 mL portions of pentane until complete removal of a magenta impurity. The solid was then stirred in 10 mL of Et_2O, followed by the addition of 10 mL of pentane before subsequent filtration. The solid was recollected and this process was repeated twice more to remove a brown impurity. The remaining dark green solids were dissolved in pyridine (*ca.* 25-30 mL) and layered with acetonitrile. Diffusion of the solvent layers yielded long, green rods of the product (0.217 g, 44%). Anal. Calcd. for $C_{43}H_{55}N_4O_2Cr$: C, 72.54; H, 7.79; N, 7.87. Found: C, 72.55; H, 7.80; N, 8.16. UV-vis-NIR (toluene) λ_{max}/nm (ε/M^{-1} cm^{-1}): 352 (15900), 408 (3820), 730 (1640).

[(ONO^{cat})Cr(bipy)]$_2$ (14). A vial was charged with (ONO^{sq})CrCl(bipy) (0.365 g, 0.548 mmol) which was dissolved in 10 mL of THF. A separate vial was charged with elemental potassium (0.022 g, 0.562 mmol) and 2 mL of THF. Both mixtures were frozen in a cold well and, upon thawing, the solution of (ONO^{sq})CrCl(bipy) was added to the elemental potassium. An additional 5 mL of room temperature THF was used to aid transfer of precipitated (ONO^{sq})CrCl(bipy). After stirring overnight the reaction mixture was dried under vacuum, extracted with toluene, filtered, and dried. The solids were washed with toluene, and the remaining solids were dissolved in THF and layered with pentane. The initial set of impure solids were removed, and the mother liquor dried. The solid obtained from the mother liquor was dissolved in THF and layered with pentane. Crystalline needles of [(ONO^{cat})Cr(bipy)]$_2$ were obtained from this fraction (0.083 g, 24 %). Anal. Calcd. for $C_{76}H_{96}N_6O_4Cr_2$: C, 72.35; H, 7.67; N, 6.66. Found: C, 72.26; H, 8.06; N, 6.00. UV-vis-NIR (THF) λ_{max}/nm (ε/M^{-1} cm^{-1}): 604 (910).

[(ONO^{cat})Cr(py)$_2$]$_2$ (15). A vial was charged with (ONO^{q})$CrCl_2$(THF) (0.157 g, 0.254 mmol) which was dissolved in 8 mL of THF. A separate vial was charged with KC_8 (0.071 g, 0.526 mmol) which was slurried in 2 mL of THF. Both mixtures were frozen in a cold well. Upon thawing, pyridine (0.300 mL, 3.72 mmol) was added to the solution of (ONO^q)CrCl$_2$(THF). This solution was then added to the freshly thawed slurry of KC$_8$. After stirring for 2 ¾ hours the mixture was filtered and dried under vacuum. The crude solids were dissolved in pyridine and layered with acetonitrile. Diffusion of the layers yielded large, green blocks of the product (0.045 g, 28 %). Anal. Calcd. for $C_{76}H_{100}N_6O_4Cr_2$: C, 72.12; H, 7.96; N, 6.64. Found: C, 71.80; H, 7.96; N, 6.92. UV-vis-NIR (toluene) λ_{max}/nm (ε/M^{-1} cm^{-1}): 312 (19600), 514 (1170), 610 (1050).

Reactivity of 11 with PhLi

A.) Two equivalents. A vial was charged with (ONO^q)CrCl$_2$(THF) (0.050 g., 0.081 mmol) and 5 mL of THF. This solution was frozen in a cold well and just after thawing a cold solution of PhLi (1 mL, 0.162 M, 0.162 mmol) was added. After stirring for 3 hours an aliquot was removed for gas chromatographic analysis.

B.) Two equivalents. Identical conditions and procedures as above were used, but the initial solution of **11** was made in 10 mL of THF.

Sequential additions. A vial was charged with (ONO^q)CrCl$_2$(THF) (0.050 g., 0.081 mmol) and 5 mL of THF. This solution was frozen in a cold well and just after thawing a cold solution of PhLi (0.5 mL, 0.162 M, 0.081 mmol) was added. After stirring for 1.5 hours a 1 mL aliquot was removed for gas chromatographic analysis. The remaining solution was refrozen, and upon thawing a second addition of PhLi (0.410 mL, 0.162 M, 0.066 mmol) was performed. After 1.5 hours an aliquot was removed for gas chromatographic analysis.

Reactivity with 4-*tert*-butylphenyllithium. A vial was charged with (ONO^q)CrCl$_2$(THF) (0.058 g, 0.094 mmol) which was dissolved in 5 mL of THF and frozen in a cold well. Another vial was filled with 3 mL of THF and frozen. Upon thawing of both solutions, the cold THF was used to dissolve 4-*tert*-butylphenyllithium (0.027 g, 0.197 mmol) which was added to the freshly thawed solution of $(ONO^q)CrCl_2(THF)$. After stirring overnight the reaction was dried under vacuum. The crude solid was extracted with pentane in small portions and filtered through a 5 cm plug of silica in a pipette. The pentane extracts were dried under vacuum to yield 4,4'-di-*tert*-butylbiphenyl (0.005 g, 20%).

References

(1) Davison, A.; Edelstein, N.; Holm, R. H.; Maki, A. H. *J. Am. Chem. Soc.* **1964**, *86*, 2799.
(2) Schrauzer, G. N.; Mayweg, V. P.; Finck, H. W.; Muller-Westerhoff, U.; Heinrich, W. *Angew. Chem. Int. Ed. Engl.* **1964**, *3*, 381.
(3) Schrauzer, G. N.; Mayweg, V. P.; Finck, H. W. *Angew. Chem. Int. Ed. Engl.* **1964**, *3*, 639.
(4) Eisenberg, R.; Stiefel, E. I.; Rosenberg, R. C.; Gray, H. B. *J. Am. Chem. Soc.* **1966**, *88*, 2874.
(5) Schrauzer, G. N.; Mayweg, V. P. *J. Am. Chem. Soc.* **1966**, *88*, 3235.
(6) Wharton, E. J.; McCleverty, J. A. *J. Chem. Soc.* **1969**, 2258.
(7) Stiefel, E. I.; Eisenberg, R.; Rosenberg, R. C.; Gray, H. B. *J. Am. Chem. Soc.* **1966**, *88*, 2956.
(8) Stiefel, E. I.; Bennett, L. E.; Dori, Z.; Crawford, T. H.; Simo, C.; Gray, H. B. *Inorg. Chem.* **1970**, *9*, 281.
(9) McCleverty, J. A.; Locke, J.; Wharton, E. J.; Gerloch, M. *J. Chem. Soc.* **1968**, 816.
(10) Kapre, R. R.; Bothe, E.; Weyhermuller, T.; George, S. D.; Muresan, N.; Wieghardt, K. *Inorg. Chem.* **2007**, *46*, 7827.
(11) Banerjee, P.; Sproules, S.; Weyhermüller, T.; Debeer George, S.; Wieghardt, K. *Inorg. Chem.* **2009**, *48*, 5829.
(12) Scarborough, C. C.; Sproules, S.; Doonan, C. J.; Hagen, K. S.; Weyhermuller, T.; Wieghardt, K. *Inorg. Chem.* **2012**, *51*, 6969.
(13) Scarborough, C. C.; Sproules, S.; Weyhermu, T.; Debeer, S.; Wieghardt, K. *Inorg. Chem.* **2011**, *50*, 12446.
(14) Saito, Y.; Takemoto, J.; Hutchinson, B.; Nakamoto, K. *Inorg. Chem.* **1972**, *11*, 2003.
(15) Isaacs, M.; Sykes, A. G.; Ronco, S. *Inorganica Chim. Acta* **2006**, *359*, 3847.
(16) Gao, B.; Luo, X.; Gao, W.; Huang, L.; Gao, S.; Liu, X.; Wu, Q.; Mu, Y. *Dalton Trans.* **2012**, *41*, 2755.
(17) McDaniel, A. M.; Tseng, H. W.; Damrauer, N. H.; Shores, M. P. *Inorg. Chem.* **2010**, *49*, 7981.
(18) Theopold, K. H. *Chem. Commun.* **2014**, *50*, 2.
(19) Pierpont, C. G. *Inorg. Chem.* **2001**, *40*, 5727.
(20) Pierpont, C. G.; Downs, H. H. *J. Am. Chem. Soc.* **1976**, *98*, 4834.
(21) Shiren, K.; Tanaka, K. *Inorg. Chem.* **2002**, *41*, 5912.
(22) Sofen, S.; Ware, D.; Cooper, S.; Raymond, K. *Inorg. Chem.* **1979**, *18*, 234.
(23) Chun, H.; Verani, C. N.; Chaudhuri, P.; Bothe, E.; Bill, E.; Weyhermuller, T.; Wieghardt, K. *Inorg. Chem.* **2001**, *40*, 4157.
(24) Zhou, W.; Patrick, B. O.; Smith, K. M. *Chem. Commun.* **2014**, *50*, 9958.
(25) Ranis, L. G.; Werellapatha, K.; Pietrini, N. J.; Bunker, B. A.; Brown, S. N. *Inorg. Chem.*

2014, *53*, 10203.
(26) Szigethy, G.; Shaffer, D. W.; Heyduk, A. F. *Inorg. Chem.* **2012**, *51*, 12606.
(27) Lu, F.; Zarkesh, R. A.; Heyduk, A. F. *Eur. J. Inorg. Chem.* **2012**, *2012*, 467.
(28) Zarkesh, R.; Ziller, J. W.; Heyduk, A. F. *Angew. Chem. Int. Ed. Engl.* **2008**, *47*, 4715.
(29) Szigethy, G.; Heyduk, A. *Dalt. Trans.* **2012**, *41*, 8144.
(30) Simpson, C.; Boone, S.; Pierpont, C. *Inorg. Chem.* **1989**, *28*, 4379.
(31) Speier, G.; Csihony, J.; Whalen, A.; Pierpont, C. *Inorg. Chem.* **1996**, *35*, 3519.
(32) Girgis, A.; Balch, A. *Inorg. Chem.* **1975**, *14*, 2724.
(33) Bruni, S.; Caneschi, A.; Cariati, F.; Delfs, C.; Dei, A.; Gatteschi, D. *J. Am. Chem. Soc.* **1994**, *116*, 1388.
(34) Larsen, S.; Pierpont, C. *J. Am. Chem. Soc.* **1988**, *110*, 1827.
(35) Chaudhuri, P.; Hess, M.; Hildenbrand, K.; Bill, E.; Weyhermüller, T.; Wieghardt, K. *Inorg. Chem.* **1999**, *38*, 2781.
(36) Zarkesh, R. A.; Heyduk, A. F. *Organometallics* **2011**, *30*, 4890.
(37) Wong, J. L.; Sánchez, R. H.; Logan, J. G.; Zarkesh, R. A.; Ziller, J. W.; Heyduk, A. F. *Chem. Sci.* **2013**, *4*, 1906.
(38) Heyduk, A.; Zarkesh, R.; Nguyen, A. *Inorg. Chem.* **2011**, *50*, 9849.
(39) Wright, D. D.; Brown, S. N. *Inorg. Chem.* **2013**, *52*, 7831.
(40) Brown, S. N. *Inorg. Chem.* **2012**, *51*, 1251.
(41) Cordero, B.; Gómez, V.; Platero-Prats, A. E.; Revés, M.; Echeverría, J.; Cremades, E.; Barragán, F.; Alvarez, S. *Dalt. Trans.* **2008**, 2832.
(42) Adams, R. D.; Collins, D. E.; Cotton, F. A. *J. Am. Chem. Soc.* **1974**, *96*, 749.
(43) Cotton, F. A.; Daniels, L. M.; Murillo, C. A.; Pascual, I. *J. Am. Chem. Soc.* **1997**, *119*, 10223.
(44) Edema, J. J. H.; Gambarotta, S.; Meetsma, A.; Spek, A. L.; Smeets, W. J. J.; Chiang, M. Y. *J. Chem. Soc.* **1993**, 789.
(45) Haftbaradaran, F.; Mund, G.; Batchelor, R. J.; Britten, J. F.; Leznoff, D. B. *Dalton Trans.* **2005**, 2343.
(46) Irrgang, T.; Kempe, R. *Eur. J. Inorg. Chem.* **2005**, 4382.
(47) Jabri, A.; Temple, C.; Crewdson, P.; Gambarotta, S.; Korobkov, I.; Duchateau, R. *J. Am. Chem. Soc.* **2006**, *128*, 9238.
(48) McGuinness, D. S.; Brown, D. B.; Tooze, R. P.; Hess, F. M.; Dixon, J. T.; Slawin, A. M. Z. *Organometallics* **2006**, *25*, 3605.
(49) Ni, C.; Long, G. J.; Grandjean, F.; Power, P. P. *Inorg. Chem.* **2009**, *48*, 11594.
(50) Rozenel, S. S.; Chomitz, W. A.; Arnold, J. *Organometallics* **2009**, *28*, 6243.
(51) Sukcharoenphon, K.; Ju, T. D.; Abboud, K. A.; Hoff, C. D. *Inorg. Chem.* **2002**, *41*, 6769.
(52) Huang, Y. L.; Lu, D. Y.; Yu, H. C.; Yu, J. S. K.; Hsu, C. W.; Kuo, T. S.; Lee, G. H.; Wang, Y.; Tsai, Y. C. *Angew. Chemie - Int. Ed.* **2012**, *51*, 7781.
(53) Herwig, W.; Zeiss, H. *J. Am. Chem. Soc.* **1957**, *79*, 6561.
(54) Bennet, G. M.; Turner, E. E. *J. Chem. Soc.* **1914**, *105*, 1057.
(55) Evans, D. *J. Chem. Soc.* **1959**, 2003.
(56) Bain, G. A.; Berry, J. F. *J. Chem. Educ.* **2008**, *85*, 532.
(57) Schubert, E. M. *J. Chem. Educ.* **1992**, *69*, 62.
(58) Aranzaes, J. R.; Daniel, M.-C.; Astruc, D. *Can. J. Chem.* **2006**, *84*, 288.
(59) APEX2, Version 2014.11-0, Bruker AXS, Inc.; Madison, WI 2014.
(60) SAINT, Version 8.34a, Bruker AXS, Inc.; Madison, WI 2013.

(61) Sheldrick, G. M. SADABS, Version 2014/5, Bruker AXS Inc.; Madison, WI 2014.
(62) Sheldrick, G. M. SHELXTL, Version 2014/7, Bruker AXS Inc.; Madison, WI 2014.
(63) International Tables for Crystallography 1992, Vol C., Dordrecht: Kluwer Academic Publishers.

Chapter 5

Reactivity of Chromium Complexes of the Redox-Active ONO and DOPO Ligands

Introduction

Oxidation reactions mediated by high-valent chromium are well known and highly studied, most notably in their application to the stoichiometric and catalytic oxidation of alcohols.[1–10] The use of chromium complexes in oxygen-atom transfer reactivity has also been well studied, with olefin epoxidation[11–17] and sulfide oxidation[18–22] both afforded catalytically. While these approaches typically utilize an oxygen atom transfer reagent (i.e. iodosobenzene, mCPBA, H_2O_2, etc.), an alternative method for oxygen atom transfer could be envisioned using water as the O-atom source, with concomitant oxidation and deprotonation steps to afford intermediate in metal-hydroxo and metal-oxo moieties (though the oxidation steps may precede water coordination and deprotonation).[23–31] This latter alternative has been investigated with aqua complexes of Cr(III) and their deprotonation to hydroxo- complexes, yielding pK_a values of the coordinated water ranging from 4-9.[32–37] Further deprotonation reactions have been studied within the context of oxidation reactions, where stepwise oxidation and deprotonation steps yielded Cr(V)-oxo complexes.[32]

Recently Tanaka and coworkers set out to determine the impact that a redox-active catecholate ligand might have on the properties of a chromium(III) aqua ligand (Scheme 5.1).[34] Their approach yielded Cr(III)–hydroxo complexes upon single deprotonation, however, complete deprotonation to yield a chromium–oxo species was not reported. Notably, under elevated pH conditions Cr(III)–hydroxo complexes bearing 3,5-di-*tert*-butylsemiquinone undergo a ligand-based reduction to generate a Cr(III)–aqua complex of 3,5-di-*tert*-butylcatecholate. With these results in mind, chromium(III) complexes of the redox-active ONO ligand have been prepared and used to pursue chromium-oxo species in an approach analogous to that reported by Tanaka.

Scheme 5.1. Reactivity of semiquinonate-chromium complexes reported by Tanaka et al.

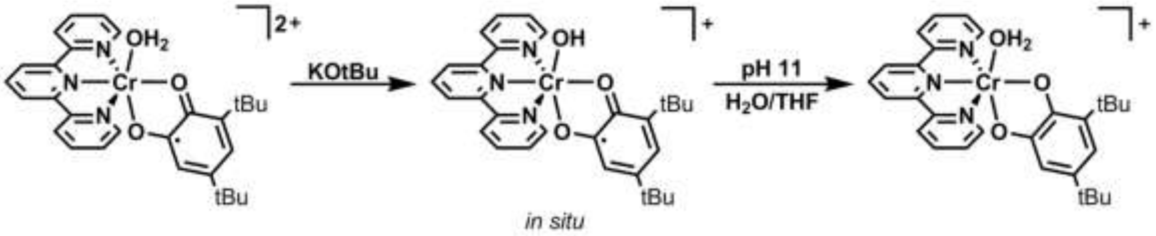

Results and Discussion

Triflate Complexes of (ONO)Cr

As an initial approach to enabling water coordination to the chromium center, abstraction of the chloride anion in $(ONO^{sq})CrCl(bipy)$ **(12**) and replacement for a weakly coordinating triflate group was pursued. This was attempted through the treatment of **12** with an equivalent of silver triflate (AgOTf) (Scheme 5.2). Upon addition of AgOTf to a THF solution of **12**, a color change from green to dark orange/brown was observed with the formation of a dark precipitate (Ag^0). Upon workup, UV-vis-NIR spectroscopy revealed a spectrum indicative of the $(ONO^{q})^{1-}$ form of the ligand (Figure 5.1), with NIR bands at 847 and 949 nm. These data and observations suggested that oxidation of **12** to $[(ONO^{q})CrCl(bipy)]OTf$ (**15**) had occurred instead of chloride abstraction. This was unequivocally proven when electrochemical analysis yielded a cyclic voltammogram with identical events to **12**, with the only difference being a one electron anodic shift in the bulk of the material. Evans method analysis confirmed the Cr(III) assignment of the metal center, yielding a μ_{eff} of 3.85 μB, consistent with the presence of an S=3/2 high spin Cr(III) center.

Scheme 5.2. Synthesis of complexes **15** and **16**.

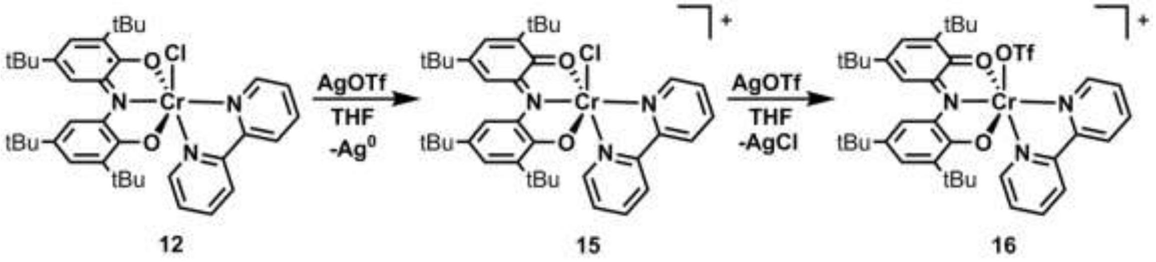

Although this step resulted in oxidation and the isolation of **15**, chloride abstraction from this complex could yield a bis-triflate complex, which could enable water as an oxygen atom source via water coordination and subsequent double deprotonation. To achieve this, **12** was treated sequentially with AgOTf (Scheme 5.2) to yield a dark yellow/brown solid. Analysis by UV-vis-NIR spectroscopy showed NIR bands at 847 and 948 nm, consistent with an $(ONO^{q})^{1-}$ ligand and essentially unshifted from **15**. Notable shifts between **15** and the new complex occur in the visible region, with the band at 537 nm present in the spectrum of **15** blue-shifting to a shoulder at *ca.* 525 nm. Furthermore, the intense band located at 466 nm in **15** is red shifted to 478 nm. Absolute confirmation of the abstraction of chloride was provided by solid state analysis of single crystals of the product, yielding the structure of $[(ONO^{q})Cr(bipy)OTf]OTf$ (**16**) in Figure 5.2.

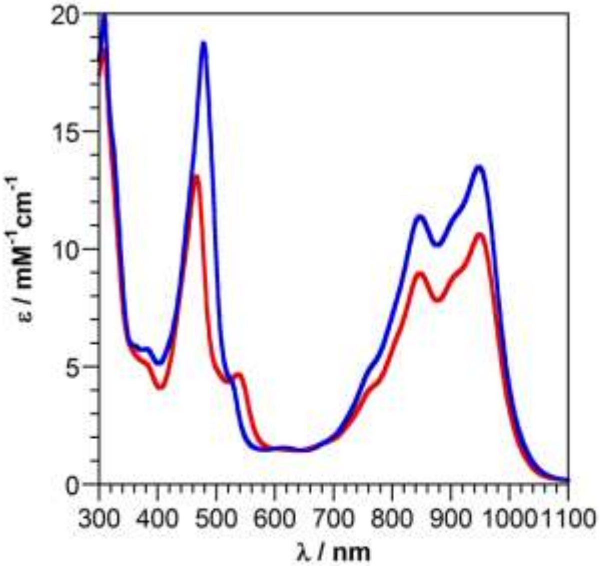

Figure 5.1. UV-vis NIR spectra of complexes **15** (**red**) and **16** (**blue**) recorded in THF.

Complex **16** adopts the expected pseudo-octahedral coordination geometry around the chromium center, with the most significant structural deviations occurring from the movement of the chromium center out of the ONO ligand binding pocket, giving an O(1)–Cr(1)–O(2) bond angle of 163.37(8)°. The bite angle of the bipy ligand also causes deviation from the ideal 90° angle in octahedral geometry, giving an N(2)–Cr(1)–N(3) bond angle of 79.36(9)°. Bond distances within the ONO ligand are consistent with its formulation as $(\text{ONO}^{\text{q}})^{1-}$, with contracted C–O and C–N bond lengths of 1.30 and 1.36 Å (avg.) and localized double-bond character in the aryl backbone (Table 5.1). The N(1)–Cr(1) bond distance of 2.011(2) Å is also common of (ONO^{q})Cr complexes, lengthening relative to bond distances observed in $(\text{ONO}^{\text{cat}})^{3-}$ and $(\text{ONO}^{\text{sq}})^{2-}$ complexes due to the diminished donor ability of the oxidized ONO ligand. Calculation of the MOS yields a value of −1.30, consistent with the $(\text{ONO}^{\text{q}})^{1-}$ assignment. Evans method analysis provided analogous results to **15**, yielding a μ_{eff} of 3.78 μB, indicative of a high spin S=3/2 Cr(III) metal center.

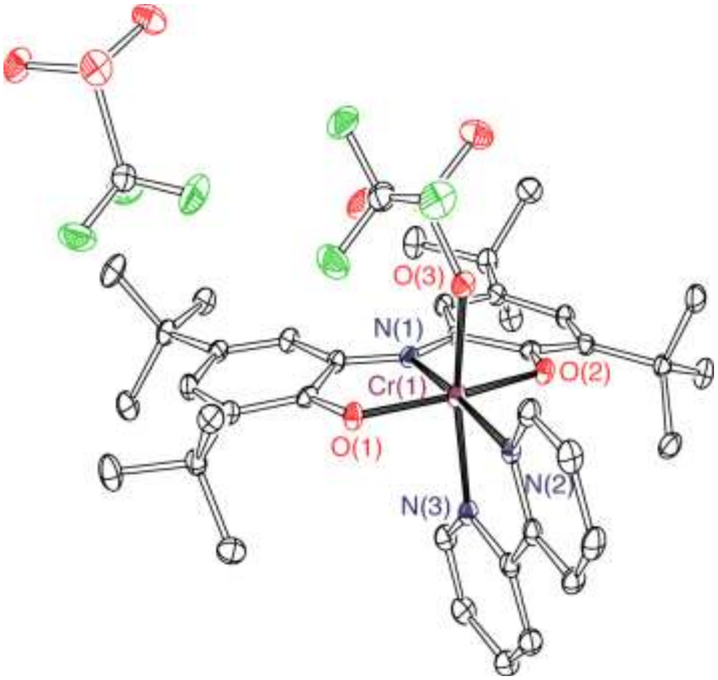

Figure 5.2. ORTEP diagram of [(ONO^q)Cr(bipy)OTf]OTf (**16**). Thermal ellipsoids are shown at 50% probability. Hydrogen atoms have been omitted for clarity.

Facile chemical reduction of **16** was achieved by treatment with decamethylferrocene (Cp_2*Fe) in a mixture of MeCN and toluene, resulting in an immediate color change from orange/brown to dark green. The isolated product displayed UV-vis-NIR bands indicative of the (ONO^{sq})$^{2-}$ ligand, with a broad NIR band at 1178 nm and a series of bands spanning the 400-700 nm visible region (Figure 5.4). Solid state analysis of (ONO^{sq})Cr(bipy)OTf (**17**) was performed on crystals grown from a solution of THF and pentane. The as-obtained single crystals show that a molecule of THF has coordinated to the metal center, displacing the triflate group, which is observed as an outer sphere anion. As expected, the metal center adopts a pseudo-octahedral coordination geometry, with the most significant deviations from an ideal octahedral geometry being the O(1)–Cr(1)–O(2) angle of 163.36(12)° and the N(2)–Cr(1)–N(3) angle of 79.07(15)° in the bipy chelate. Bond distances within the ONO ligand are indicative of the (ONO^{sq})$^{2-}$ assignment, with contracted C–O bond distances of 1.33 Å (avg.), though the C–N bonds (1.380 Å avg.) do not show significant contraction. The aryl backbone shows some degree of localized double bond character (Table 5.1), as observed in other $(ONO^{sq})^{2-}$ coordinated complexes. Application of Browns MOS calculation yields a value of −2.13, consistent with the assignment of the ligand as $(ONO^{sq})^{2-}$. Evans method analysis yields a μ_{eff} of 2.78 μB, indicating antiferromagnetic coupling between the $(ONO^{sq})^{2-}$ ligand-radical and a high-spin Cr(III) metal center, yielding an overall S=1 system.

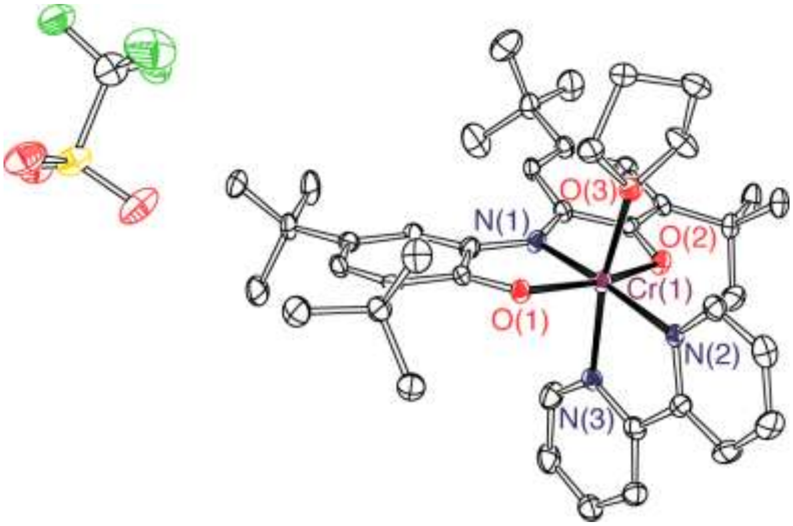

Figure 5.3. ORTEP diagram of $[(ONO^{sq})Cr(bipy)THF]OTf$ (**17-THF**). Thermal ellipsoids are shown at 50% probability. Hydrogen atoms have been omitted for clarity.

Table 5.1. Selected bond distances (Å) and angles (°) for **16** and **17-THF**.

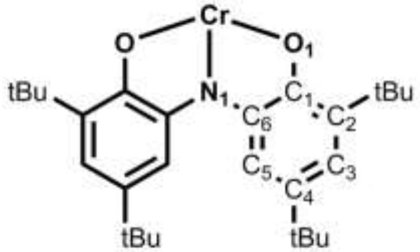

	[(ONO^{q})Cr(bipy)OTf]OTf **16**	[(ONO^{sq})Cr(bipy)THF]OTf **17-THF**
	Bond Lengths (Å)	
N(1)–Cr(1)	2.011(2)	1.922(3)
O(1)–Cr(1)	1.939(2)	1.945(3)
O(1)–C(1)	1.299(3)	1.322(5)
N(1)–C(6)	1.357(3)	1.368(5)
C(1)–C(2)	1.436(4)	1.422(6)
C(2)–C(3)	1.372(4)	1.382(6)
C(3)–C(4)	1.441(4)	1.412(6)
C(4)–C(5)	1.359(4)	1.377(6)
C(5)–C(6)	1.419(3)	1.410(6)
C(1)–C(6)	1.463(4)	1.434(6)
Cr(1)–O(3)	1.986(2)	2.027(3)
Cr(1)–N(2)	2.063(2)	2.082(3)
	Bond Angles (°)	
N(1)–Cr(1)–O(1)	81.65(9)	81.49(13)
N(1)–Cr(1)–O(3)	96.81(9)	93.98(15)
O(1)–Cr(1)–O(2)	163.37(8)	163.36(12)

Electrochemical characterization of **17** supports the formulation of the product as (ONO^{sq})Cr(bipy)OTf, with no coordinated MeCN. Dissolving the complex in MeCN and immediately collecting a voltammogram yields a reversible oxidation event at 0.10 V. However, within minutes a new event anodically shifted to 0.23 V is observed. This process proceeds until only the event at 0.23 V is present (Figure 5.4), while the reduction event shows no notable shift during this process, which is assigned as simple displacement of triflate with MeCN. This is also consistent with the anodic shift in the oxidation event since formation of a cationic species should yield a species more difficult to oxidize. The ligand-based oxidation event at 0.23 V is reversible, and further anodic scanning reveals an irreversible oxidation event near the edge of the solvent window at 1.35 V. Two semi-reversible reduction events are observed on cathodic scanning at −0.934 and −1.74 V, as is a daughter species at −1.39 V.

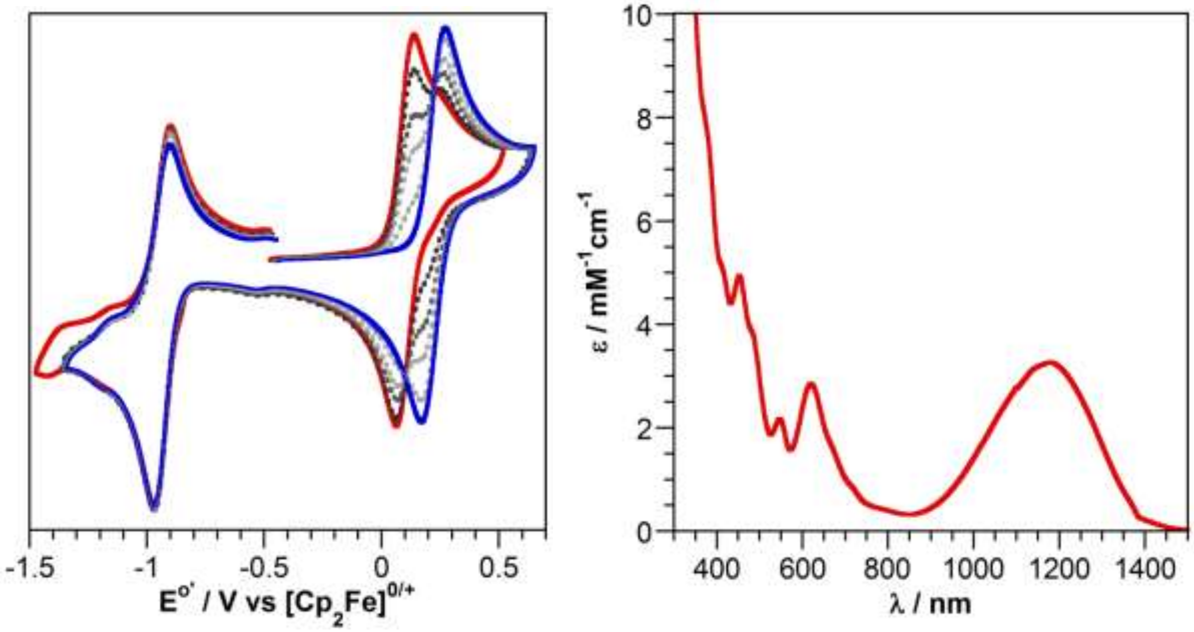

Figure 5.4. **Left**. Cyclic voltammogram of (ONO^{sq})Cr(bipy)OTf immediately upon dissolving (**red**) and monitored until complete conversion to putative [(ONO^{sq})Cr(bipy)MeCN]OTf (**blue**). Recorded in acetonitrile with 0.1 M TBAPF$_6$ at 1 mM analyte and scan rates of 200 mV/s. **Right**. UV-vis-NIR spectrum of (ONO^{sq})Cr(bipy)OTf recorded in toluene.

Reactivity of [(ONO^{q})Cr(bipy)OTf]OTf

In a method similar to that reported by Tanaka, water coordination to **16** and subsequent deprotonation was pursued as a route to generate chromium–oxo complexes. While single deprotonation is reasonable given the relative acidity of Cr(III)–aqua complexes, we reasoned that juxtaposition of an electron sink (the (ONO^{q})$^{1-}$ ligand) may allow electron transfer from the chromium center to the ligand and enable the second deprotonation. This second deprotonation step is less likely in classical octahedral coordination complexes of Cr(III), given the two-electron occupation of the metal π^* orbitals which would result. Indeed, no reports of observable Cr(III)–oxo complexes in an octahedral ligand field could be found.

Addition of excess water and pyridine to an MeCN solution of [(ONO^{q})Cr(bipy)OTf]OTf (**16**) resulted in a color change from dark brown to green. The isolated product yielded a UV-vis-NIR spectrum indicative of the (ONO^{sq})$^{2-}$ form of the ligand. Unexpectedly, this spectrum matched that of the pyridine adduct of **17**, [(ONO^{sq})Cr(bipy)(py)]OTf (**17-py**), which was confirmed by the *in situ* formation of **17-py** from **17** and pyridine (Figure 5.5). These results indicate that instead of installing an oxo group, complex **16** had been reduced by one electron to yield **17-py** (Scheme 5.3). This was further supported by mass spectrometry, which yielded a major set of isotope peaks at 709.69 m/z corresponding to the pyridine adduct [(ONO^{sq})Cr(bipy)(py)]$^{+}$. This reduction is notably similar to that observed by Tanaka et al. where a semiquinonate supported Cr(III)–hydroxo species was reduced to a catecholate bound Cr(III)–aqua.[34]

Scheme 5.3. Reactivity of [(ONO^{q})Cr(bipy)OTf]OTf with water and pyridine.

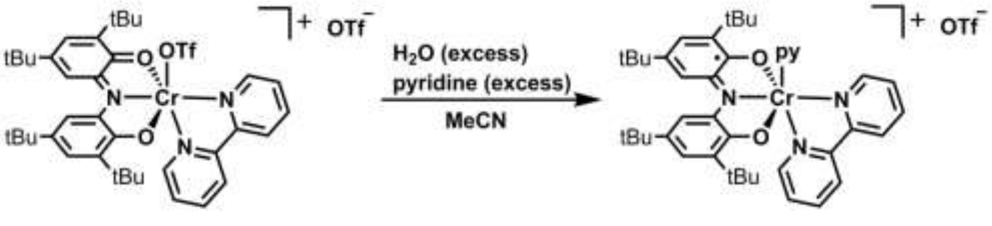

16 **17-py**

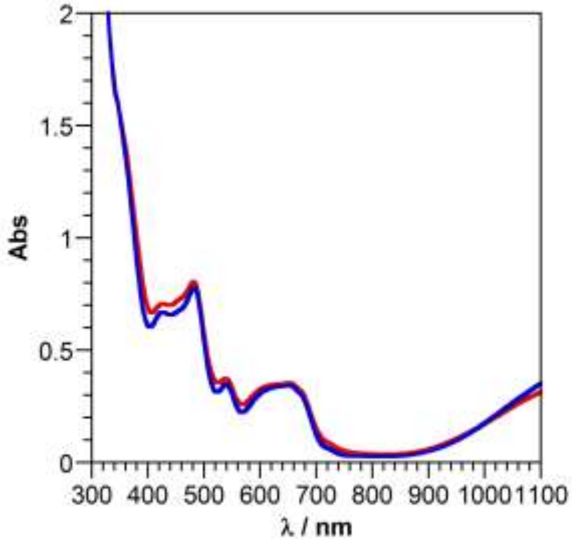

Figure 5.5. UV-vis-NIR spectra of the reaction product of **16** with water and pyridine (**red**) and **17** with pyridine added to the sample (**blue**). Both spectra recorded in MeCN.

Reasoning that a reactive oxo intermediate might be present through the course of the reaction, as outlined in Scheme 5.4, the treatment of [(ONO^q)Cr(bipy)OTf]OTf (**16**) with water and pyridine was performed in the presence of the oxygen-atom acceptor thioanisole. Monitoring the reaction in CD_3CN confirmed the formation of the oxidized product methyl phenyl sulfoxide. However, performing the reaction with an internal standard showed that the yield of the oxidized product was only 6% (considering a theoretical 2:1 stoichiometry, as per Scheme 5.4). Moreover, the ligand-oxidation by-product 2,4,6,8-tetra-*tert*-butyl-1-phenoxazinone was observed in the reaction mixture, indicating instability of the ONO ligand towards oxidation and providing one viable explanation as to the source of the reducing equivalents needed to generate **17**.

Scheme 5.4. Proposed and observed reactivity of **16** upon treatment with H_2O and pyridine. The substrate utilized as the oxygen-atom acceptor, thioanisole, is abbreviated as S.

Proposed Reaction Pathway

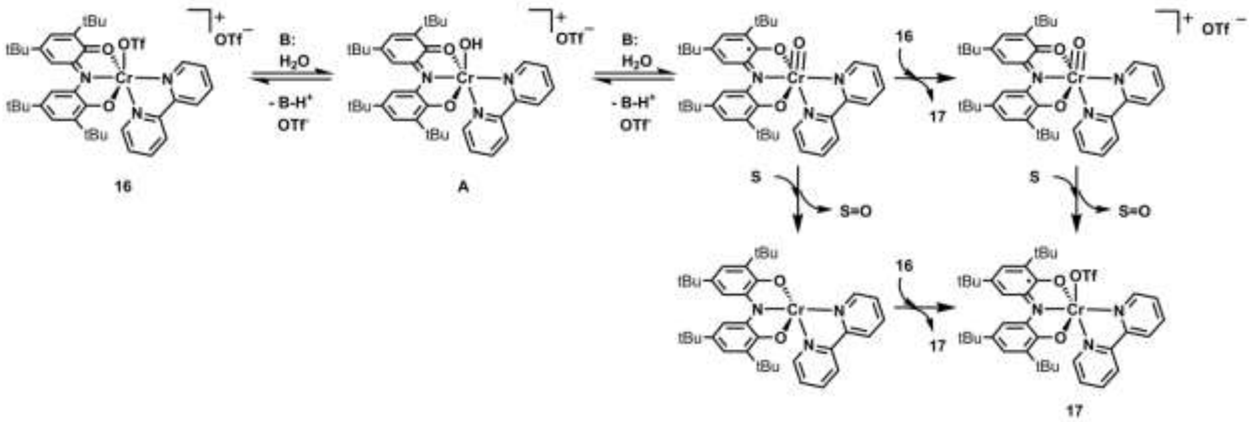

Observed Reactivity

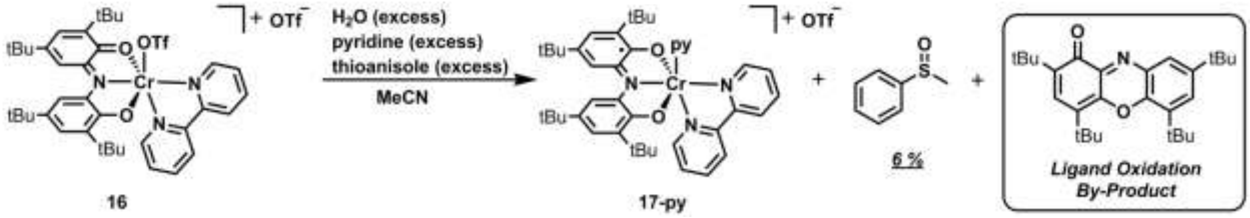

In an attempt to observe reaction intermediates from the proposed reaction pathway, a UV-vis-NIR scale solution of [(ONO^q)Cr(bipy)OTf]OTf (**16**) was treated with water and 2,6-

lutidine (Scheme 5.5). A drastic spectral change was noted upon this reaction: the visible region band at 478 nm is blue shifted to 458 nm and a smaller band at 538 nm appeared (Figure 5.6, Left). The spectral features at 458 and 538 nm, which have demonstrated sensitivity to the nature of the anionic donor group, are strikingly similar to those of **15**, [(ONO^{q})CrCl(bipy)]OTf. The similarity of these spectral bands suggested the installation of a new X-type donor group, which led to the proposal that this species corresponded to intermediate **A**, [(ONO^{q})Cr(OH)(bipy)]OTf. This is also consistent with the relative ease of deprotonation of other Cr(III)–aqua complexes. With the hypothesis that this proposed species is in equilibrium with **16**, acid additions were performed to favor formation of **16** and provide further evidence for the assignment of **A**. Stepwise additions of triflic acid (HOTf) solutions to the sample resulted in the reappearance of the spectral bands associated with **16** (Figure 5.6, Right), though a small portion of the sample remained as an unidentified (ONO^{sq})$^{2-}$ coordinated complex (based on the increased absorbance at 1100 nm, likely corresponding to (ONO^{sq})Cr(bipy)OTf). These data are consistent with single deprotonation of a chromium–aqua complex "[(ONO^{q})Cr(H$_2$O)(bipy)] 2OTf", yielding the intermediate [(ONO^{q})Cr(OH)(bipy)]OTf which does not appear to undergo facile deprotonation to yield (ONO^{sq})CrO(bipy). Instead, the majority of [(ONO^{q})Cr(OH)(bipy)]OTf is reduced to (ONO^{sq})Cr(bipy)OTf through an unknown mechanism.

Scheme 5.5. Proposed reaction intermediates formed on treatment of **16** with water and 2,6-lutidine (abbreviated B).

Potential Reaction Intermediates

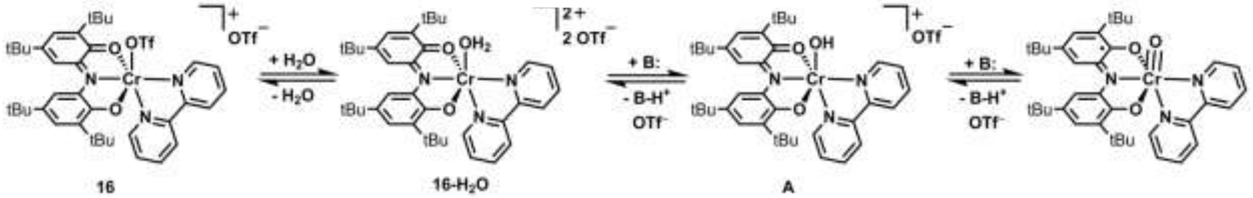

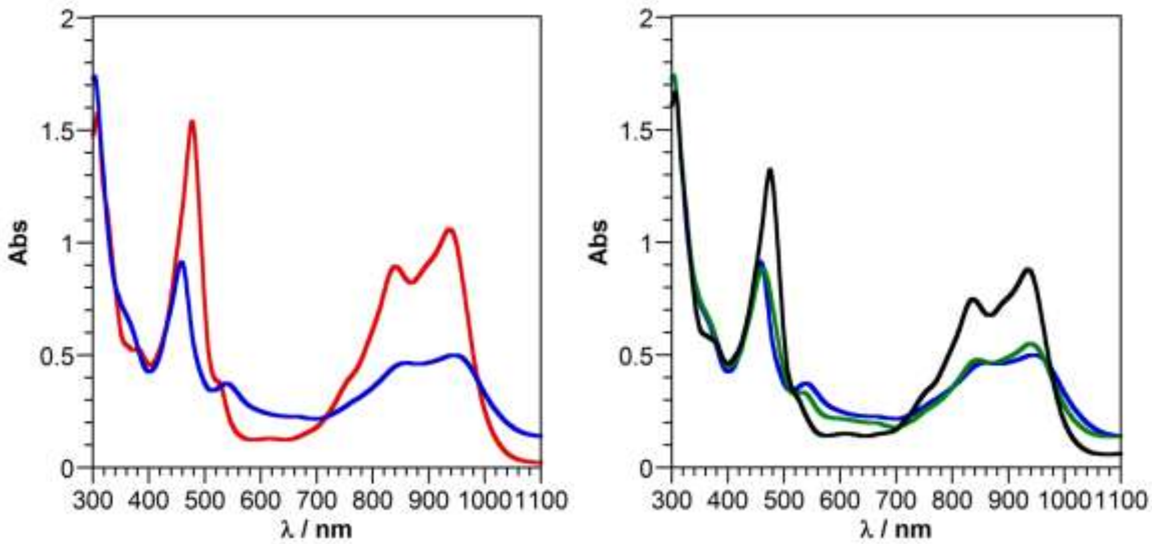

Figure 5.6. **Left**. UV-vis-NIR spectrum of **16** (**red**) and the putative intermediate [(ONO^q)Cr(OH)(bipy)]OTf (**blue**) formed upon treatment of **16** with H_2O and 100 equiv. 2,6-lutidine. **Right**. The *in situ* formed putative intermediate [(ONO^q)Cr(OH)(bipy)]OTf (**blue**) and the subsequent reaction mixtures formed upon treatment with 100 equiv. HOTf (**green**) and subsequent treatment with an additional 100 equiv. HOTf (**black**).

To further test the assertion that the observed intermediate is [(ONO^q)Cr(OH)(bipy)]OTf, a result of single deprotonation of coordinated water, the above reaction was performed with adamantyl alcohol in the place of water. Analogously to the results with water, treating an MeCN solution of [(ONO^q)Cr(bipy)OTf]OTf (**16**) with excess adamantyl alcohol and 2,6-lutidine resulted in a blue shift of the intense visible region band from 478 to 466 nm concurrent with the appearance of a smaller band at 529 nm (Figure 5.7). The spectroscopic changes observed upon the putative formation of [(ONO^q)Cr(OAd)(bipy)]OTf mirror those observed upon putative formation of [(ONO^q)Cr(OH)(bipy)]OTf, supporting the assignment of the hydroxide species upon single deprotonation.

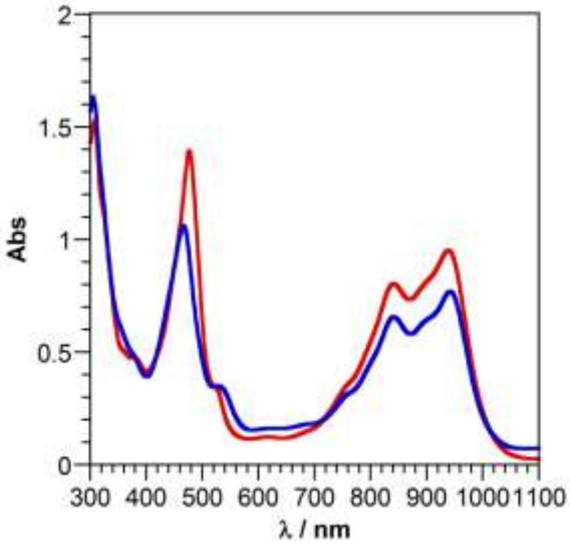

Figure 5.7. UV-vis-NIR spectrum of the putative intermediate [(ONO^q)Cr(OAd)(bipy)]OTf (**blue**) observed upon treatment of [(ONO^q)Cr(bipy)OTf]OTf (**red**) with 1000 equiv. of adamantyl alcohol and 100 equiv. of 2,6-lutidine.

Replacement of ONO for DOPO

Upon observing the oxidized, ring-cyclized by-product oxazinone, a new ligand set was targeted that could avoid this ligand-oxidation route. A structurally similar analogue to the ONO ligand which already features an oxygen-linked aryl backbone has been reported.[38–40] This ligand, 2,4,6,8-tetra-*tert*-butyl-1,9-dioxophenoxazinate (DOPO), has demonstrated similar redox-activity to the parent ONO ligand. Drawing on the similarities to ONO, the reported ligand precursor (DOPO^q)H[39,40] was converted to (DOPO^q)K through simple treatment with KH, providing the analogue to the commonly used precursor (ONO^q)K. This product yielded shifted ^{1}H-NMR resonances from the proteo version and revealed a broad near-IR band centered at 735 nm. Addition of one equivalent of this reagent to a slurry of $CrCl_2$(bipy) yielded a maroon product with a broad, red-shifted near-IR band at 900 nm (Figure 5.9). Mass spectroscopic analysis yielded a m/z isotope pattern at 680.17, consistent with the desired product (DOPO^{sq})CrCl(bipy) (**18**).

Scheme 5.6. Synthetic approaches to complexes **18-20**.

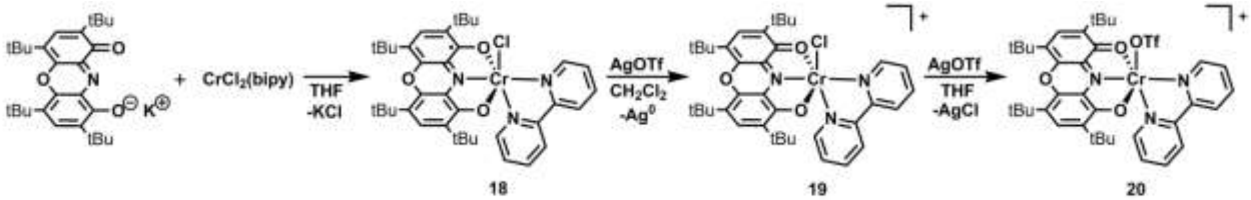

Structural characterization of **18** revealed a coordination environment analogous to that of $(ONO^{sq})CrCl(bipy)$ (**12**), with meridional coordination of the DOPO ligand and bidentate binding of the bipy group, with chloride occupying the final coordination site (Figure 5.8). The N(1)–Cr(1) bond length of 1.867(3) Å is shorter than the 1.9263(15) Å length observed in the ONO congener **12**, though unexpectedly, the O(1)–Cr(1)–O(2) bond angle of 158.24(9)° is smaller than the 163.56(6)° angle observed in **12**. The decreased N(1)–Cr(1) bond length would be expected to increase the O(1)–Cr(1)–O(2) angle as the metal center moves into the ligand binding pocket, however, the less rigid backbone of the ONO ligand allows the aryl–O groups to bend forward about the C(6)–N(1)–C(20) bonds around the central amide (angle of 130.49(15)° in **12**) to increase linearity of the O(1)–Cr(1)–O(2) bond angle while, consequently, decreasing the O–Cr(1) bond distance (1.9413(14) and 1.9428(13) Å for O(1) and O(2) in **12**, respectively). Though closer to the central nitrogen in **18**, the chromium center has longer O–Cr(1) bonds (2.006(2) and 2.035(2) Å) than **12** because the aryl-O groups are locked in place by the aryl linkage at O(3) within DOPO, which holds the C(6)–N(1)–C(20) bond angle in place at 119.9(3)°. These general structural features have also been noted between homoleptic $M(ONO)_2$ and $M(DOPO)_2$ complexes of the Group VI metals.[39] The ligand C–O bond distance of 1.34 Å (avg.) in **18** is shorter than those observed in $(DOPO^{cat})^{3-}$ complexes (*ca.* 1.37 Å).[39] Only one $(DOPO^{sq})^{2-}$ supported complex, $Sn(DOPO^{sq})_2$, has been reported in the literature, enabling limited direct bond-length comparison.[41] Within the solid state structure of $Sn(DOPO^{sq})_2$, C–O bond distances range from 1.335-1.346 Å, and localization of double-bond character in the aryl backbone is limited to a minimum distance of 1.392(4) Å. These structural features of Sn(DOPO^{sq})$_2$ are consistent with the (DOPO^{sq})$^{2-}$ assignment of the ligand in **18**. While the presence of the π-donating O(3) aryl linker appears to alter the intraligand bond features typically observed in ONO upon sequential oxidation, Brown et al. have applied the ONO MOS calculation to DOPO supported complexes.[39] This calculation, however, yielded higher values than expected, likely a result of the diminished bond localization resulting from the O(3) aryl linker. For complex **18** this calculation yields a value of −2.44, expectedly high, but consistent with the (DOPO^{sq})$^{2-}$ formulation. Evans method analysis yields a μ_{eff} of 2.75 μB, which is analogous to that obtained with the ONO analogue and consistent with the presence of a (DOPO^{sq})$^{2-}$ based radical antiferromagnetically coupled to a high-spin Cr(III) center.

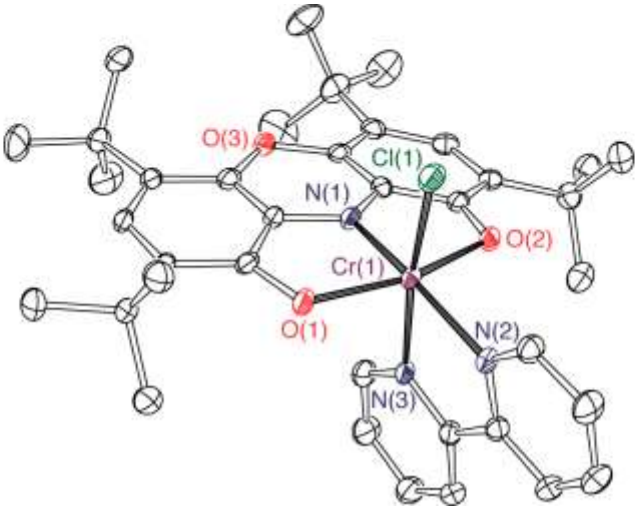

Figure 5.8. ORTEP diagram of (DOPO^{sq})CrCl(bipy) (**18**). Thermal ellipsoids are shown at 50% probability. Hydrogen atoms and three cocrystallized molecules of THF have been omitted for clarity.

Electrochemical characterization of **18** yielded general features that paralleled those observed in **12**, with a reversible oxidation event corresponding to the DOPO$^{sq/q}$ couple at 0.02 V and a semi-reversible reduction event corresponding, nominally, to the DOPO$^{sq/cat}$ couple at −1.59 V (reported as E_{pc} for direct comparison to **12**) (Figure 5.9). As with **12**, further cathodic scanning reveals reversible reductions at −1.90 and −2.64 V. The effect of DOPO substitution for

ONO cannot simply be described as cathodically or anodically shifting the ligand-based redox events; the oxidation event anodically shifts from −0.10 V to 0.02 V upon DOPO substitution for ONO while the reduction event is cathodically shifted from −1.43 to −1.59 V. In this case, substitution of DOPO serves to widen the resting potential of the complex, though, compared with the limited reports detailing the electrochemical behavior of DOPO, this does not appear to be a general trend.[39]

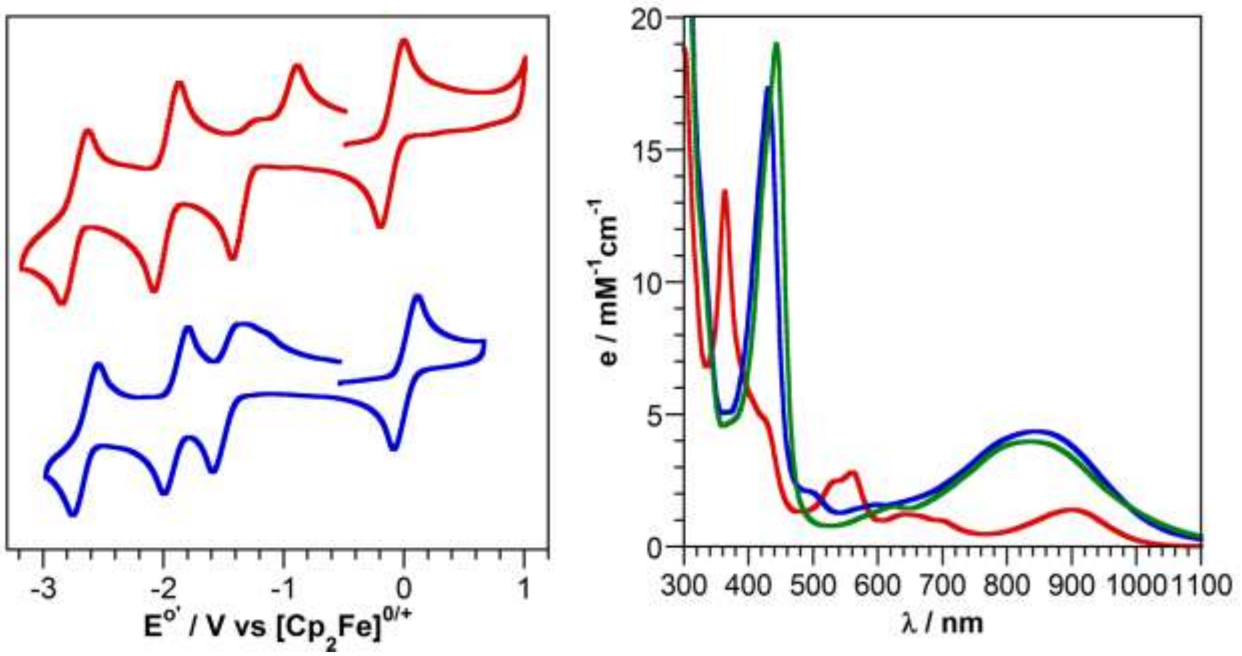

Figure 5.9. **Left**. Cyclic voltammograms of **18** (**blue**) and **12** (**red**) both recorded in THF with 0.1 M $TBAPF_6$ and 1 mM analyte at a scan rate of 200 mV/s. **Right**. UV-vis-NIR spectra of **18** (**red**), **19** (**blue**), and **20** (**green**) recorded in THF.

In a synthetic approach analogous to that used for the ONO analogue, oxidation of **18** with AgOTf yielded the putative cationic complex $[(DOPO^q)CrCl(bipy)]OTf$ (**19**) (Scheme 5.6). Notable shifts were observed by UV-vis-NIR spectroscopy (Figure 5.9), with the broad near-IR band appearing at 844 nm, a blue shift of only 56 nm relative to that of **17**, whereas this same set of complexes for the ONO congener yielded a shift of >200 nm. As with the ONO ligand, the intensity of the near-IR band shows a dramatic increase upon oxidation from the semiquinonate form to the quinonate form. A visible region band appears at 431 nm with a shoulder at 495 nm, similar to **17**. Evans method analysis yields a μ_{eff} of 3.70 μB, consistent with a high spin S=3/2 Cr(III) metal center.

Exchange of the chloride ligand in **19** for triflate was accomplished with AgOTf, resulting in a mild red shift of the visible region band from 431 to 443 nm and accompanied with a disappearance of the shoulder at 495 nm (Figure 5.9). These spectral changes are similar to those observed with the ONO variants, and is consistent with the formation of [(DOPO^q)Cr(bipy)OTf]OTf (**20**). This assignment was confirmed by single crystal X-ray diffraction analysis, which provided the structure in Figure 5.10.

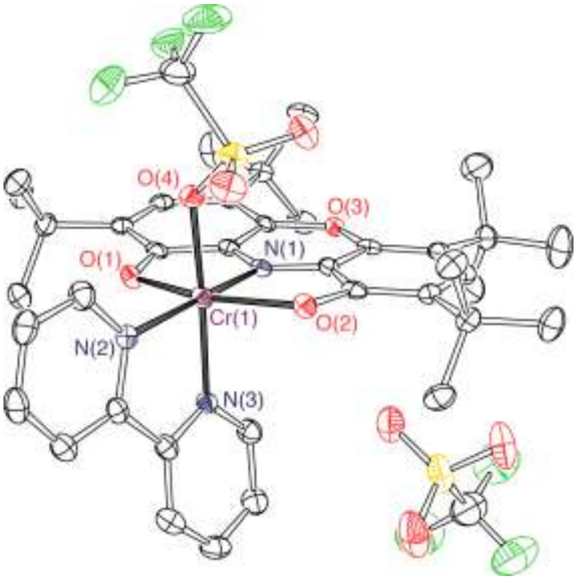

Figure 5.10. ORTEP diagram of [(DOPO^q)Cr(bipy)OTf]OTf (**20**). Thermal ellipsoids are shown at 50% probability. Hydrogen atoms have been omitted for clarity.

Table 5.2. Selected bond distances (Å) and angles (°) for **18** and **20**.

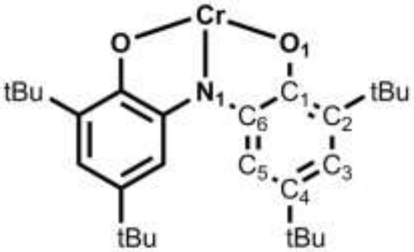

	(DOPO^{sq})CrCl(bipy) **18**	[(DOPO^{q})Cr(bipy)OTf]OTf **20**
	Bond Lengths (Å)	
N(1)–Cr(1)	1.867(3)	1.963(2)
O(1)–Cr(1)	2.006(2)	1.983(2)
O(2)–Cr(1)	2.035(2)	2.047(2)
O(1)–C(1)	1.333(4)	1.315(3)
N(1)–C(6)	1.357(4)	1.322(4)
C(1)–C(2)	1.406(4)	1.401(4)
C(2)–C(3)	1.400(5)	1.390(4)
C(3)–C(4)	1.411(5)	1.435(4)
C(4)–C(5)	1.396(5)	1.375(4)
C(5)–C(6)	1.399(4)	1.410(4)
C(1)–C(6)	1.407(5)	1.429(4)
O(3)–C(5)	1.404(4)	1.398(3)
Cr(1)–O(4)	-----	1.983(2)
Cr(1)–Cl(1)	2.3141(10)	-----
	Bond Angles (°)	
N(1)–Cr(1)–O(1)	79.46(11)	78.93(9)
N(1)–Cr(1)–O(4)	-----	91.78(9)
N(1)–Cr(1)–Cl(1)	95.41(9)	-----
O(1)–Cr(1)–O(2)	158.24(9)	156.03(8)
C(6)–N(1)–C(20)	119.9(3)	122.7(2)

As with [(ONO^{q})Cr(bipy)OTf]OTf (**16**), in complex **20** the ligand environment around the chromium center allows for coordination of a single triflate group and forces the second triflate to remain as a non-coordinating anion. The ligand-centered nature of the oxidation from **18** to **20** is evidenced by the contraction of the C–O bonds lengths, which average 1.34 Å in **18** and 1.31 Å in **20**, and by the contraction of the C–N bonds which average 1.36 Å in **18** and 1.32

Å in **20**. The C–O bond lengths in **20** are, however, slightly longer than other reported C–O bond lengths in $(DOPO^{q})^{1-}$ which range from 1.266(2)-1.296(5) Å.[38] Localized double bond character within the aryl backbone is apparent, but is less pronounced than observed in the $(ONO^{q})^{1-}$ ligand of **16**. Moreover, the decreased charge on the ligand in **20** results in increased bond lengths from the chromium center to donor groups on the ligand, a consequence of the decreased donor ability of monoanionic $(DOPO^{q})^{1-}$ relative to dianionic $(DOPO^{sq})^{2-}$. Evans method yielded a μ_{eff} of 3.62 μB, consistent with a high spin S=3/2, Cr(III) assignment of the metal center.

With the new DOPO complex **20** in hand, identical reaction conditions to those used for **16** were used to interrogate its ability to affect oxygen-atom transfer to thioanisole. Treating a CD_3CN solution of **20** with water, pyridine, thioanisole, and an internal standard resulted in a green to dull maroon color change and the appearance of methyl phenylsulfoxide. The yield of methyl phenylsulfoxide increased to 15%, a small improvement compared to that of **16**, but indicating that the oxidative instability of ONO is not the primary culprit in the low-yielding reaction. The UV-vis-NIR spectrum of the reaction mixture is consistent with the formation of a $(DOPO^{sq})^{2-}$ containing complex, likely the pyridine adduct $[(DOPO^{sq})Cr(bipy)(py)]OTf$, as was observed in the ONO variant. Though not independently synthesized for spectroscopic comparison, mass spectroscopy indicated $[(DOPO^{sq})Cr(bipy)(py)]OTf$ as the dominant product with a set of isotopic peaks at m/z 723.57, which matches the expected mass for $[(DOPO)Cr(bipy)(py)]^{+}$.

Summary and Conclusions

The chromium complex $(ONO^{sq})CrCl(bipy)$ reported in Chapter 4 was used to prepare highly oxidized chromium complexes of the ONO ligand. Treatment with AgOTf results in oxidation to yield $[(ONO^{q})CrCl(bipy)]OTf$, which can undergo chloride abstraction with AgOTf to generate [(ONO^{q})Cr(bipy)OTf]OTf. These complexes show similar electronic absorption spectra indicative of the (ONO^{q})$^{1-}$ form of the ligand, though the absorption bands in the 460-540 nm region demonstrate a marked dependence on the identity of the anionic donor group, making this region of the spectrum a useful indicator for ligand exchange in (ONO^{q})Cr complexes. Facile reduction of [(ONO^{q})Cr(bipy)OTf]OTf is achieved with decamethylferrocene to yield (ONO^{sq})Cr(bipy)OTf. The ligand based-nature of the reduction is observed in the UV-vis-NIR spectra of the complexes and also in their solid state structures. The Cr(III) oxidation state is maintained throughout the series of complexes, as observed in the chromium complexes described in Chapter 4.

Attempts at using [(ONO^{q})Cr(bipy)OTf]OTf to access chromium–oxo species through deprotonation of intermediate aqua complexes yielded, instead, the product of a simple reduction, [(ONO^{sq})Cr(bipy)(py)]OTf. While the nature of this reduction process is not known, the intermediacy of the hydroxo- complex [(ONO^{q})Cr(OH)(bipy)]OTf is supported by UV-vis-NIR spectroscopy, and the ability of the system to achieve low yields of thioanisole to methyl phenyl sulfoxide oxidation suggests the putative oxo intermediate may form in small amounts.

Homologous complexes to those described for ONO were prepared with the related DOPO ligand in an attempt to avoid deleterious oxidation of the ONO ligand. The DOPO complex (DOPO^{sq})CrCl(bipy) was prepared and used to access [(DOPO^{q})CrCl(bipy)]OTf and [(DOPO^{q})Cr(bipy)OTf]OTf in the same manner as the ONO variants. These complexes similarly showed a dependence of the near-IR features of the electronic absorbance spectrum on ligand oxidation state, but show significant overlap and are not as distinct as the spectral differences in the ONO ligand. The DOPO complexes show similar electrochemical behavior to their ONO counterpart, though they demonstrate non-negligible shifts in redox potential. When

[(DOPO^q)Cr(bipy)OTf]OTf is subjected to the same conditions of water, pyridine, and thioanisole used with [(ONO^q)Cr(bipy)OTf]OTf, an improvement in the yield of methyl phenyl sulfoxide from 6 to 15% occurs, indicating that the oxidation of ONO is only a minor contributing factor in the low yield.

Experimental

General Considerations. Manipulations were performed using standard Schlenk line techniques or in a N_2 filled glovebox. Diethyl ether, pentane, benzene, toluene, and tetrahydrofuran were sparged with argon and then dried and deoxygenated by passage through activated alumina and Q5 columns, respectively. Silver trifluoromethanesulfonate (AgOTF) was dried under high vacuum prior to use. (DOPO^q)H was synthesized according to literature procedures.[39,40]

Physical Methods. Solution UV-vis-NIR spectra were recorded in 1-cm path-length cuvettes on a Shimadzu UV-1700 spectrophotometer. Extinction coefficients were determined from Beer-Lambert Law plots. Solution magnetic moments (μ_{eff}) were determined using Evans Method.[42–44] Electrospray ionization mass spectrometry (ESI-MS) data were collected on a Waters LCT Premier mass spectrometer. Elemental analyses were collected on a Perkin-Elmer 2400 Series II CHNS/O analyzer.

Electrochemical Methods. Electrochemical measurements were recorded with a Gamry G300 potentiostat using a standard three-electrode configuration including a 3.0 mm glassy carbon working electrode, a platinum wire auxiliary electrode, and a silver wire pseudo-reference electrode. All measurements were made on solutions that contained 1 mM analyte and 0.1 M NBu_4PF_6 in THF at an ambient temperature of ca. 21 °C in a glovebox under a N_2 atmosphere. Potentials were referenced to $Cp_2Fe^{+/0}$ using an internal standard of ferrocene or decamethylferrocene ($E°' = -0.440$ V vs $Cp_2Fe^{+/0}$ in THF, -0.510 V vs $Cp_2Fe^{+/0}$ in MeCN).[45]

Crystallographic Methods. X-ray diffraction data were collected on single crystals mounted on a glass fiber using a Bruker SMART APEX II diffractometer. Measurements were carried out using Mo Kα (λ = 0.71073 Å) radiation, wavelength selected with a single-crystal graphite monochromator. A full sphere of data was collected for each crystal structure. The APEX[46] program package was used to determine the unit cell parameters and for data collection. The raw frame data was processed using SAINT[47] and SADABS[48] to yield the reflection data files. Subsequent calculations were carried out using the SHELXTL[49] program. The structures were solved by direct methods and refined on F^2 by full matrix least-squares techniques. The analytical scattering factors[50] for neutral atoms were used throughout the analysis. Hydrogen atoms were included using a riding model. ORTEP diagrams were generated using ORTEP-3 for Windows.

Table 5.3. Data collection and refinement parameters for **16**, **17**, **18**, and **20**.

	16	**17**	**18**	**20**
Empirical Formula	$C_{40}H_{48}F_6N_3O_8S_2Cr$	$C_{54}H_{72}CrF_3N_3O_7S$	$C_{50}H_{70}ClCrN_3O_6$	$C_{40}H_{46}CrF_6N_3O_9S_2$
Formula Weight	928.93	1016.20	896.54	942.92
Crystal System	Monoclinic	Monoclinic	Monoclinic	Monoclinic
Space Group	*Pn*	$P2_1$	$P2_1/c$	$C2/c$
a (Å)	10.0683(6)	12.7887(7)	14.3425(7)	39.600(3)
b (Å)	10.8726(6)	10.1653(6)	35.1736(17)	9.9395(7)
c (Å)	20.1507(12)	20.8675(12)	10.2027(5)	26.2705(18)
α (°)	90	90	90	90
β (°)	99.5904(7)	104.5022(8)	109.6868(7)	120.7569(8)
γ (°)	90	90	90	90
Volume (Å^3)	2175.0(2)	2626.4(3)	4846.2(4)	8885.8(11)
Z	2	2	4	8
F(000)	966	1080	1920	3912
Rflns. collected	16335	29153	53580	51654
Ind. rflns. (R_{int})	9772 (0.0181)	10717 (0.0564)	9908 (0.0808)	10859 (0.0909)
GOF	1.086	1.014	1.033	1.008
R1 [I > 2σ(I)][a]	0.0297	0.0503	0.0633	0.0588
wR2 (all data)[a]	0.0653	0.1107	0.1765	0.1419

[a] $R1 = \Sigma||F_o|-|F_c|| / \Sigma|F_o|$; $wR2 = [\Sigma[w(F_o^2-F_c^2)^2] / \Sigma[w(F_o^2)^2]\ ]^{1/2}$; $GOF= S = [\Sigma[w(F_o^2-F_c^2)^2] / (n-p)]^{1/2}$

[(ONO^{q})CrCl(bipy)]OTf (15). A vial was charged with (ONO^{sq})CrCl(bipy) (0.092 g, 0.138 mmol) which was dissolved in 10 mL of THF. A 4 mL THF solution of AgOTf (0.035 g, 0.136 mmol) was added dropwise to the solution of (ONO^{sq})CrCl(bipy). After stirring for 1 hour the reaction was filtered, concentrated to 3 mL under vacuum, and layered with 15 mL of pentane. After diffusion of the layers the product was collected as dark rust/orange solids (0.075 g, 68%). Anal. Calcd. for $C_{39}H_{48}N_3O_5F_3SClCr$: C, 57.45; H, 5.93; N, 5.15. Found: C, 56.70; H, 5.77; N, 5.20. UV-vis-NIR (THF) λ_{max}/nm (ε/M^{-1} cm^{-1}): 308 (18200), 466 (13100), 537 (4670), 847 (8980), 949 (10600).

[(ONO^q)Cr(bipy)OTf]OTf (16). A vial was charged with (ONO^{sq})CrCl(bipy) (0.127 g, 0.191 mmol) which was dissolved in 8 mL of THF. A 2 mL THF solution of AgOTf (0.049 g, 0.191 mmol) was added dropwise to the solution of (ONO^{sq})CrCl(bipy). After stirring for 2 hours the reaction was filtered and another batch of AgOTf (0.049 g, 0.191 mmol) was added. After stirring overnight the reaction was filtered and dried. The crude material was redissolved in 4 mL of THF, allowed to sit for 3 hours, and then filtered and dried under vacuum. The material was recrystallized by layering a THF solution with pentane and allowing diffusion of the layers. The material obtained was rinsed with 3 mL of Et_2O, then redissolved in 4 mL of MeCN, allowed to sit for 3 hours, then filtered and dried under vacuum. The material was again dissolved in 4 mL of MeCN and allowed to sit overnight. The solution was then filtered and dried under vacuum. Precipitation of AgCl was typically complete at this point. The product was obtained as a dark brown/yellow solid (0.165 g, 93%). Anal. Calcd. for $C_{40}H_{48}N_3O_8F_6S_2Cr$: C, 51.72; H, 5.21; N, 4.52. Found: C, 51.66; H, 4.91; N, 4.32. UV-vis-NIR (THF) λ_{max}/nm (ε/M^{-1} cm^{-1}): 309 (18600), 478 (18200), 847 (11000), 948 (13200).

(ONO^{sq})Cr(bipy)OTf (17). A vial was charged with [(ONO^q)Cr(bipy)OTf]OTf (0.096 g, 0.103 mmol) which was dissolved in 4 mL of MeCN. An 8 mL toluene solution of Cp_2*Fe (0.044 g, 0.135 mmol) was added dropwise to the solution of [(ONO^q)Cr(bipy)OTf]OTf. After stirring for 30 minutes the reaction was dried under vacuum. The solids were extracted with toluene, filtered, and dried under vacuum. The green solid was washed multiple times with pentane to remove unreacted Cp_2^*Fe. The remaining green solid was dried under vacuum, yielding the product in quantitative yield. Anal. Calcd. for $C_{39}H_{48}N_3O_5F_3SCr$: C, 60.06; H, 6.20; N, 5.39. Found: C, 60.31; H, 6.12; N, 5.11. UV-vis-NIR (toluene) λ_{max}/nm (ε/M^{-1} cm^{-1}): 453 (5060), 482 (shoulder) (3970), 547 (2180), 620 (2850), 1178 (3350).

[(ONO^q)Cr(bipy)OTf]OTf mediated oxidation of thioanisole. A vial was charged with [(ONO^q)Cr(bipy)OTf]OTf (0.020 g, 0.022 mmol) and dissolved in 0.5 mL of CD_3CN. An internal standard of bromomesitylene (0.13 M in C_6D_6, 10 µL, 0.001 mmol), pyridine (15 µL, 0.186 mmol), and thioanisole (25 µL, 0.213 mmol) were added and the mixture was transferred to a J. Young NMR tube. In a glovebox, degassed D_2O (4 µL, 0.245 mmol) was added under a nitrogen atmosphere and the J. Young NMR tube was sealed. After sitting overnight ^{1}H-NMR analysis showed a 6% yield of methyl phenyl sulfoxide.

[(ONO^q)Cr(bipy)OTf]OTf conversion to [(ONO^q)Cr(OH)(bipy)]OTf. A 2.5 mL solution of **16** in MeCN (8.60 x10^{-5} M) was added to a UV-vis cell. Another cell was filled as a reference, to which was added 50 µL of MeCN. To the solution of **16** was added 2.5 µL of 2,6-lutidine (100 equiv.) and then 50 µL of H_2O. Conversion to the observed intermediate occurred within minutes. A trifluoromethanesulfonic acid solution (2 M in H_2O) was prepared by diluting 0.300 g of the acid in 1 mL of H_2O. To the solution of intermediate **A** was added 10.7 µL (100 equiv.) of the 2M acid solution. This was followed by stepwise 5 µL additions.

[(ONO^q)Cr(bipy)OTf]OTf conversion to [(ONO^q)Cr(OAd)(bipy)]OTf. A 2.5 mL solution of **16** in MeCN (8.6 x10^{-5} M) was added to a UV-vis cell as a reference. A vial was charged with adamantanol (0.066 g, 0.434 mmol, 1000 equiv.) and 5 mL of the stock solution of **16** was added to the adamantanol. A UV-vis cell was filled with 2.5 mL of this mixture, to which was then added 2.5 µL of 2,6-lutidine.

(DOPO^q)K. A vial was charged with KH (0.033 g, 0.823 mmol) and 2 mL of THF. A 13 mL THF solution of (DOPO^q)H (0.355 g, 0.811 mmol) was added to the slurry of KH. After stirring overnight the reaction was dried under vacuum. The residue was dissolved in toluene, filtered, and dried under vacuum. The blue solid was redissolved in toluene and dried again. The material was slurried in 4 mL of pentane and chilled in a freezer at −35 °C. The precipitated solids were collected, washed with 1 mL of cold pentane and dried to yield the product as a dark purple solid (0.360 g, 93%). ^{1}H-NMR (400 MHz, $CDCl_3$) δ/ppm: 7.40 (s, 2H, aryl-H), 1.46 (s, 18H, tBu), 1.30 (s, 18H, tBu). UV-vis-NIR (THF) λ_{max}/nm (ε/M^{-1} cm^{-1}): 380 (11900), 676 (sh.) (10800), 735 (13700), 790 (sh.) (10900).

($DOPO^{sq}$)CrCl(bipy) (18). A vial was charged with $CrCl_2$(bipy) (0.160 g, 0.559 mmol) to which was added 5 mL of THF. This slurry was stirred vigorously and a 10 mL THF solution of ($DOPO^q$)K (0.251 g, 0.528 mmol) was added dropwise to the slurry of $CrCl_2$(bipy). After stirring overnight the reaction was filtered and the filter cake washed with 10 mL of THF. The filtrate was dried under vacuum and the resulting solids were stirred in 10 mL of toluene. The mixture was filtered and the solid filtrand washed with 1 mL of Et_2O and 10 mL of pentane. The solid was dried under vacuum to yield the product as a dull maroon/brown solid (0.301 g, 84%). UV-vis-NIR (THF) λ_{max}/nm (ε/M^{-1} cm^{-1}): 363 (13200), 425 (shoulder) (4860), 536 (2490), 561 (2810), 643 (1240), 694 (1020), 900 (1400). MS (ESI+) *m/z*: 680.17 (MH+).

[($DOPO^q$)CrCl(bipy)]OTf (19). A vial was charged with ($DOPO^{sq}$)CrCl(bipy) (0.160 g, 0.235 mmol) which was dissolved in 8 mL of CH_2Cl_2. To this solution was added AgOTf (0.060 g, 0.234 mmol) in 2 mL of Et_2O. An additional 4 mL of Et_2O was used to aid transfer and increase AgOTf solubility in CH_2Cl_2. After stirring for 1 hour the reaction was filtered and dried. The resulting solids were washed with 4x2 mL portions of Et_2O to yield the product as a dark green solid (0.160 g, 82%). Anal. Calcd. for $C_{39}H_{46}N_3O_6F_3SCr$: C, 56.48; H, 5.59; N, 5.07. Found: C, 56.07; H, 5.47; N, 4.99. UV-vis-NIR (THF) λ_{max}/nm (ε/M^{-1} cm^{-1}): 307 (22000), 431 (17300), 495 (shoulder) (2020), 598 (1560), 844 (3330).

[(DOPO^q)Cr(bipy)OTf]OTf (20). A vial was charged with (DOPO^{sq})CrCl(bipy) (0.095 g, 0.140 mmol) which was dissolved in 10 mL of THF. A 2 mL THF solution of AgOTf (0.036 g, 0.140 mmol) was added to this solution. After 5 minutes the reaction mixture was filtered into another vial, to which was then added another portion of AgOTf (0.036 g, 0.140 mmol) in THF. After stirring for 5 hours the reaction was filtered and dried under vacuum. The crude solid was redissolved in 5 mL of MeCN and allowed to sit overnight. The mixture was filtered and dried under vacuum. The crude solids were dissolved in 3 mL of THF and allowed to sit overnight, then filtered and dried under vacuum. The crude solid was redissolved in 4 mL MeCN, allowed to sit overnight, then filtered and dried. The crude was slurried in 4 mL of toluene and chilled in a freezer at −35 °C. The precipitated solids were collected and recrystallized by layering a saturated THF solution with pentane, yielding dark green crystalline material (0.079 g, 60%). Anal. Calcd. for $C_{40}H_{46}N_3O_9F_6S_2Cr$: C, 50.95; H, 4.92; N, 4.46. Found: C, 50.49; H, 4.96; N, 4.27. UV-vis-NIR (THF) λ_{max}/nm (ε/M^{-1} cm^{-1}): 308 (20600), 443 (19000), 626 (1520), 836 (3990).

[(DOPO^q)Cr(bipy)OTf]OTf mediated oxidation of thioanisole. A vial was charged with [(DOPO^q)Cr(bipy)OTf]OTf (0.020 g, 0.021 mmol) and dissolved in 0.5 mL of CD_3CN. An internal standard of bromomesitylene (0.13 M in C_6D_6, 10 µL, 0.001 mmol), pyridine (15 µL, 0.186 mmol), and thioanisole (25 µL, 0.213 mmol) were added and the mixture was transferred to a J. Young NMR tube. In a glovebox, degassed D_2O (4 µL, 0.245 mmol) was added under a nitrogen atmosphere and the J. Young NMR tube was sealed. After sitting overnight ^{1}H-NMR analysis showed a 15% yield of methyl phenyl sulfoxide.

References

(1) Kwart, H.; Francis, P. S. *J. Am. Chem. Soc.* **1955**, *81*, 4907.
(2) Kwart, H.; Francis, P. S. *J. Am. Chem. Soc.* **1959**, *81*, 2116.

(3) Holum, J. R. *J. Org. Chem.* **1961**, *26*, 4814.

(4) Lee, D. G.; Stewart, R. *J. Am. Chem. Soc.* **1964**, *86*, 3051.

(5) Wiberg, K. B.; Mukherjee, S. K. *J. Am. Chem. Soc.* **1974**, *96*, 1884.

(6) Ratcliffe, R.; Rodehorst, R. *J. Org. Chem.* **1970**, *35*, 4000.

(7) Adam, W.; Hajra, S.; Herderich, M.; Saha-Möller, C. R. *Org. Lett.* **2000**, *2*, 2773.

(8) González-Núñez, M. E.; Mello, R.; Olmos, A.; Acerete, R.; Asensio, G. *J. Org. Chem.* **2006**, *71*, 1039.

(9) Noshiranzadeh, N.; Bikas, R.; Ślepokura, K.; Mayeli, M.; Lis, T. *Inorganica Chim. Acta* **2014**, *421*, 176.

(10) Wu, G.; Wang, X.; Liu, X.; Ding, K.; Zhang, F.; Zhang, X. *Catal. Letters* **2014**, *144*, 364.

(11) Bryliakov, K. P.; Talsi, E. P. *Inorg. Chem.* **2003**, *42*, 7258.

(12) Dalton, C. T.; Ryan, K. M.; Langan, I. J.; Coyne, É.´ J.; Gilheany, D. G. *J. Mol. Catal. A Chem.* **2002**, *187*, 179.

(13) Li, Z. K.; Liang, L.; Yang, L.; Chen, H.; Zhou, X. G. *J. Mol. Catal. A Chem.* **2005**, *235*, 108.

(14) McGarrigle, E. M.; Gilheany, D. G. *Chem. Rev.* **2005**, *105*, 1563.

(15) Siddall, T. L.; Miyaura, N.; Huffman, J. C.; Kochi, J. K. *J. Chem. Soc.* **1983**, *21*, 1185.

(16) Srinivasan, K.; Kochi, J. K. *J. Am. Chem. SOC* **1985**, *107*, 7606.

(17) Wu, G. De; Wang, X. L.; Zhai, Z. L. *Appl. Mech. Mater.* **2014**, *692*, 240.

(18) Kim, S. S.; Rajagopalba, G. *Synthesis (Stuttg).* **2003**, *16*, 1461.

(19) Sevvel, R.; Rajogopal, S.; Srinivasan, C.; Alhaji, N. I.; Chellamani, A. *J Org Chem* **2000**, *65*, 3334.

(20) Supale, A. R.; Gokavi, G. S. *Catal. Letters* **2008**, *124*, 284.

(21) Venkataramanan, N. S.; Premsingh, S.; Rajagopal, S.; Pitchumani, K. *J. Org. Chem.* **2003**, *68*, 7460.

(22) Venkataramanan, N. S.; Rajagopal, S. *Tetrahedron* **2006**, *62*, 5645.

(23) Borovik, A. S. *Acc. Chem. Res.* **2004**, *38*, 54.

(24) Chantarojsiri, T.; Sun, Y.; Long, J. R.; Chang, C. J. *Inorg. Chem.* **2015**, *54*, 5879.

(25) Chatterjee, D.; Mitra, A. *J. Mol. Catal. A Chem.* **2008**, *282*, 124.

(26) Gupta, R.; MacBeth, C. E.; Young, V. G.; Borovik, A. S. *J. Am. Chem. Soc.* **2002**, *124*, 1136.

(27) Kolb, H. C.; VanNieuwenhze, M. S.; Sharpless, K. B. *Chem. Rev.* **1994**, *94*, 2483.

(28) Lõpez, I.; Ertem, M. Z.; Maji, S.; Benet-Buchholz, J.; Keidel, A.; Kuhlmann, U.; Hildebrandt, P.; Cramer, C. J.; Batista, V. S.; Llobet, A. *Angew. Chemie - Int. Ed.* **2014**, *53*, 205.

(29) MacBeth, C. E.; Hammes, B. S.; Young Jr., V. G.; Borovik, A. S. *Inorg. Chem.* **2001**, *40*, 4733.

(30) Ohzu, S.; Ishizuka, T.; Hirai, Y.; Jiang, H.; Sakaguchi, M.; Ogura, T.; Fukuzumi, S.; Kojima, T. *Chem. Sci.* **2012**, *3*, 3421.

(31) Yoshida, M.; Kondo, M.; Torii, S.; Sakai, K.; Masaoka, S. *Angew. Chemie Int. Ed.* **2015**, *54*, 7981.

(32) Garrison, J. M.; Lee, R. W.; Bruice, T. C. *Inorg. Chem.* **1990**, *29*, 2019.

(33) Kanthimathi, M.; Jebanesan, D.; Unni Nair, B.; Jeyakanthan, J. *Transit. Met. Chem.* **2002**, *27*, 895.

(34) Shiren, K.; Tanaka, K. *Inorg. Chem.* **2002**, *41*, 5912.

(35) Schenk, V. C.; Stieger, H.; Kelm, H. *Zeitschrift für Anorg. und Allg. Chemie* **1972**, *391*, 1.

(36) Ashley, K. R.; Leipoldt, J. G.; Joshi, V. K. *Inorg. Chem.* **1980**, *19*, 1608.

(37) Jeon, S.; Bruice, T. C. *Inorg. Chem.* **1992**, *31*, 4843.

(38) Ivakhnenko, E. P.; Starikov, A. G.; Minkin, V. I.; Lyssenko, K. A.; Antipin, M. Y.; Simakov, V. I.; Korobov, M. S.; Borodkin, G. S.; Knyazev, P. A. *Inorg. Chem.* **2011**, *50*, 7022.

(39) Ranis, L. G.; Werellapatha, K.; Pietrini, N. J.; Bunker, B. A.; Brown, S. N. *Inorg. Chem.* **2014**, *53*, 10203.

(40) Simakov, V. I.; Gorbanev, Y. Y.; Ivakhnenko, T. E.; Zaletov, V. G.; Lyssenko, K. A.; Starikova, Z. A.; Ivakhnenko, E. P.; Minkin, V. I. *Russ. Chem. Bull.* **2009**, *58*, 1361.

(41) Romanenko, G. V.; Ivakhnenko, E. P.; Minkin, V. I.; Starikov, A. G.; Bogomyakov, A. S.; Veber, S. L. *Inorganica Chim. Acta* **2014**, *418*, 66.

(42) Bain, G. A.; Berry, J. F. *J. Chem. Educ.* **2008**, *85*, 532.

(43) Evans, D. *J. Chem. Soc.* **1959**, 2003.

(44) Schubert, E. M. *J. Chem. Educ.* **1992**, *69*, 62.

(45) Aranzaes, J. R.; Daniel, M.-C.; Astruc, D. *Can. J. Chem.* **2006**, *84*, 288.

(46) APEX2, Version 2014.11-0, Bruker AXS, Inc.; Madison, WI 2014.

(47) SAINT, Version 8.34a, Bruker AXS, Inc.; Madison, WI 2013.

(48) Sheldrick, G. M. SADABS, Version 2014/5, Bruker AXS Inc.; Madison, WI 2014.

(49) Sheldrick, G. M. SHELXTL, Version 2014/7, Bruker AXS Inc.; Madison, WI 2014.

(50) International Tables for Crystallography 1992, Vol C., Dordrecht: Kluwer Academic Publishers.

Chapter 6

Synthesis of First Row Transition Metal Complexes of the ONO Ligand

Introduction

The coordination chemistry of the redox-active ONO ligand has been well studied and documented over a span of decades, culminating in the recent completion of the entire first row series of homoleptic M(ONO)$_2$ complexes.[1–5] While studies on homoleptic M(ONO)$_2$ complexes provided a fundamental basis for determining metal and ligand charge distribution in complexes of the ONO ligand, their coordinatively saturated nature precludes their application to reactivity and catalysis.[6–11] More recently, this shortfall has been addressed in reports detailing heteroleptic ONO complexes (those with a single ONO ligand) of vanadium[12], iron[13], cobalt[14], copper[11,15], and zinc[9,16]. Theses pursuits yielded ONO complexes of iron which could perform the reductive elimination of disulfide[13] and copper complexes which enabled catalytic alcohol oxidation[15]. This ligand-enabled reactivity extends beyond the d^0 complexes described earlier, which necessitate the redox-mediating action of the ligand, and indicates that even mid- to late-transition metal species can perform novel reactivity enabled by a redox-active ligand. Despite promising results with heteroleptic ONO complexes, a majority of the transition metal ions remain unexplored. With respect to the entire *d*-block, heteroleptic complexes have also been reported for zirconium[17], niobium[12], rhodium[18], tantalum[19], and rhenium[20], while homoleptic complexes of molybdenum[5], tungsten[5], ruthenium[21], osmium[21], and cadmium[1] have also been described.

To expand the coordination chemistry of the ONO ligand platform, we have targeted the synthesis and characterization of heteroleptic complexes of the remaining members of the first-row series. Herein is reported the completion of this series with the synthesis and characterization of titanium, manganese, and nickel complexes of the ONO ligand.

Results and Discussion

Titanium Complexes of ONO

Synthetic methods used to access ONO complexes of vanadium and chromium with a single ONO ligand have utilized the monoanionic salt $(ONO^q)K$ and the metal(III) salts $VCl_3(THF)_3$ and $CrCl_3(THF)_3$, respectively.[12] Extending this approach with the analogous titanium precursor $TiCl_3(THF)_3$ and $(ONO^q)K$, dark green/brown crystals obtained upon workup displayed prototypical $(ONO^{sq})^{2-}$ bands by UV-vis-NIR spectroscopy (Figure 6.3). A broad NIR band was observed at 903 nm with an additional visible region band at 573 nm, common for d^0 $(ONO^{sq})^{2-}$ complexes, as typified in $(ONO^{sq})Ta(OR)_3$ complexes described in Chapter 2.[4,19] The assignment of a ligand-based radical was further substantiated by EPR analysis, which showed a narrow, 14-line signal at $g = 1.999$ with an isotropic hyperfine coupling constant of 2 G (Figure 6.2). Single crystal X-ray diffraction analysis yielded the structure of $(ONO^{sq})TiCl_2(THF)$ (**21**) in Figure 6.1.

Scheme 6.1. Synthetic route used to obtain **21**.

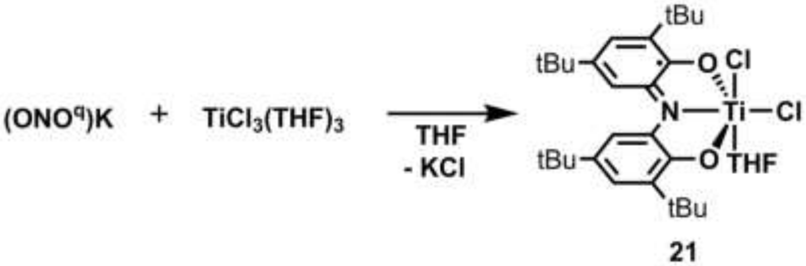

21

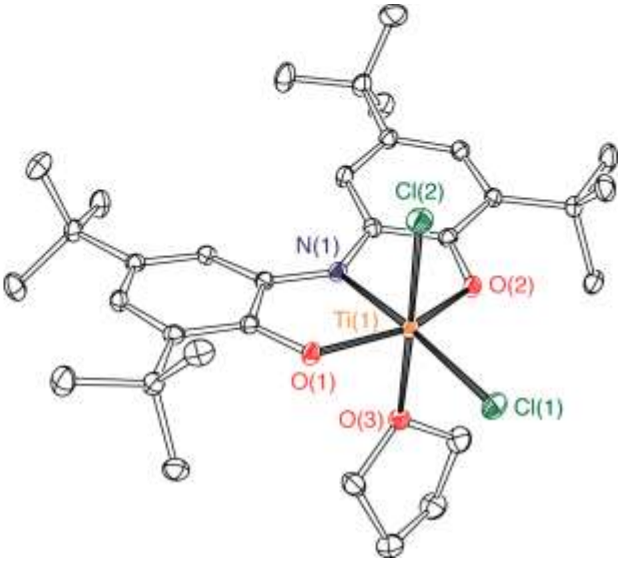

Figure 6.1. ORTEP diagram of $(ONO^{sq})TiCl_2(THF)$ (**21**). Thermal ellipsoids are shown at 50% probability. Hydrogen atoms have been omitted for clarity.

In the solid state, **21** exhibits pseudo-octahedral geometry about the titanium metal center, with the most significant deviation from pure octahedral geometry arising from the bond angles within the ONO binding pocket, most notably the O(1)–Ti(1)–O(2) angle of 150.84(4)°. Contracted C–O bond distances of 1.3344(16) and 1.3365(16) Å for O(1)–C(2) and O(2)–C(8), respectively, and localized double bond character within the aryl backbone of the ONO ligand are indicative of the $(ONO^{sq})^{2-}$ formulation of the ligand.[2,4,9,16,19] Application of Brown's MOS calculation yields a value of −2.16, confirming the dianionic semiquinonate assignment of the ligand.[5] Bond metrics for **21** are provided in Table 6.1 alongside the first row structural analogues of vanadium[12] and chromium.

Table 6.1. Selected bond lengths and angles for **21** and the vanadium and chromium congeners.

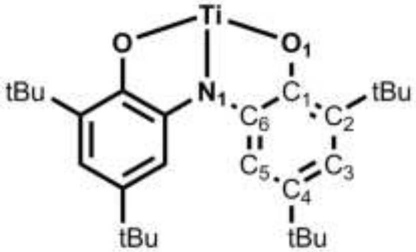

	$(ONO^{sq})TiCl_2(THF)$ **21**	$(ONO^{sq})VCl_2(THF)$	$(ONO^{q})CrCl_2(THF)$ **11**
		Bond Lengths (Å)	
M(1)–N(1)	2.1353(11)	1.9955(19)	1.998(3)
M(1)–O(1)	1.8894(10)	1.811(2)	1.962(3)
O(1)–C(1)	1.3344(16)	1.336(3)	1.280(5)
N(1)–C(6)	1.3662(17)	1.381(4)	1.355(5)
C(1)–C(2)	1.4121(19)	1.409(4)	1.449(6)
C(2)–C(3)	1.3887(19)	1.376(4)	1.373(6)
C(3)–C(4)	1.4202(18)	1.410(4)	1.430(6)
C(4)–C(5)	1.3770(19)	1.389(4)	1.378(6)
C(5)–C(6)	1.4105(18)	1.400(4)	1.419(6)
C(1)–C(6)	1.4261(18)	1.412(4)	1.455(6)
M(1)–O(3)	2.1441(10)	2.0632(18)	2.003(3)
M(1)–Cl(1)	2.2967(4)	2.3399(9)	2.3188(14)
		Bond Angles (°)	
N(1)–M(1)–O(1)	75.69(4)	77.51(9)	81.32(13)
O(1)–M(1)–O(2)	150.84(4)	155.21(8)	162.63(13)
Cl(1)–M(1)–Cl(2)	96.453(15)	166.31(3)	176.56(5)
O(3)–M(1)–Cl(2)	177.50(3)	84.29(7)	87.82(11)

A striking feature of the solid state structure of **21** is the coordination of the THF ligand *cis* to the nitrogen of the ONO ligand. In all other crystallographically characterized $(ONO)MCl_2L$ complexes the neutral L donor coordinates *trans* to the central nitrogen of the ONO ligand. This structural feature transcends the oxidation state assignment of the ONO ligand; $(ONO^{cat})TaCl_2(Et_2O)$,[22] $(ONO^{cat})NbCl_2(Et_2O)$,[12] $(ONO^{sq})VCl_2(THF)$,[12] $(ONO^{q})CrCl_2(THF)$, and $(ONO^{q})CoCl_2(py)$[14] all show the neutral L donor *trans* to the nitrogen of the ONO ligand. No current explanation seems to fit this observed difference, though it may simply be that this conformation is the most prone to crystallization for **21**, and the L ligands are possibly dynamic in most of the aforementioned cases.

Electrochemical analysis of **21** yielded the voltammogram in Figure 6.2. A semi-reversible reduction event appears at −0.35 V along with an irreversible oxidation event at 0.37 V. Scan direction dependence of the events located between the primary oxidation and reduction events identifies them as daughter species arising from instability of the *in situ* formed oxidized and reduced species $[(ONO^{q})TiCl_2(THF)]^+$ and $[(ONO^{cat})TiCl_2(THF)]^-$, respectively. Further cathodic scanning reveals an irreversible reduction at −2.36 V (E_{pc}), nominally corresponding to the Ti(IV)/Ti(III) redox couple. With the synthesis and electrochemical characterization of **21**, a three-membered series of homologous $(ONO)MCl_2(THF)$ complexes (where M=Ti, V, and Cr) of the first row series could be compared (Figure 6.3 and Table 6.2). In traversing the series from Ti→V→Cr, a notable widening of the resting potential of the complex occurs, with a window of 0.72 V for [Ti], 1.13 V for [V], and 1.40 V for [Cr]. This results both from an anodic shift of the 1st oxidation event and from a cathodic shift of the 1st reduction event in the series. While the chromium species demonstrates similar electrochemical behavior to the titanium and vanadium congeners, its ground state assignment as an $(ONO^{q})^{1-}$ coordinated complex precludes its inclusion in the direct comparison of the metal effects on the ONO^{cat}/ONO^{sq} and ONO^{sq}/ONO^{q} redox couples. Both $(ONO^{sq})TiCl_2(THF)$ and $(ONO^{sq})VCl_2(THF)$ possess the $(ONO^{sq})^{2-}$ form of the ligand, allowing direct comparison of the metal effects on these ligand processes. While a simple lewis acid effect would be expected to shift both the oxidation and reduction events in the same direction, the observed effect is an anodic shift in the oxidation and a cathodic shift in the reduction. It therefore seems, within this limited data set, that alteration of the metal center will not yield simple anodic shifts as a function of increased lewis acidity, but will yield more complex redox effects.

Table 6.2. Redox potentials for complexes of the general formula (ONO)MCl$_2$(THF) ([M]) where M = Ti, V, Cr.

	E°' (V vs Cp$_2$Fe$^{0/+}$)		
	[M]$^{-/2-}$	[M]$^{0/-}$	[M]$^{0/+}$
(ONO^{q})CrCl$_2$(THF)	−1.53[a]	−0.49	0.91
(ONO^{sq})VCl$_2$(THF)	−1.66[a]	−0.45	0.69
(ONO^{sq})TiCl$_2$(THF)	−2.36[a]	−0.35	0.37

[a] Irreversible electrochemical event (E$_{pc}$).

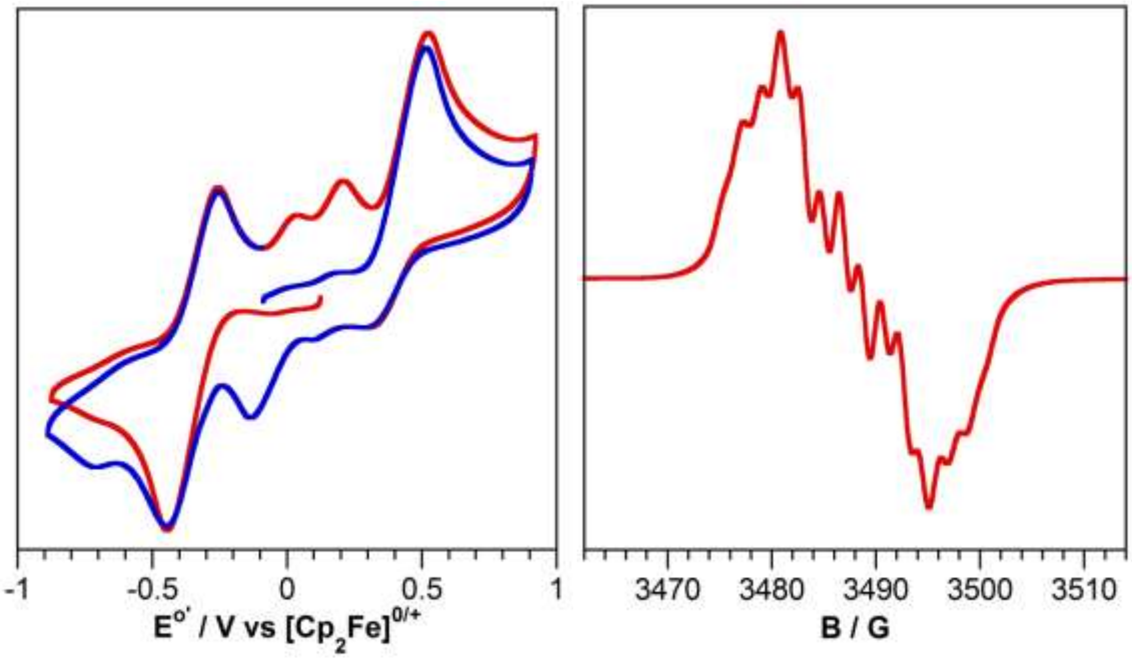

Figure 6.2. **Left**. Cyclic voltammogram of (ONO^{sq})TiCl$_2$(THF) with initial scanning in the cathodic direction (**red**) and in the anodic direction (**blue**). Voltammograms collected in THF with 0.1 M TBAPF$_6$ and 1 mM analyte at a scan rate of 200 mV/s. **Right**. EPR spectrum of (ONO^{sq})TiCl$_2$(THF) collected in THF at room temperature.

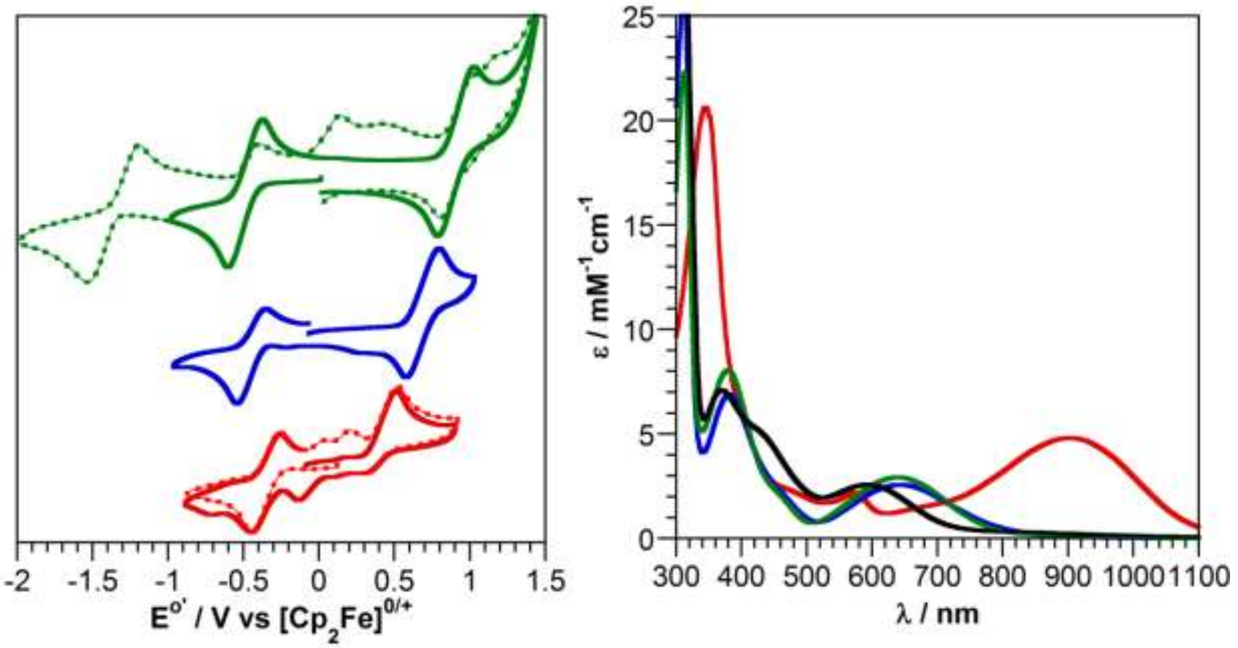

Figure 6.3. **Left**. Cyclic voltammograms of (ONO^{sq})TiCl$_2$(THF) (**red**), (ONO^{sq})VCl$_2$(THF) (**blue**), and (ONO^{q})CrCl$_2$(THF) (**green**) collected in THF with 0.1 M TBAPF$_6$ and 1 mM analyte at a scan rate of 200 mV/s. **Right**. UV-vis-NIR spectra of (ONO^{sq})TiCl$_2$(THF) (**red**), (ONO^{cat})TiCl(THF)$_2$ (**blue**), (ONO^{cat})TiCl(py)$_2$ (**green**), and (ONO^{cat})TiCl(bipy) (**black**). THF coordinated complexes recorded in THF and pyridine/bipy coordinated complexes recorded in toluene.

An alternative route to titanium complexes of the ONO ligand was devised utilizing the fully reduced (ONO^{cat})$^{3-}$ precursor, (ONO^{cat})Li$_3$, formed *in situ* by deprotonation of (ONO^{cat})H$_3$. Addition of (ONO^{cat})Li$_3$ to a slurry of TiCl$_4$(THF)$_2$ and subsequent workup yielded the diamagnetic complex (ONO^{cat})TiCl(THF)$_2$ (**22**). The presence of two coordinated THF molecules is indicated by ^{1}H-NMR, which shows two broad resonances at 4.48 and 1.21 ppm which are shifted from that of free THF.

Scheme 6.2. Synthetic methods used to obtain complexes **22-24**.

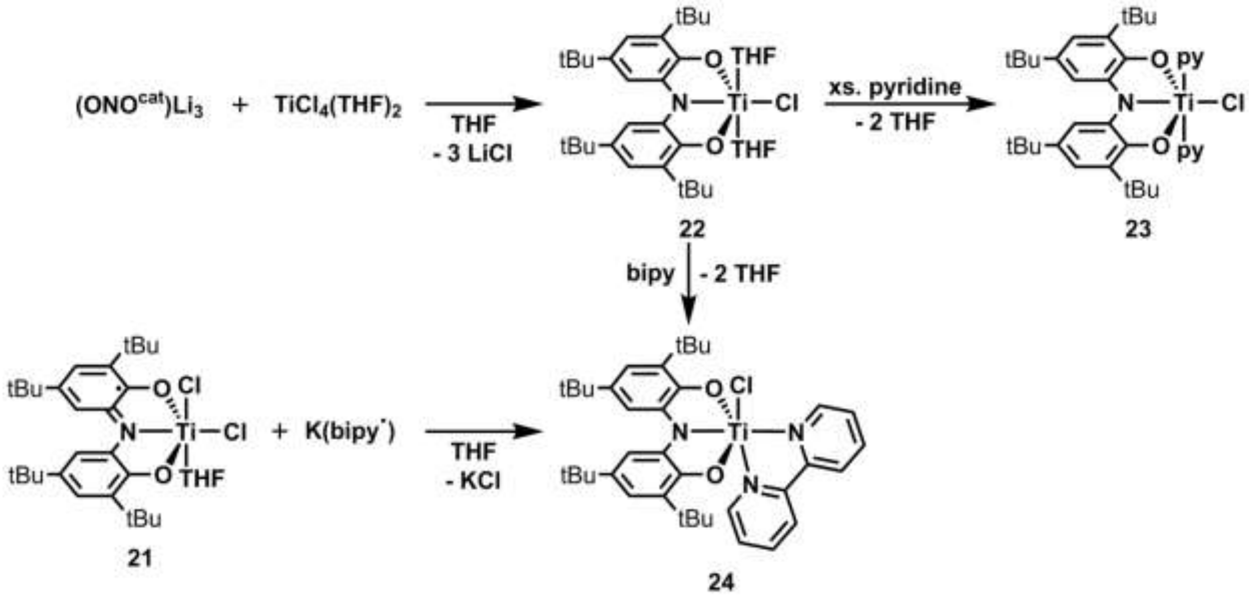

Electrochemical analysis of **22** and subsequent complexes showed complicated behavior in THF, and were therefore recorded in CH_2Cl_2. Complex **22** showed multiple species in solution in CH_2Cl_2, which converged to a single species upon addition of excess THF, suggesting dissociation of THF and formation of either $(ONO^{cat})TiCl(THF)$ or $[(ONO^{cat})Ti(\mu\text{-}Cl)(THF)]_2$ under dilute conditions in CH_2Cl_2 (Figure 6.4). With added THF, a semi-reversible oxidation event occurs at 0.01 V, with significant formation of a daughter species at −0.37 V (E_{pc}). Multiple oxidation events are present, potentially a result of further chemical reactivity of the *in situ* formed $[(ONO^{sq})TiCl(THF)_2]^+$ to yield an unidentified by-product, or simply from another unrelated species in solution. To improve the electrochemical behavior of **22**, substitution of the THF ligands for pyridine ligands was achieved through simple treatment of **22** with a slight excess of pyridine and removal of reaction volatiles. Analysis by ^{1}H-NMR and UV-vis-NIR spectroscopy confirmed the formation of the desired product $(ONO^{cat})TiCl(py)_2$ (**23**). Complex **23** showed improved electrochemical stability, displaying a semi-reversible oxidation event at 0.09 V and an irreversible oxidation event at 0.69 V. This suggests the additional oxidation event observed in **22** at 0.34 V is likely a result of an unknown species which forms from the instability of the *in situ* formed $[(ONO^{sq})TiCl(THF)_2]^+$. Cathodic scanning reveals an irreversible, nominally metal-based, reduction of **23** at −1.99 V (E_{pc}).

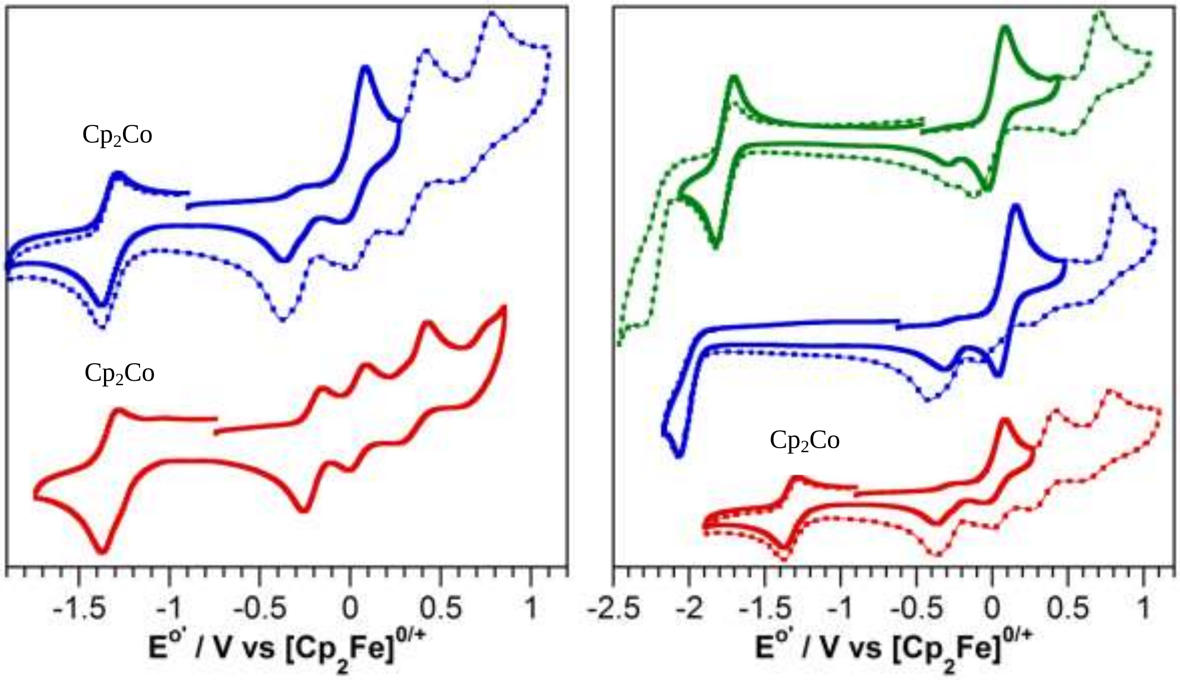

Figure 6.4. **Left**. Cyclic voltammograms of $(ONO^{cat})TiCl(THF)_2$ collected in CH_2Cl_2 without added THF (**red**) and after the addition of 100 µL of THF (**blue**). Solution contained 0.1 M $TBAPF_6$, 1 mM analyte, an internal standard of Cp_2Co^+ PF_6^-, collected at a scan rate of 200 mV/s. **Right**. Cyclic voltammograms of $(ONO^{cat})TiCl(THF)_2$ with 100 µL THF (**red**), $(ONO^{cat})TiCl(py)_2$ (**blue**), and $(ONO^{cat})TiCl(bipy)$ (**green**) collected in CH_2Cl_2 with 0.1 M $TBAPF_6$ and 1 mM analyte at a scan rate of 200 mV/s. Dotted traces were collected with a wider electrochemical window.

Further stabilization of the $(ONO^{cat})TiCl$ platform was pursued using the bidentate ligand bipyridine. Simple ligand displacement of bipy for the THF ligands in **22** yielded the diamagnetic complex $(ONO^{cat})TiCl(bipy)$ (**24**), which displayed a ^{1}H-NMR spectrum with a broadened resonance at 9.65 ppm corresponding to two protons of the bipyridine ligand, while the other six appeared as sharp multiplets at 8.19, 8.12, and 7.64 ppm. No near-IR bands were evident in the electronic absorbance spectrum of **24**, consistent with the $(ONO^{cat})^{3-}$ formulation of the ligand. Alternatively, treating $(ONO^{sq})TiCl_2(THF)$ with *in situ* generated $K(bipy^{\cdot})$ yielded the same product. The electrochemical behavior of **24** was analogous to that of

$(\mathrm{ONO^{cat}})\mathrm{TiCl(py)_2}$, displaying a semi-reversible oxidation event at 0.03 V and an irreversible oxidation event at 0.61 V. Notably, the intensity of the daughter peak at −0.29 V formed upon the first oxidation diminished in **24**, and it is clear that stabilization of the $(\mathrm{ONO^{cat}})\mathrm{TiCl(L)_x}$ fragment increases on the order of bipy>py>THF. As expected with the incorporation of the redox-active bipy, a reversible reduction event appears at −1.76 V, consistent with the reduction of a titanium coordinated bipy ligand.[23] Further cathodic scanning yields an additional, irreversible reduction event at −2.19 V (E_{pc}) which is just discernible within the edge of the solvent window.

Synthesis of $(\mathrm{ONO^{cat}})\mathrm{VCl(bipy)}$

Concurrent with the overarching pursuit of first-row complexes with a singly coordinated ONO ligand, extension of the (ONO)MCl(bipy) morphology to other metal centers was pursued with the previously described $(\mathrm{ONO^{sq}})\mathrm{VCl_2(THF)}$. With the same method used in the titanium and chromium congeners, $(\mathrm{ONO^{sq}})\mathrm{VCl_2(THF)}$ was treated with an equivalent of *in situ* generated $\mathrm{K(bipy^{\cdot})}$. The isolated product showed a UV-vis-NIR spectrum devoid of NIR bands, consistent with a ligand-based reduction to yield a fully reduced $(\mathrm{ONO^{cat}})^{3-}$ ligand. Analysis by EPR spectroscopy revealed a broad isotropic signal located at $g = 1.964$. This signal displayed an 8 line pattern from coupling to the $S = 7/2$ $^{51}\mathrm{V}$ nucleus with a large isotropic hyperfine coupling constant (A_{iso}) of 83 G (avg.), consistent with a vanadium-based radical (Figure 6.5).[24] This data suggests the coordination of a fully reduced $(\mathrm{ONO^{cat}})^{3-}$ ligand to a V(IV) metal center in $(\mathrm{ONO^{cat}})\mathrm{VCl(bipy)}$ (**25**).

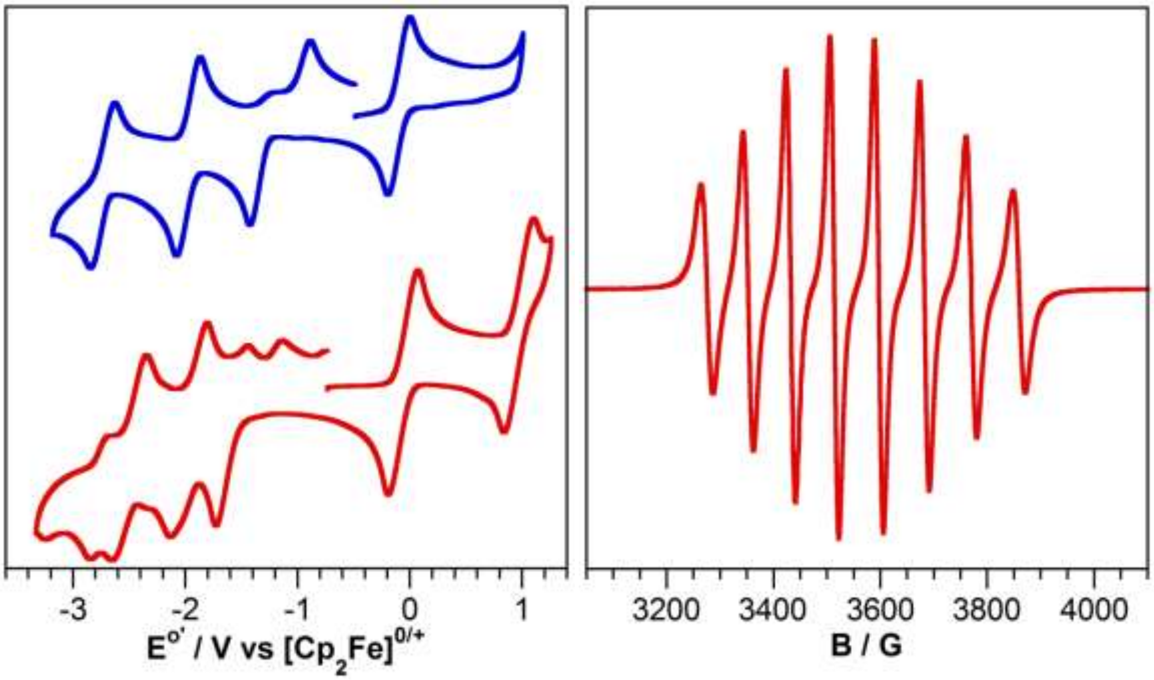

Figure 6.5. **Left**. Cyclic voltammograms of $(ONO^{cat})VCl(bipy)$ (**red**) and $(ONO^{sq})CrCl(bipy)$ (**blue**) collected in THF with 0.1 M $TBAPF_6$ and 1 mM analyte at a scan rate of 200 mV/s. **Right**. EPR spectrum of $(ONO^{cat})VCl(bipy)$ collected in toluene at room temperature.

Analysis of **25** by cyclic voltammetry revealed similar electrochemical behavior to the chromium analogue $(ONO^{sq})Cr(bipy)Cl$ (**12**) (Figure 6.5). Both complexes undergo reversible oxidations at similar potentials: **25** undergoes oxidation at −0.06 V while **12** is oxidized at −0.10 V. For complex **12** this has been determined to correspond to the $ONO^{sq/q}$ ligand-based redox couple, while for **25** this redox couple would correspond to the $ONO^{cat/sq}$ redox couple. This simple comparison highlights that when comparing the redox potentials of ligand-based electrochemical events care must be taken when comparing complexes of differing metals. The tentatively assigned $ONO^{sq/q}$ redox couple can be observed for **25** upon further anodic scanning at 0.97 V, appearing as a reversible event. The assignment as the $ONO^{sq/q}$ redox couple is based on the results of chemical oxidation of $(ONO^{sq})VCl_2(THF)$ to $(ONO^{q})VCl_3$.[12] Cathodic scanning reveals an irreversible reduction event at −1.73 V (E_{pc}) for complex **25**, likely a metal-based V(IV)→V(III) reduction event considering the reports on $V(bipy)_3$ electron transfer series and their electronic structure.[25–27] Further cathodic scanning reveals a number of additional reduction events, likely including both vanadium and bipy reductions, though the nature of these events have not been investigated and are therefore not explicitly assigned.

Notably, the trend observed in the family of (ONO)MCl_2(THF) complexes is reversed in the (ONO)MCl(bipy) manifold (for M = V and Cr). While the resting potential was wider for chromium in the (ONO)MCl_2(THF) series, the opposite was true for (ONO)MCl(bipy), wherein vanadium possessed a wider resting potential. These results suggest that predicting periodic trends based on a single family of isostructural complexes should not be done.

Manganese Complexes of ONO

As was the case with titanium, the only reported ONO complex of manganese was the homoleptic Mn(ONO^{sq})$_2$. Since the manganese variant of $MCl_3$$(THF)_3$ is not commercially available and it's synthesis and isolation is exceedingly complex[28], the (ONO)$MnCl_2$(THF) analogue of **11**, **21**, and (ONO^{sq})VCl_2(THF) was not pursued. Instead, an *in situ* formed slurry of $MnCl_2$(bipy) was treated with the dianionic ONO salt (ONO^{sq})K_2 (Scheme 6.3). Single crystal x-ray diffraction analysis of the product yielded the structure [(ONO)Mn(bipy)]$_2$ (**26**) shown in Figure 6.6. While dimer formation of (ONO)M(bipy) units shouldn't be surprising given the results observed with chromium, it was unusual that the dimer formation did not necessitate a bridging function of the central nitrogen. Moreover, if the five-coordinate geometry at the metal center is most energetically favorable, it would be expected that tridentate binding of the ONO ligand and bipy binding would fulfill this geometric preference. Partial oxidation of the ONO ligand and its formulation as $(ONO^{sq})^{2-}$ is supported by bond metrics within the ONO backbone, with localized double bond character noted (Table 6.3). Contracted C–O bond distances of 1.33 Å (avg.) are also consistent with this assignment, however, the non-planar geometry around the central nitrogen could be contributing to these contracted distances in the manner described in

Chapter 4 for complex **14**. The extremely long N(1)–C(6) bond distance of 1.467(2) Å is a result of the significant pyramidalization of the central nitrogen, and this elongation is a significant contributor to the higher than expected MOS calculation of −2.78, which is more consistent with an $(ONO^{cat})^{3-}$ assignment. The drastic structural deviation of the ONO ligand in **26** from those used to develop Browns MOS calculation, therefore, preclude a meaningful use of this metric. Therefore, no explicit assignment of the ligand in **26** is proposed. Whether this dimeric structure is maintained in solution has not been established, as significant amounts of **26** free of $Mn(ONO^{sq})_2$ have been difficult to obtain. This has also precluded the measurement of the electronic absorption spectrum of **26**.

Scheme 6.3. Synthesis of complex **26**.

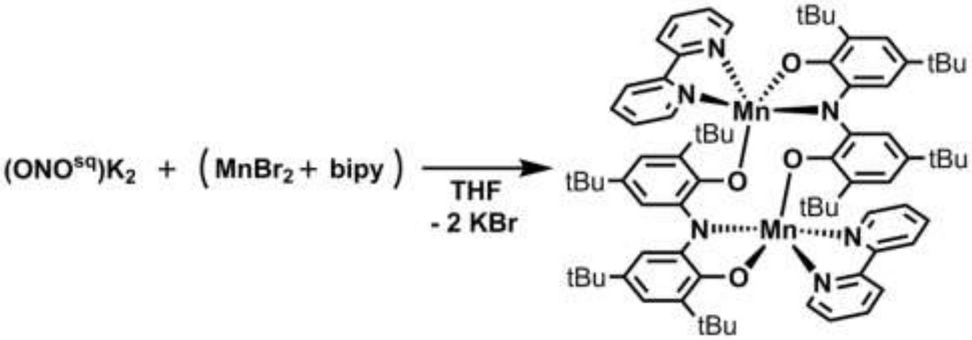

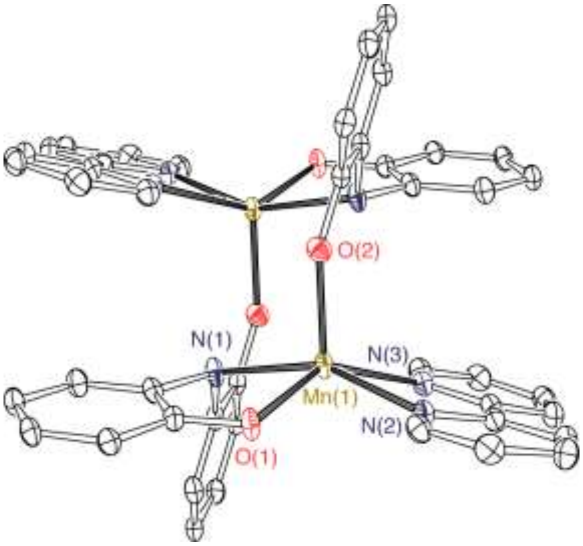

Figure 6.6. ORTEP diagram of $[(ONO)Mn(bipy)]_2$ (**26**). Thermal ellipsoids are shown at 50% probability. Hydrogen atoms and the *tert*-butyl groups of the ONO ligand have been omitted for clarity.

The difficulty in manipulating **26** was further demonstrated when purification from pyridine solutions was attempted. Dissolving **26** in pyridine yields vibrant purple solutions, and crystallization from pyridine using pentane, hexamethyldisiloxane, or MeCN as antisolvent yields purple solids which regenerate brown solutions if redissolved in toluene. The identity of the crystalline product was determined through X-ray diffraction analysis of single crystals obtained from slow diffusion of an analyte solution in pyridine into hexamethyldisiloxane, which showed the product to be $(ONO^{cat})Mn(py)_3$ (**27**) (Figure 6.7). While the significant structural deviation of the ONO ligand in **26** from the tridentate, meridional binding mode typical of ONO (and used to develop MOS calculations) precludes trustworthy application of MOS values, this binding mode is present in **27** and allows for a useful metrical analysis. Complex **27** exhibits a distorted pseudo-octahedral coordination geometry, similar to that observed in the chromium and iron analogues.[13] Most notable are the lengths of the ligand C–O and C–N bonds which average 1.36 Å and 1.39 Å, respectively, indicative of a fully reduced $(ONO^{cat})^{3-}$ ligand. This assignment is also consistent with the lack of localized double bond character in the aryl backbone of the ONO ligand. A MOS value of −2.88 (average of all four aryl rings in the asymmetric unit) further supports the presence of a trianionic $(ONO^{cat})^{3-}$ ligand. Bond metrics are provided for chromium, manganese, and iron complexes of the $(ONO^{cat})M(py)_3$ platform in Table 6.3.

Bond metrics around the metal center show periodic trends consistent with the *d*-orbital occupation of the metal. In the chromium containing complex, the axial pyridine donors show an average Cr–N bond distance of 2.12 Å. Moving one group over in the periodic table to manganese adds an electron to the *d*-manifold, resulting in a drastic elongation of the axial Mn–N bond to an average distance of 2.38 Å. This elongation, and the minimal difference of the equatorial pyridine M–N bond distance in the chromium and manganese complexes, indicates d_{z2}

occupation of the fourth electron in the Mn(III) center. The observed Jahn-Teller distortion is common in octahedral d^4 Mn(III) complexes, affecting loss of degeneracy of the d_{z2} and d_{x2-y2} orbitals.[29–33] The effects of Jahn-Teller distortion in **27** is further observed in the contracted equatorial bonds Mn(1)–N(1), Mn(1)–O(1), Mn(1)–O(2), and Mn(1)–N(3) as compared to the chromium and iron congeners. A similar, though less pronounced, elongation of the axial pyridine Fe–N bond is observed in the iron complex (average of 2.24 Å). The high-spin d^5 formulation of the iron center results in occupation of both the d_{z2} and d_{x2-y2} orbitals, resulting in a slight elongation of the equatorial pyridine bond, showing an Fe–N distance of 2.145(2) Å.[13]

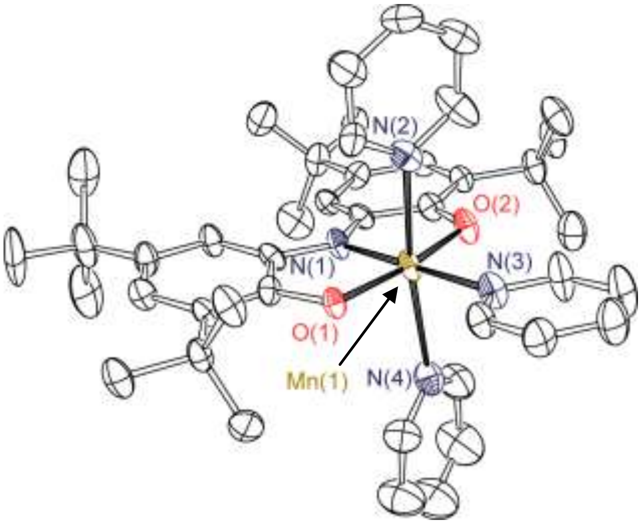

Figure 6.7. ORTEP diagram of (ONO^{cat})Mn(py)$_3$ (**27**). Thermal ellipsoids are shown at 50% probability. Hydrogen atoms have been omitted for clarity. A second crystallographically unique but chemically identical molecule of **27** has also been omitted.

Table 6.3. Selected bond lengths and angles for **26** and **27**, along with the chromium and iron analogues of **27**.

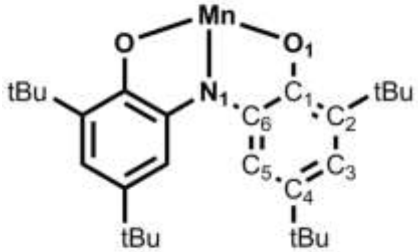

	(ONO)Mn(bipy) **26**	$(ONO^{cat})Mn(py)_3$ **27**	$(ONO^{cat})Cr(py)_3$ **13**	$(ONO^{cat})Fe(py)_3$
		Bond Lengths (Å)		
M(1)–N(1)	2.2926(16)	1.903(3)	1.923(2)	1.982(2)
M(1)–O(1)	2.0336(13)	1.897(2)	1.939(2)	1.949(2)
M(1)–O(2)	1.9987(14)	1.888(2)	1.939(2)	1.950(2)
O(1)–C(1)	1.329(2)	1.358(4)	1.356(3)	1.344(2)
N(1)–C(6)	1.467(2)	1.387(4)	1.389(4)	1.392(3)
C(1)–C(2)	1.427(2)	1.389(4)	1.396(4)	1.402(3)
C(2)–C(3)	1.389(3)	1.416(5)	1.411(4)	1.401(3)
C(3)–C(4)	1.403(3)	1.392(5)	1.388(4)	1.392(3)
C(4)–C(5)	1.385(3)	1.401(5)	1.402(4)	1.400(3)
C(5)–C(6)	1.392(3)	1.393(5)	1.385(4)	1.401(3)
C(1)–C(6)	1.405(3)	1.430(4)	1.432(4)	1.441(3)
M(1)–N(2)	2.2204(16)	2.380(3)	2.123(3)	2.238(2)
M(1)–N(3)	2.2725(15)	2.079(3)	2.093(3)	2.145(2)
M(1)–N(4)	-----	2.404(3)	2.130(3)	2.252(2)
		Bond Angles (°)		
N(1)–M(1)–O(1)	78.51(5)	83.69(10)	83.45(9)	81.97(7)
N(1)–M(1)–O(2)	94.04(6)	84.22(10)	83.03(9)	81.71(7)
O(1)–M(1)–O(2)	113.35(5)	167.91(10)	166.48(9)	163.68(6)
N(1)–M(1)–N(2)	155.22(6)	96.90(11)	92.30(10)	93.70(7)
N(1)–M(1)–N(3)	109.17(6)	179.13(11)	178.99(11)	178.73(7)
O(1)–M(1)–N(2)	85.52(5)	89.76(10)	90.04(9)	90.85(6)

Expanding the family of (ONO)Mn complexes was met with considerable synthetic difficulties; attempts to convert **26** into (ONO)MCl(bipy) through the use of the chlorine atom surrogate iodosobenzene dichloride ($PhICl_2$) yielded, instead, large amounts of $Mn(ONO^{sq})_2$. This homoleptic complex was also produced upon treating *in situ* generated $(bipy)MnCl_2$ with $(ONO^{q})K$. The complicated and difficult nature of ONO complexes of manganese, demonstrated through the behavior of **26** and **27** and its general proclivity to form Mn(ONO^{sq})$_2$, have therefore precluded significant expansion of (ONO)Mn coordination chemistry.

Nickel Complexes of ONO

In a similar approach used to synthesize (ONO)Mn(bipy), nickel complexes of ONO were pursued utilizing (ONO^{sq})K$_2$ and the nickel starting material NiCl$_2$(py)$_4$. Treating a THF slurry of NiCl$_2$(py)$_4$ with (ONO^{sq})K$_2$ and subsequent workup yielded a dark purple solid (Scheme 6.4). Consistent with the expected Ni(II) product bearing an (ONO^{sq})$^{2-}$ ligand, UV-vis-NIR spectroscopy revealed a broad near-IR band whose intensity peaked at 1130 nm and extended beyond 1500 nm (Figure 6.10). The intensity of this band was notably diminished and peak width widened relative to the *d*^{0} and *d*^{3} (ONO^{sq})$^{2-}$ complexes described in previous chapters. This difference from the (ONO^{sq})$^{2-}$ complexes described throughout could be due to either the altered coordination geometry at the metal center or the increased d count of the metal center, both of which may impact the near-IR absorbance. Supporting the assignment of the ligand as (ONO^{sq})$^{2-}$ with an organic radical, a narrow isotropic signal at g=2.003 was observed by EPR spectrospcopy (Figure 6.8). Mass spectrometry revealed the expected set of peaks for (ONO^{sq})Ni(py) (**28**) at 559.38 m/z.

Scheme 6.4. Synthesis of complexes **28-30**.

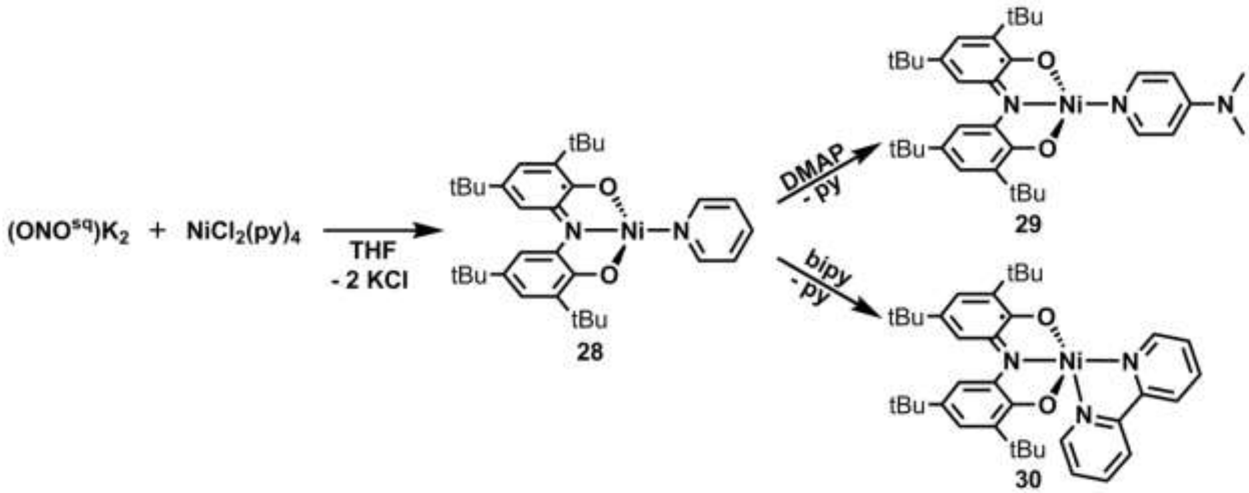

Cyclic voltammetry revealed rich electrochemical behavior for **28**, yielding two reversible oxidation events at −0.51 and 0.68 V (Figure 6.8). An assignment of the first oxidation as corresponding to the ONO^{sq}/ONO^{q} redox couple is consistent with the reported electronic structure of Ni(ONO^{q})$_2$, though chemical oxidation has not been performed to confirm this assignment. Electrochemical characterization of Ni(ONO^{q})$_2$ was reported to exhibit anodic events assigned as ligand-based oxidations of the monoanionic (ONO^{q})$^{1-}$ ligand to the neutral radical (ONO$^{\bullet}$)^{0} form of the ligand, which may be the nature of the second oxidation event of **28** at 0.68 V.[3] Cathodic scanning revealed a reversible reduction event at −1.14 V corresponding to the ONO^{sq}/ONO^{cat} redox couple. Further cathodic scanning revealed a semi-reversible reduction event at −2.94 V, nominally arising from the Ni(II)/(I) couple.

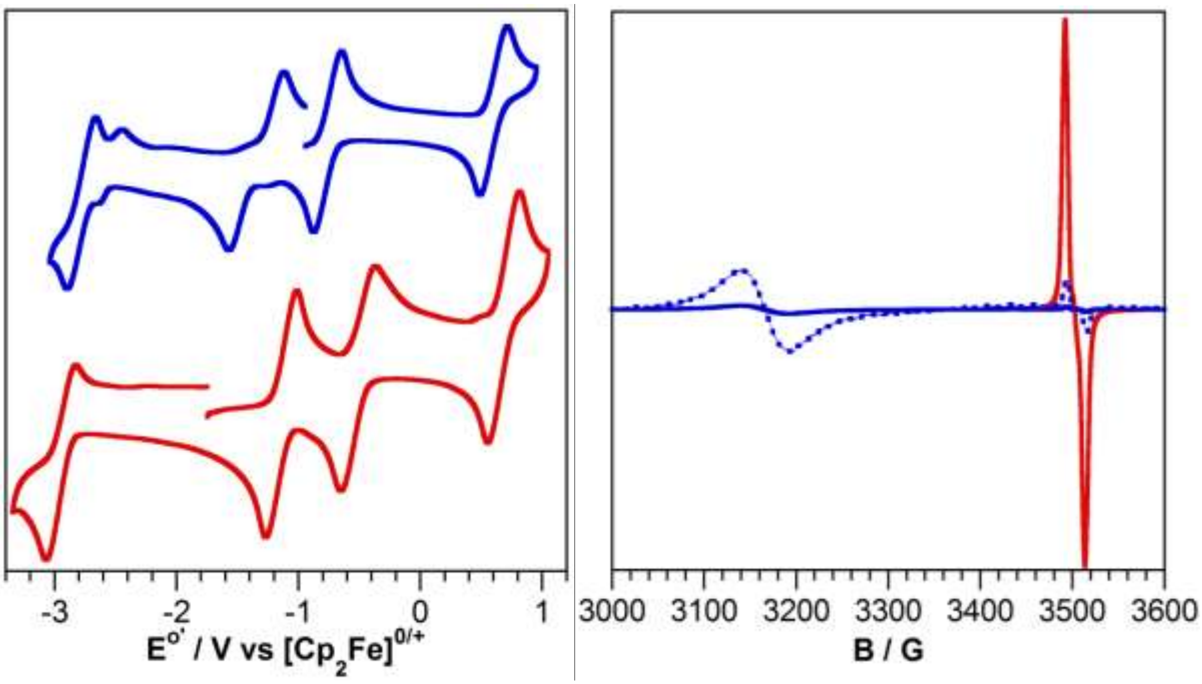

Figure 6.8. **Left**. Cyclic voltammograms of (ONO^{sq})Ni(py) (**red**) and (ONO^{sq})Ni(bipy) (**blue solid**) recorded in THF with 0.1 M TBAPF$_6$ and 1 mM analyte at a scan rate of 200 mV/s. **Right**. EPR spectra of (ONO^{sq})Ni(py) (**red**) and (ONO^{sq})Ni(bipy) (as is - **blue solid**, 10x magnification - **blue dotted**) recorded in toluene at room temperature and concentrations of 1 mM. *A minor amount of (ONO^{sq})Ni(py) was observable in the sample of (ONO^{sq})Ni(bipy).

Single crystals of **28** suitable for X-ray diffraction analysis could not be obtained, therefore substitution of the pyridine ligand for 4-dimethylaminopyridine (DMAP) was performed to achieve crystalline samples while conferring minimal structural and electronic changes. This substitution was achieved in a straightforward manner by mixing **28** and DMAP in toluene and evaporating the more volatile pyridine from the product. The desired product (ONO^{sq})Ni(DMAP) (**29**) was confirmed by mass spectroscopy with a m/z peak at 602.25 and by the nearly identical electronic absorption spectrum to that of **28**, confirming that this reaction resulted in simple ligand substitution. This approach towards crystalline material proved successful, with single crystal X-ray diffraction analysis of **29** yielding the structure provided in Figure 6.9.

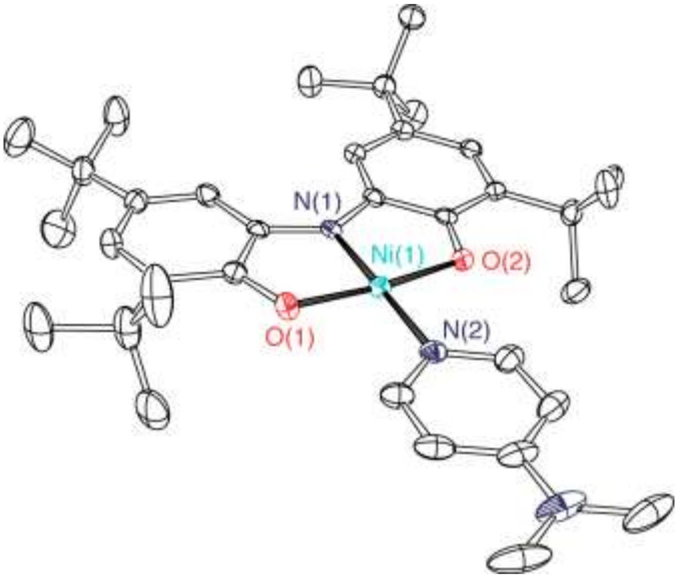

Figure 6.9. ORTEP diagram of (ONO^{sq})Ni(DMAP) (**29**). Thermal ellipsoids are shown at 50% probability. Hydrogen atoms have been omitted for clarity.

The solid state structure of **29** revealed a nearly square planar geometry about the nickel center, expected for Ni(II) complexes. The (ONO^{sq})$^{2-}$ assignment is confirmed by the ligand bond metrics, which show contracted C–O bond distances of 1.322(3) Å and localized double bond character within the aryl backbone (Table 6.4).[2,4,9,16,19] The nickel center shows minimal deviation from planarity, with a Ni(1)–N(1)–O(1)–O(2) torsion angle of 0.16°. Calculation of the MOS yields a value of −2.05, further supporting the (ONO^{sq})$^{2-}$ assignment of the ligand.

Table 6.4. Selected bond lengths and angles for **29** and **30**.

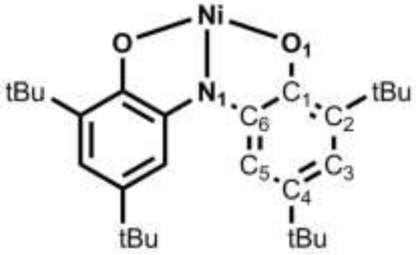

	(ONO^{sq})Ni(DMAP) **29**	(ONO^{sq})Ni(bipy) **30**
	Bond Lengths (Å)	
Ni(1)–N(1)	1.831(2)	1.932(2)
Ni(1)–O(1)	1.8590(17)	2.033(2)
O(1)–C(1)	1.322(3)	1.313(3)
N(1)–C(6)	1.376(3)	1.357(4)
C(1)–C(2)	1.416(3)	1.432(4)
C(2)–C(3)	1.385(3)	1.381(4)
C(3)–C(4)	1.416(3)	1.424(4)
C(4)–C(5)	1.370(3)	1.369(4)
C(5)–C(6)	1.408(3)	1.415(4)
C(1)–C(6)	1.428(3)	1.443(4)
Ni(1)–N(2)	1.913(2)	2.038(2)
Ni(1)–N(3)	-----	1.996(3)
O(3)---O(2)	-----	2.930
O(3)---O(1)	-----	2.939
	Bond Angles (°)	
N(1)–Ni(1)–O(1)	85.93(8)	81.22(9)
O(1)–Ni(1)–O(2)	171.96(7)	150.36(9)
N(1)–Ni(1)–N(2)	179.29(10)	173.93(10)
N(2)–Ni(1)–N(3)	-----	80.54(10)
N(3)–Ni(1)–O(1)	-----	97.69(9)
N(3)–Ni(1)–O(2)	-----	109.70(9)

Treating **28** with bipyridine in toluene and evaporation of the volatiles yielded (ONO^{sq})Ni(bipy) (**30**), with ligand substitution confirmed by mass spectroscopy, m/z peak at 636.17, and displaying an electronic absorption spectrum with a significant decrease in the intensity of the near-IR band at 1150 nm. Complex **30** also featured a new set of near-IR bands at 778 and 890 nm (Figure 6.10). Conjecturing that this could be a consequence of the metal center adopting a five-coordinate geometry, a UV-vis solution of complex **29** was treated with excess DMAP to force equilibrium towards $(ONO^{sq})Ni(DMAP)_2$ (Figure 6.10). Addition of excess DMAP revealed the appearance of a near-IR band at 892 nm with a decreased intensity of the broad near-IR feature beyond 1000 nm, similar to that seen in **30** and consistent with the spectral feature being highly sensitive to the coordination geometry around the nickel center. This is supported by the reported electronic absorption spectrum of $(ONO^{sq})Zn(NEt_3)$, which displayed a set of near-IR absorption bands at 769 and 867 nm in THF which were absent in non-coordinating CH_2Cl_2 solutions.[11] The appearance of the bands at 769 and 867 nm in THF were accompanied by a decrease in the intensity of the near-IR band beyond 1000 nm, analogous to the spectral changes in **29**. In the reported five-coordinate $(ONO^{sq})Zn(py)_2$ the near-IR band is slightly red shifted, appearing at 956 nm.[16] These data contend that, while often used generally to assign ligand oxidation states, the near-IR features of ONO supported metal complexes are highly dependent on both the *d*-electron count of the metal center and, unexpectedly, the coordination environment of the metal center.

Electronic absorption spectroscopy indicated significant electronic effects upon axial ligand incorporation, and analysis of **30** by EPR further corroborated the importance of coordination geometry in $(ONO^{sq})Ni$ systems; the narrow, isotropic signal observed at $g=2.003$ in **28** broadened and shifted to $g=2.216$ in **30** (Figure 6.8). This deviation of the g value from 2, typically observed for ligand-based radicals, likely indicates significant nickel character in the SOMO of **30**. This can be explained by the generation of a high-spin Ni(II) center in a five-coordinate geometry.[34–39] Antiferromagnetic coupling of the ligand-based radical with a nickel-based radical would therefore leave a remaining unpaired electron on the nickel center, consistent with the observed EPR spectrum.

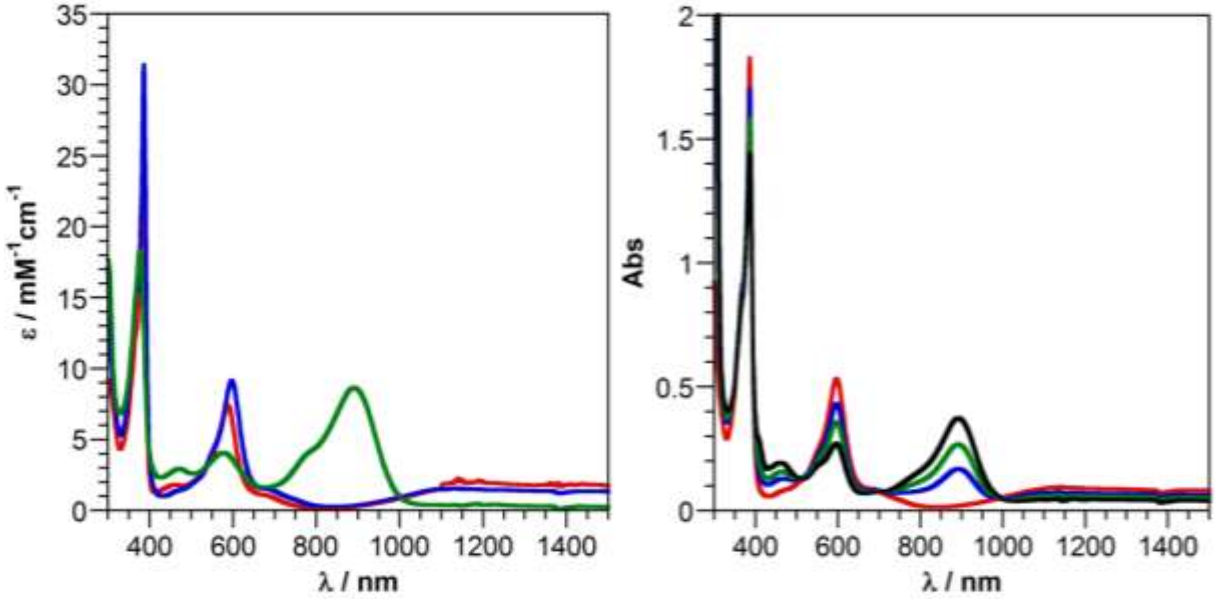

Figure 6.10. **Left**. UV-vis-NIR spectra of (ONO^{sq})Ni(py) (**red**), (ONO^{sq})Ni(DMAP) (**blue**), and (ONO^{sq})Ni(bipy) (**green**) recorded in toluene. **Right**. UV-vis-NIR spectrum of 5.5 x10^{-5} M (ONO^{sq})Ni(DMAP) (**red**) in toluene upon addition of excess DMAP: 500 equiv. (**blue**), 1000 equiv. (**green**), and 2000 equiv. (**black**).

Over a period of months, a concentrated pentane solution of **30** yielded single crystals which had grown with the incorporation of a molecule of water (Figure 6.11). The solid state structure revealed a five-coordinate metal center with a distorted square pyramidal geometry about the nickel center. Most striking is the deviation of O(2) from planarity, a result of hydrogen bonding between O(2) and O(3) of the water molecule which show a separation of 2.930 Å. This interaction results in a large Ni(1)–N(1)–O(1)–O(2) torsion angle of 18.38°, as compared to the angle of 0.16° observed in **29**. The assignment of the ligand as (ONO^{sq})$^{2-}$ is confirmed by the ligand bond metrics, which show similar bond lengths to those observed in **29**, with contracted C–O bonds of 1.31 Å (avg.) and localized double bond character in the aryl backbone. Metrical oxidation state calculation yields a value of −1.73, consistent with the (ONO^{sq})$^{2-}$ assignment of the ligand.

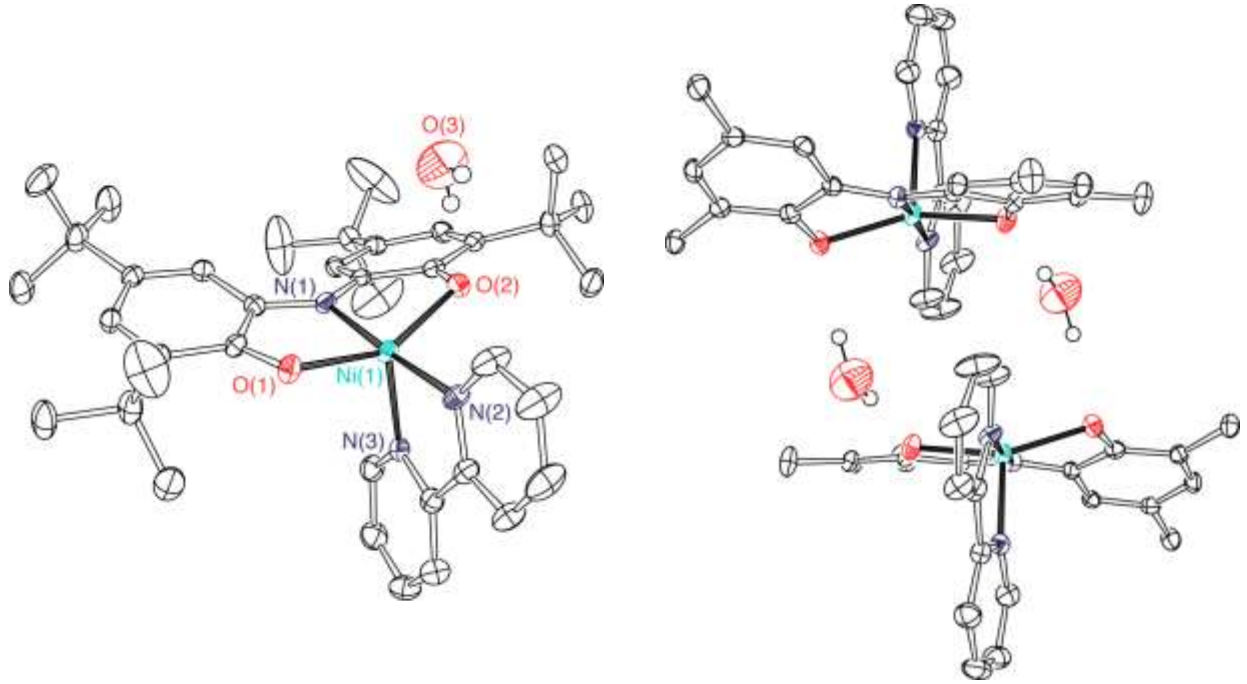

Figure 6.11. **Left**. ORTEP diagram of (ONO^{sq})Ni(bipy) (**30**). Thermal ellipsoids are shown at 50% probability. Hydrogen atoms have been omitted for clarity. **Right**. ORTEP diagram of adjacent molecules of (ONO^{sq})Ni(bipy) (**29**). Thermal ellipsoids are shown at 50% probability. Hydrogen atoms and the ligand *tert*-butyl groups have been omitted for clarity.

Complex **30** displayed similar electrochemical behavior to that of **28**, but with cathodically shifted oxidation events occurring at −0.76 and 0.60 V (Figure 6.8). The incorporation of the fifth donor group provides greater stabilization of the Ni(II) lewis acidity, increasing the electron density on the ONO ligand and making it easier to oxidize (an effect akin to that described in Chapter 2). By the same effect, the onset of the first reduction event observed in **30** is cathodically shifted by 300 mV relative to **28**. This event is irreversible, and given the similar potential of the return wave to that observed in **28**, the irreversibility is likely a result of dissociation of one of the bipyridine arms to yield a four-coordinate anion.

Although the pyridine and bipyridine coordinated complexes **28** and **30** show reversible oxidation events, attempts at converting these species to (ONO^{q})NiCl and (ONO^{q})NiCl(bipy), respectively, through delivery of a chlorine atom resulted in decomposition and the formation of the reported complex Ni(ONO^{q})$_2$.

Summary and Conclusions

With the successful synthesis of the titanium, manganese, and nickel complexes described, the first row transition-metal series of heteroleptic ONO complexes has been completed. The titanium complexes were prepared with both the $(\mathrm{ONO^{cat}})^{3-}$ and $(\mathrm{ONO^{sq}})^{2-}$ forms of the ligand, in both cases yielding Ti(IV) metal centers with one to two X-type ligands balancing the remaining charge. The family of isostructural complexes of the formula $(\mathrm{ONO})\mathrm{MCl_2(THF)}$ with M=Ti, V, and Cr demonstrated broadened resting potentials upon traversing the series from Ti→V→Cr. This trend was reversed when complexes of the (ONO)MCl(bipy) manifold with M=V and Cr were compared, indicating that care must be taken when attempting to establish periodic trends within the (ONO)M family of complexes. This cautionary result was further exemplified with the characterization of Ni complexes $(\mathrm{ONO^{sq}})\mathrm{Ni(py)}$, $(\mathrm{ONO^{sq}})\mathrm{Ni(DMAP)}$, and $(\mathrm{ONO^{sq}})\mathrm{Ni(bipy)}$. These complexes demonstrated that the near-IR bands typically observed in $(\mathrm{ONO^{sq}})^{2-}$ complexes bear significant dependence on the coordination environment and *d*-count of the transition metal center, again, suggesting that care must be taken when attempting to establish general properties for ONO complexes across the transition metal series.

Experimental

General Considerations. Manipulations were performed using standard Schlenk line techniques or in a N_2 filled glovebox. Diethyl ether, pentane, benzene, toluene, and tetrahydrofuran were sparged with argon and then dried and deoxygenated by passage through activated alumina and Q5 columns, respectively. Pyridine was dried over elemental sodium, vacuum transferred, and stored over molecular sieves. The reagents $(\mathrm{ONO^{sq}})\mathrm{K_2}$ and $(\mathrm{ONO^{q}})\mathrm{K}$ were prepared according to literature procedures.[40]

Physical Methods. Solution UV-vis-NIR spectra were recorded in 1-cm path-length cuvettes on a Shimadzu UV-1700 spectrophotometer. Extinction coefficients were determined from Beer-Lambert Law plots. EPR spectra were collected on a Bruker EMX X-band spectrometer equipped with an ER041XG microwave bridge. Electrospray ionization mass spectrometry (ESI-MS) data were collected on a Waters LCT Premier mass spectrometer. Elemental analyses were collected on a Perkin-Elmer 2400 Series II CHNS/O analyzer.

Electrochemical Methods. Electrochemical measurements were recorded with a Gamry G300 potentiostat using a standard three-electrode configuration including a 3.0 mm glassy carbon working electrode, a platinum wire auxiliary electrode, and a silver wire pseudo-reference electrode. All measurements were made on solutions that contained 1 mM analyte and 0.1 M NBu_4PF_6 in THF at an ambient temperature of ca. 21 °C in a glovebox under a N_2 atmosphere. Potentials are referenced to $Cp_2Fe^{+/0}$ using an internal standard of ferrocene, decamethylferrocene ($E°' = -0.440$ V vs $Cp_2Fe^{+/0}$ in THF)[41], or cobaltocenium hexafluorophosphate ($E°' = -1.33$ V vs $Cp_2Fe^{+/0}$ in CH_2Cl_2)[42].

Crystallographic Methods. X-ray diffraction data were collected on single crystals mounted on a glass fiber using a Bruker SMART APEX II diffractometer. Measurements were carried out using Mo Kα (λ = 0.71073 Å) radiation, wavelength selected with a single-crystal graphite monochromator. A full sphere of data was collected for each crystal structure. The APEX[43] program package was used to determine the unit cell parameters and for data collection. The raw frame data was processed using SAINT[44] and SADABS[45] to yield the reflection data files. Subsequent calculations were carried out using the SHELXTL[46] program. The structures were solved by direct methods and refined on F^2 by full matrix least-squares techniques. The analytical scattering factors[47] for neutral atoms were used throughout the analysis. Hydrogen atoms were included using a riding model. ORTEP diagrams were generated using ORTEP-3 for Windows.

Table 6.5. Data collection and refinement parameters for **21**, **26**, **27**, **29**, and **30**.

	21	**26**	**27**	**29**	**30**
Empirical Formula	$C_{32}H_{48}Cl_2NO_3Ti$	$C_{76}H_{96}N_6O_4Mn_2$	$C_{43}H_{55}MnN_4O_2$	$C_{35}H_{50}N_3O_2Ni$	$C_{38}H_{50}N_3NiO_3$
Formula Weight	613.51	1267.46	714.85	603.49	655.52
Crystal System	Monoclinic	Triclinic	Orthorhombic	Monoclinic	Monoclinic
Space Group	$C2/c$	$P\bar{1}$	$Pbca$	$P2_1/n$	$P2_1/c$
a (Å)	26.2579(14)	10.0620(9)	22.6786(11)	6.8552(5)	9.7251(8)
b (Å)	13.6036(7)	13.3484(12)	28.6621(14)	28.786(2)	16.4326(14)
c (Å)	19.3999(10)	15.4373(14)	32.3829(16)	17.5988(12)	22.4455(19)
α (°)	90	103.6617(11)	90	90	90
β (°)	106.6920(10)	93.1408(12)	90	93.2115(11)	96.6707(11)
γ (°)	90	108.1835(11)	90	90	90
Volume ($Å^3$)	6637.7(6)	1895.5(3)	21049.4(18)	3467.4(4)	3562.7(5)
Z	8	1	16	4	4
F(000)	2616	676	6112	1300	1404
Rflns. collected	39236	21338	215222	7958	40976
Ind. rflns. (R_{int})	8103 (0.0317)	9239 (0.0409)	20057 (0.0781)	7958	8672 (0.0680)
GOF	1.030	1.037	1.084	1.122	1.031
R1 [I > 2σ(I)][a]	0.0330	0.0449	0.0704	0.0475	0.0599
wR2 (all data)[a]	0.0853	0.1214	0.1930	0.0917	0.1644

[a] $R1 = \Sigma||F_o|-|F_c|| / \Sigma|F_o|$; $wR2 = [\Sigma[w(F_o^2-F_c^2)^2] / \Sigma[w(F_o^2)^2]\ ]^{1/2}$; $GOF= S = [\Sigma[w(F_o^2-F_c^2)^2] / (n-p)]^{1/2}$

$(ONO^{sq})TiCl_2(THF)$ (21). A vial was charged with $TiCl_3(THF)_3$ (0.150 g, 0.405 mmol) which was dissolved in 3 mL of THF. A 14 mL THF solution of $(ONO^q)K$ (0.186 g, 0.402 mmol) was chilled in a freezer at −35 °C and then added dropwise to the solution of $TiCl_3(THF)_3$. After stirring for 4 hours the reaction was dried under vacuum and the resulting material extracted with toluene, filtered, and dried under vacuum. The crude material was dissolved in THF and layered with pentane. After diffusion of the layers and chilling at −35 °C the product was isolated as dark brown/green crystals (0.124 g., 50%). UV-vis-NIR (THF) λ_{max}/nm (ε/M^{-1} cm^{-1}): 344 (21000), 473 (shoulder) (2390), 573 (2230), 903 (4840).

(ONO^{cat})TiCl(THF)$_2$ (22). A vial was charged with (ONO^{cat})H_3 (0.400 g, 0.940 mmol) which was dissolved in 6 mL of a 1:1 mixture of THF:Et_2O and then frozen in a cold well. Upon thawing, nBuLi (1 mL, 2.7 M, 2.70 mmol) was added. In a separate vial, $TiCl_4(THF)_2$ (0.314 g, 0.940 mmol) was slurried in 5 mL of THF and frozen in a cold well. After stirring for 25 minutes, the solution of (ONO^{cat})Li_3 was frozen in a cold well. Upon thawing of both mixtures, the solution of (ONO^{cat})Li_3 was added to $TiCl_4(THF)_2$. After stirring overnight the reaction mixture was dried under vacuum. The resulting solids were co-evaporated with toluene, then extracted with toluene, filtered, and dried under vacuum. The residue was transferred with THF to a vial, dried, pentane co-evaporated, and then washed with pentane to yield the product as a dark green solid (0.289 g, 47%). ^{1}H-NMR (400 MHz, C_6D_6) δ/ppm: 7.16 (overlapping solvent), 6.94 (d, J=2 Hz, 2H, aryl-H), 4.48 (br, 8H, THF), 1.54 (s, 18H, tBu), 1.38 (s, 18H, tBu), 1.21 (br, 8H, THF). UV-vis-NIR (THF) λ_{max}/nm (ε/M^{-1} cm^{-1}): 311(24000), 382 (6840), 460 (shoulder) (2240), 643 (2560).

(ONO^{cat})TiCl(py)$_2$ (23). A vial was charged with (ONO^{cat})TiCl(THF)$_2$ (0.052 g, 0.080 mmol) which was dissolved in 4 mL of toluene. To this solution was added pyridine (50 µL, 0.619 mmol). After 15 minutes the reaction was dried under vacuum and then coevaporated with pentane to yield the product as a green solid in quantitative yield. ^{1}H-NMR (400 MHz, C_6D_6) δ/ppm: 9.42 (dt, J=1.6, 4.9 Hz, 4H, py aryl-H), 7.14 (d, J=2 Hz, 2H, aryl-H), 6.94 (d, J=2 Hz, 2H, aryl-H), 6.63 (ddt, J=1.6, 7.3, 8.0 Hz, 2H, py aryl-H), 6.43 (ddd, J=1.6, 4.9, 7.5 Hz, 4H, py aryl-H), 1.56 (s, 18H, tBu), 1.29 (s, 18H, tBu). Anal. Calcd. For $C_{38}H_{50}N_3O_2ClTi$: C, 68.72; H, 7.59;

N, 6.33. Found: C, 68.74; H, 7.70; N, 6.15. UV-vis-NIR (toluene) λ_{max}/nm (ε/M^{-1} cm^{-1}): 312 (21300), 379 (8040), 460 (shoulder) (2120), 638 (3080).

(ONO^{cat})TiCl(bipy) (24). A vial was charged with (ONO^{cat})TiCl(THF)$_2$ (0.031 g, 0.048 mmol) which was dissolved in 4 mL of toluene. Into another vial was added 2,2'-bipyridine (0.008 g, 0.051 mmol) which was dissolved in 2 mL of toluene and added to the solution of (ONO^{cat})TiCl(THF)$_2$. After stirring for 15 minutes the solution was dried under vacuum. The crude solids were washed with four 2 mL portions of pentane, yielding the product as a dark green solid (0.027g, 84%). ^{1}H-NMR (500 MHz, $CDCl_3$) δ/ppm: 9.65 (br s, 2H, bipy aryl-H), 8.19 (d, J=8 Hz, 2H, bipy aryl-H), 8.12 (7, J=8 Hz, 2H, bipy aryl-H), 7.64 (t, J=6.5 Hz, 2H, bipy aryl-H), 6.84 (d, J=2 Hz, 2H, aryl-H), 6.60 (d, J=2 Hz, 2H, aryl-H), 1.30 (s, 18H, tBu), 1.01 (s, 18H, tBu). UV-vis-NIR (toluene) λ_{max}/nm (ε/M^{-1} cm^{-1}): 310 (33300), 370 (7270), 428 (shoulder) (5290), 592 (2640), 820 (shoulder) (330).

(ONO^{cat})TiCl(bipy) (24). Method 2. A vial was charged with KC_8 (0.024 g, 0.178 mmol) to which was added 2 mL of THF. In a separate vial was added 2,2'-dipyridine (0.026 g, 0.166 mmol) and 2 mL of THF. Both mixtures were frozen in a cold well and upon thawing the solution of bipy was added to the slurry of KC_8. After 1 hour this mixture was frozen in a cold well. In another vial was added (ONO^{sq})TiCl$_2$(THF) (0.101 g, 0.165 mmol) and 10 mL of THF. This solution was frozen in a cold well. Upon thawing of both mixtures, the *in situ* formed mixture of K(bipy$^{\cdot}$) was added dropwise to the solution of (ONO^{sq})TiCl$_2$(THF). After stirring for 2.5 hours the mixture was dried under vacuum. The crude solids were extracted with toluene, filtered, and dried under vacuum. The resulting solids were dissolved in THF and layered with pentane. Upon diffusion a first crop of green solids was collected and upon chilling the mother liquor to −35 °C a second crop was collected, yielding the product as a dark green solid (0.083 g, 76%). The product was a spectroscopic match to that obtained by Method 1.

(ONO^{cat})VCl(bipy) (25). A vial was charged with KC_8 (0.056 g, 0.414 mmol) to which was added 2 mL of THF. In a separate vial was added 2,2'-dipyridine (0.065 g, 0.416 mmol) and 2 mL of THF. Both mixtures were frozen in a cold well and upon thawing the solution of bipy was added to the slurry of KC_8. After 30 minutes this mixture was frozen in a cold well. In another vial was added (ONO^{sq})VCl_2(THF) (0.254 g, 0.412 mmol) and 7 mL of THF. This solution was frozen in a cold well. Upon thawing of both mixtures, the *in situ* formed mixture of K(bipy$^{\cdot}$) was added dropwise to the solution of (ONO^{sq})VCl_2(THF). After stirring overnight the mixture was dried under vacuum. The crude solids were extracted with toluene, filtered, and dried under vacuum. The resulting solids were dissolved in THF and layered with pentane. The dark blue precipitate was collected and dried under vacuum (0.221 g, 81%). Anal. Calcd. For $C_{38}H_{48}N_3O_2ClV$: C, 68.61; H, 7.27; N, 6.32. Found: C, 68.29; H, 7.49; N, 6.42. UV-vis-NIR (THF) λ_{max}/nm (ε/M^{-1} cm^{-1}): 305 (21900), 341 (shoulder) (11000), 422 (shoulder) (5320), 461 (5840), 606 (7750), 760 (shoulder) (1180).

(ONO)Mn(bipy) (26). A vial was charged with $MnBr_2$ (0.096 g, 0.447 mmol) and 2 mL of THF. To this slurry was added a 2 mL THF solution of 2,2'-bipyridine (0.070 g, 0.448 mmol). This mixture was stirred for 3.3 hours, at which point a 12 mL THF solution of (ONO^{sq})K_2 (0.223 g, 0.445 mmol) was added slowly dropwise. After stirring overnight the reaction was dried under vacuum. The crude solids were extracted with toluene, filtered, and dried under vacuum. The solids were dissolved in THF and layered with pentane. Upon diffusion of the layers, the mixture was filtered and the mother liquor chilled in a freezer at −35 °C. Brown solids were collected, redissolved in toluene, filtered, and dried to yield the product (0.066 g, 23%).

(ONO^{sq})Mn(py)$_3$. Crystallization of crude solids of (ONO)Mn(bipy) from pyridine solutions layered with pentane yields the product (ONO^{sq})Mn(py)$_3$. Anal. Calcd. for $C_{43}H_{55}N_4O_2Mn$: C, 72.25; H, 7.76; N, 7.84. Found: C, 72.13; H, 7.87; N, 7.67.

(ONO^{sq})Ni(py) (28). A vial was charged with $NiCl_2(py)_4$ (0.198 g, 0.444 mmol) to which was added 4 mL of THF. A 10 mL THF solution of (ONO^{sq})K_2 (0.224 g, 0.447 mmol) was added dropwise to the slurry of $NiCl_2(py)_4$. After stirring overnight the reaction was dried under vacuum. The crude material was extracted with toluene, filtered, and dried under vacuum. The resulting solids were slurried in 2 mL of pentane and chilled overnight in a freezer at −35 °C. Removal of the mother liquor yielded the product as a purple solid (0.201 g, 81%). Anal. Calcd. For $C_{33}H_{45}N_2O_2Ni$: C, 70.73; H, 8.09; N, 5.00. Found: C, 70.27; H, 8.01; N, 4.98. UV-vis-NIR (toluene) λ_{max}/nm (ε/M^{-1} cm^{-1}): 366 (shoulder) (12300), 384 (24700), 462 (1880), 588 (7460), 680 (shoulder) (1130), 1150 (1660). MS (ESI+) *m/z*: 559.38 (M+).

(ONO^{sq})Ni(dmap) (29). A vial was charged with (ONO^{sq})Ni(py) (0.082 g, 0.152 mmol) which was dissolved in 4 mL of toluene. A 2 mL toluene solution of 4-dimethylaminopyridine (0.018 g, 0.147 mmol) was added to the solution of (ONO^{sq})Ni(py). After 20 minutes the reaction was dried under vacuum, slurried in 2 mL of pentane, and chilled overnight in a freezer at −35 °C. The mother liquor was removed to yield blue solids, which were washed with 4x2 mL portions of pentane to yield the product (0.075 g, 84%). Anal. Calcd. For $C_{35}H_{50}N_3O_2Ni$: C, 69.66; H, 8.35; N, 6.96. Found: C, 69.43; H, 8.44; N, 6.92. UV-vis-NIR (toluene) λ_{max}/nm (ε/M^{-1} cm^{-1}): 368 (shoulder) (15300), 386 (30100), 597 (9290), 1130 (1620). MS (ESI+) *m/z*: 602.25 (M+).

(ONO^{sq})Ni(bipy) (30). A vial was charged with (ONO^{sq})Ni(py) (0.072 g, 0.128 mmol) which was dissolved in 4 mL of toluene. A 2 mL toluene solution of 2,2’-bipyridine (0.020 g, 0.128 mmol) was added to the solution of (ONO^{sq})Ni(py). After 30 minutes the reaction was dried under vacuum, slurried in 2 mL of pentane, and chilled overnight in a freezer at −35 °C. The mother liquor was removed to yield purple solids, which were washed with 3x2 mL portions of pentane to yield the product (0.081 g, 99%). Anal. Calcd. For $C_{38}H_{48}N_3O_2Ni$: C, 71.59; H, 7.59; N, 6.59. Found: C, 71.02; H, 7.75; N, 6.25. UV-vis-NIR (toluene) λ_{max}/nm (ε/M^{-1} cm^{-1}): 376 (18300), 471 (3140), 576 (4100), 778 (shoulder) (4230), 890 (9250), 1140 (350). MS (ESI+) *m/z*: 636.17 (M+).

Titration of (ONO^{sq})Ni(DMAP). Solutions of (ONO^{sq})Ni(DMAP) (2.5 mL, 5.53 $x10^{-5}$M) were treated with varying amounts of either solid DMAP or a 0.65 M solution in toluene: 50 equiv. (10.6 µL of 0.65 M solution), 100 equiv. (21.2 µL of 0.65 M solution), 500 equiv. (8.4 mg. solid DMAP), 1000 equiv. (17.0 mg. solid DMAP), 2000 equiv. (33.8 mg. solid DMAP). The stock solution was examined with no added DMAP for direct comparison.

References

(1) Girgis, A.; Balch, A. *Inorg. Chem.* **1975**, *14*, 2724.
(2) Larsen, S.; Pierpont, C. *J. Am. Chem. Soc.* **1988**, *110*, 1827.
(3) Simpson, C.; Boone, S.; Pierpont, C. *Inorg. Chem.* **1989**, *28*, 4379.
(4) Bruni, S.; Caneschi, A.; Cariati, F.; Delfs, C.; Dei, A.; Gatteschi, D. *J. Am. Chem. Soc.* **1994**, *116*, 1388.
(5) Ranis, L. G.; Werellapatha, K.; Pietrini, N. J.; Bunker, B. A.; Brown, S. N. *Inorg. Chem.* **2014**, *53*, 10203.
(6) Bencini, A.; Ciofini, I.; Giannasi, E.; Daul, C. a.; Doclo, K. *Inorg. Chem.* **1998**, *37*, 3719.
(7) Cador, O.; Chabre, F.; Dei, A.; Sangregorio, C.; van Slageren, J.; Vaz, M. G. F. *Inorg. Chem.* **2003**, *42*, 6432.
(8) Caneschi, A.; Cornia, A.; Dei, A. **1998**, *1669*, 3419.
(9) Chaudhuri, P.; Hess, M.; Hildenbrand, K.; Bill, E.; Weyhermüller, T.; Wieghardt, K. *Inorg. Chem.* **1999**, *38*, 2781.
(10) Evangelio, E.; Bonnet, M.-L.; Cabañas, M.; Nakano, M.; Sutter, J.-P.; Dei, A.; Robert, V.; Ruiz-Molina, D. *Chemistry* **2010**, *16*, 6666.
(11) Speier, G.; Csihony, J.; Whalen, A.; Pierpont, C. *Inorg. Chem.* **1996**, *35*, 3519.
(12) Hananouchi, S.; Krull, B. T.; Ziller, J. W.; Furche, F.; Heyduk, A. F. *Dalton Trans.* **2014**, *43*, 17991.
(13) Wong, J. L.; Sánchez, R. H.; Logan, J. G.; Zarkesh, R. A.; Ziller, J. W.; Heyduk, A. F. *Chem. Sci.* **2013**, *4*, 1906.
(14) Szigethy, G. *Unpubl. Results*.
(15) Chaudhuri, P.; Hess, M.; Weyhermüller, T.; Wieghardt, K. *Angew. Chemie Int. Ed.* **1999**,

38, 1095.
(16) Wong, J. L.; Higgins, R. F.; Bhowmick, I.; Cao, D. X.; Szigethy, G.; Ziller, J. W.; Shores, M. P.; Heyduk, A. F. *Chem. Sci.* **2015**, 1.
(17) Lu, F.; Zarkesh, R. A.; Heyduk, A. F. *Eur. J. Inorg. Chem.* **2012**, *2012*, 467.
(18) Szigethy, G.; Shaffer, D. W.; Heyduk, A. F. *Inorg. Chem.* **2012**, *51*, 12606.
(19) Zarkesh, R.; Ziller, J. W.; Heyduk, A. F. *Angew. Chem. Int. Ed. Engl.* **2008**, *47*, 4715.
(20) Wright, D. D.; Brown, S. N. *Inorg. Chem.* **2013**, *52*, 7831.
(21) Cipressi, J.; Brown, S. N. *Chem. Commun.* **2014**, *50*, 7956.
(22) Heyduk, A.; Zarkesh, R.; Nguyen, A. *Inorg. Chem.* **2011**, *50*, 9849.
(23) Saji, T.; Aoyagui, S. *J. Electroanal. Chem.* **1975**, *63*, 405.
(24) Zah-Letho, J.; Samuel, E.; Livage, J. *Inorg. Chem.* **1988**, *27*, 2233.
(25) Konig, E.; Herzog, S. *J. Inorg. Nucl. Chem.* **1970**, *32*, 601.
(26) Shah, S. S.; Maverick, A. W. *Inorg. Chem.* **1986**, *25*, 1867.
(27) Toma, H. E.; Santos, P. S.; Lellis, F. T. P. *J. Coord. Chem.* **1988**, *18*, 307.
(28) Nachtigall, O.; Pataki, A.; Molski, M.; Lentz, D.; Spandl, J. *Zeitschrift für Anorg. und Allg. Chemie* **2015**, *641*, 1164.
(29) Bartlett, M.; Palenik, G. J. *J. Chem. Soc. Chem. Commun.* **1994**, 416.
(30) Chun, H.; Chaudhuri, P.; Weyhermüller, T.; Wieghardt, K. *Inorg. Chem.* **2002**, *41*, 790.
(31) Das, G.; Shukla, R.; Mandal, S.; Singh, R.; Bharadwaj, P. K.; Hall, J. Van; Whitmire, K. H. *Inorg. Chem.* **1997**, *36*, 323.
(32) Lis, T. *Acta Crystallogr.* **1980**, *B36*, 2042.
(33) Mantel, C.; Hassan, A. K.; Pécaut, J.; Deronzier, A.; Collomb, M. N.; Duboc-Toia, C. *J. Am. Chem. Soc.* **2003**, *125*, 12337.
(34) Ciampolini, M. *Inorg. Chem.* **1966**, *5*, 35.
(35) Furlani, C. *Coord. Chem. Rev.* **1968**, *3*, 141.
(36) Legg, I. J.; Nielson, D. O.; Smith, D. L.; Larson, M. L. *J. Am. Chem. Soc.* **1968**, *90*, 5030.
(37) Sacconi, L.; Bertini, I. *J. Am. Chem. Soc.* **1968**, *90*, 5443.
(38) Sacconi, L.; Orioli, P. L.; Di Vaira, M. *J. Am. Chem. Soc.* **1965**, *87*, 2059.
(39) Yamada, S.; Ohno, E.; Kuge, Y.; Takeuchi, A.; Yamanouchi, K.; Iwasaki, K. *Coord. Chem. Rev.* **1968**, *3*, 247.
(40) Szigethy, G.; Heyduk, A. *Dalt. Trans.* **2012**, *41*, 8144.
(41) Aranzaes, J. R.; Daniel, M.-C.; Astruc, D. *Can. J. Chem.* **2006**, *84*, 288.
(42) Connelly, N. G.; Geiger, W. E. *Chem. Rev.* **1996**, *96*, 877.
(43) APEX2, Version 2014.11-0, Bruker AXS, Inc.; Madison, WI 2014.
(44) SAINT, Version 8.34a, Bruker AXS, Inc.; Madison, WI 2013.
(45) Sheldrick, G. M. SADABS, Version 2014/5, Bruker AXS Inc.; Madison, WI 2014.
(46) Sheldrick, G. M. SHELXTL, Version 2014/7, Bruker AXS Inc.; Madison, WI 2014.
(47) International Tables for Crystallography 1992, Vol C., Dordrecht: Kluwer Academic Publishers.